UNIVERSITY OF SOUTHAMPTON

Hyperpolarized Long-Lived States in Monodeuterated Methyl Groups & Singlet-Scalar Relaxation in the Regime of Slow Quadrupolar Relaxation

by

Stuart James Elliott

A thesis submitted in partial fulfillment for the degree of Doctor of Philosophy

in the
Faculty of Natural and Environmental Sciences
School of Chemistry

06/01/2019

UNIVERSITY OF SOUTHAMPTON

ABSTRACT

FACULTY OF NATURAL AND ENVIRONMENTAL SCIENCES
SCHOOL OF CHEMISTRY

Doctor of Philosophy

by Stuart James Elliott

Nuclear magnetic resonance (NMR) experiments are time-limited by relaxation dynamics. Observing non-equilibrium magnetization is restricted to timescales governed by the longitudinal relaxation time T_1. The use of long-lived states (LLS) offers a promising means to transcend this limitation. LLS are configurations of nuclear spins that are protected against the in pair dipole-dipole relaxation mechanism, with other sources of relaxation significantly attenuated. In systems of spin-1/2 pairs, the LLS is called singlet order and the decay time constant is denoted T_S.

The field of LLS NMR is now flourishing, LLS lifetimes exceeding T_1 by a factor of 50 have been observed, with a lifetime $T_S > 1$ hour observed in room-temperature solution in one case. LLS have even been observed in the 3-spin-1/2 systems of rapidly rotating methyl groups in solution.

The work presented in this thesis builds on previous efforts from the LLS community. Most notably, prior attempts at methyl LLS are restricted to just a single case. Through my work, I have extended the family of molecules in which methyl LLS are accessible, achieved with high conversion efficiencies in suitable cases. The use of *monodeuterated* methyl groups as coherently accessible reservoirs for nuclear singlet order has lead to the longest observed methyl LLS. The relaxation dynamics of two motionally different cases are examined and geometrical models are presented to explain the experimental results. Hyperpolarization results for these systems are also presented.

My work has lead to the investigation of more curious phenomena such as the singlet-scalar relaxation of the second kind (S-SR2K) mechanism. In the regime of slow quadrupolar relaxation, where T_1 is significantly slower than the timescale of the nuclear Larmor period, this relaxation mechanism dramatically shortens singlet lifetimes. An experimental demonstration is provided for the case of a ^{13}C labelled, deuterated fumarate derivative. This study differs from previous work on this subject, which examines the limit where the T_1 of the third spin is on the timescale of the nuclear Larmor frequency, rarely the case for deuterium nuclei. I provide rate expressions and numerical simulations for the LLS decay in the S-SR2K regime of slow quadrupolar relaxation.

Contents

List of Figures

List of Tables

Thesis Outline

The work presented in this thesis is the result of multiple research projects undertaken whilst in candidature for a PhD at the University of Southampton. The work is centred around long-lived nuclear spin states, which is an ongoing research effort in the group of Prof. Malcolm H. Levitt. The two main research themes of this thesis are hyperpolarized long-lived states in monodeuterated methyl groups, and singlet state relaxation via scalar relaxation of the second kind. The thesis is organised as follows:

Chapter 1: Introduction

- Introduction to the basics of nuclear magnetic resonance (NMR).
- A discussion of angular momentum, spin, precession, relaxation and other topics relevant to NMR.
- Particular attention is paid to near chemically equivalent spin systems, and the effects on NMR spectra.
- A summary of rotations and other mathematical/quantum mechanical tools.
- A presentation of the main interactions covered by the work in this thesis.

Chapter 2: Hyperpolarization and singlet states

- A section on NMR hyperpolarization and dissolution-dynamic nuclear polarization (D-DNP).
- An in depth coverage of singlet state NMR, including the key properties of nuclear singlet states.
- Discussion is facilitated by quantum mechanical descriptions and useful mathematical instruments.
- A small section on singlet NMR techniques, such as the use of radiofrequency pulse sequences, is included to provide background for the reader before discussion of the experimental results.

Chapter 3: Long-lived nuclear spin states in monodeuterated methyl groups

- Results of long-lived state NMR experiments on monodeuterated methyl group (CH_2D) bearing compounds.
- A constant ratio between the lifetimes of singlet order and longitudinal magnetization was observed over a wide range of conditions.
- A distorted CH_2D geometry is put forward to describe the experimental results.
- Examples are presented for two compounds with different motional regimes.

Chapter 4: Direct hyperpolarization and coherent readout of long-lived proton singlet order

- Hyperpolarization experiments on CH_2D containing molecules.
- Hyperpolarized singlet order is generated directly from D-DNP.
- CH_2D singlet order was found to be long-lived under hyperpolarized conditions.

Chapter 5: Singlet-scalar relaxation of the second kind in the regime of slow quadrupolar relaxation

- A discussion of the singlet-scalar relaxation of the second kind (S-SR2K) mechanism.
- The theoretical aspects of the mechanism are described, supported by numerical simulations.
- Experimental findings are presented for the case of a ^{13}C-labelled, deuterated fumarate diester.

Conclusions and further work are presented at the end of each chapter, including a summary of the main results found. Perspectives on hyperpolarized singlet NMR are given at the end of the thesis.

Acknowledgements

I would like to begin by thanking my supervisor, Professor Malcolm H. Levitt. He has been a tremendously supportive and encouraging supervisor at all times throughout my PhD. Somehow, with everything else he has to do, he finds the time to help *all* of his students, not just myself. He really is the supervisor that everybody wishes they could have. He has been a patient and knowledgable figure, from whom I have learnt a great deal and will continue to do so long into the future. Thank you for everything.

I also owe many thanks to my co-supervisor, Professor Marcel Utz. Marcel has been an incredibly understanding supervisor, especially during the early phase of my PhD where nothing seemed to be going to plan. He is a constant source of ideas and inspiration, of which I am very grateful.

I am wholly indebted to Dr. Lynda J. Brown, who has provided almost all the molecules presented in this thesis. Without Lynda, this PhD would not have been possible. I must also thank Dr. Joseph T. Hill-Cousins and Stuart Sawyer for synthesising the remaining compounds.

Now, I must acknowledge my collaborators outside of Southampton, of which there are a great deal. Firstly, I would like to thank Dr. Jean-Nicolas Dumez (CNRS, Saclay) for his involvement in my work on monodeuterated methyl groups. I wish him all the best with his high-quality work but also with his young family.

Furthermore, I need to thank Professor Daniel J. O'Leary (Pomona College, USA). I met Dan "online" and we have been talking ever since. Dan shared his vast computational chemistry knowledge with me, from which we created a very profitable collaboration. He has been an incredibly kind person and always has the time to provide useful insights. I have very much enjoyed my time working with him. I must also thank his postdoc, Dr. O. Maduka Obga, who is genuinely one of the nicest people I have ever met. Finally, I must thank David A. Kolin and Sebastian Cevallos for their efforts in our collaboration.

I would like to thank my collaborators Prof. Sami Jannin and Dr. Basile Vuichoud (Université de Lyon, France), and Prof. Lyndon Emsley (EPFL, Switzerland), for assistance with dissolution-dynamic nuclear polarization experiments. Their insights and help have provided me with a great deal of results for my thesis, and have made it complete.

I must also thank my collaborators in industry, namely Dr. James G. Kempf, Dr. Robert Krull and Dr. Melanie Rosay (Bruker Biospin, USA) for absolutely everything whilst I was on a internship with them in Billerica. My thanks also to everyone at Billerica who made the experience as fantastic as it was.

People to whom I owe my thanks in other collaborations include; Professor Robert G. Griffin (MIT, USA), Dr. Robert Silvers (MIT, USA), Dr. P. Jan. M. van Bentum (Radboud University Nijmegen, The Netherlands), Professor Arno G.M. Kentgens (Radboud University Nijmegen, The Netherlands), Sebastian (Bas) van Meertens (Radboud

University Nijmegen, The Netherlands), Dr. Fabien Ferrage (CNRS, Paris) and Dr. Pavel Kadeřávek (CNRS, Paris).

I owe a great deal to those past and present at Southampton, particularly Dr. Giuseppe Pileio for his guidance with my work on singlet-scalar relaxation of the second kind in the regime of slow quadrupolar relaxation. Dr. Benno Meier and Dr. Gabriele "S2M" Stevanato (EPFL, Switzerland) for their highly impressive efforts with the hyperpolarized experiments and putting up with me being ill at the same time. I must also express my gratitude towards; Dr. Soumya Singha Roy (University of York, UK), Dr. Stefan Glöggler (MPI-Göttingen, Germany), Dr. Javier Alonso-Valdesuerio (University of the Basque Country, Spain), Dr. Karel Kouřil, Dr. Pär Håkansson (University of Oulu), Dr. Maria Concistrè, Dr. Hana Kouřilova, Dr. Salvatore Mamone (MPI-Göttingen, Germany), Manvendra Sharma, Shamim Alom, Dr. Ilya Kuprov, Dr. Elizaveta A. Suturina and Professor Phillip W. Kuchel from Sydney (University of Sydney, Australia).

I wish Michael M. Jolly, David L. Goodwin, Luke S. Edwards and Eva E. Scherer the best of luck with writing their theses and passing their VIVAs. I would like to wish Ahmed Jassim Allami, James Eills, William Hale, Jai Balachandra, Steven Worswick, Aliki Moysiadi and Christian Bengs a great deal of luck with the rest of their PhDs.

I would like to thank my sponsors for providing funds throughout the course of my studentship, these sponsors include: grant codes EP/N002482 and EP/L505067/1, EPSRC (UK), Bruker (UK), iMR CDT, BBSRC, STSM COST Action "EURELAX", Pomona College, ENC and IOP. A special thank you to Dr. Christopher J. Wedge (University of Huddersfield, UK) for assistance with EPR experiments and simulations.

Last, but not least, I owe so much to my incredibly supportive family, who have stood by my side the whole way through this process, and are probably quite excited that I might get a job out of all this. My partner Danny has been just as supportive, and was able to be a calming influence under all the stress I felt whilst writing this thesis.

Declaration

This thesis is the result of work done wholly while I was registered in candidature for a PhD at the University of Southampton. The material presented herein is based on work mostly completed by myself. Where work was carried out jointly with others a substantial part is my own original research, and co-workers and their roles have been clearly indicated. The material contained herein has not been submitted by the author for a degree at any other institution. Appropriate figures have been reproduced from Phys. Chem. Chem. Phys. 18, 17965-17972 (2016) with permission from the PCCP Owner Societies.

Supervisor: Malcolm Harris Levitt
Co-supervisor: Marcel Utz

External examiner: Alexej Jerschow
Internal examiner: Joern Werner

It is a good morning exercise for
a research scientist to discard a
pet hypothesis every day before
breakfast. It keeps him young.

Konrad Lorenz

To my father

Chapter 1

Introduction

1.1 NMR spectroscopy

Spectroscopy is a scientific territory concerning the interaction between energy and matter. Matter either emits or absorbs radiation and the resulting change in energy is detected and interpreted. Spectroscopic techniques can ultimately provide information on the substructure of atoms and molecules in a variety of systems. In chemistry, scientists are involved with the reactivity and kinetics of matter, in which molecular structure and motion play a vital role. Nuclear magnetic resonance (NMR) spectroscopy is a widely used technique in the physical sciences and can reveal information regarding transformation and dynamics over a wide range of timescales. NMR is a powerful analytical tool and is also able to correctly determine material structures. Structural interpretation is often found to be in good agreement with elegant data-to-structure techniques such as X-ray crystallography, see figure 1.1a). The non-invasive nature of magnetic resonance is additionally highly suitable for *in vivo* work in hospital clinics and magnetic resonance imaging (MRI) is at the forefront of medical healthcare diagnostics.

Magnetic resonance phenomena were first observed by Rabi in 1938 using molecular beams [3]. Rabi, together with coworkers, developed a new method for measuring nuclear magnetic moments, which was awarded the Nobel prize in physics in 1944 [4]. A short while later, Purcell, Torrey and Pound [5], with simultaneous development efforts offered by Bloch and Packard [6], invented and expanded the relatively new field of NMR in bulk matter. In 1952, Purcell and Bloch shared the Nobel prize in physics

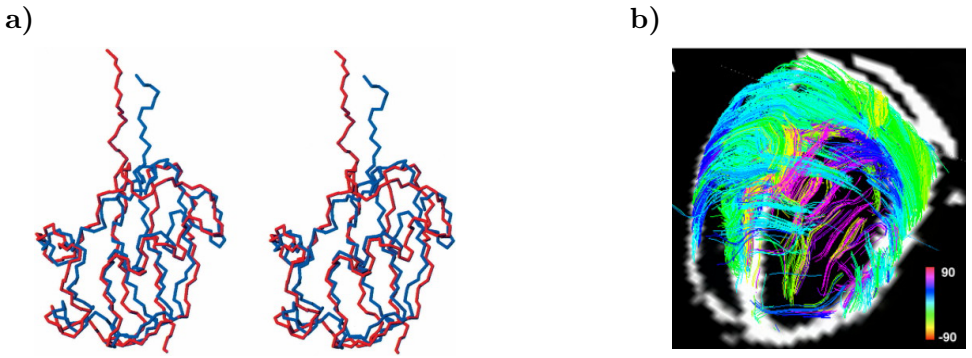

FIGURE 1.1: a) Superimposed structures of ubiquitin determined by x-ray crystallography (red) and NMR (blue). The structural determination of ubiquitin by NMR is remarkably accurate and in this case was achieved purely by using two-dimensional techniques, without assignments of one-dimensional spectra [1]. b) Diffusion spectrum imaging (DSI) tractography of a rat heart. The muscle fibres of the rat heart are colour coded with respect to helix angle [2].

for these feats. It must be noted that the effect was narrowly missed by Gorter in 1942 due to the long relaxation times of the LiCl crystals used in his experiments [7]. NMR has come a long way in just 65 years. For example, modern day NMR magnets provide large magnetic fields ($> 10\,\mathrm{T}$) through the use of superconducting materials which are cooled to $\sim 4\,\mathrm{K}$ by cryogenic substances. The improved resolution and sensitivity granted by large magnetic fields has advanced NMR spectroscopy and surrounding scientific fields, such that previously troublesome structure assignments [8] and metabolic tracing experiments [9] are now common practices.

NMR spectroscopy concerns the behaviour of a nuclear ensemble in the presence of a magnetic field. Particles with inherent nuclear spin are subjected to manipulation of their quantum mechanical properties by interactions with intricately designed electromagnetic pulses. In this way, a real grasp of the microscopic world around us may be achieved and the probing of complicated systems is made possible. A well harnessed phenomenon in NMR, which is used for structural assignment and process monitoring, is the loss of spin order during the relaxation times T_1 and T_2. After the excitation of a particular isotopic species in a sample, or molecular tag in a human patient, information is continuously lost until the unperturbed starting conditions are restored. Although typically restricted to a just a few seconds, relaxation times have already served research and clinical scientists in efforts to probe regimes of slow molecular motion such as diffusion [10], which can be used to investigate the structure of muscle fibres in the heart, see figure 1.1b). Measurements of proton T_1 and T_2 have allowed a preview into the world of protein folding and unfolding [11], and conformational exchange [12]. Labelling

of biologically relevant materials with ^{13}C and ^{15}N isotopes has also become increasing popular, as NMR not only provides clear cut information regarding molecular structure but the longer lifetimes of these agents opens up the possibility to study exchange rates and obtain diffusion coefficients over extended time periods [11, 13].

A relatively new form of nuclear information storage is provided by long-lived states [14–23, 23–27] which aims to overcome the limiting nuclear relaxation time in an alternative fashion. The pioneering work of Levitt and co-workers has unequivocally demonstrated that, by using the symmetry properties of nuclear spin-1/2 pairs, it is possible to extend the lifetime of spin order, and lengthen relaxation times by more than an order of magnitude [28–35]. Previously undetectable quantum states are now accessed via novel pulsed methods, and the slow harvesting of spin order is facilitated by symmetry protected molecular systems. A particularly successful early case of a long-lived bearing substance was a partially deuterated saccharide system [18] with a "hidden" relaxation time 37 times longer than that associated with T_1. An equally impressive achievement came from Pileio and coworkers, who recorded a 9 minute lifetime for N_2O dissolved in blood. Recently, a Naphthalene derivative with a long-lived lifetime exceeding 1 hour in a room temperature solution has been observed.

The opening couple of chapters in this thesis are intended to assist the reader in understanding how some of the phenomena described above are possible.

1.2 The basics of NMR

1.2.1 Spin angular momentum

Atoms and molecules are known to carry two distinct forms of momentum. Angular momentum arises when a particle executes a trajectory along a curved path, much like the electron orbiting the nucleus. Spin is the second variety of angular momentum and is intrinsic to the majority of nuclei in nature. However, spin is not related in any way to the rotation of a molecule. In quantum mechanics, spin angular momentum $\vec{I}$ is quantized in units of $\hbar$ ($6.63 \times 10^{-34}/2\pi$ Js). The allowed, quantized values of $\vec{I}$ are:

$$\vec{I} = \hbar\sqrt{I(I+1)}, \tag{1.1}$$

where I is the principal spin quantum number and can be any non-negative n-integer value of $n/2$, i.e. 0, 1/2, 1, 3/2, etc.

The initial formalism of spin was gradually accepted by the scientific community, and was later supported by clear-cut experimental evidence. One confounding finding emerged from the Stern-Gerlach experiment in 1922 [36], some years before Uhlenbeck and Goudsmit formulated the hypothesis of the spin-1/2 electron [37]. Later, in 1928, Dirac successfully modelled a spin-1/2 electron from a theory of relativistic quantum mechanics [38].

The spin angular momentum of a nucleus manifests itself as a discrete set of energy levels governed by a certain group of quantization conditions: m_I = -I, -I+1, ..., I -1, I, where m_I is known as the spin projection quantum number. The energy levels of a nucleus are $2I+1$ degenerate, meaning there are $2I+1$ spin states of equal energy in the absence of a magnetic field. The degeneracy is lifted in the presence of a magnetic field $\vec{B}$ and the $2I+1$ sublevels are consequently unveiled [39]. This is an important feature of quantum mechanics which, in magnetic surroundings, allows NMR to function. In the simplest case, one might consider the primary isotope of the hydrogen atom, the nucleus of which consists of a single proton (^{1}H) with a nuclear spin $I = 1/2$ [40]. Therefore, for the hydrogen nucleus in a magnetic field, the degenerate energy levels are split into two sublevels, with $m_I = \pm 1/2$. The quantized energy difference ΔE between the two states in the revealed energy level structure is the subject of interrogation by NMR spectroscopy, see figure 1.2.

1.2.2 Magnetic moments

The interaction between a nuclear spin and its magnetic environment is expressed by the magnetic moment $\vec{\mu}$. A scalar product between $\vec{\mu}$ and the magnetic field vector $\vec{B}$ leads to the magnetic energy V_m of such an interaction:

$$V_m = -\vec{\mu} \cdot \vec{B} = -\left|\vec{\mu}\right| \left|\vec{B}\right| \cos(\phi), \tag{1.2}$$

where ϕ is the angle between the nuclear magnetic moment and the magnetic field. In NMR, the direction of the static magnetic field $\vec{B}$ is defined to be along the z-axis of a right-handed Cartesian coordinate system, which has orthonormal unit vectors. The

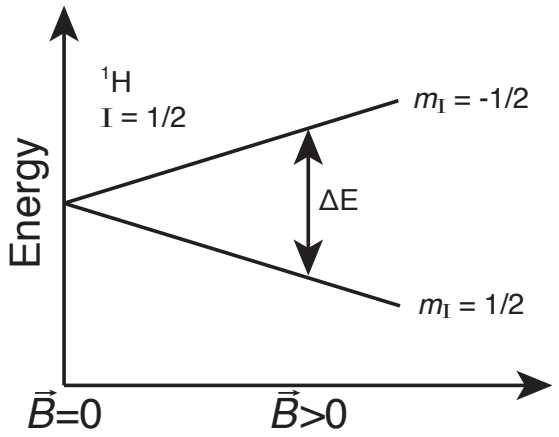

FIGURE 1.2: The presence of a magnetic field lifts the energy degeneracy for a nucleus with inherent nuclear spin. An energy level structure with splittings proportional to the nuclear spin number I is revealed. This phenomenon is known as the Zeeman effect and is shown for the case of $I = 1/2$.

orientational dependence of V_m on the magnetic moments alignment with or against $\vec{B}$ is clear. When the two vectors are aligned parallel the energy achieved is lower than any other orientational configuration. Therefore, any free magnetic moment in a magnetic field will minimize its magnetic energy and align parallel to the magnetic field [41].

1.2.3 Microscopic magnetism

Magnetism on the microscopic scale is dictated by three major sources:

- electrical currents on the molecular length scale
- magnetic moments of electrons
- magnetic moments of nuclei

The circulation of electronic currents contribute negatively to the magnetic susceptibility (a measure of the extent to which a material develops a magnetic moment on exposure to a magnetic field). The presence of magnetic moments contributes positively to the magnetic susceptibility, i.e. these properties tend to align with an external magnetic field.

Nuclei, like electrons, simply possess an intrinsic permanent magnetism, as they do intrinsic spin, which is *not* a consequence of an electrical current. The nuclear magnetic

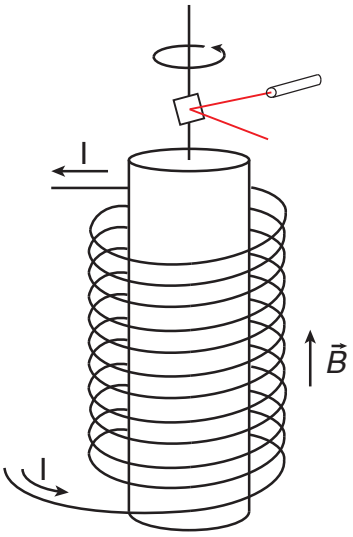

FIGURE 1.3: The Einstein-de Haas effect. A ferromagnetic rod is vertically magnetized by a current passing through an encasing solenoid. The rod rotates in order to conserve angular momentum and its motion is captured via the use of a laser and mirror. In this figure, I represents the current in the solenoid [43].

moment is a fundamental property and is related to the spin angular momentum:

$$\hat{\mu} = \gamma \hat{I}, \tag{1.3}$$

where the "hats" indicate that these two properties are quantum mechanical operators. γ is the gyromagnetic ratio and as a scalar may carry either sign. Hence, the magnetic moment can either orient parallel or anti-parallel to the spin angular momentum, depending on the sign of γ. A positive γ implies that the nuclear magnetic moment and spin angular momentum point in the same direction in space. A similar relationship was cleverly demonstrated for the orbital angular momentum of the electron by Einstein and de Haas in 1915. An experiment was constructed whereby a ferromagnetic rod suspended vertically by its long axis was subsequently magnetised along its entire length by an aligned magnetic field emanating from a surrounding coil [42]. As a net magnetization attributed to an alignment of magnetic moments corresponds to a gain in angular momentum, the rod began to rotate in the opposite sense to fulfil the conservation laws of angular momentum, see figure 1.3.

1.2.4 Spin polarization vector

As shown in equation 1.2, the magnetic moment is described by using a vector representation. In the same way, the spin angular momentum of a nucleus is also represented as a vector. The direction of the spin angular momentum vector is more commonly referred to as *spin polarization*. The spin polarization vector may point in any direction in space. From previous arguments one may assume that only two directions of spin polarization are permitted, with and against the magnetic field. However, this perception is incorrect and fuller quantum mechanical description is necessary [44]. In the language of quantum mechanics, the direction of the spin polarization vector may be expressed as a superposition of well defined quantum states. The expectation value of the operator $\hat{I}$ acting on this state would return the classical analogue, see chapter 2 for more details [39].

The concept of the spin polarization vector may too be applied to an ensemble of nuclei in order to describe the direction of the overall spin angular momentum vector at thermal equilibrium. The governing state of the entire system would be written as a superposition of quantum states summed over the entire nuclear ensemble. The expectation integral of this overall state would yield a small but non-zero measurement in the absence of a magnetic field. In this a case, the individual angular momentum vectors for an ensemble of spins would maintain a completely isotropic geometrical distribution [41], leading to a near zero net spin polarization or magnetization $\vec{M}$:

$$\vec{M} = \sum_{i}^{N} \vec{\mu}_i \approx 0, \tag{1.4}$$

for N spins in the nuclear ensemble. Suppose the nuclear ensemble is instantaneously moved into a region of non-zero magnetic field. The lowest energy orientation for a single spin occurs from an alignment of the magnetic moment with the magnetic field, see equation 1.2. Therefore, a free spin will align its magnetic moment along the magnetic field axis. Under these conditions, the expectation value of $\hat{I}$ for the ensemble of nuclei corresponds to a larger net spin polarization which is aligned with the static magnetic field, see section 1.2.6 for more details.

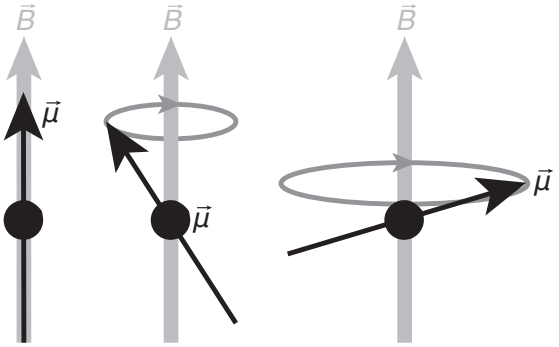

FIGURE 1.4: Precession cones of three spin-1/2 nuclei (γ>0) oriented at various angles with respect to the static magnetic field. If the spin polarization vector is tilted away from the axis of the static magnetic field, precessional motion sweeps out a cone of constant angle.

1.2.5 Precession

A torque or turning force $\vec{G}$ acts upon a magnetic moment when situated in a magnetic field:

$$\vec{G} = \vec{\mu} \wedge \vec{B} = |\vec{\mu}|\,|\vec{B}|\sin(\phi), \tag{1.5}$$

where the vector $\vec{G}$ is orthogonal to both vectors $\vec{\mu}$ and $\vec{B}$ provided $\vec{\mu} \wedge \vec{B} \neq \vec{0}$. The direction of $\vec{G}$ is determined by the "right-hand rule". Torque is a property related to the rate of change of angular momentum. By using equations 1.3 and 1.5 one achieves:

$$\frac{d\vec{\mu}}{dt} = \gamma\vec{\mu} \wedge \vec{B}. \tag{1.6}$$

Hence, motion is perpendicular to both $\vec{\mu}$ and $\vec{B}$ and the effect is for the spin polarization to precess around the magnetic field in a cone, see figure 1.4. The cone angle depends on the initial direction of the nuclear spin polarization vector in space with respect to the static magnetic field. This type of motion is called *precession*. Precessional motion is shown in figure 1.4 for nuclei with different orientations of the nuclear spin polarization vector. This idea can also be translated to the overall spin polarization vector and is used when considering the application of radiofrequency pulses to the nuclear ensemble.

The frequency of spin precession $\vec{\omega}_0$ is known as the nuclear Larmor frequency and is related to the magnetic field strength and direction via γ:

$$\vec{\omega}_0 = -\gamma\vec{B}_0, \tag{1.7}$$

where $\vec{B}_0$ is the magnetic field at the location of the nucleus. The sign of the spin precession indicates its direction. Most nuclei have a positive gyromagnetic ratio resulting in a negative Larmor frequency, viewed as a clockwise precession when observing down the positive magnetic field axis [42].

1.2.6 Relaxation

The majority of the research effort associated with the work in this thesis concerns the relaxation of singlet states in NMR. As will be seen the chapters that follow, relaxation is shown to be heavily dependent on the nuclear environment i.e. the structure and dynamics of the spin system. In this section, a concise description of longitudinal and transverse relaxation of the spin polarization vector is presented.

When a nuclear spin undergoes precessional motion in a magnetic field the angle between the magnetic moment and the magnetic field is always conserved. Now consider a molecule tumbling in an isotropic liquid inside a magnetic field. The orientation and position of the molecule will fluctuate wildly as a function of space and time but the nuclear spin polarization for each nucleus will retains its precessional motion. This infers that the translational and diffusive motions of nuclei in solution has little effect on the behaviour of nuclear spins.

However, the immediate magnetic environment for a nuclear spin plays a far more significant role. A microscopic field, caused by the inherent magnetism of a neighbouring nucleus or electron, will fluctuate vigorously due to the thermal energy transferred to the spin ensemble from the surroundings [45]. The external magnetic field will be perturbed slightly on the molecular-length scale by a microscopic magnetic field which contains a variable spatial and temporal dependence. Therefore, the total magnetic field experienced by a single spin differs from that of a neighbouring spin, on the microscopic level.

The precession of an individual magnetic moment is affected by the rapidly fluctuating magnetic field, which is the sum of the external and local fields and may point in any direction in space. The nuclear Larmor precession of each nuclear spin contains a time-dependent component and may be different to the nuclear Larmor frequency of its neighbour. The "constant angle" of Larmor precession between the magnetic moment

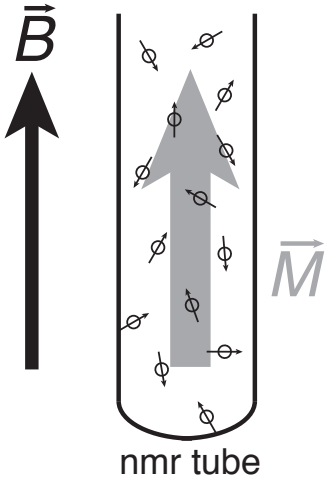

FIGURE 1.5: In a standard NMR sample there are around 10^{23} spins, represented here by empty circles, each with a magnetic moment which may point in any direction in space. As lower energy configurations, i.e. magnetic moment aligned with the static magnetic field $\vec{B}_0$, are preferred there is a *slight* preference for this orientation of magnetic moments throughout the sample. A net magnetic moment $\vec{M}$ therefore exists throughout the entire sample, which is also aligned with the z-axis of the static magnetic field.

and the magnetic field breaks down. Over a long time, the angle between the magnetic moment and the magnetic field samples all possible orientations.

But are some orientations more preferable? The answer is yes. Equation 1.2 states that the magnetic energy is lower when the magnetic moment points with the magnetic field. Since the surroundings are at a finite temperature, a nuclear spin is more likely to be thermally driven into a lower energy configuration. Hence, an entire spin ensemble is naturally driven towards a stable state of *thermal equilibrium*, where the net distribution of spin polarizations favour alignment with the magnetic field [46], see figure 1.5.

Nuclear spin populations for a spin-1/2 nucleus at thermal equilibrium obey the Boltzmann distribution:

$$\frac{N_{parallel}}{N_{antiparallel}} = e^{-\frac{\Delta E}{\kappa_B T}}. \tag{1.8}$$

where $\kappa_B = 1.38 \times 10^{-23}\,\mathrm{JK}^{-1}$ is the Boltzmann constant, and T is the finite temperature of the surroundings. The relative number of nuclear spins populating the parallel and anti-parallel configurations is given as a function of the quantized splitting between the nuclear spin states [47]. However, the polarization bias towards the preferential orientation is only slight at room temperature, as ΔE is $\sim 10^4$ times smaller than the

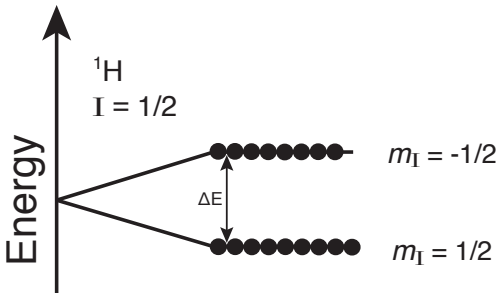

FIGURE 1.6: A populated energy level diagram for a spin-1/2 nucleus in a magnetic field at thermal equilibrium. The figure greatly exaggerates the population bias. Due to the finite temperature of the local environment, the population of nuclear spins is marginally imbalanced in favour of the energy level associated with parallel nuclear spin alignment. Filled balls represent nuclear spins.

energy of thermal fluctuations, and is approximately 1 spin in 15,625 at 9.4 T for protons, see figure 1.6.

1.2.7 T_1 and T_2

Consider a nuclear spin system at a state of thermal equilibrium in a magnetic field. The net spin polarization has an equilibrium value $M_{z,equil}$ which is aligned parallel to the magnetic field. The majority of nuclear spins will be precessing on a cone of "constant" angle with respect to the magnetic field, but there is no transverse magnetization at thermal equilibrium as the distribution of nuclear spin polarizations is symmetric about the z-axis of the magnetic field [41]. Consider a $\pi/2$ rotation of $M_{z,equil}$ about the x-axis as a result of a radiofrequency (rf) pulse, the effect being to tilt the magnetization vector parallel with the -y-axis. Each individual nuclear spin is assumed to be equally affected by the rf-pulse. In cases where the net nuclear magnetic moment is oriented perpendicular to the static magnetic field the term as transverse magnetization is used. This is a subtle but essential objective of nearly all NMR experiments because typically the nuclear spin magnetization is detected in the plane perpendicular to the static magnetic field of the NMR magnet. As the nuclear contribution to the samples magnetism is orders of magnitude smaller than the electronic contributions, observation of $M_{z,equil}$ parallel to the magnetic field is highly impractical.

Bloch formulated the first classical description of magnetization using a vector model, which is valid for N non-interacting spin-1/2 nuclei. His description is adequate for use here on the removal of the rf-pulse [4, 6, 48]. The behaviour of the magnetization

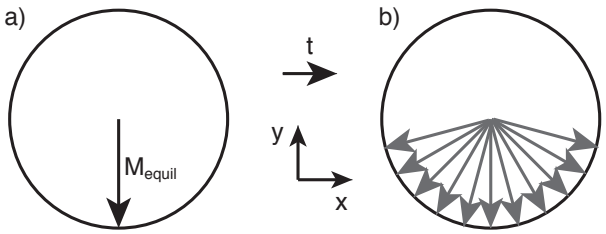

FIGURE 1.7: Nuclear spins dephasing under a magnetic field inhomogeneity. a) At an instantaneous time point after the rf-pulse is removed the magnetization vector is assumed to be pointing along the -y-axis. b) Over time the dephasing of nuclear spins spreads out the individual nuclear spin polarizations destroying all available NMR signal in the xy-plane.

$\vec{M}$ in the presence of a magnetic field $\vec{B}$ and relaxation R is given by:

$$\frac{d\vec{M}(t)}{dt} = \gamma\vec{M}(t) \wedge \vec{B} - R\left(\vec{M}(t) - \vec{M}(0)\right). \tag{1.9}$$

Precession of individual magnetic moments forces the magnetization vector to precess likewise in the xy-plane and relaxation will force the system to return to thermal equilibrium [49]. This can occur via various mechanisms which are discussed in detail in section 1.8. For simplicity, I will ignore the precessional motion and concentrate on the effects of longitudinal relaxation R_1. For the case of magnetization aligned with the magnetic field M_z, equation 1.9 simplifies to:

$$\frac{dM(t)}{dt} = -R_1\left(M_z(t) - M_{z,equil}\right), \tag{1.10}$$

where $M_z(t)$ is the magnetization aligned with the z-axis of the magnetic at a time t. Equation 1.10 states that the rate of change of magnetization is proportional to the deviation of $M_z(t)$ from thermal equilibrium. The solution of this equations yields the relaxation behaviour of the magnetization component parallel to the external magnetic field. $M_z(t)$ can be shown to relax with the characteristic time constant $T_1 = 1/R_1$:

$$M_z(t) = M_{z,equil} - (M_{z,equil} - M_z(0))e^{-t/T_1}, \tag{1.11}$$

as shown in appendix B. Different parts of the sample will relax with slightly different rates due to small, local inhomogeneities in the magnetic field. Therefore, the wandering motion of each nuclear spins precessional cone eventually causes the resulting signal to slowly dephase, gradually losing all phase coherence with distinctive rate constant $R_2 = 1/T_2$, see figure 1.7. The transverse components of the magnetization vector therefore

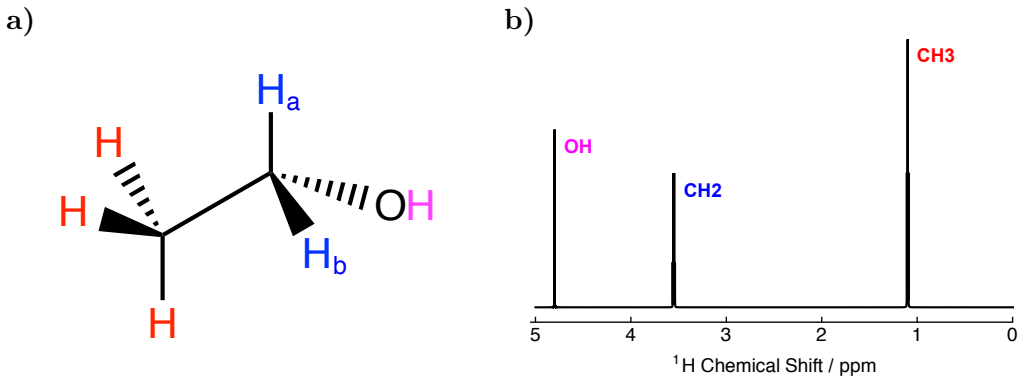

FIGURE 1.8: a) Molecular structure of ethanol. Methyl protons are indicated in red, CH_2 protons are indicated in blue, and the hydroxyl proton is indicated in pink. b) ^{1}H NMR spectrum of ethanol. The J-couplings are small relative to the spectral width and are not clearly visible at the current magnification.

evolve with the following form:

$$M_x(t) = M_{equil} \sin(\omega_0 t) e^{-t/T_2}, \tag{1.12}$$

$$M_y(t) = -M_{equil} \cos(\omega_0 t) e^{-t/T_2}. \tag{1.13}$$

Unfortunately, the vector model of magnetization is limited as internuclear couplings, non-selective rf pulses and magnetization transfer are not accounted for. A fuller, quantum mechanical description of magnetization evolution is therefore warranted, see sections 1.5 and 1.6.

1.3 Symmetry and properties of molecules

1.3.1 Chemical shift

NMR has the superior capability to distinguish between nuclear spins in differing magnetic environments, such as those located in distant parts of the same organic material. The dependence of the nuclear Larmor frequency on the strength of the local magnetic field allows for this determination. This is increasingly evident for more sensitive nuclei, such a protons, which is useful for the assignment of large structures, such as proteins, by NMR. It should be noted that here I am assuming that the static magnetic field is perfectly homogeneous. The classic question given to test undergraduate chemists when first discovering NMR is: from the structure of ethanol, figure 1.8a), how are the peaks in the NMR spectrum, figure 1.8b), assigned?

Ignoring the splitting of the resonances, which is attributed to an phenomenon known as scalar (J) coupling where the nuclear Larmor frequency depends on the direction of coupled magnetic moments in the same molecule, the answer relies on differences in *microscopic* magnetic fields. The differences in local magnetic field are not explained by an external magnetic field gradient, such as in magnetic resonance imaging (MRI) experiments [41, 50], but purely on the makeup of the molecule and how magnetic environments are averaged as the molecule tumbles isotropically in solution.

As the electrons are not separated from the nuclei of the molecule, the resonance position of a molecular group is also dependent on the electrons. In diamagnetic materials this is an effect known as chemical shift. Consider the methyl group (CH_3) protons, which are resonant at $\sim$1.1 ppm. CH_3 groups rotate rapidly in solution, and so the nuclei are protected by a cloud of high electron density. This *shielding* effect from the outer electrons shifts the methyl group resonance upfield, towards 0 ppm. The hydroxyl resonance is often broad due to exchange of the proton with the solvent, and is found downfield (>4 ppm) as the oxygen nucleus is heavily electronegative and pulls the electron density away from the adjacent proton.

As the nuclear Larmor frequency, and to good approximation the chemical shift, are proportional to the applied magnetic field, the ratio of these two quantities is fixed. A field-independent expression of the chemical shift δ is expressed as:

$$\delta = \frac{\omega_0 - \omega_0^{\mathrm{REF}}}{\omega_0^{\mathrm{REF}}}, \tag{1.14}$$

where ω_0^{REF} is the nuclear Larmor frequency of the same isotope in a reference compound at the same magnetic field.

1.3.2 Chemical equivalence

Some nuclei, such as those labelled blue in figure 1.8a), have nuclei which resonate at the same nuclear Larmor frequency. Therefore, the magnetic field experienced by the protons H_a and H_b is the same, and the CH_2 protons all appear at the same resonance frequency in the ^{1}H NMR spectrum. These spins are defined as "chemically equivalent". Chemical equivalence is also a common feature for CH_3 groups. In chapter 3, I will

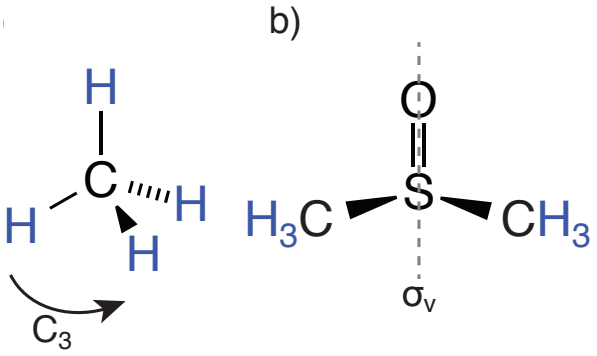

FIGURE 1.9: The equivalent protons of a) methane and b) DMSO are highlighted in blue. In each molecule, the protons are exchanged by a symmetry operation, such as a three-fold rotation (C_3) or reflection (σ_v).

show how chemical inequivalence can be induced and detected between the protons of a rotating CH_2D group.

For two or more spins in the same molecule, chemical equivalence is achieved if both of the following criteria are satisfied:

- The nuclear spins are of the same isotope,
- A molecular symmetry operation exists which exchanges the nuclear spins.

If both of these criteria cannot be satisfied, then the spins are said to be chemically inequivalent. As an example, consider the protons in a molecule of water. The two protons are chemically equivalent. Each spin is of the same isotope and both spins sense the electron withdrawal due to the electronegativity of the oxygen, shifting the resonance frequency for both protons downfield simultaneously. Furthermore, a reflection operation, which runs down a line of symmetry within the molecule, exists and interchanges the position of the two protons. Similar is true for the protons in a molecule of methane, the CH_2 protons in a molecule of ethanol, or the methyl groups in a molecule of DMSO, see the blue protons in figure 1.9.

1.3.3 Magnetic equivalence

Another widely used category to establish equivalence between the nuclei of a molecule is magnetic equivalence. Two nuclei are said to be magnetically equivalent if:

- The two nuclei have identical chemical shifts,

- The two nuclei have identical scalar couplings to all other nuclei in the molecule (or if there are no other spins present in the molecule).

If both of these criteria cannot be satisfied, then the spins are said to be chemically inequivalent.

Again, one could consider a molecule of water, but this time the water is labelled with an ^{17}O nucleus ($I(^{17}\mathrm{O})>0$) such that a J-coupling exists between the protons and the oxygen. As discussed above, the two protons in water have identical chemical shifts. In this case, the J-coupling is also identical and the protons of water are said to be magnetically equivalent. Magnetic equivalence does also imply chemical equivalence, but chemical equivalence does not necessarily imply magnetic equivalence.

In the field of singlet-state NMR, an ideal molecular candidate is often chosen if a pair of nuclei (of the same isotope) have almost identical nuclear Larmor frequencies, such that a small chemical shift difference exists between the pair. Magnetic equivalence is therefore a far more restrictive condition for singlet NMR.

1.4 Types of NMR spectra

The consequences of chemical and magnetic equivalence has interesting repercussions for the outcome of the NMR spectrum. The size of the chemical inequivalence plays a particular role in the frequency of the signal resonances and the relative signal intensities. For a pair of spin-1/2 nuclei (i and j) there are three types of spectra (A_2, AB and AX) which can be classified by defining a parameter which quantifies the level of chemical inequivalence. Traditionally, the coupling regime in solution NMR is defined by the spin system parameters J_{ij} and Ω_{Δ}^{ij}. J_{ij} is the in pair scalar coupling between spins i and j, and Ω_{Δ}^{ij} is the difference in chemical shift between the two spins. A new parameter $\tan(\theta_{ij})$, which is dimensionless, is constructed from these two properties:

$$\tan(\theta_{ij}) = \frac{2\pi J_{ij}}{\Omega_{\Delta}^{ij}}. \tag{1.15}$$

When $\theta_{ij} \to 0$ the system is *weakly coupled* and when $\theta_{ij} \to \pi/2$ the system is *strongly coupled*. The coherent Hamiltonian for a 2-spin-1/2 system with a scalar coupling J_{ij}

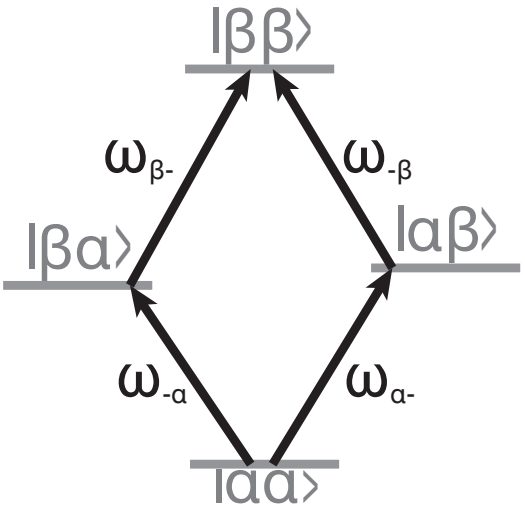

FIGURE 1.10: Energy level diagram in the Zeeman product basis for 2-spin-1/2 nuclei in a magnetic field. The spin state of the spin-1/2 pair is represented as $|\psi_1\psi_2\rangle$, where $|\psi_i\rangle$ can be either $|\alpha\rangle$ or $|\beta\rangle$. Single quantum (-1) transitions between spin states are shown by the direction of the arrows.

and a chemical shift difference Ω_Δ^{ij}, written in the Zeeman product basis, is shown in equation 2.46 of chapter 2. The $|\alpha\beta\rangle$ and $|\beta\alpha\rangle$ subspace yields the following polynomial:

$$\omega_0^2 + \pi J_{ij}\omega_0 - \frac{(3\pi^2 J_{ij}^2 + (\Omega_\Delta^{ij})^2)}{4} = 0, \tag{1.16}$$

and hence provides the eigenvalues for the states $|\alpha\beta\rangle$ and $|\beta\alpha\rangle$:

$$|\alpha\beta\rangle : \frac{1}{2}(-\pi J_{ij} + \sqrt{(2\pi J_{ij})^2 + (\Omega_\Delta^{ij})^2}), \tag{1.17}$$

$$|\beta\alpha\rangle : \frac{1}{2}(-\pi J_{ij} - \sqrt{(2\pi J_{ij})^2 + (\Omega_\Delta^{ij})^2}). \tag{1.18}$$

A second polynomial is additionally tractable in the $|\alpha\alpha\rangle$ and $|\beta\beta\rangle$ subspace:

$$\omega_0^2 - \pi J_{ij}\omega_0 + \frac{\pi^2 J_{ij}^2 - (\Omega_\Sigma^{ij})^2}{4} = 0. \tag{1.19}$$

The eigenvalues for states $|\alpha\alpha\rangle$ and $|\beta\beta\rangle$ are:

$$|\alpha\alpha\rangle : \frac{1}{2}(\pi J_{ij} - \Omega_\Sigma^{ij}), \tag{1.20}$$

$$|\beta\beta\rangle : \frac{1}{2}(\pi J_{ij} + \Omega_\Sigma^{ij}). \tag{1.21}$$

Ω_Σ^{ij} is the sum of chemical shift terms, and is zero if the resonance offset is assumed to be

placed at the mean resonance frequency of the 2-spin-1/2 nuclei. The signal frequencies are given by the difference in eigenvalues between spin states which are connected by single quantum (-1) transitions, see figure 1.10. The signal frequencies are shown using the notation $S(\omega_{ij})$, where i and j represent either the spin state or -1 coherence for spins i and j, see below. The signal frequencies of the four single quantum (-1) transitions are given by:

$$S(\omega_{\alpha-}) = \pi J_{ij} - \frac{1}{2}\sqrt{(2\pi J_{ij})^2 + (\Omega_{\Delta}^{ij})^2}, \tag{1.22}$$

$$S(\omega_{-\alpha}) = \pi J_{ij} + \frac{1}{2}\sqrt{(2\pi J_{ij})^2 + (\Omega_{\Delta}^{ij})^2}, \tag{1.23}$$

$$S(\omega_{-\beta}) = -\pi J_{ij} + \frac{1}{2}\sqrt{(2\pi J_{ij})^2 + (\Omega_{\Delta}^{ij})^2}, \tag{1.24}$$

$$S(\omega_{\beta-}) = -\pi J_{ij} - \frac{1}{2}\sqrt{(2\pi J_{ij})^2 + (\Omega_{\Delta}^{ij})^2}. \tag{1.25}$$

The signal intensities $i(S_{ij})$ in the NMR spectrum after the application of a $\pi/2$ pulse are:

$$i(S_{\alpha-}) = \frac{1}{2}(1 + \sin(\theta_{ij})), \tag{1.26}$$

$$i(S_{-\alpha}) = \frac{1}{2}(1 - \sin(\theta_{ij})), \tag{1.27}$$

$$i(S_{-\beta}) = \frac{1}{2}(1 + \sin(\theta_{ij})), \tag{1.28}$$

$$i(S_{\beta-}) = \frac{1}{2}(1 - \sin(\theta_{ij})). \tag{1.29}$$

1.4.1 A_2 spectra

For an A_2 spin system the chemical shift difference Ω_{Δ}^{ij} approaches zero. This leaves $S(\omega_{-\alpha})$ and $S(\omega_{\beta-})$ with a 0 Hz resonance offset, whilst $S(\omega_{\alpha-})$ and $S(\omega_{-\beta})$ are situated at $\pm J_{ij}$ Hz, respectively. Furthermore, the parameter $\tan(\theta_{ij})$ tends to ∞ as θ_{ij} tends to $\pi/2$. Signal intensities in the resulting spectrum for a "ideal" A_2 system are as follows:

$$i(S_{\alpha-}) \to 1, \tag{1.30}$$

$$i(S_{-\alpha}) \to 0, \tag{1.31}$$

$$i(S_{-\beta}) \to 1, \tag{1.32}$$

$$i(S_{\beta-}) \to 0, \tag{1.33}$$

with $\sin(\pi/2) = 1$. It therefore follows that the transition frequencies at $\pm J_{ij}$ have no overall signal intensity, with the transition frequencies at zero resonance offset having the fullest possible signal intensity.

1.4.2 AB spectra

In the case of an AB spin system the chemical shift difference Ω_{Δ}^{ij} is on the order of the scalar coupling J_{ij}. Let's consider the case of $\Omega_{\Delta}^{ij} = 2\pi J_{ij}$, for an unspecified value of Ω_{Δ}^{ij} and J_{ij}. The ratio $\frac{2\pi J_{ij}}{\Omega_{\Delta}^{ij}} = 1$. The resulting NMR signals appear at the following frequencies:

$$S(\omega_{\alpha-}) \rightarrow \pi J_{ij}(1 - \sqrt{2}), \tag{1.34}$$

$$S(\omega_{-\alpha}) \rightarrow \pi J_{ij}(1 + \sqrt{2}), \tag{1.35}$$

$$S(\omega_{-\beta}) \rightarrow -\pi J_{ij}(1 + \sqrt{2}), \tag{1.36}$$

$$S(\omega_{\beta-}) \rightarrow -\pi J_{ij}(1 - \sqrt{2}), \tag{1.37}$$

with the signal intensities $i(S_{-\alpha})$ and $i(S_{-\beta})$ being $\frac{\sqrt{2}+1}{2\sqrt{2}}$, and the signal intensities $i(S_{\alpha-})$ and $i(S_{\beta-})$ being $\frac{\sqrt{2}-1}{2\sqrt{2}}$.

1.4.3 AX spectra

AX spectra are far more common for spin-1/2 pairs in nature, due to the environments of the molecules in which these pairs are situated. In this example, the scalar coupling J_{ij} will be finite but small in comparison with the chemical shift difference Ω_{Δ}^{ij}. The ratio $\frac{2\pi J_{ij}}{\Omega_{\Delta}^{ij}}$ tends to zero, with $\tan(\theta_{ij})$ and θ_{ij} (small angle approximation) also tending to zero. Assignment of signal frequencies and intensities is again relatively simple. The resonance frequencies are given by equations 1.22-1.25, and the signal intensities are all equal.

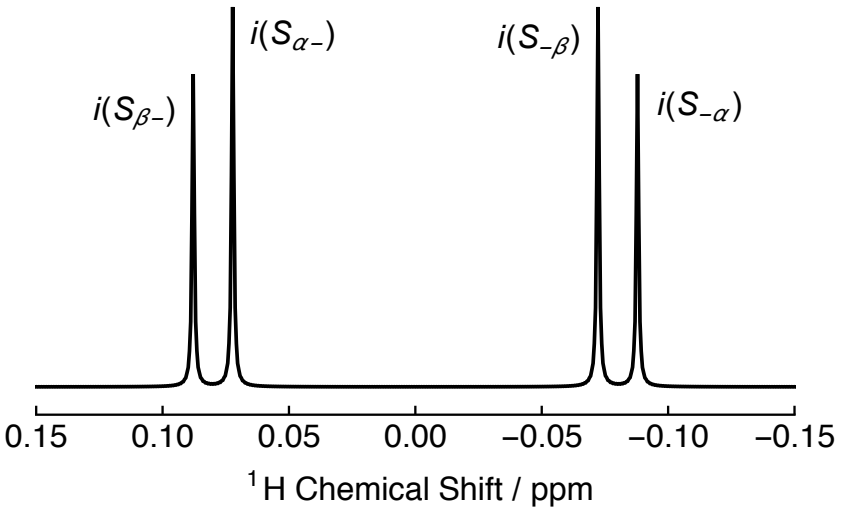

FIGURE 1.11: AX spectrum for a pair of weakly coupled spin-1/2 nuclei. $J_{ij} = 15.55\,\text{Hz}$ and $\Omega_{\Delta}^{ij} = 160\,\text{Hz}$. The signal intensity of each peak is labelled as $i(S_{ij})$. An effect known as "roofing" is clearly visible in the NMR spectrum of this system.

1.5 Ensembles of spins

1.5.1 Spin density operator

Consider an ensemble of identical spin-1/2 nuclei in solution. Each nucleus has a spin polarization vector which may point in any direction in space. If one were to take a snapshot of the ensemble at any given point in time, the spin polarization vectors would be pointing in all possible directions in a uniform manner. In section 1.2, I discussed that the lowest energy orientation for a spin-1/2 nucleus in a magnetic field occurs when the intrinsic magnetism of the nucleus is aligned with the static magnetic field. This alignment is represented quantum mechanically by the state $|\alpha\rangle$. The opposite case, when the magnetic moment of the spin-1/2 nucleus is aligned anti-parallel to the static magnetic field, is represented by the state $|\beta\rangle$. A quantum state is represented by the numbers I and m_I as the ket $|I, m_I\rangle$, using Dirac notation. The $|\alpha\rangle$ and $|\beta\rangle$ states are therefore defined as:

$$|\alpha\rangle = |\frac{1}{2}, \frac{1}{2}\rangle\,, \tag{1.38}$$

$$|\beta\rangle = |\frac{1}{2}, -\frac{1}{2}\rangle\,, \tag{1.39}$$

i.e. an isolated spin-1/2 nucleus has two eigenstates, $|\alpha\rangle$ and $|\beta\rangle$, of angular momentum along the z-axis. The Zeeman eigenstates obey the following equations:

$$\hat{I}_z |\alpha\rangle = +\frac{1}{2} |\alpha\rangle , \tag{1.40}$$

$$\hat{I}_z |\beta\rangle = -\frac{1}{2} |\beta\rangle , \tag{1.41}$$

where $\hat{I}_z$ is the z-projection angular momentum operator, see chapter 2 for more details. A spin in state $|\alpha\rangle$ is said to be polarized along the z-axis, with eigenvalue $+\frac{1}{2}$. All of the spin polarization vectors in the nuclear ensemble can easily be described by a superposition state. The quantum state of a spin $|\psi\rangle$ can be expanded according to linear combination of ket vectors $|\psi_i\rangle$:

$$|\psi\rangle = \sum_i c_i |\psi_i\rangle , \tag{1.42}$$

where c_i is a complex coefficient, and $|\psi\rangle$ is a superposition of states $|\psi_i\rangle$. If c_i is time dependent, then it must also be a solution of the Schrödinger equation. In the current case, it is convenient to write the spin state for an individual nucleus $|\psi\rangle$ as a superposition of "spin-up" $|\alpha\rangle$ and "spin-down" $|\beta\rangle$ states:

$$|\psi\rangle = c_\alpha |\alpha\rangle + c_\beta |\beta\rangle , \tag{1.43}$$

where the superposition coefficients c_α and c_β may again be complex, and quantify the contribution of the $|\alpha\rangle$ and $|\beta\rangle$ states to the superposition state $|\psi\rangle$. The values of the superposition coefficients are restricted via normalization:

$$|c_\alpha|^2 + |c_\beta|^2 = 1. \tag{1.44}$$

In this way, nuclear spins are not restricted simply to the $|\alpha\rangle$ and $|\beta\rangle$ states.

The total spin polarization for the entire spin-1/2 ensemble is the sum over all nuclear magnetic moments. This calculation is exceedingly difficult considering the ensemble will have $\sim 10^{23}$ spins at 1 M concentration. The "spin density operator" is therefore used to describe the dynamics of the whole nuclear ensemble, and can report on the overall spin state for the "entire" nuclear ensemble [41]. To find the form of the spin density operator, I begin by constructing a superposition state for a spin-1/2

nucleus using the superposition coefficients:

$$|\psi\rangle = \begin{bmatrix} c_\alpha \\ c_\beta \end{bmatrix}. \tag{1.45}$$

The expectation value of the operator $\hat{Q}$ acting on $|\psi\rangle$ is given by:

$$\langle\hat{Q}\rangle = \langle\psi|\,\hat{Q}\,|\psi\rangle\,. \tag{1.46}$$

To have a well defined value of $\hat{Q}$, $|\psi\rangle$ must be an eigenvalue of $\hat{Q}$, i.e. $\hat{Q}\,|\psi\rangle = \langle\hat{Q}\rangle\,|\psi\rangle$. The expectation value $\langle\hat{Q}\rangle$ may be expanded to reveal complex products of the coefficients c_α and c_β. A matrix is constructed by the column vector $|\psi\rangle$ and the row vector $\langle\psi|$ which contains the complex product of these coefficients:

$$|\psi\rangle\langle\psi| = \begin{bmatrix} c_\alpha \\ c_\beta \end{bmatrix} \cdot \left(c_\alpha, c_\beta\right) = \begin{pmatrix} c_\alpha c_\alpha^* & c_\alpha c_\beta^* \\ c_\beta c_\alpha^* & c_\beta c_\beta^* \end{pmatrix}. \tag{1.47}$$

The expectation value of the operator $\hat{Q}$ is extracted as follows:

$$\langle\hat{Q}\rangle = \mathrm{Tr}\left[|\psi\rangle\langle\psi|\,\hat{Q}\right], \tag{1.48}$$

where Tr represents the trace operation. Now suppose that two identical spin-1/2 nuclei are involved. The first spin is in state $|\psi_1\rangle$ and the second spin is in state $|\psi_2\rangle$. The most likely outcome of measuring $\hat{Q}$ is the sum of the two expectation values:

$$\langle\hat{Q}\rangle = \langle\psi_1|\,\hat{Q}\,|\psi_1\rangle + \langle\psi_2|\,\hat{Q}\,|\psi_2\rangle\,. \tag{1.49}$$

For a large number of spins (i.e. all the spins in the ensemble) this expression can again be rewritten:

$$\langle\hat{Q}\rangle = \langle\psi_1|\,\hat{Q}\,|\psi_1\rangle + \langle\psi_2|\,\hat{Q}\,|\psi_2\rangle + ... + \langle\psi_N|\,\hat{Q}\,|\psi_N\rangle\,, \tag{1.50}$$

and as such allows equation 1.48 to be rewritten as:

$$\langle\hat{Q}\rangle = \mathrm{Tr}\left[\left(|\psi_1\rangle\langle\psi_1| + |\psi_2\rangle\langle\psi_2| + ... + |\psi_N\rangle\langle\psi_N|\right)\hat{Q}\right]. \tag{1.51}$$

The operator $\hat{\rho}$ is defined as:

$$\hat{\rho} = N^{-1}(|\psi_1\rangle\langle\psi_1| + |\psi_2\rangle\langle\psi_2| + ... + |\psi_N\rangle\langle\psi_N|), \tag{1.52}$$

where N is the number of spins in the ensemble. The above expression of $\hat{\rho}$ may also be rewritten as:

$$\hat{\rho} = \overline{|\psi\rangle\langle\psi|}, \tag{1.53}$$

where the overbar indicates an average over all the spins in the ensemble. For NMR spectroscopy, the concept of the spin density operator $\hat{\rho}$ is important for the macroscopic observation of the operator $\hat{Q}$ for an entire ensemble of spins:

$$N^{-1}\langle\hat{Q}_{macro}\rangle \cong \mathrm{Tr}\left[\hat{\rho}\hat{Q}\right], \tag{1.54}$$

where $N^{-1}\langle\hat{Q}_{macro}\rangle$ is the average contribution of each ensemble member to the final macroscopic result. This can be considered as the "average expectation value" for the entire spin system. This result suggests that a macroscopic observable may be extracted from the current state the spin system as a whole, and the observable. This dramatic simplification therefore allows the entire spin ensemble to be described by just a single operator $\hat{\rho}$.

1.5.2 Populations and coherences

For an ensemble of non-interacting spin-1/2 particles, the matrix representation for the spin density operator $\hat{\rho}$ is as follows:

$$\hat{\rho} = \begin{pmatrix} \rho_\alpha & \rho_+ \\ \rho_- & \rho_\beta \end{pmatrix} = \begin{pmatrix} \overline{c_\alpha c_\alpha^*} & \overline{c_\alpha c_\beta^*} \\ \overline{c_\beta c_\alpha^*} & \overline{c_\beta c_\beta^*} \end{pmatrix}, \tag{1.55}$$

where the diagonal components ρ_α and ρ_α are the populations of states $|\alpha\rangle$ and $|\beta\rangle$, respectively, and the off-diagonal components ρ_+ and ρ_- are the coherences between states $|\alpha\rangle$ and $|\beta\rangle$, respectively. The populations of states $|\alpha\rangle$ and $|\beta\rangle$ are defined as:

$$\rho_\alpha = \langle\alpha|\,\hat{\rho}\,|\alpha\rangle = \overline{c_\alpha c_\alpha^*}, \tag{1.56}$$

$$\rho_\beta = \langle\beta|\,\hat{\rho}\,|\beta\rangle = \overline{c_\beta c_\beta^*}, \tag{1.57}$$

and the coherences between states $|\alpha\rangle$ and $|\beta\rangle$ are defined as:

$$\rho_+ = \langle\alpha|\,\hat{\rho}\,|\beta\rangle = \overline{c_\alpha c_\beta^*}, \tag{1.58}$$

$$\rho_- = \langle\beta|\,\hat{\rho}\,|\alpha\rangle = \overline{c_\beta c_\alpha^*}. \tag{1.59}$$

The spin density operator $\hat{\rho}$ may also be expressed as:

$$\hat{\rho} = \rho_\alpha \hat{I}^\alpha + \rho_+ \hat{I}^+ + \rho_- \hat{I}^- + \rho_\beta \hat{I}^\beta, \tag{1.60}$$

using the shift operators $\hat{I}^+$ and $\hat{I}^-$, and the projection operators $\hat{I}^\alpha$ and $\hat{I}^\beta$. As the spin state of a nucleus is normalized, the nuclear spin populations are mutually dependent:

$$c_\alpha c_\alpha^* + c_\beta c_\beta^* = 1. \tag{1.61}$$

Equation 1.61 applies to all the nuclear spins in the ensemble, and hence the average over the nuclear spin ensemble. The sum of the populations is therefore unity:

$$\rho_\alpha + \rho_\beta = 1. \tag{1.62}$$

Populations are real, positive and in this case range from 0 to 1. Coherences are complex numbers. The ρ_+ and ρ_- coherences are complex conjugates of one and other, i.e. a conjugate pair:

$$\rho_+ = \overline{c_\alpha c_\beta^*} = \left[\overline{c_\alpha c_\beta^*}\right]^* = \rho_-. \tag{1.63}$$

1.5.3 Thermal equilibrium

The principle of the spin density operator is to specify the state of an entire spin-1/2 ensemble with only a small number of parameters. These parameters can be used to predict the evolution of the nuclear ensemble by applying the Schrödinger equation, see equation 1.83. Consider an ensemble of spins which has been left to make thermal contact with its surroundings for a considerable length of time. One would say that the system is in *thermal equilibrium* with its surroundings. One can make an educated guess as to the populations of the spin density operator $\hat{\rho}$ at any point in time, assuming there are no coherences between spin states.

Consider the Hamiltonian for an ensemble with eigenstates $|n\rangle$, and energies ω_n:

$$\hat{H}\,|n\rangle = \omega_n\,|n\rangle\,. \tag{1.64}$$

An eigenequation of this kind has already been shown in equations 1.40 and 1.41. For the case of a spin-1/2 nucleus, the eigenstates correspond to:

$$\omega_\alpha = \frac{1}{2}\gamma\vec{B}_0, \tag{1.65}$$

$$\omega_\beta = -\frac{1}{2}\gamma\vec{B}_0. \tag{1.66}$$

The populations should obey the Boltzmann distribution:

$$\rho_n^{eq} = \frac{exp\left(-\frac{\hbar\omega_n}{\kappa_B T}\right)}{\sum_N exp\left(-\frac{\hbar\omega_N}{\kappa_B T}\right)}, \tag{1.67}$$

where ρ_n^{eq} is the relative population of the state $|n\rangle$ at thermal equilibrium, one can define the Boltzmann factor B_f:

$$B_f = \frac{\hbar\gamma\vec{B}_0}{\kappa_B T}. \tag{1.68}$$

The exponential population factors may therefore written as:

$$exp\left(-\frac{\hbar\omega_\alpha}{\kappa_B T}\right) = exp\left(\frac{1}{2}B_f\right), \tag{1.69}$$

$$exp\left(-\frac{\hbar\omega_\beta}{\kappa_B T}\right) = exp\left(-\frac{1}{2}B_f\right). \tag{1.70}$$

Each exponential may be extended as a power series considering that $B_f \ll 1$.

$$exp\left(\frac{1}{2}B_f\right) \to 1 + \frac{1}{2}B_f, \tag{1.71}$$

$$exp\left(-\frac{1}{2}B_f\right) \to 1 - \frac{1}{2}B_f. \tag{1.72}$$

The denominator of equation 1.67 is $\sim$2. The populations of the α and β states are therefore:

$$p(\alpha) = \frac{1}{2} + \frac{1}{4}B_f, \tag{1.73}$$

$$p(\beta) = \frac{1}{2} - \frac{1}{4}B_f, \tag{1.74}$$

and the thermal equilibrium spin density operator may be written as:

$$\rho_{\text{equil}} = \frac{\hat{1}}{2} + \frac{1}{2} B_f \hat{I}_z \tag{1.75}$$

This situation is known as the high temperature approximation, and means that for nuclei with $\gamma > 0$ the $|\alpha\rangle$ state is *slightly* more populated than the $|\beta\rangle$ state at room temperature. This means that there is only a very small polarization vector for the total angular momentum of the nuclear spin-1/2 ensemble in the direction of the static magnetic field. As mentioned in section 1.2.6, this population difference corresponds to 1 spin in 15,625 for protons at 9.4 T. Hyperpolarization techniques (as described in chapter 2, section 2.3) can boost the population difference between the eigenstates of spin-1/2 ensembles.

1.6 Evolution of observables

1.6.1 Introduction to Quantum Mechanics

The wavefunction acts as a bridge between the classical and quantum worlds for large spin systems, and clearly describes the properties and evolution for a single spin, or even a small cluster of spins, but calculations remains troublesome for large numbers or ensembles of spins. The wavefunction $\psi(t)$ may depend on the variables position, momentum, time, and other parameters of the spin ensemble. It is possible to reformulate $\psi(t)$ such that it does not depend on a particular representation. Using Dirac notation, each state of the spin ensemble is associated a vector $|\psi(t)\rangle$ called a ket. $|\psi(t)\rangle$ describes the state of a spin within the ensemble. An important postulate of quantum mechanics states that $|\psi(t)\rangle$ contains all the known information about the spin state. The bra vector $\langle\psi(t)|$ is the counterpart of the ket, the two are related by complex conjugation:

$$(c_i \, |\psi_i(t)\rangle)^* = c_i^* \, \langle\psi_i(t)| \, , \tag{1.76}$$

where c_i is a scalar. The wavefunction $\psi(t)$ is correspondingly normalized:

$$\langle\psi(t)|\psi(t)\rangle = \int_{-\infty}^{+\infty} d\tau \psi^*(t)\psi(t) = \int_{-\infty}^{+\infty} d\tau \|\psi(t)\|^2 = 1, \tag{1.77}$$

where $\|\psi(t)\|^2$ is the probability distribution of $\psi(t)$. Two separate wavefunctions $|\psi_i(t)\rangle$ and $|\psi_j(t)\rangle$ with different eigenvalues are orthonormal (orthogonal and normalized) if:

$$\langle\psi_i(t)|\psi_j(t)\rangle = \int_{-\infty}^{+\infty} d\tau \psi_i^*(t)\psi_j(t) = \delta_{ij}, \tag{1.78}$$

where δ_{ij} is the Kronecker delta:

$$\delta_{ij} = \left\{ \begin{array}{ll} 1 & \text{for } i = j \\ 0 & \text{for } i \neq j \end{array} \right\}. \tag{1.79}$$

An operator $\hat{O}_H$ is Hermitian if:

$$\langle\psi_i(t)|\,\hat{O}_H\,|\psi_j(t)\rangle = (\langle\psi_j(t)|\,\hat{O}_H\,|\psi_i(t)\rangle)^\dagger, \tag{1.80}$$

i.e. $\hat{O}_H = \hat{O}_H^\dagger$. A Hermitian (or self-adjoint) operator $\hat{O}_H$ has defined kets $|\psi(t)\rangle$ for which:

$$\hat{O}_H\,|\psi(t)\rangle = a_H\,|\psi(t)\rangle\,, \tag{1.81}$$

where a_H is shown to be a real number by using the Hermicity condition from equation 1.80,

$$\langle\psi_i(t)|\hat{O}_H|\psi_j(t)\rangle = a_H^*\,\langle\psi_i(t)|\psi_j(t)\rangle = \langle\psi_i(t)|\psi_j(t)\rangle\,a_H, \tag{1.82}$$

demonstrating that $a_H = a_H^*$.

1.6.2 Evolution in Hilbert space

The state space spanned by the kets $|\psi(t)\rangle$ is known as a Hilbert space. The time evolution of a state $|\psi(t)\rangle$ in Hilbert space is controlled by the equation of motion, known as the Schrödinger equation:

$$\frac{d}{dt}\,|\psi(t)\rangle = -i\hat{H}(t)\,|\psi(t)\rangle\,, \tag{1.83}$$

where i is the imaginary number ($i = \sqrt{-1}$), $\hat{H}$ is the Hamiltonian, and the "hat" signifies that the Hamiltonian is an operator. The properties of the Hamiltonian dictate the time evolution of the spin state $|\psi(t)\rangle$. The initially known state $|\psi(t)\rangle$ is propagated

forward in time in the following way:

$$|\psi(t_b)\rangle = \hat{U}(t_b, t_a)\,|\psi(t_a)\rangle\,, \tag{1.84}$$

where time propagator $\hat{U}(t_b, t_a)$ is given by:

$$\hat{U}(t_b, t_a) = exp[-i\int_{t_a}^{t_b} dt'\hat{H}(t')]. \tag{1.85}$$

$\hat{U}(t, 0)$ is the exact solution to a time-independent Schrödinger equation:

$$i\frac{d}{dt}e^{-i\hat{H}t}\,|\psi(0)\rangle = \hat{H}e^{-i\hat{H}t}\,|\psi(0)\rangle\,. \tag{1.86}$$

For details of time dependent Hamiltonian propagation, see appendix B. The time propagator allows for the deterministic prediction, or target, of a state at some point in the future, given a set of initial conditions:

$$\lim_{t\to 0}\hat{U}(t, 0)\,|\psi(0)\rangle \to |\psi(0)\rangle\,. \tag{1.87}$$

The time propagator $\hat{U}(t_b, t_a)$ is also a unitary operator, i.e.:

$$\hat{U}(t_a, t_a) = \hat{\mathbb{1}}, \tag{1.88}$$

$$\hat{U}^{-1}(t_b, t_a) = \hat{U}(t_a, t_b), \tag{1.89}$$

$$\hat{U}(t_c, t_a) = \hat{U}(t_c, t_b)\hat{U}(t_b, t_a), \tag{1.90}$$

where $t_a < t_b < t_c$. The time evolution of an observable $\langle Q(t)\rangle$, on the other hand, is predictable by the use of a time propagator sandwich:

$$\langle Q(t_b)\rangle = \hat{U}(t_b, t_a)\langle Q(t_a)\rangle\hat{U}(t_b, t_a)^\dagger = \langle\psi(t_a)|\,\hat{U}(t_b, t_a)Q(t_a)\hat{U}(t_b, t_a)^\dagger\,|\psi(t_a)\rangle\,, \tag{1.91}$$

where $\hat{U}(t_b, t_a)^\dagger$ is the Hermitian adjoint of the time propagator $\hat{U}(t_b, t_a)$. The operator $\hat{U}(t_b, t_a)$ acts directly on a constantly evolving state $|\psi(t)\rangle$, and hence the expectation value $\langle Q(t)\rangle$ evolves simultaneously.

1.6.3 Liouville space

In Hilbert space, quantum states represented by basis kets are written using column vectors, with the operators which act upon the quantum states written as matrices. However, the transformation between two operators $\hat{A}$ and $\hat{B}$ takes places in a higher-dimensional space, called Liouville space, where the *operators* are represented as column vectors. This is an n^2-dimensional space, where n^2 is the number of elements in the predefined operator basis. Mapping Hilbert space to Liouville space can be shown by an example using the operator $\hat{A}_{ij}$, which in Hilbert space is written as a $n \times n$ matrix:

$$\hat{A}_{ij} = \begin{bmatrix} \langle 1|\hat{A}|1\rangle & \langle 1|\hat{A}|2\rangle & \cdots & \langle 1|\hat{A}|N\rangle \\ \langle 2|\hat{A}|1\rangle & \langle 2|\hat{A}|2\rangle & \cdots & \langle 2|\hat{A}|N\rangle \\ \vdots & \vdots & & \vdots \\ \langle N|\hat{A}|1\rangle & \langle N|\hat{A}|2\rangle & \cdots & \langle N|\hat{A}|N\rangle \end{bmatrix}. \tag{1.92}$$

In Liouville space, the operator is represented as a $1 \times n^2$ column vector or list:

$$\hat{A}_{ij} = \begin{bmatrix} \langle 1|\hat{A}|1\rangle \\ \langle 1|\hat{A}|2\rangle \\ \vdots \\ \langle 1|\hat{A}|N\rangle \\ \langle 2|\hat{A}|1\rangle \\ \vdots \\ \langle N|\hat{A}|N\rangle \end{bmatrix} \rightarrow \begin{bmatrix} \hat{A}_1 \\ \hat{A}_2 \\ \vdots \\ \hat{A}_N \\ \hat{A}_{N+1} \\ \vdots \\ \hat{A}_{N^2} \end{bmatrix}, \tag{1.93}$$

which uses the same set of indices i and j as in the Hilbert space representation of the operator $\hat{A}_{ij}$. For convenience, the elements of $\hat{A}_{ij}$ are relabelled in such a way that: $\hat{A}_1 = \langle 1|\hat{A}|1\rangle$ etc. It is therefore clear that there are n^2 components in the Liouville space representation of the operator $\hat{A}_{ij}$, and that the Liouvillian operator basis also has n^2 components.

1.6.4 Superoperators

Working with the spin density operator requires double sided multiplications, and most notably commutation operations. A repercussion, however, is the extensive and complicated expressions that ultimately describe any intricate NMR experiment, and which are occasionally computationally demanding. The use of superoperators greatly simplifies these efforts [51]. Superoperators are generally sparse, and block-diagonal substructures can be often used for calculations of reduced computational size. The operands in Liouville space are operators, and these are transformed or acted upon by superoperators [51]. For example, the operator $\hat{A}$ is acted upon by a superoperator $\hat{\hat{Q}}_{ij}$ and "maps" the operator $\hat{A}$ onto another operator $\hat{B}$, in a similar manner to how the Schrödinger equation considers quantum state to quantum state transformations in Hilbert space. The superoperator $\hat{\hat{Q}}_{ij}$ maps the operator $\hat{A}$ onto the operator $\hat{B}$ in the following way:

$$\hat{\hat{Q}}_{ij}\hat{A} \rightarrow \hat{B}. \tag{1.94}$$

Operators and superoperators are distinguished by the use of a single hat $\hat{}$ for operators and a double hat $\hat{\hat{}}$ for superoperators. The salient point from section 1.6.3 is that a $n \times n$ matrix representation of an operator in Hilbert space is represented as a $1 \times n^2$ column vector in Liouville space. This principle can be used to deduce *via inspection* that a superoperator in Liouville space behaves in the following way:

$$\begin{bmatrix} \langle 1|\hat{\hat{Q}}|1\rangle & \langle 1|\hat{\hat{Q}}|2\rangle & \cdots & \langle 1|\hat{\hat{Q}}|N\rangle \\ \langle 2|\hat{\hat{Q}}|1\rangle & \langle 2|\hat{\hat{Q}}|2\rangle & \cdots & \langle 2|\hat{\hat{Q}}|N^2\rangle \\ \vdots & \vdots & & \vdots \\ \langle N^2|\hat{\hat{Q}}|1\rangle & \langle N^2|\hat{\hat{Q}}|2\rangle & \cdots & \langle N^2|\hat{\hat{Q}}|N^2\rangle \end{bmatrix} \begin{bmatrix} \hat{A}_1 \\ \hat{A}_2 \\ \vdots \\ \hat{A}_N \\ \hat{A}_{N+1} \\ \vdots \\ \hat{A}_{N^2} \end{bmatrix} = \begin{bmatrix} \hat{B}_1 \\ \hat{B}_2 \\ \vdots \\ \hat{B}_N \\ \hat{B}_{N+1} \\ \vdots \\ \hat{B}_{N^2} \end{bmatrix}. \tag{1.95}$$

The superoperator $\hat{\hat{Q}}_{ij}$ is represented as a $n^2 \times n^2$ matrix in Liouville space, with n^4 elements. The indices i and j of $\hat{\hat{Q}}_{ij}$ both extend from 1 to n^2. It should be noted that the use of the word *super* has no connection to other areas of physics such as

supersymmetry but is instead employed to distinguish this higher class of mathematical object from the state operators which are acted upon.

1.6.5 Evolution in Liouville space

For tracking the evolution of a large group of spins, the spin density operator is the weapon of choice. The state of the entire nuclear ensemble may be represented by the state of a single spin, which simplifies enormously the task at hand. An alternative approach is to propagate a state wavefunction in Hilbert space, construct the operator $|\psi\rangle\langle\psi|$, and take the ensemble average $\overline{|\psi\rangle\langle\psi|}$. The spin density operator is propagated forward in time in Liouville space. One of the defining properties of Liouville space, is the representation of operators as vectors, see section 1.6.3. The spin density operator $\hat{\rho}$, previously defined in Hilbert space by using equation 1.55, has the following vector representation in Liouville space:

$$\hat{\rho} = \begin{bmatrix} \rho_\alpha \\ \rho_+ \\ \rho_- \\ \rho_\beta \end{bmatrix}. \tag{1.96}$$

$\hat{\rho}$ has been flattened from a $n \times n$ matrix in Hilbert space into a state operator with dimension $1 \times n^2$ in Liouville space. The time evolution of $\hat{\rho}$ in Liouville space is governed by a super-time propagator $\hat{\hat{U}}(t_b, t_a)$, which acts on the operator vector representation of $\hat{\rho}$ in the following way:

$$\hat{\rho}(t_b) = \hat{\hat{U}}(t_b, t_a)\hat{\rho}(t_a) = \hat{U}(t_b, t_a)\hat{\rho}(t_a)\hat{U}(t_b, t_a)^\dagger, \tag{1.97}$$

where the super-time propagator has the following form:

$$\hat{\hat{U}}(t_b, t_a) = exp[-i \int_{t_a}^{t_b} dt' \hat{\hat{H}}(t')]. \tag{1.98}$$

In Liouville space, $\hat{\hat{U}}(t_b, t_a)$ has a dimension $n^2 \times n^2$, i.e. the square of the operator basis dimension n^2.

1.6.6 Evolution with relaxation

A magnetic nucleus attached to a molecule will evolve under time dependent and independent dynamics. Time dependent dynamics may be caused by the rotational modulation of the molecule tumbling in solution or by fluctuating interactions with other magnetic nuclei. This phenomenon occurs for each spin and will differ slightly depending on the location of the spins in the molecule. The rate of relaxation for each spin will therefore have a likewise spatial dependence. Over time an effect known as relaxation occurs, and nuclear spin order for an ensemble of spins is gradually lost. Relaxation is a one-way process, and returns perturbed nuclear spin order towards thermal equilibrium.

The time evolution of an ensemble of spins, where the overall spin state is represented by the spin density operator $\hat{\rho}(t)$, is governed by the Liouville-von Neumann equation:

$$\frac{d}{dt}\hat{\rho}(t) = \hat{\hat{L}}\hat{\rho}(t), \tag{1.99}$$

where $\hat{\hat{L}}$ is the Liouvillian superoperator, and is expressed as:

$$\hat{\hat{L}} = -i\hat{\hat{H}}_0 + \hat{\hat{\Gamma}}, \tag{1.100}$$

where $\hat{}$ identifies the interaction frame of $\hat{H}_0$. The Hamiltonian $\hat{H}$ is split into a uniform, coherent part $\hat{H}_0$ and an incoherent, fluctuating term $\hat{H}_1 = \hat{H}$ - $\hat{H}_0$. The coherent Hamiltonian $\hat{H}_0$ is responsible for the spin system evolution without relaxation. The spin density operator $\hat{\rho}$ has the following time dependence on the coherent Hamiltonian commutation superoperator $\hat{\hat{H}}_0$:

$$\frac{d}{dt}\hat{\rho}(t) = -i\hat{\hat{H}}_0[\hat{\rho}(t)], \tag{1.101}$$

with $\hat{\hat{H}}_0$ acting on $\hat{\rho}(t)$ expressed by using the commutator relations:

$$\hat{\hat{H}}_0[\hat{\rho}(t)] = [\hat{\hat{H}}_0, \hat{\rho}(t)] = \hat{\hat{H}}_0 \otimes \hat{\rho}(t) - \hat{\rho}(t) \otimes \hat{\hat{H}}_0, \tag{1.102}$$

i.e. the commutation superoperator generates the commutator of the two operators, with $\otimes$ indicating an outer-product. This is a primary example of commutation superoperator usage, and the results of this formalism are widely used across the field of NMR [51, 52].

The Liouville-von Neumann equation includes an additional term $\hat{\hat{\Gamma}}$ attributed to the incoherent relaxation of the spin ensemble towards thermal equilibrium after an rf-perturbation of the nuclear spin populations. $\hat{\hat{\Gamma}}$ is the relaxation superoperator, and is written as follows:

$$\hat{\hat{\Gamma}} = -\int_{-\infty}^{0} d\tau \overline{\hat{\hat{H}}_1(t+\tau)\hat{\hat{H}}_1(t)}, \tag{1.103}$$

where $\hat{\hat{H}}_1(t)$ is the time dependent, perturbing part of the nuclear spin Hamiltonian. Equation 1.103 is derived, and only valid, in the extreme narrowing regime: $\langle \hat{H}_1^2 \rangle^{1/2} \tau_C \ll 1$, where $\langle \hat{H}_1^2 \rangle^{1/2}$ is the root-mean-square fluctuation of the perturbing Hamiltonian $\hat{H}_1$, and τ_C is the correlation time for the motions in the environment surrounding the spins, i.e. the lattice. Inside the relaxation integral lies a double commutation superoperator, consisting of a commutation superoperator inside a commutation superoperator, which acts on $\hat{\rho}$ to give:

$$\overline{\hat{\hat{H}}_1(t+\tau)\hat{\hat{H}}_1(t)}\hat{\rho}(t) = \hat{\hat{H}}_1(t+\tau)[\hat{\hat{H}}_1(t)[\hat{\rho}(t)]]. \tag{1.104}$$

Using the commutator relations, the double commutation relaxation superoperator $\hat{\hat{\Gamma}}$ acting on the spin density operator $\hat{\rho}$ may be expressed as:

$$\hat{\hat{H}}_1(t+\tau)[\hat{\hat{H}}_1(t)[\hat{\rho}(t)]] = [\hat{H}_1(t+\tau), [\hat{H}_1(t), \hat{\rho}(t)]], \tag{1.105}$$

with the continued expansion of $\hat{\hat{\Gamma}}$ described by equation 1.102. The double commutation relaxation superoperator is widely used in this thesis to describe perturbative relaxation processes for an ensemble of spins diluted in a "lattice". For longitudinal and singlet relaxation, intermolecular interactions are ignored and $\hat{H}_1$ is associated with interactions between the spins and the lattice.

1.7 Tools for NMR relaxation

1.7.1 Rotations

Rotations are useful tools in NMR, and allow a pictorial grasp of a few fundamental concepts. For example, the application of a 90° pulse about the x-axis of a right-handed coordinate system can easily be visualized by the rotation of the spin polarization

vector into the $-y$-axis. More complex examples of when rotations are used in NMR include the rotation of an object between frames of reference, such as the rotating frame transformation (see appendix B). Rotations are primarily defined in terms of exponential operators, where the exponent itself is an operator. An exponential operator is defined through an exponential series expansion:

$$e^{\hat{Q}} = 1 + \hat{Q} + \frac{\hat{Q}^2}{2!} + ... \tag{1.106}$$

If operators $\hat{P}$ and $\hat{Q}$ commute, then the following relationship also holds:

$$e^{\hat{P}} e^{\hat{Q}} = e^{(\hat{P}+\hat{Q})}. \tag{1.107}$$

Complex exponentials of the angular momentum operators are rotation operators. Consider an xyz Cartesian axis system, the rotation operators around these axes are given by:

$$\hat{R}_x(\theta) = e^{-i\theta\hat{I}_x}, \tag{1.108}$$

$$\hat{R}_y(\theta) = e^{-i\theta\hat{I}_y}, \tag{1.109}$$

$$\hat{R}_z(\theta) = e^{-i\theta\hat{I}_z}, \tag{1.110}$$

where the subscript denotes the axis of rotation through an angle θ. In general, the operators $\hat{I}_x$, $\hat{I}_y$ and $\hat{I}_z$ do not commute. However, a rotation operator commutes with the angular momentum operator about the same axis:

$$\hat{R}_x(\theta)\hat{I}_x = \hat{I}_x\hat{R}_x(\theta), \tag{1.111}$$

which implies the following sandwich relation:

$$\hat{R}_x(\theta)\hat{I}_x\hat{R}_x(-\theta) = \hat{I}_x, \tag{1.112}$$

where $\hat{R}_x(-\theta)$ is the reverse rotation through an angle θ about the x-axis, i.e. $\hat{R}_x(-\theta)\hat{R}_x(\theta) = \hat{\mathbb{1}}$. Since the angular momentum operators are Hermitian, the rotation operators are unitary:

$$\hat{R}_x(\theta)^\dagger = \hat{R}_x(\theta)^{-1} = \hat{R}_x(-\theta), \tag{1.113}$$

and therefore equation 1.112 may be rewritten as:

$$\hat{R}_x(\theta)\hat{I}_x\hat{R}_x^{-1}(\theta) = \hat{I}_x. \tag{1.114}$$

When a rotation operator is applied to the angular momentum operator about a different axis, the sandwich relationship reads:

$$\hat{R}_z(\theta)\hat{I}_x\hat{R}_z^{-1}(\theta) = \hat{I}_x\cos(\theta) + \hat{I}_y\sin(\theta). \tag{1.115}$$

This relationship can be proved as follows. Explicitly write out $\hat{R}_x(\theta)\hat{I}_x\hat{R}_x^{-1}(\theta)$:

$$= \quad e^{-i\phi\hat{I}_z}\hat{I}_x e^{i\phi\hat{I}_z} \tag{1.116}$$

$$= \quad \left(1 - i\theta\hat{I}_z - \frac{\theta^2}{2}\hat{I}_z^2 + ...\right)\hat{I}_x\left(1 + i\theta\hat{I}_z - \frac{\theta^2}{2}\hat{I}_z^2 + ...\right) \tag{1.117}$$

$$= \quad \hat{I}_x - i\theta[\hat{I}_z, \hat{I}_x] + -\frac{\theta^2}{2}[\hat{I}_z, [\hat{I}_z, \hat{I}_x]] + \frac{i\theta^3}{6}[\hat{I}_z, [\hat{I}_z, [\hat{I}_z, \hat{I}_x]]] + ... \tag{1.118}$$

This appears to be quite a formidable equation. Luckily, the angular momentum operators possess cyclic commutivity, i.e. $[\hat{I}_x, \hat{I}_y] = i\epsilon_{xyz}\hat{I}_z$, where $\epsilon_{xyz} = +1$ if the permutation order xyz is maintained. The above equation is therefore simplified to:

$$\hat{R}_z(\theta)\hat{I}_x\hat{R}_z^{-1}(\theta) = \hat{I}_x + \theta\hat{I}_y - \frac{\theta^2}{2}\hat{I}_x - \frac{\theta^3}{6}\hat{I}_y + ... \tag{1.119}$$

A parallel series of sines and cosines is cleanly produced:

$$\hat{R}_z(\theta)\hat{I}_x\hat{R}_z^{-1}(\theta) = \hat{I}_x\left(1 - \frac{\theta^2}{2} + ...\right) + \hat{I}_y\left(\theta - \frac{\theta^3}{6} + ...\right), \tag{1.120}$$

where the $\cos(\theta)$ and $\sin(\theta)$ series are identified as:

$$\cos(\theta) \quad = \quad \left(1 - \frac{\theta^2}{2} + ...\right), \tag{1.121}$$

$$\sin(\theta) \quad = \quad \left(\theta - \frac{\theta^3}{6} + ...\right), \tag{1.122}$$

resulting in:

$$\hat{R}_z(\theta)\hat{I}_x\hat{R}_z^{-1}(\theta) = \hat{I}_x\cos(\theta) + \hat{I}_y\sin(\theta). \tag{1.123}$$

The sandwich relation described in equation 1.123 also follows a cyclic commutation rule, and implies a second sandwich relation:

$$\hat{R}_z(\theta)\hat{R}_x(\phi)\hat{R}_z(-\theta) = e^{-i\phi(\hat{I}_x\cos(\theta)+\hat{I}_y\sin(\theta))}. \tag{1.124}$$

1.7.2 Euler angles

The orientation of an object in three-dimensional (3D) space can be specified by three finite, arbitrary rotations around the axes of an orthogonal coordinate system $\{x, y, z\}$. NMR spectroscopy makes use of the Euler angle conventions, which become particularly useful when discussing magnetic interactions and relaxation theory (see chapter 3). Throughout this thesis, the Euler angle convention used is zyz. This convention indicates that the orientation of an object in 3D space is given by the product of three general rotations with respect to a single axis frame $\{x, y, z\}$; firstly a rotation around the z-axis, followed by a rotation around the y-axis, followed by a final rotation around the z-axis again:

$$\hat{R}(\Omega) = \hat{R}(\alpha, \beta, \gamma) = \hat{R}_z(\alpha)\hat{R}_y(\beta)\hat{R}_z(\gamma), \tag{1.125}$$

where Ω provides a quick substitution for α, β, γ. The set of Euler angles presented in equation 1.125 allow the transformation of an object in the $\{x, y, z\}$ frame to a second frame, with orthogonal $\{X, Y, Z\}$ axes. One can consider this to be the rotation of a frame coincident with the starting $\{x, y, z\}$ axis system. The first rotation reorients the object by an angle γ about the z-axis of the $\{x, y, z\}$ axis system, taking the coincident frame into an axis system described by the axes $\{x', y', z'\}$. The second rotation reorients the object by an angle β about the y-axis of the original $\{x, y, z\}$ frame. The frame $\{x', y', z'\}$ is rotated into the frame $\{x'', y'', z''\}$. The final rotation reorients the object by an angle α about the z-axis of the $\{x, y, z\}$ frame, and hence the $\{x, y, z\}$ and $\{X, Y, Z\}$ frames are now coincident. As is the convention with matrix multiplication, the right-most operator is applied first. A second way to think of how to apply the Euler angles is to give the object being reoriented an axis system $\{x, y, z\}$ of its own, and then apply the rotations in the opposite order, with the first rotation being $\hat{R}_z(\alpha)$ around the z-axis of the $\{x, y, z\}$ axis system. Apply the second rotation $\hat{R}_y(\beta)$ around the new y-axis of the objects own coordinate system y', therefore the second rotation is $\hat{R}_{y'}(\beta)$. Consequently, the final rotation $\hat{R}_z(\gamma)$ reorients the object about the newest z-axis of

the objects coordinate system z'', with the final rotation being $\hat{R}_{z''}(\alpha)$. The two sets of Euler angles are equivalent:

$$\hat{R}_z(\alpha)\hat{R}_y(\beta)\hat{R}_z(\gamma) = \hat{R}''_z(\gamma)\hat{R}'_y(\beta)\hat{R}_z(\alpha). \tag{1.126}$$

The Euler angle rotation matrices $\mathbf{R}_i(\theta)$, the matrix equivalent of the rotation operator $\hat{R}_i(\theta)$, for a rotation in 3D space (zyz convention) are expressed as follows:

$$\mathbf{R}_z(\gamma) = \begin{bmatrix} \cos(\gamma) & -\sin(\gamma) & 0 \\ \sin(\gamma) & cos(\gamma) & 0 \\ 0 & 0 & 1 \end{bmatrix}, \tag{1.127}$$

$$\mathbf{R}_y(\beta) = \begin{bmatrix} \cos(\beta) & 0 & -\sin(\beta) \\ 0 & 1 & 0 \\ \sin(\beta) & 0 & cos(\beta) \end{bmatrix}, \tag{1.128}$$

$$\mathbf{R}_z(\alpha) = \begin{bmatrix} \cos(\alpha) & -\sin(\alpha) & 0 \\ \sin(\alpha) & cos(\alpha) & 0 \\ 0 & 0 & 1 \end{bmatrix}. \tag{1.129}$$

The rotation matrix $\mathbf{R}_z(\gamma)$ is verified by taking the unit vectors $\{\hat{e}_x, \hat{e}_y, \hat{e}_z\}$ for the $\{x, y, z\}$ frame, which are coincident with the axis system, and performing the operation $\mathbf{R}_z(\gamma)\hat{e}_i$, where $i = x, y, z$. The rotated unit vector points along the appropriate axis of the rotated frame. Rotation matrices $\mathbf{R}_y(\beta)$ and $\mathbf{R}_z(\alpha)$ are verified in the same manner. The rotation matrices $\mathbf{R}_z(\gamma)$, $\mathbf{R}_y(\beta)$ and $\mathbf{R}_z(\alpha)$ lead to the following accumulative rotation of an object between two axis systems, given by the Euler angle rotation matrix $\mathbf{R}(\alpha, \beta, \gamma)$:

$$\mathbf{R}(\alpha, \beta, \gamma) = \tag{1.130}$$
$$\begin{bmatrix} \cos(\alpha)\cos(\beta)\cos(\gamma) - \sin(\alpha)\sin(\gamma) & -\sin(\alpha)\cos(\gamma) - \cos(\alpha)\cos(\beta)\sin(\gamma) & \cos(\alpha)\sin(\beta) \\ \sin(\alpha)\cos(\beta)\cos(\gamma) + \cos(\alpha)\sin(\gamma) & \cos(\alpha)\cos(\gamma) - \sin(\alpha)\cos(\beta)\sin(\gamma) & \sin(\alpha)\sin(\beta) \\ -\sin(\beta)\cos(\gamma) & \sin(\beta)\sin(\gamma) & \cos(\beta) \end{bmatrix}.$$

Often one would like to rotate a Cartesian tensor, which describes a physical quantity, expressed in a frame $\{x, y, z\}$ to a frame $\{X, Y, Z\}$. The appropriate transformation for

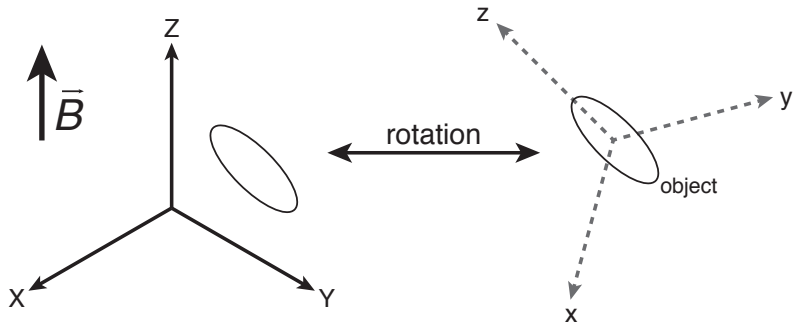

FIGURE 1.12: The rotation operator $\hat{R}(\Omega)$ specified by the Euler angles $\{\alpha, \beta, \gamma\}$ rotates an object from a frame with axes $\{x, y, z\}$ to a frame with axes $\{X, Y, Z\}$ in which the Z axis is defined to be parallel with the static magnetic field $\vec{B}$.

a tensor A under these circumstances is:

$$A\{X, Y, Z\} = \mathbf{R}(\alpha, \beta, \gamma) A\{x, y, z\} \mathbf{R}^{-1}(\alpha, \beta, \gamma), \tag{1.131}$$

where $\mathbf{R}^{-1}(\alpha, \beta, \gamma)$ specifies the reverse rotation $\mathbf{R}(-\alpha, -\beta, -\gamma)$. Two successive Euler rotations, $\mathbf{R}(\Omega_1)$ and $\mathbf{R}(\Omega_2)$, are also accumulative: $\mathbf{R}(\Omega_1, \Omega_2) = \mathbf{R}(\Omega_2)\mathbf{R}(\Omega_1)$.

1.7.3 Wigner rotation matrices

The Euler angles are a useful tool for defining the relative orientations of orthogonal axis systems, such as those defined by the laboratory frame and the molecular frame, see figure 1.12. Using equations 1.108-1.110, the rotation operator can be rewritten as [53]:

$$\hat{R}(\alpha, \beta, \gamma) = e^{-i\alpha \hat{I}_z} e^{-i\beta \hat{I}_y} e^{-i\gamma \hat{I}_z}. \tag{1.132}$$

The Wigner function $D^l_{m'm}$ is the rotation operator $\hat{R}(\alpha, \beta, \gamma)$ in the eigenket basis of the Hamiltonian, with matrix elements:

$$\langle lm' | \hat{R}(\alpha, \beta, \gamma) | lm \rangle = D^l_{m'm}(\alpha, \beta, \gamma). \tag{1.133}$$

The Wigner function $D^l_{m'm}(\alpha, \beta, \gamma)$ is of $2l + 1$ dimension, where l is the rank of the Wigner rotation matrix. The indices m and m' indicate the components of the Wigner function $D^l_{m'm}(\alpha, \beta, \gamma)$. The Wigner function is a matrix of complex numbers, and complex exponentials which define the reorientation of an object in 3D space.

$(D^l_{m'm}(\alpha,\beta,\gamma))^\dagger$ is the adjoint of $D^l_{m'm}(\alpha,\beta,\gamma)$ and hence the matrix elements are related by:

$$\langle lm'|\,\hat{R}^\dagger(\alpha,\beta,\gamma)\,|lm\rangle = (\langle lm'|\,\hat{R}(\alpha,\beta,\gamma)\,|lm\rangle)^{-1} = (D^l_{m'm}(\alpha,\beta,\gamma))^{-1}. \tag{1.134}$$

Furthermore, as the rotation operators $\hat{R}(\alpha,\beta,\gamma)$ are unitary:

$$(D^l_{m'm}(\alpha,\beta,\gamma))^{-1} = D^l_{m'm}(-\alpha,-\beta,-\gamma), \tag{1.135}$$

the Wigner rotation matrices are also unitary:

$$\sum_{m'} = (D^l_{m'n}(\alpha,\beta,\gamma))^{-1} D^l_{m'm}(\alpha,\beta,\gamma) = \delta_{mn}. \tag{1.136}$$

As the basis vectors are given by the angular momentum eigenfunctions $\hat{I}_x, \hat{I}_y$ and $\hat{I}_z$, equation 1.133 becomes:

$$\begin{aligned} D^l_{m'm}(\alpha,\beta,\gamma) &= \langle lm'|\,e^{-i\gamma\hat{I}_z}e^{-i\beta\hat{I}_y}e^{-i\alpha\hat{I}_z}\,|lm\rangle\,, & (1.137)\\ &= e^{-i(m'\alpha+m\beta)}\,\langle lm'|\,e^{-i\beta\hat{I}_y}\,|lm\rangle\,, & (1.138)\\ &= e^{-i(m'\alpha+m\beta)}d^l_{mm'}(\beta), & (1.139) \end{aligned}$$

where $d^l_{m'm}(\beta)$ is the reduced Wigner matrix element. For the rotations of rank-2 spherical tensors, the reduced Wigner matrix becomes large and complicated. A key element of this matrix is d^2_{00}:

$$d^2_{00} = \frac{3\cos^2(\beta)-1}{2}. \tag{1.140}$$

This component vanishes at the magic angle $\tan^{-1}(\sqrt{2})$, and is useful property for the technique of singlet-filtration [54–56].

1.7.4 Spherical tensors

So far during this chapter I have discussed NMR using a Cartesian operator basis, which provides a simple way of describing nuclear spin interactions. The NMR Hamiltonian can be written using either Cartesian operators or spherical tensor operators [57]. The operator basis is largely a matter of choice but there will likely be situations in which a certain operator basis is more convenient to use than another. For example, the spherical

tensor operator basis has specific symmetry properties which prove more convenient for 3D rotations in space, such as the rank of the spherical tensor operator being an invariant property under a rotation, compared with using a Cartesian operator basis.

In general, an NMR Hamiltonian is expressed in the following way:

$$\hat{H}_{\text{local}} = -\gamma \hat{I} \cdot A_{\text{local}} \cdot \hat{K}, \tag{1.141}$$

where A_{local} is a second-rank Cartesian tensor describing the interaction strength and orientational dependence of a local interaction A. The vector operator $\vec{K}$ depends on the type of spin interaction. Expanding the scalar product allows one to restructure the Hamiltonian:

$$\hat{H}_{\text{local}} = \sum_{i,j} A_{ij} \hat{I}_i \hat{K}_j, \tag{1.142}$$

with $-\gamma A_{\text{local}} \rightarrow A_{ij}$. Collecting the vector operators $\hat{I}_i$ and $\hat{K}_j$ simplifies the Hamiltonian further:

$$\hat{H}_{\text{local}} = \sum_{i,j} A_{ij} \hat{T}_{ij}, \tag{1.143}$$

with $\hat{I}_i \otimes \hat{K}_j \rightarrow \hat{T}_{ij}$. $\hat{T}$ is a second rank Cartesian tensor operator with nine elements T_{ij} that can be decomposed into:

$$\hat{T}_{ij} = \delta_{ij} \hat{T}_{ij}^{(0)} + \hat{T}_{ij}^{(1)} + \hat{T}_{ij}^{(2)}, \tag{1.144}$$

or more specifically:

$$\hat{I}_i \otimes \hat{K}_j = \delta_{ij} \frac{\hat{I} \cdot \hat{K}}{3} + \frac{\hat{I}_i \hat{K}_j - \hat{I}_j \hat{K}_i}{2} + \left(\frac{\hat{I}_i \hat{K}_j + \hat{I}_j \hat{K}_i}{2} - \delta_{ij} \frac{\hat{I} \cdot \hat{K}}{3} \right). \tag{1.145}$$

The index in brackets represents the rank of the *spherical* tensor operator. $\delta_{ij} \hat{T}_{ij}^{(0)}$ is a scalar and is hence invariant under rotations. The three components of $\hat{T}_{ij}^{(1)}$ form a vector, and transform between themselves under rotations. The five (6-1) components of $\hat{T}_{ij}^{(2)}$ form a linear superposition under a rotation of a single component of $\hat{T}_{ij}^{(2)}$. The matrix representation of these objects is discussed in terms of the chemical shift interaction in section 1.8.3. The number of components for each rank matches the multiplicities of an object with angular momentum l=0, l=1 and l=2, respectively. Therefore, we have successfully decomposed a Cartesian tensor operator into spherical

tensors operators.

Earlier I discussed the consequences of degenerate nuclear spin energy levels in the presence of a magnetic field. For an angular momentum quantum number I, the spin state is $2I + 1$ degenerate. Spherical tensor operators possess a similar property. A spherical tensor operator of rank l is formally a set of $2l + 1$ objects. These objects all possess the following property: if a single object in the $2l + 1$ set is arbitrarily rotated in 3D space about any axis and any angle, the result is a linear superposition of the same $2l + 1$ objects. Therefore, to rewrite equation 1.143 in terms of spherical tensor operators, one must use the definition of the transformation properties for a spherical tensor operator, of rank l and component m, under a rotation defined by the axes and angles of $\hat{R}(\Omega)$. A component of the spherical tensor operator $\hat{T}_{lm}$ must transform under a rotation, in the axis system defining $\hat{T}_{lm}$, according to:

$$\hat{\hat{R}}(\alpha,\beta,\gamma)\hat{T}_{lm} = \hat{R}(\alpha,\beta,\gamma)\hat{T}_{lm}\hat{R}^{-1}(\alpha,\beta,\gamma), \tag{1.146}$$

$$= \sum_{m'=-l}^{l} \hat{T}_{lm'} D^{l}_{m'm}(\alpha,\beta,\gamma), \tag{1.147}$$

where $D^{l}_{m'm}(\alpha,\beta,\gamma)$ is the Wigner rotation matrix for the rotation $\hat{R}(\alpha,\beta,\gamma)$ and is defined in section 1.7.3. The rotation superoperator $\hat{\hat{R}}(\alpha,\beta,\gamma)$ is constructed from the unitary rotation operator $\hat{R}(\alpha,\beta,\gamma)$ as follows:

$$\hat{\hat{R}}(\alpha,\beta,\gamma) = \hat{R}(\alpha,\beta,\gamma) \otimes \hat{R}(\alpha,\beta,\gamma)^{-1}. \tag{1.148}$$

As expected, the result of this general 3D rotation is a linear superposition of a $2l + 1$ set of operators, with the value of l conserved. Spherical tensor components A_{lm} also have a similar rotational property:

$$\hat{R}(\alpha,\beta,\gamma)A_{lm} = \sum_{m'=-l}^{l} A_{lm'} D^{l}_{m'm}(\alpha,\beta,\gamma). \tag{1.149}$$

The representation of the Hamiltonian operator in NMR is usually of the form:

$$\hat{H}^{\Lambda} = \sum_{l} \sum_{m=-l}^{l} (-1)^{m} A^{\Lambda}_{lm}(t)\hat{T}^{\Lambda}_{l-m}, \tag{1.150}$$

for an interaction λ with $A^{\Lambda}_{lm}(t)$ and $\hat{T}^{\Lambda}_{l-m}$ defined in equations 1.149 and 1.146, respectively. This definition of the NMR Hamiltonian, which uses spherical tensor operators, is exploited in chapter 3 during a discussion of intra-methyl group interactions.

A nice aftereffect of equation 1.146 is the mathematical foundation for the laws of commutation between the components of the angular momentum $\hat{I}_{\lambda}$ and the components of the spherical tensor operator $\hat{T}_{lm}$. Consider the infinitesimal rotation operator which rotates an object through an infinitesimal angle α about the z-axis: $\hat{R}_{\alpha} = \hat{\mathbb{1}}$ - $i\alpha\hat{I}_z$, where $\hat{I}_z$ is Hermitian. This can be demonstrated by transforming the operator $\hat{I}_x$ from a frame with axes $\{x, y, z\}$ to a frame with axes $\{X, Y, Z\}$ as follows:

$$\begin{aligned} \hat{I}_X &= \hat{R}_{\alpha}\hat{I}_x\hat{R}^{-1}_{\alpha}, & (1.151)\\ &= (\hat{\mathbb{1}} - i\alpha\hat{I}_z)\hat{I}_x(\hat{\mathbb{1}} + i\alpha\hat{I}_z), & (1.152)\\ &= \hat{I}_x + i\alpha(\hat{I}_z\hat{I}_x - \hat{I}_x\hat{I}_z). & (1.153) \end{aligned}$$

By using know commutation relations, equation 1.153 becomes:

$$\hat{I}_X = \hat{I}_x + i\alpha[\hat{I}_z, \hat{I}_x] = \hat{I}_x - \alpha\hat{I}_y. \tag{1.154}$$

The commutation relation for angular momentum and spherical tensor operators is derived by using equation 1.133:

$$D^{l}_{m'm} = \langle lm'|\,\hat{\mathbb{1}} - i\alpha\hat{I}_{\lambda}\,|lm\rangle = \delta_{m'm} - i\alpha\,\langle lm'|\,\hat{I}_{\lambda}\,|lm\rangle\,. \tag{1.155}$$

With this rotation and equation 1.146 one finds:

$$(\hat{\mathbb{1}} - i\alpha\hat{I}_{\lambda})\hat{T}_{lm}(\hat{\mathbb{1}} + i\alpha\hat{I}_{\lambda}) = \sum_{m'}\hat{T}_{lm'}D^{l}_{m'm}, \tag{1.156}$$

which simplifies to:

$$\hat{I}_{\lambda}\hat{T}_{lm} - \hat{T}_{lm}\hat{I}_{\lambda} = \sum_{m'}\hat{T}_{lm'}\,\langle lm'|\,\hat{I}_{\lambda}\,|lm\rangle\,. \tag{1.157}$$

For example, substituting λ for $\pm$ yields [53]:

$$[\hat{I}_{\pm}, \hat{T}_{lm}] = [(l \pm m + 1)(l \mp m)]^{1/2}\hat{T}_{lm\pm1}, \tag{1.158}$$

using the relation:

$$\langle lm \pm 1|\hat{I}_{\pm}|lm\rangle = [(l \pm m + 1)(l \mp m)]^{1/2}. \tag{1.159}$$

In the case of $\lambda = z$:

$$[\hat{I}_z, \hat{T}_{lm}] = m\hat{T}_{lm}. \tag{1.160}$$

In chapter 2 similar properties are used to show that the scalar operator $\hat{T}_{ij}^{(0)} = \hat{T}_{00}^{ij}$ is a constant of the motion for the Liouville-von Neumann equation, see equation 1.99.

1.8 NMR interactions

In general, the nuclear spin Hamiltonian is the summation of a number of individual Hamiltonians which each represent an interaction in NMR:

$$\hat{H} = \hat{H}_Z + \hat{H}_{DD} + \hat{H}_Q + \hat{H}_{CS} + \hat{H}_{\text{other}} + \hat{H}_{RF}, \tag{1.161}$$

where $\hat{H}_Z$ represents the Zeeman Hamiltonian (the Zeeman effect has previously been discussed in section 1.2, and the Zeeman Hamiltonian is discussed in chapter 2, section 2.9). $\hat{H}_{DD}$ represents the dipole-dipole Hamiltonian defining the direct magnetic interaction between two nuclei. $\hat{H}_Q$ describes the quadrupole interaction for spins with an angular momentum quantum number $I > 1/2$. $\hat{H}_{CS}$ is the chemical shift Hamiltonian and governs the orientationally dependent interaction between a nuclear spin and the immediate electronic environment. Other Hamiltonians include the scalar (J) coupling Hamiltonian $\hat{H}_J$, and the spin-rotation Hamiltonian $\hat{H}_{SR}$. These additional interactions, including interactions with externally applied radiofrequency fields $\hat{H}_{RF}$, are not covered in this thesis, and the details of which are found in references [41, 45, 47, 50, 58–61]. In this section I will discuss the dipole-dipole, quadrupole and chemical shift Hamiltonians, and the interaction each Hamiltonian describes.

1.8.1 Dipole-dipole interaction

Most nuclear spins are inherently magnetic, and possess an intrinsic magnetic moment. Magnetic nuclei also generate a dipole field, see figure 1.13. A two-dimensional projection of the dipole field can easily be observed by the traditional “bar magnet and iron filings” experiment. The direction of the magnetic field vector (along a magnetic field loop)

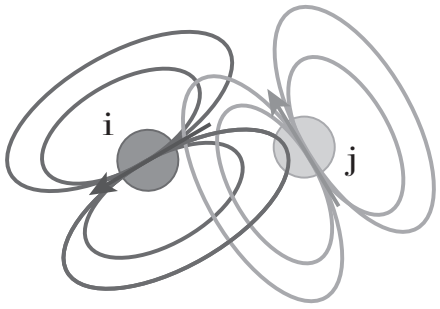

FIGURE 1.13: Schematic depicting the direct dipole-dipole interaction. The magnetic field generated by spin i is experienced at the site of spin j, i.e. the local field emanating from one magnetic nucleus influences any neighbouring nuclei, and vice versa. The strength of the interaction depends on the distance and relative orientation of the magnetic moments. The loops represent the magnetic field lines.

depends on the orientation of the magnetic moment. Suppose that a magnetic nucleus i is brought into the close proximity of a second nucleus j. Here close proximity is associated with the molecular length scale, which is on the order of Angstroms. As each magnetic nucleus naturally generates its own dipole field, the two fields can mutually interact *through space*, i.e. the first spin experiences the field from the second spin, and vice versa. The full form of the dipole-dipole interaction between spins i and j is given by the dipole-dipole Hamiltonian $\hat{H}^{ij}_{DD}$:

$$\hat{H}^{ij}_{DD} = b_{ij}(3(\hat{I}_i \cdot \hat{e}_{ij})(\hat{I}_j \cdot \hat{e}_{ij}) - \hat{I}_i \cdot \hat{I}_j), \tag{1.162}$$

where b_{ij} is the dipole-dipole coupling constant between spins i and j and is expressed as:

$$b_{ij} = -\frac{\mu_0 \hbar^2 \gamma_i \gamma_j}{4\pi r^3_{ij}}, \tag{1.163}$$

where μ_0 is the magnetic constant: $\mu_0 = 4\pi \times 10^{-7}\,\mathrm{H\,m^{-1}}$, γ_i and γ_j are the gyromagnetic ratios of spins i and j, respectively, r_{ij} is the internuclear separation between the two spins, and $\hat{e}_{ij}$ is a unit vector parallel to the internuclear vector connecting the two nuclei [50]. The dipole-dipole coupling constant b_{ij} determines the size of the dipole-dipole interaction. Dipole-dipole couplings can either be homonuclear (same isotopic type) or heteronuclear (different isotopic type). Homonuclear dipole-dipole couplings always have a negative sign. It should be noted that b_{ij} is a constant for a fixed internuclear separation r_{ij} between spins i and j, and is a function of the third power of the internuclear separation. b_{ij} is not orientationally dependent, i.e. it is a constant for any relative orientation of the two magnetic nuclei. However, the dipole-dipole Hamiltonian

$\hat{H}_{DD}$ is orientationally dependent due to the scalar product of the unit vector $\hat{e}_{ij}$ with the spin angular momentum $\hat{I}_i$. The direction in which the unit vector $\hat{e}_{ij}$ points, relative to a fixed frame of reference, can change due to e.g. molecular tumbling in solution. The negative sign of the dipole-dipole Hamiltonian $\hat{H}_{DD}$ indicates that the overall energy of the interaction is minimized when both nuclei point in the same direction, i.e. along the internuclear vector. This interaction can be extended to a cluster of magnetic nuclei, where each spin pair has a mutual dipole-dipole interaction. The cluster dipole-dipole Hamiltonian in this case is given by:

$$\hat{H}_{DD}^{\text{cluster}} = \sum_{i} \sum_{j}^{i-1} \hat{H}_{DD}^{ij}, \tag{1.164}$$

which considers all pairs of spins ij with $i \neq j$ in the cluster. At high magnetic field, the cluster dipole-dipole Hamiltonian containing the double summation can be simplified depending on whether spins i and j are of the same isotopic species. This process is known as the *secular approximation*:

- The secular approximation concerns the general case where a nuclear spin Hamiltonian is comprised of two separate sub-Hamiltonians $\hat{H}_A$ and $\hat{H}_B$, where $\hat{H}_A \gg \hat{H}_B$. Since $\hat{H}_A$ and $\hat{H}_B$ are assumed to be hermitian, if $\hat{H}_B$ does not commute with $\hat{H}_A$ then the matrix representation of $\hat{H}_B$ in the orthonormal eigenbasis of $\hat{H}_A$ will consist of finite elements at all positions. The *secular approximation* etches a block-diagonal structure from this matrix, and disregards all connecting components, generating a new matrix $\hat{H}'_B$. The block-diagonal subspaces denote degenerate or near-degenerate eigenvalues of $\hat{H}_A$. The ignored off-diagonal components include those with amplitudes which are significantly smaller than the difference in the connected terms.

In the case of a homonuclear spin pair (same isotopic species), the secularized dipole-dipole Hamiltonian is written as:

$$\hat{H}_{DD}^{ij}(\Theta_{ij}) = d_{ij}(\Theta_{ij})(3\hat{I}_{iz} \cdot \hat{I}_{jz} - \hat{I}_i \cdot \hat{I}_j), \tag{1.165}$$

where d_{ij} is the secular dipole-dipole coupling, and is given by:

$$d_{ij}(\Theta_{ij}) = b_{ij} \frac{3\cos^2(\Theta_{ij}) - 1}{2}, \tag{1.166}$$

where Θ_{ij} is the angle between the internuclear vector connecting spins i and j, and the static magnetic field $\vec{B}_0$:

$$\cos(\Theta_{ij}) = \hat{e}_{ij} \cdot \hat{e}_z. \tag{1.167}$$

The secularized dipole-dipole coupling $d_{ij}(\Theta_{ij})$ differs from the non-secularized dipole-dipole coupling b_{ij} by its orientational dependence. In the case of a heteronuclear spin pair (different isotopic species), the secular part of the dipole-dipole Hamiltonian is written as:

$$\hat{H}^{ij}_{DD}(\Theta_{ij}) = 2d_{ij}\hat{I}_{iz} \cdot \hat{I}_{jz}. \tag{1.168}$$

The homonuclear secular dipole-dipole coupling is equal to zero when Θ_{ij}, the angle between the internuclear vector and the static magnetic field, satisfies:

$$\Theta_{ij} = \tan^{-1}(\sqrt{2}). \tag{1.169}$$

This solution is referred to as the "magic angle" and has important consequences in solid-state NMR. Spinning samples at frequencies in excess of $\sim$1 kHz at the magic angle relative to the static magnetic field significantly improves spectral resolution as the resonance lines are narrowed upon the removal of dipole-dipole (and other second rank) interactions [50].

Liquid state NMR on the other hand is typically performed in isotropic solution. This is of important consequence for the acquired NMR spectra. In isotropic liquids, the secular parts of the intramolecular dipole-dipole coupling average to zero, to good approximation. Consider the following integral:

$$\int_0^\infty d\Theta_{ij} b_{ij} \sin(\Theta_{ij}) \left(\frac{3\cos^2(\Theta_{ij}) - 1}{2} \right) = 0, \tag{1.170}$$

with the factor of $\sin(\Theta_{ij})$ necessary to give all possible orientations equal probability. The short range dipole-dipole couplings are completely averaged by the rotational and translational motions of the molecules in solution. Long range dipole-dipole couplings are not completely averaged out by the same motions, but are relatively small and can often be neglected. The dipole-dipole Hamiltonian in an isotropic liquid therefore becomes, too good approximation:

$$\hat{H}^{ij}_{DD}(\Theta_{ij}) \cong 0. \tag{1.171}$$

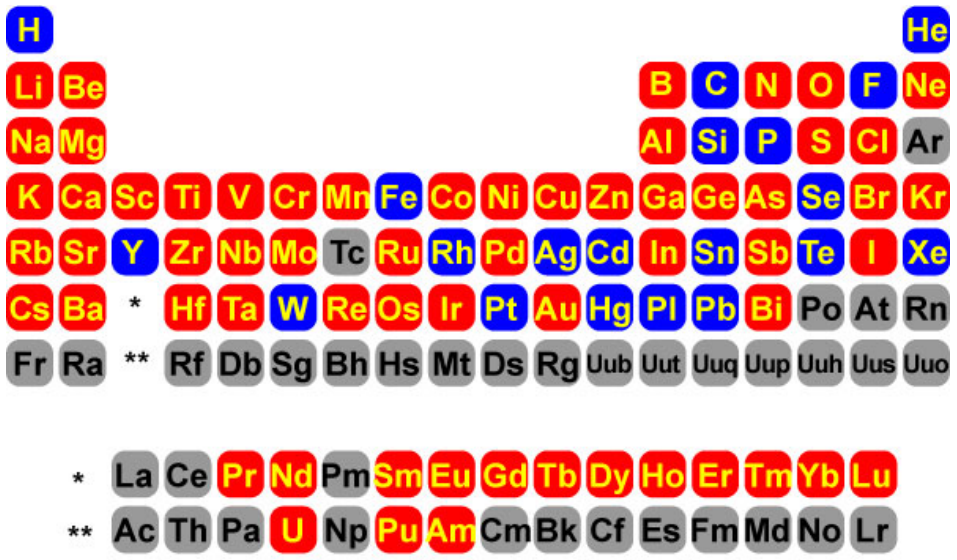

FIGURE 1.14: The majority (∼74 %) of active NMR nuclei are quadrupolar, as depicted by the periodic table of quadrupole nuclei. $I = 1/2$ isotopes are coloured blue, $I > 1/2$ isotopes are coloured red. Magnetically inert nuclei are coloured grey. The most abundant, NMR active isotope is shown for each element. For example, a spin-1/2 isotope of nitrogen (^{15}N) also exists and has many important uses in magnetic resonance spectroscopy. Source: http://kuchem.kyoto-u.ac.jp/bun/projects/microMAS/microMAS_e.html.

Appendix B covers this topic in more detail. The non-secular parts of the dipole-dipole Hamiltonian are not averaged out in solution, and this has consequences for NMR relaxation in isotropic liquids, see appendix B.

1.8.2 Electric quadrupole interaction

As of yet, discussion of magnetic nuclei and spin angular momentum has been limited to spins with an angular momentum quantum number $I = 1/2$. Quadrupolar nuclei on the other hand, identify nuclear spins with an angular momentum quantum number $I > 1/2$. Such nuclei are very common in the periodic table, see figure 1.14.

Quadrupolar nuclei possess an electric quadrupole moment. The electric quadrupole moment arises from the non-spherical distribution of charge in the nucleus. The distribution of charge for a quadrupole nucleus cannot be adequately described by the total charge, and should be treated as a series of multipoles, known as a multipole expansion, see figure 1.15. Details of the multipole expansion for a quadrupolar nucleus are given in appendix B. The second-order term in the multipole series expansion yields the electric quadrupole moment. The electric quadrupole moment interacts strongly with an

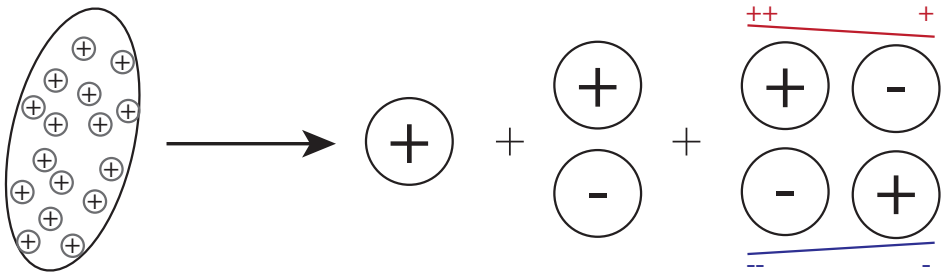

FIGURE 1.15: A non-spherical nuclear charge structure can be described by a series expansion of multipoles. The zeroth-order multipole term is the total charge, the first-order multipole term is the electric dipole moment, and the second-order multipole term is the electric quadrupole moment. The high (red +) and low (blue -) electron density around the nucleus creates an electric field gradient (EFG) which interacts with the electric quadrupole moment [50].

electric field gradient (EFG) present at the nucleus due to the asymmetric distribution of the surrounding electron density. Quadrupolar nuclei therefore have both nuclear (magnetic moment) and electric (quadrupole moment) properties, and as a consequence quadrupolar nuclei interact with all applied and local magnetic fields, and electric field gradients.

The static magnetic field $\vec{B}_0$ acts to align the magnetic dipole moment of a nucleus with the magnetic field, for the case of $\gamma > 0$. The electric field gradient on the other hand depends on the immediate environment of the nucleus, through the whereabouts of other nuclei and electrons, i.e. the geometry of the bonds attached the nucleus. The size of the electric quadrupole interaction therefore depends on more than just the size of the quadrupole moment, namely:

- The orientation of the molecule with respect to $\vec{B}_0$,
- The environment in which the quadrupolar nucleus is located.

Large quadrupolar couplings may be cancelled by symmetrical environments, and small quadrupolar couplings may be amplified by large electric field gradients.

The electric field gradient (EFG) at a quadrupolar nucleus is classified with respect to two properties:

1. eq the largest principal value of the EFG tensor,
2. η_Q the biaxality of the EFG tensor.

These two properties are defined as follows:

$$eq = V_{zz}, \tag{1.172}$$

$$\eta_Q = \frac{(V_{xx} - V_{yy})}{V_{zz}}, \tag{1.173}$$

where eq is a constant and is independent of the molecular environment. η_Q is a scalar and has values between 0 and 1. The EFG tensor V is written as:

$$V = \begin{bmatrix} V_{xx} & 0 & 0 \\ 0 & V_{yy} & 0 \\ 0 & 0 & V_{zz} \end{bmatrix}, \tag{1.174}$$

where V has a zero-trace, i.e. $V_{xx} + V_{yy} + V_{zz} = 0$, and is symmetric, i.e. $V_{ij} = V_{ji}$. The EFG tensor in the principal axis system (PAS) frame is strictly diagonal. The diagonal components V_{ii} are called the principal components. The principal components correspond to the principal axes of the EFG tensor. The principal axes of the EFG tensor are defined by: $V_{zz} \geq V_{yy} \geq V_{xx}$. Interaction tensors, such as those for the quadrupolar interaction, are often represented by ellipsoids. Figure 1.16 shows the ellipsoids representing the quadrupolar interaction for different values of V_{zz} and η_Q. The principal axes for different values of V_{zz} and η_Q are also shown pictorially in figure 1.16. Figure 1.16a) gives the case of an isotropic quadrupole tensor $V_{zz} = 0$ since the quadrupolar interaction has a zero isotropic average, b) describes the case of a uniaxial quadrupole tensor $V_{zz} \neq 0$, $\eta_Q = 0$, and c) shows the case of a biaxial tensor $V_{zz} \neq 0$, $\eta_Q \neq 0$. It should be noted that for the quadrupolar interaction situation a) is not realistic, and is far more present for the case of chemical shift anisotropy (CSA) interaction, see section 1.8.3. The one case where situation a) is present in quadrupolar NMR is for a molecule of $^{14}NH_4^+$, which has a remarkably symmetric electron density surrounding the ^{14}N nucleus. As a result, the magnitude of the quadrupolar interaction is very small, and the tensor is highly symmetric. This outcome is brought about because the electric field gradients cancel at the centre of the ^{14}N nucleus. Situation b) is common for deuterium nuclei in methyl groups [62], and case c) arises for nuclei such as ^{17}O in $H_2{}^{17}O$, in which the EFG tensor shows a large biaxality for the ^{17}O nucleus ($\eta_Q \sim 0.8$) [63].

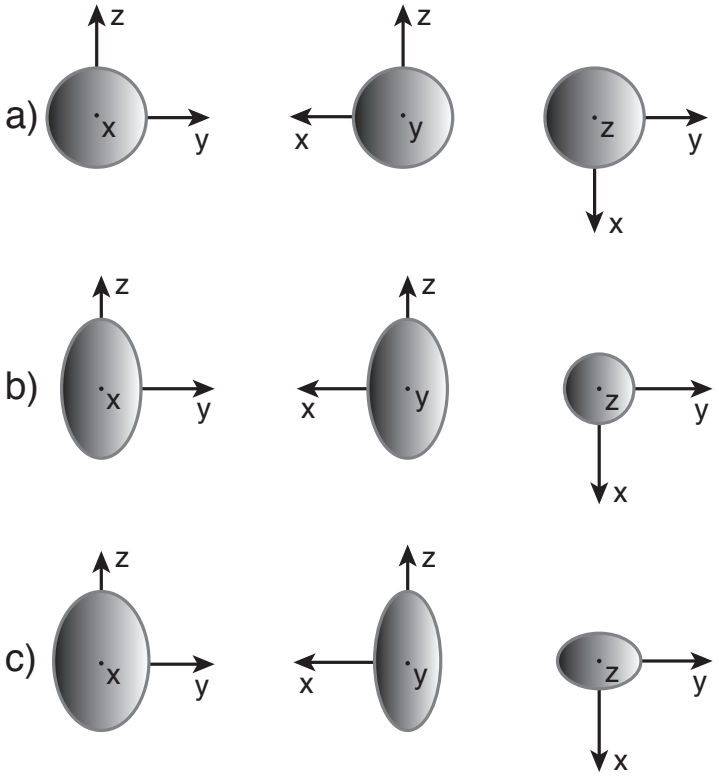

FIGURE 1.16: Ellipsoids representing the quadrupolar interaction. a) isotropic EFG tensor: $V_{zz} = 0$. b) uniaxial EFG tensor: $V_{zz} \neq 0$, $\eta_Q = 0$. c) biaxial EFG tensor: $V_{zz} \neq 0$, $\eta_Q \neq 0$. Arrows point in the direction of the principal axes of the EFG tensor. Adapted from reference [41].

For any arbitrary molecular orientation, with respect to the static magnetic field, the quadrupolar Hamiltonian is expressed in the PAS frame as:

$$\hat{H}_Q = \frac{\omega_Q}{2}\left[3\hat{I}_z^2 - \hat{I}(\hat{I}+1) + \frac{\eta}{2}(\hat{I}_+^2 + \hat{I}_-^2)\right]. \tag{1.175}$$

where the nuclear quadrupolar coupling frequency ω_Q is defined as:

$$\omega_Q = \frac{e^2qQ}{2I(2I-1)\hbar} = \frac{2\pi C_Q}{2I(2I-1)}, \tag{1.176}$$

where C_Q is referred to as the "quadrupole coupling constant". Another convention which is often used is ω_q'. In units of hertz, this quantity is given as:

$$f_Q = \frac{3\omega_Q}{2\pi} = \frac{3e^2qQ}{2I(2I-1)h}. \tag{1.177}$$

This parameter corresponds to the distance between the outer lines in the NMR spectrum of a quadrupolar nucleus where the biaxality of the EFG tensor is zero. Half this value

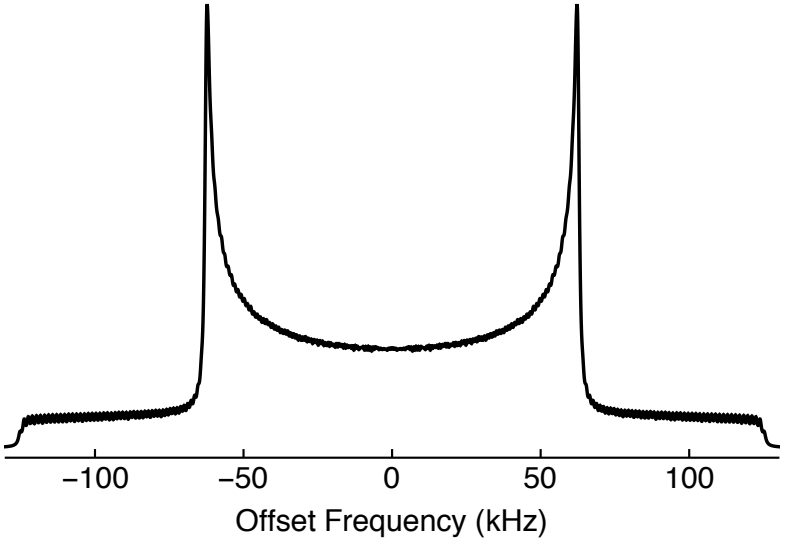

FIGURE 1.17: A simulated example of a solid-state NMR spectrum for a spin I=1 nucleus with a quadrupolar coupling constant $C_Q/2\pi = 167\,\text{kHz}$, and with $\eta = 0$. $\omega_Q/2\pi$ therefore corresponds to 83.5 kHz. The spectrum was simulated using the Hamiltonian in equation 1.175. The distance between the resonance lines is given by: $f_Q = 250.5\,\text{kHz}$. The distance between the peaks in the Pake doublet is given by $f_Q/2$. The powder averaged solid-state NMR spectrum was simulated by using the "ZCW538" orientational sampling scheme available in the *Mathematica*-based NMR software package *SpinDynamica*. An artificial Lorentzian line broadening of 1.2 kHz was also applied.

is also occasionally used, which corresponds to the distance between the peaks in a Pake doublet, again for a quadrupolar nucleus with $\eta = 0$. A typical scenario for the NMR Hamiltonian is the Zeeman splitting dwarfing the size of all other interactions. In this case approximations can be made to simplify the NMR Hamiltonian. Consider the quadrupole interaction, the Hamiltonian of which can be written as a series:

$$\hat{H}_Q = \hat{H}_Q^{(1)} + \hat{H}_Q^{(2)} + ..., \tag{1.178}$$

where the number in brackets corresponds to the order of the term in the quadrupolar Hamiltonian. The case: $\hat{H}_Q = \hat{H}_Q^{(1)}$ is equivalent to the secular approximation for the quadrupolar Hamiltonian, and is sufficient for small scale quadrupolar interactions. $\hat{H}_Q^{(1)}$ is written as:

$$\hat{H}_Q^{(1)} = \frac{\omega_Q}{2}(3\hat{I}_z^2 - \hat{I}(\hat{I}+1)). \tag{1.179}$$

Second order terms $\hat{H}_Q^{(2)}$ are required when ω_Q becomes large. It should also be noted that in isotropic liquids the first order term of the quadrupolar Hamiltonian averages to zero. The removal of this interaction does not influence the NMR peak positions but has important consequences for the relaxation of quadrupolar spins in solution.

1.8.3 Chemical shift interaction

The magnetic field experienced by a nucleus at two separate sites in a molecule may differ. This has previously been demonstrated in section 1.3.1 for the case of ethanol, see figure 1.8. The ^{1}H NMR spectrum has peaks at known chemical shifts, and serves a useful probe for determining the molecular structure of ethanol. The principle reason for this phenomenon is the magnetic fields generated by the electrons circulating each nucleus. The electrons of a molecule placed in a magnetic field behave in the following way:

1. The static magnetic field $\vec{B}_0$ induces "currents" in the molecules electronic clouds,
2. The molecular currents generate a back magnetic field, the "induced" field, via Lenz's law.

The induced magnetic field is experienced by the nucleus at the centre of the molecular currents. The total magnetic field experienced by a nucleus is therefore the combination of static and induced magnetic fields, with the induced magnetic field acting to shield or deshield the nucleus from the static magnetic field.

Note: This is a very small effect. Chemical shifts are measured on the "parts per million" or ppm scale. However, the effect is certainly large enough as to create observably different magnetic environments and hence deviations in nuclear Larmor frequencies at distinct locations within a molecule.

The induced field is approximately linearly dependent on the applied field, the chemical shift tensor δ is therefore used and takes into account the fact that the induced magnetic field may not be parallel to the direction of the static magnetic field $\vec{B}_0$:

$$\begin{bmatrix} \vec{B}^x_{ind} \\ \vec{B}^y_{ind} \\ \vec{B}^z_{ind} \end{bmatrix} = \begin{bmatrix} \delta_{xx} & \delta_{xy} & \delta_{xz} \\ \delta_{yx} & \delta_{yy} & \delta_{yz} \\ \delta_{zx} & \delta_{zy} & \delta_{zz} \end{bmatrix} \times \begin{bmatrix} 0 \\ 0 \\ \vec{B}_0 \end{bmatrix}, \tag{1.180}$$

assuming that, in this case, the static magnetic field is parallel to the z-axis of the laboratory frame. $\vec{B}^i_{ind}$ is the i^{th} component of the induced magnetic field, and δ_{ij} is the ij^{th} component of the chemical shift tensor. The chemical shift tensor δ may

be decomposed into symmetric and antisymmetric parts. The symmetric part of the chemical shift tensor δ^+ is defined as [53]:

$$\delta^+ = \frac{1}{2}\left(\delta + \delta^{\mathrm{T}}\right), \tag{1.181}$$

where δ^{T} is the transpose of δ. The symmetric part of the chemical shift tensor δ^+ has the following form:

$$\delta^+ = \frac{1}{2}\begin{bmatrix} \delta_{xx} & (\delta_{xy}+\delta_{yx}) & (\delta_{xz}+\delta_{zx}) \\ (\delta_{xy}+\delta_{yx}) & \delta_{yy} & (\delta_{yz}+\delta_{zy}) \\ (\delta_{xz}+\delta_{zx}) & (\delta_{yz}+\delta_{zy}) & \delta_{zz} \end{bmatrix}. \tag{1.182}$$

The symmetric part of the chemical shift tensor δ^+ can be decomposed again into isotropic and traceless symmetric parts:

$$\delta^+ = \delta_{\mathrm{iso}} + \delta^+_{traceless}. \tag{1.183}$$

The isotropic chemical shift δ_{iso} is the mean value of the principal values of the symmetric chemical shift tensor δ^+ and is defined as:

$$\delta_{iso} = \frac{\mathrm{Tr}[\delta^+]}{3}.\mathbb{1} = \begin{bmatrix} \delta_{xx} & 0 & 0 \\ 0 & \delta_{yy} & 0 \\ 0 & 0 & \delta_{zz} \end{bmatrix}, \tag{1.184}$$

where Tr is the trace operation and $\mathbb{1}$ is the identity matrix. The antisymmetric part of the chemical shift tensor δ^- is defined as:

$$\delta^- = \frac{1}{2}\left(\delta - \delta^{\mathrm{T}}\right), \tag{1.185}$$

and has the following form:

$$\delta^- = \frac{1}{2}\begin{bmatrix} 0 & (\delta_{xy}+\delta_{yx}) & (\delta_{xz}+\delta_{zx}) \\ (\delta_{yx}-\delta_{xy}) & 0 & (\delta_{yz}+\delta_{zy}) \\ (\delta_{zx}-\delta_{xz}) & (\delta_{zy}-\delta_{yz}) & 0 \end{bmatrix}. \tag{1.186}$$

The reason for this decomposition is that only the symmetric part of the chemical shift tensor effects the lineshape of the NMR spectrum [50]. These concepts are covered in more detail in section 1.7.4. The chemical shift Hamiltonian represents the interaction between the nuclear magnetic moment and the magnetic field, and is expressed as:

$$\hat{H}_{CS} = \sum_i \gamma_i \hat{I}_i \delta \vec{B}_0. \tag{1.187}$$

This equation implies that if the magnetic field is applied along one of three directions, the principal axes, then the induced field is parallel to the applied field, i.e. $\delta_{II} = \vec{B}^I_{ind}/\vec{B}_0$ if $\vec{B}_0$ is applied along the I^{th} principal axis. The chemical shift Hamiltonian retained after the secular approximation is [41]:

$$\hat{H}_{CS} = -\gamma \hat{I}_z \delta_{zz}(\theta) \vec{B}_0, \tag{1.188}$$

where the zz-component of δ depends on the orientation of the molecule θ with respect to the static magnetic field $\vec{B}_0$. The true Larmor frequency of a nucleus therefore includes the presence of the induced magnetic field:

$$\omega_0(\theta) = -\gamma \vec{B}_0(1 + \delta_{zz}(\theta)), \tag{1.189}$$

and is shifted in frequency from the nuclear Larmor frequency of an isolated nucleus ω_0 by $-\gamma\delta_{zz}(\theta)\vec{B}_0$.

Consider the following for a molecule of cyclopentadiene. The small magnetic fields generated by the atom's electrons run in loops, as the first of Maxwell's equations states. Therefore, the direction of the magnetic field changes around the molecule, see figure 1.18. Here, the electrons are circulating through the doughnut-like hole in the middle of the cyclopentadiene ring and then around the sides of the ring before joining up again. If the ring is fixed in a particular orientation with respect to the static magnetic field, the magnetic field induced at a nuclear site will depend on the orientation of the cyclopentadiene ring with respect to the static magnetic field, and also the location of the spin inside the molecule. The anisotropy in magnetic field around the nucleus, known as the chemical shift anisotropy (CSA), is defined as the largest deviation in chemical shift from the isotropic value:

$$\delta^{aniso} = \delta^+_{zz} - \delta^{iso}. \tag{1.190}$$

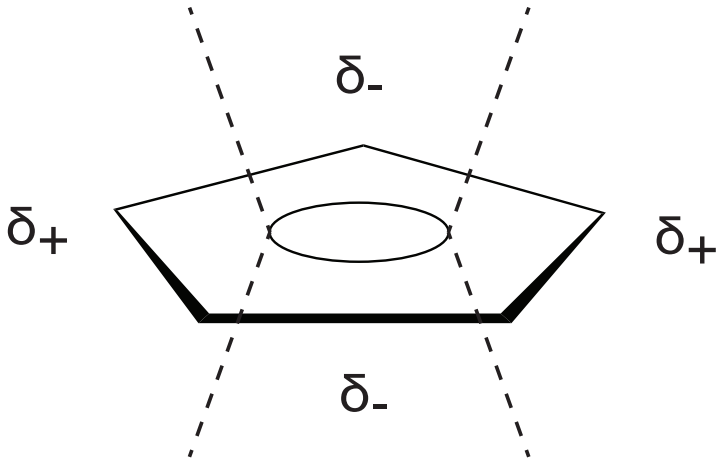

FIGURE 1.18: Schematic depiction of the chemical shift anisotropy in cyclopentadiene. $\delta_{\pm}$ denotes high (+) and low (-) electron density surrounding the ring. The magnetic field of the electrons runs through the doughnut shaped hole in the centre of the ring and around the molecule before joining up again. This results in an electron deficient zone above and below the plane of the cyclopentadiene ring.

The biaxality of the CSA tensor η is defined as the difference between the other two principal values:

$$\eta = \frac{\delta_{yy} - \delta_{xx}}{\delta^{aniso}}. \tag{1.191}$$

These principal axes are defined in a similar way to the quadrupolar interaction, but with X and Y principal axes reversed.

Chapter 2

Hyperpolarization and singlet states

2.1 NMR Sensitivity

Sensitivity is one of the primary concerns in the magnetic resonance community, and limits a number of experiments from solid-state NMR to medical imaging [64]. As previously discussed, the small population imbalance between the spin states of a nuclear ensemble in thermal equilibrium at room temperature leads to inherently weak NMR signals. In some cases, the readout of an NMR signal can be almost indistinguishable from the random noise associated with the signal detection itself. In the context of this work, the two most influential factors which determine the sensitivity level of an NMR experiment are the initial polarization of the spin ensemble and the relaxation phenomena which occur before detection. The two effects are interlinked, and can be partially controlled by a favourable choice of spin system and experimental conditions. In this chapter, I begin with a discussion regarding the concept of signal sensitivity in NMR, and how the influence of additional experimental complexity can considerably improve the initial spin polarization for an ensemble of nuclear spins. The reality of longer-lived encodement for nuclear spin order is additionally addressed by selecting substances which are sympathetic to nuclear spin relaxation. The symmetry properties of spin-1/2 pairs in contrasting regimes of equivalence are discussed, along with the radiofrequency pulse sequences designed to access the long-lived nuclear spin order.

2.1.1 Signal summation

Sensitivity can be improved in its most basic form by repeated signal summation. When a signal $S(t)$ is detected in the NMR coil surrounding the sample, the pickup coil senses: 1. the perturbation of nuclear spin populations from thermal equilibrium; and 2. an additional contribution in the form of *random noise*:

$$S(t) = S_{\text{sample}}(t) + S_{\text{electronics}}(t), \tag{2.1}$$

where $S_{\text{sample}}(t)$ is the signal contribution from the spins in the sample, and $S_{\text{electronics}}(t)$ is the signal contribution from noise. The coil induction is time-dependent and proportional to magnetization precessing in the xy-plane. The signal $S(t)$ is recorded until decoherence renders $S_{\text{sample}}(t)$ undetectable against a noise level determined by $S_{\text{electronics}}(t)$, which is mainly attributed to the thermal noise of the resonant radiofrequency circuit in the probehead, and the preamplifier of the spectrometer.

Suppose one intends to sum the NMR signals from two identical experiments. After the first signal is detected, the spin ensemble is permitted to return to thermal equilibrium (see section 1.2.6) before the second experiment commences. The NMR signal detected in the second experiment should therefore be indistinguishable from that of the first experiment. The signals sampled in each case have a decaying profile known as a free induction decay or FID, see figure 2.1. The noise associated with each experiment has an "irreproducible" random profile. Therefore, accumulation of NMR signals is a surefire way of differentiating the FID from the noise. But how does this work in practice? And how does this achieve spectra in which the dominant source of the NMR signal comes from the sample? The sample is assumed to be well controlled in these two experiments, the parameters of the spectrometer and probe are well defined and are constant, and the sample is allowed sufficient time between experiments to reach thermal equilibrium. The NMR signals associated with the spins in the sample are assumed to generate identical signals such that:

$$S_{\text{sample}}(t_1) + S_{\text{sample}}(t_2) = 2S_{\text{sample}}(t_1), \tag{2.2}$$

where (t_i) denotes the time at which the FIDs are recorded, with t_2 - $t_1 \geq 5T_1$ and $t_2 > t_1$. The uncorrelated noise contributions to the NMR signals are random, and

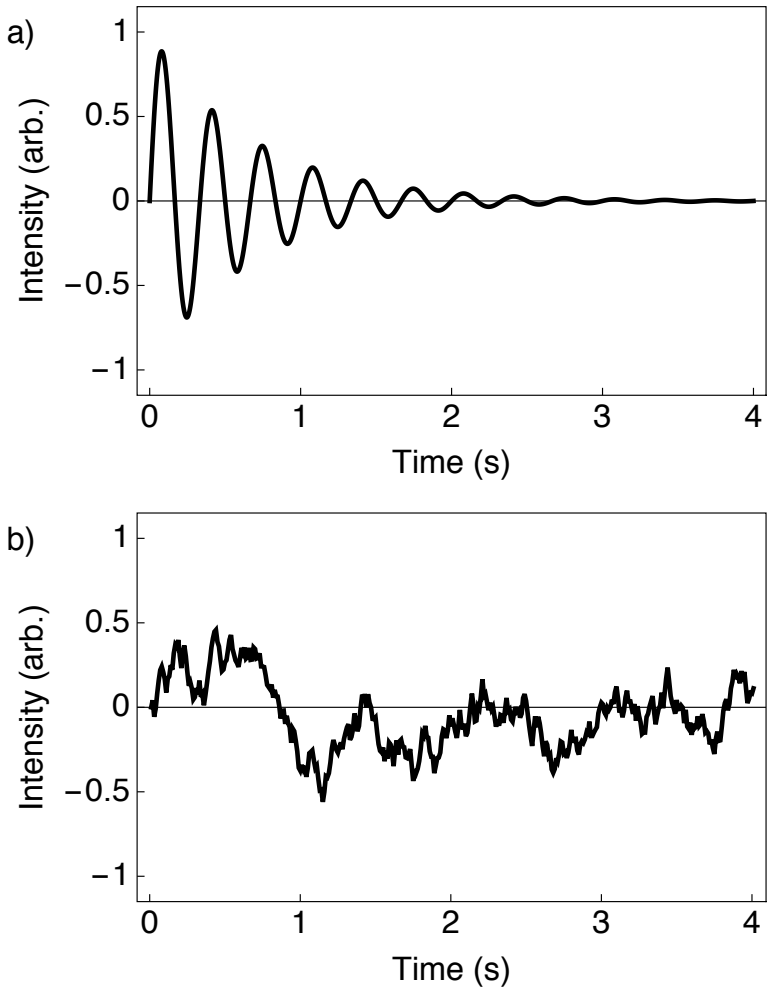

FIGURE 2.1: a) The free induction decay (FID) is the result of detecting the signal $S_{\text{sample}}(t)$ with the rf-coil of the NMR probe. The FID is a combination of a sinusoidal modulation and an exponential decay. b) The noise of an NMR experiment, assuming a noise source which is fixed in time, will oscillate randomly either side of zero intensity. The root-mean-square amplitude is therefore the most appropriate measure of the noise amplitude.

assuming the source of the noise remains fixed throughout time, i.e. stationary noise, the amplitude of the noise is given by its *root-mean-square*:

$$S_{\text{electronics}}(t_i) = \langle S_{\text{electronics}}(t_i)^2 \rangle^{1/2}. \tag{2.3}$$

This definition of the noise amplitude is used as the motion of the noise is random, and wanders back and forth between positive and negative values, and hence the average noise of an NMR experiment is zero. Using this definition:

$$S_{\text{electronics}}(t_1) + S_{\text{electronics}}(t_2) = \sqrt{2} S_{\text{electronics}}(t_1), \tag{2.4}$$

where $S_{\text{electronics}}(t_1) \simeq S_{\text{electronics}}(t_2)$. The ratio of the signal to the noise (signal-to-noise, SNR) is therefore given by:

$$SNR = \frac{2S_{\text{sample}}(t_1)}{\sqrt{2}S_{\text{electronics}}(t_1)} = \sqrt{2}\frac{S_{\text{sample}}(t_1)}{S_{\text{electronics}}(t_1)}. \tag{2.5}$$

Now consider a set of identical experiments which are repeated N number of times, with sufficient time between experiments for the sample to recover to thermal equilibrium. The signal-to-noise in this case is given by:

$$SNR = \sqrt{N}\frac{S_{\text{sample}}(t_1)}{S_{\text{electronics}}(t_1)}. \tag{2.6}$$

Hence signal summation does indeed enhance the signal-to-noise ratio of an NMR experiment, with the SNR improving as the square root of the number of transients. Sadly signal summation is a slow process, and experiments can sometimes take days or weeks to achieve a good SNR for a sample with low sensitivity or long relaxation times. Signal averaging is also not ideal in the context of process monitoring via NMR. The summation from signals does not allow for monitoring of chemical or kinetic reactions, and an inherently good SNR is required from the outset of the time course experiment. MRI also suffers from similar problems due to the motion of the patient between scans.

2.1.2 Other methods

Rather fortunately, other options exist which aim to improve the signal-to-noise ratio of an NMR experiment:

- **Coil design.** The design of an NMR probe can be optimized for specific nuclei by placing the pickup coil closer to the sample. This increases the filling-factor of the coil and improves the signal-to-noise ratio [65]. SNR can also be boosted by increasing the homogeneity of $\vec{B}_1$ magnetic fields, which leads to a strong electronic response from the coil.

- **Field compensation.** $\vec{B}_0$ homogeneity is improved by the process of shimming, which corrects for variations in the static magnetic field. Correcting for inhomogeneous $\vec{B}_1$ fields is facilitated by rational pulse sequence design. Levitt et al.

compensated for the poor homogeneity of rf-fields in the 1970s by developing the "composite pulse" [66].

- **Cryoprobes.** The use of cryoprobes, particularly for use in protein NMR, has become very popular in the last two decades [67]. By cooling the electronics of the detection circuit to ∼20 K with helium gas, signal-to-noise gains of ∼10 (and ∼16-fold reductions in data acquisition times) have been reported [68].

- **Pulse sequences.** Polarization is efficiently transferred between heteronuclei by familiar NMR experiments such as the *insensitive nuclei enhanced by polarization transfer* (INEPT) and *cross-polarization* (CP), with enhancements of ∼4 and ∼10 achievable for ^{13}C and ^{15}N nuclei, respectively. However, pulse schemes can only go so far in delivering signal enhancements, and are ultimately limited by the gyromagnetic ratios of the participating nuclei.

- **Sample concentration.** If in doubt, throw more sample in. The signal intensity from the sample is directly proportional to the number of spins:

$$\vec{M} = \frac{N\gamma^2\hbar^2 I(I+1)}{3\kappa_B T}\vec{B}_0, \tag{2.7}$$

  where N is the number of spins in the sample [42]. In this way, one works with an inherently greater SNR from the very first experiment, and fewer transients are ultimately required per experiment. However, this may not be so easily achievable. In solid state magic angle spinning (MAS) experiments the number of spins are limited by the volume of the MAS rotor. In liquid state NMR experiments there may be limited solubility of the material in the choice solvent, which can be a problem when investigating inherently insensitive nuclei. Gas phase NMR experiments are also known to be difficult due to the reduced number of spins available for detection [69].

NMR hyperpolarization is a technique used to vastly improve the sensitivity of NMR experiments, and comes from two main sources; electrons and spin isomers. In this thesis, the nuclear hyperpolarization presented is achieved by borrowing the strong alignment possessed by electron spins in a magnetic field at low temperature.

- **Unpaired electrons.** Unpaired electrons are persistently used in dynamic nuclear polarization (DNP) experiments as a source of high polarization at low temperature. Microwave irradiation is applied specifically "just off" the electron transition frequency in an effort to transfer the high levels of electron spin polarization to the adjacent nuclei [70]. Dissolution-DNP allows a liquid state readout of the hyperpolarized spin order in a separate magnet after the sample is flushed out of its frozen environment by a jet of superheated solvent [71].

- **Spin isomers.** The spin isomers of hydrogen (destructive addition of spin angular momentum, I=0) also serve as a means to improve sensitivity. The para-state is easily populated by cooling hydrogen gas to low temperatures ($\sim$77 K is sufficient) and flowing the cooled gas over a paramagnetic catalyst [72, 73]. The energy level separation between the para- and ortho-states of hydrogen (ortho-states are the result of a constructive interference of spin angular momentum, I=1) is sufficiently large such that the population imbalance persists upon removal of the catalyst and equilibration of the gas to room temperature. The hyperpolarized spin order can survive for many weeks before being transferred to a substance of interest via a parahydrogenation reaction [74, 75].

2.2 Polarization

A measure of the sensitivity level for an NMR experiment is achieved by considering the Zeeman polarization for a sample in a magnetic field. The Zeeman polarization corresponds to the amount of normalized longitudinal spin order contained within the spin density operator. For a single spin-1/2 nucleus, the Zeeman polarization p_{Z} may be expressed as the projection of the spin density operator $\hat{\rho}$ onto the angular momentum operator $\hat{I}_z$ (see appendix B for more details):

$$p_{\mathrm{Z}} = \frac{\mathrm{Tr}[\hat{I}_z^{\dagger}\hat{\rho}]}{\mathrm{Tr}[\hat{I}_z^{\dagger}\hat{I}_z]}, \tag{2.8}$$

where p_{Z} is normalized to establish the maximum Zeeman polarization as ± 1, i.e. the $|T_{m_{\pm 1}}\rangle$ state is saturated with population whilst the $|T_{m_{\mp 1}}\rangle$ state is entirely depleted of population. The bounds on nuclear Zeeman polarization are therefore: $-1 < p_{\mathrm{Z}} < +1$.

For an ensemble of non-interacting spin-1/2 nuclei, the eigenstates of the coherent Hamiltonian are the nuclear Zeeman states $|\alpha\rangle$ and $|\beta\rangle$. For a spin-1/2 nucleus, the states $|\alpha\rangle$ and $|\beta\rangle$ denote the alignment of the intrinsic magnetic moment parallel and anti-parallel to the static magnetic field, respectively. The Zeeman polarization for an ensemble of nuclear spins is defined as the normalized imbalance between the $|\alpha\rangle$ state population $p(\alpha)$ and the $|\beta\rangle$ state population $p(\beta)$, i.e. the net population difference $(|\alpha\rangle\langle\alpha| - |\beta\rangle\langle\beta|)$. The Zeeman polarization p_{Z} is given as follows:

$$p_{\mathrm{Z}} = p(\alpha) - p(\beta), \tag{2.9}$$

where $p(\alpha) = 1/2 + B_f/4$ and $p(\beta) = 1/2 - B_f/4$, as described in equations 1.73 and 1.74. Normalization occurs with respect to the total population of the nuclear ensemble $p(\alpha) + p(\beta)$, i.e. there is an additional constraint $p(\alpha) + p(\beta) = 1$. At room temperature, and in a field of 11.7 T, the thermal equilibrium Zeeman polarization for an ensemble of protons is $p_{\mathrm{Z}}^{\mathrm{eq}} = \sim 4 \times 10^{-5}$. A strongly hyperpolarized spin system obtains a Zeeman polarization of $p_{\mathrm{Z}} \to \pm 1$, depending on the nature of the hyperpolarization, and is considerably greater than $p_{\mathrm{Z}}^{\mathrm{eq}}$.

The population ratio $p(\alpha)/p(\beta)$ is defined as:

$$\frac{p(\alpha)}{p(\beta)} = e^{\left(\frac{-\hbar\omega_0}{\kappa_B T}\right)}, \tag{2.10}$$

where ω_0 is the nuclear Larmor frequency, κ_B is the Boltzmann constant and T is the temperature, see equation 1.8. For a thermally polarized sample, the Zeeman polarization may be rewritten by using equations 1.7 and 2.10:

$$p_{\mathrm{Z}} = \tanh\left(\frac{\hbar\gamma B_0}{2\kappa_B T}\right). \tag{2.11}$$

Equation 2.11 states that the Zeeman polarization of a thermally equilibrated sample is represented by a hyperbolic tangent which is a function of both magnetic field and temperature, see appendix B for more details. The observed NMR signal from the spins in the sample is proportional to the Zeeman polarization through:

$$S_{sample}(t) \propto tanh\left(\frac{\hbar\gamma B_0}{2\kappa_B T}\right) \cdot N_{tot} \cdot e^{\frac{-t}{T_2}} \cdot e^{-i\omega_0 t}, \tag{2.12}$$

where N is the total number of spins in the sample. The Zeeman polarization p_{Z} can

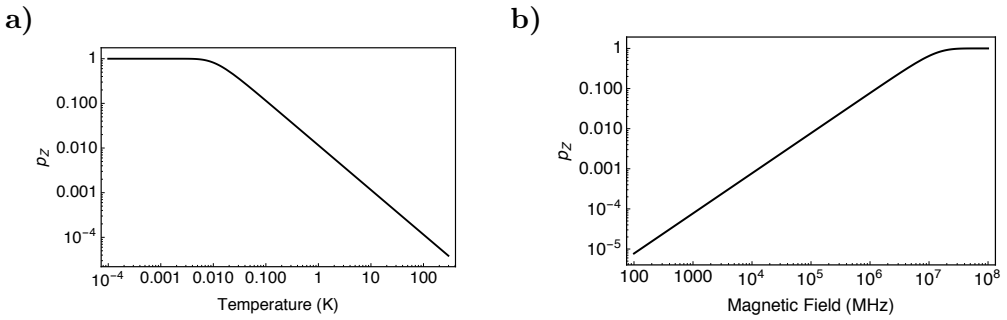

FIGURE 2.2: Zeeman polarization p_Z of a ^{1}H nucleus described by using the hyperbolic tangent in equation 2.11 as a function of: a) temperature ($\vec{B}_0$=11.7 T); and b) magnetic field ($T = 298$ K). a) A Zeeman polarization of unity is maintained until the temperature of the spin system reaches ∼10 mK, at which point there is a sharp decline in the level of Zeeman polarization. At just 1 K, ∼88.5% of Zeeman polarization has been lost, and the effect is greatly exaggerated for nuclei with lower gyromagnetic ratios. b) Over the range of magnetic fields currently produced by modern day superconducting magnet technologies ($\lesssim$ 1.2 GHz) the gains in Zeeman polarization at thermal equilibrium are relatively small (∼10^{-5}). For protons at 298 K, magnet fields exceeding 10 THz are required in order to obtain a Zeeman polarization approaching unity.

be investigated as a function of magnetic field and temperature by using equation 2.11. To achieve high levels of Zeeman polarization, i.e. $p_Z \to 1$, low temperatures and large magnetic fields are required.

Temperature. The temperature profile of p_Z for an ensemble of non-interacting, spin-1/2 protons at 500 MHz is shown in figure 2.2a). A Zeeman polarization of ∼1 is achieved for temperatures below ∼10 mK. Conventional cryostats, which are often employed in dynamic nuclear polarization (DNP) experiments, can achieve temperatures as low as ∼1.3 K. ∼4.2 K is also used as liquid helium consumption can be considerable. At 4.2 K, a Zeeman polarization of 0.27% is reached for the proton spin ensemble, which is a factor of ∼71 greater than at 298 K but remains woefully short of being considered as a hyperpolarized system.

In the majority of cases, low temperatures alone are insufficient as to achieve considerable nuclear hyperpolarization. Therefore, more than simply low temperatures are required to vastly improve the low levels of sensitivity which are common place in NMR experiments, see section 2.3. However, considerably lower temperatures remain an option. Extensive efforts have been made in the field of brute force hyperpolarization, whereby the operation of dilution fridges achieves ∼mK temperatures and can boost the Zeeman polarization level for an ensemble of protons to ∼80% [76]. Commercial instruments routinely output ∼50% ^{13}C polarization [77]. The considerable drawback of working at ∼mK temperatures is the long equilibration time of nuclear spin orders, i.e.

conventional relaxation times become increasingly longer as the temperature is lowered, and are often on the order of days or weeks in the millikelvin regime [78–82].

Magnetic field. An alternative route to improved NMR sensitivity is to construct NMR magnets capable of producing higher static magnetic fields. Difficulties in accomplishing this task include the size and weight of the magnet, the use of new superconducting materials, and most likely, the grand expense associated with developing high field magnetic resonance technologies. The magnetic field profile of the Zeeman polarization p_Z at 298 K for an ensemble of protons is shown in figure 2.2b). p_Z has a linear relationship in the regime of magnetic fields produced by superconducting NMR magnets available on today's market ($\vec{B}_0 \lesssim 1.2\,\mathrm{GHz}$). At these magnetic fields, thermal fluctuations remain large in comparison to the quantized energy difference between spin states, and low levels of Zeeman polarization p_Z are observed. This being said, the increase in resolution with magnetic field holds significant advantages in areas of solid state NMR.

As is clearly demonstrated in figure 2.2b), increasing the magnetic field by ∼100 MHz or so only raises the Zeeman polarization to a certain extent. However, the SNR of an NMR experiment can also be improved with the assistance of higher magnetic fields. The NMR signal deriving from the spins in the sample $S_{sample}(t)$ is related to the Zeeman polarization and induction processes in the rf-coil, both of which are proportional to the static magnetic field $\vec{B}_0$, and hence $S_{sample}(t)$ scales as B_0^2[83, 84]. The random noise contribution to the NMR signal $S_{electronics}(t)$ is proportional to $B_0^{1/4}$, and therefore the overall SNR of an NMR experiment scales with the magnetic field as $B_0^{7/4}$ [85, 86].

2.3 Hyperpolarization

Hyperpolarization in NMR spectroscopy concerns perturbing nuclear spin populations far from thermal equilibrium. The aim being to enhance the sensitivity of NMR experiments, spectra and images through increasing the nuclear polarization of a spin ensemble by factors of up to 10^4-10^5, compared with thermal equilibrium. Multiple hyperpolarization techniques exist; ranging from hyperpolarized gas NMR using ^{129}Xe and ^{3}He isotopes, spin exchange optical pumping (SEOP), parahydrogen induced polarization (PHIP), quantum rotor induced polarization (QRIP), and dynamic nuclear polarization

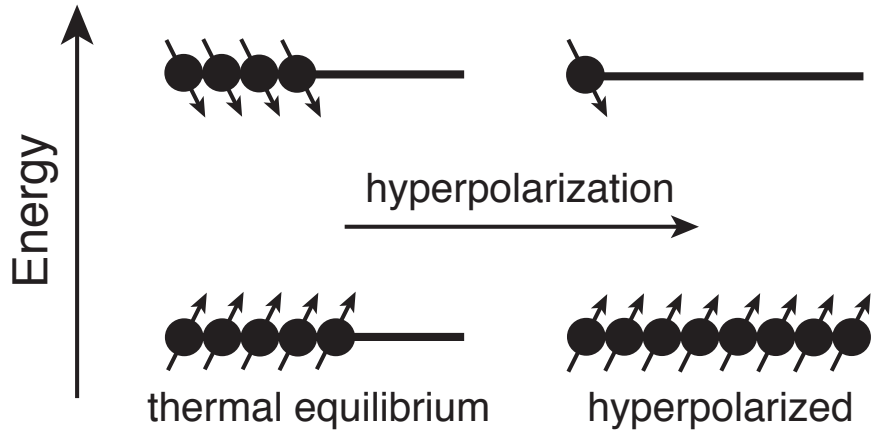

FIGURE 2.3: Schematic of nuclear hyperpolarization. Thermal equilibrium Zeeman polarization is small due to the fluctuations in room temperature which readily equilibrate the spin populations for an ensemble of nuclei in a magnetic field. Hyperpolarization techniques exist to drive the arrangement of nuclear spin populations away from thermal equilibrium, with the idea of preferentially populating a single spin state and creating an impressive population imbalance for observation.

(DNP), the latter of which is occasionally accompanied by a dissolution process to enable a liquid state readout. A schematic of the hyperpolarization ideology is shown in figure 2.3. Applications of hyperpolarized NMR are also evident, noble gases are often used to image lungs in MRI experiments [71], and hyperpolarized metabolites have been used to monitor prostate cancer in human patients [87]. In the context of this thesis, dynamic nuclear polarization (DNP) is discussed as one method to produce nuclear hyperpolarization. Later on in this thesis, DNP experiments are reviewed in conjunction with a rapid dissolution process in order to hyperpolarize long-lived nuclear spin states.

2.3.1 Dynamic nuclear polarization

The aforementioned methods have the capability to produced non-equilibrium Zeeman polarization, $p_{\mathrm{Z}} \to \pm 1$. However, each method is also limited. SEOP is restricted to hyperpolarization of a few noble gas isotopes, and PHIP depends on the presence of double or triple bonds in the substrate molecule. A highly feasible approach to improve the low levels of nuclear Zeeman polarization is to borrow the already enhanced polarization of electron spins at low temperature. The proportionality factor between the gyromagnetic ratio of an electron and a proton is: $\gamma_{^1\mathrm{H}}/\gamma_{e^-} \simeq -660$, i.e. the gyromagnetic ratio of an electron is significantly larger than that of a proton. This proportionality factor becomes even greater for nuclei with lower gyromagnetic ratios, e.g. ^{13}C, ^{15}N, with

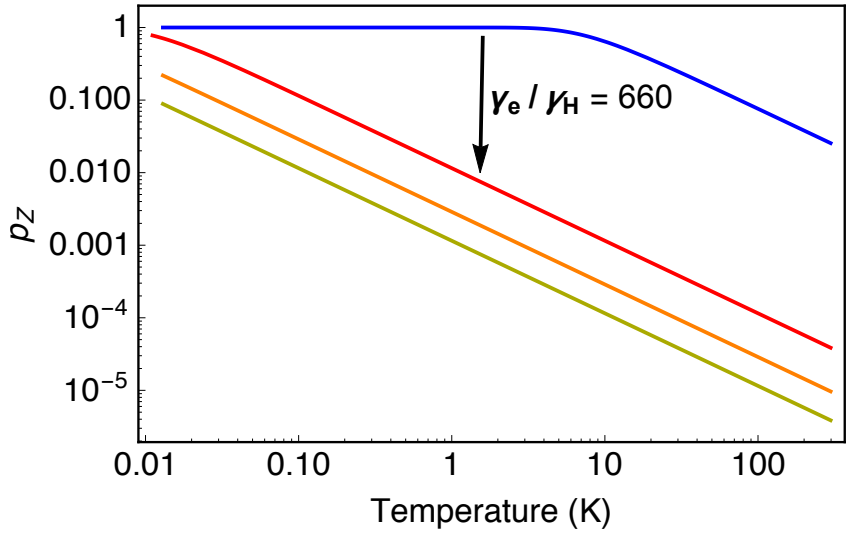

FIGURE 2.4: Thermal equilibrium Zeeman polarization p_Z as a function of temperature ($\vec{B}_0$=11.7 T) for electrons (blue), protons (red), carbon-13 (orange) and nitrogen-15 (green). Electron polarization at low temperatures ($\lesssim$10 K) is considerably greater than that of nuclei. Beyond $\sim$10 K, the electron polarization is consistently a factor of $\sim$660 greater than the proton polarization, and even more so for carbon-13 and nitrogen-15 nuclei. As conventional DNP apparatus is unable to achieve temperatures lower than $\sim$1.3 K, the level of nuclear Zeeman polarization is limited. Polarization must therefore be borrowed from the nearby electrons, and an additional factor of γ_e/γ_n can be gained in terms of the nuclear Zeeman polarization.

respect to that of a proton. Therefore, efficient or sustained transfer of electron spin polarization to nuclei can result in Zeeman polarizations on the order of $\sim$50%, a remarkable improvement over p_Z^{eq} at room temperature, see figure 2.4. This is the approach taken by dynamic nuclear polarization (DNP). DNP was first predicted by Overhauser in 1953 [88], and was met with criticism from the NMR community. However, the successful demonstration of DNP by Carver and Slichter later that year, and Abragam in 1959, cemented DNP as a powerful NMR tool for boosting the poor sensitivity levels of common NMR experiments. DNP is now a widely used technique in magnetic resonance, and has far reaching applications such as the structural determination of proteins and other materials in conjunction with magic angle spinning methodologies [89–93].

2.3.2 Elements of DNP

Before discussing the physical mechanisms of electron-nuclear polarization transfer, a discussion of the items required for a typical DNP experiment is necessary. The main prerequisites for the success of a DNP experiment are:

- **Unpaired electrons.** Traditionally in the form of a radical system; BDPA, trityl, ox63, TEMPO, TEMPOL and others [94], an added electron source is required for adequate polarization transfer. The resulting DNP mechanisms and signal enhancements are dependent on the type and concentration ($\sim$25 mM) of radicals.

- **Glassing agent.** Mixtures of common laboratory solvents; H_2O, D_2O, glycerol etc. form satisfactory glassy matrices for DNP upon freezing. H_2O and D_2O form a suitable aqueous solution in which to dissolve the sample of interest to sufficient concentration, and glycerol is a glass-former added to prevent crystallization. The radicals becomes homogeneously embedded within the amorphous solid when frozen.

- **Microwave irradiation.** Exciting electron-nuclear transitions at near-resonant microwave frequencies exchanges spin populations between coupled electron-nuclear systems in the solid state, and ultimately transfers polarization from electrons to nuclei [62, 95]. Depending on the strength of the polarizing field, either a Gunn diode (low power) or gyrotron (high power) can be used as the electron source [96–99].

- **Low temperatures.** Clearly, in order to freeze the mixture of sample, radical system and glassing agent, low temperatures are required. Near-unity electron polarization is additionally present below $\sim$10 K at 6.7 T. Low temperatures are often provided by the use of a cryostat, which will have a specially designed custom-insert for sample insertion and microwave irradiation.

2.3.3 Overview of the DNP process

The procedure for DNP experiments is now well established, and is laid out plainly below. A schematic overview of the DNP process is shown in figure 2.5.

1. The mixture of sample, electron source and glassy matrix, is cooled to $\sim$1.3 K. At this temperature, electron spin polarization is abundant, and near unity. Nuclei are weakly polarized and have long relaxation times at these temperatures.

2. Electron spin polarization is transferred to nearby nuclei by the application of a continuous microwave (μW) field with a frequency close to the EPR transition. The

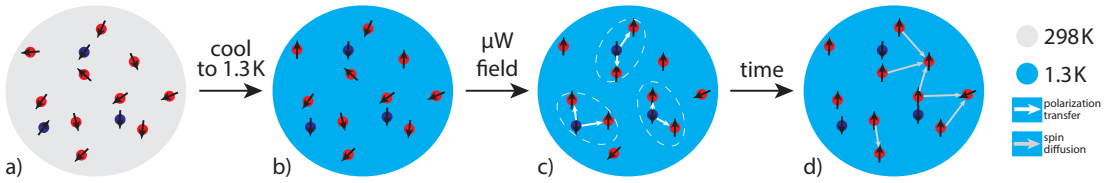

FIGURE 2.5: Overview of the DNP process. Red spheres denote nuclei ($\gamma > 0$), blue spheres denote unpaired electrons. Dashed white lines denote the core nuclei surrounding each electron. a) A mixture of sample, glassing agents and radical, is prepared by freezing beads (10 μL volume) of this concoction in liquid nitrogen. b) The frozen DNP mixture is inserted into a sample cup (approx. 150 μL volume) and placed into the cryostat (temperature = 1.3-4.2 K). c) Approximately resonant microwave fields are applied to the frozen material, and polarization is transferred from electrons to nuclei via various DNP mechanisms. d) The build up of nuclear Zeeman polarization is achieved throughout the majority of the sample by the process of spin diffusion, which transfers polarization between dipolar coupled nuclei.

polarization transfer process is constantly fighting against the return of electron spin populations to thermal equilibrium at ~1.3 K.

3. *Spin diffusion* spreads the high nuclear polarization levels among the nuclei in the sample bulk. The DNP process may therefore take many minutes or hours in order to achieve the maximum experimental polarization, but is relatively fast compared to signal summation methods.

2.4 DNP mechanisms

Multiple mechanisms have now been proposed to explain the DNP process. The predominant DNP mechanisms in the solid state are the solid-effect (SE), the cross-effect (CE), and thermal mixing (TM). Each mechanism can be responsible for the polarization of a particular molecule or material, with polarization efficiency highly dependent on nucleus, radical choice, radical concentration and magnetic field. In this section, the ESR properties of the electron species are examined, followed by an exploration of the solid-effect and cross-effect DNP mechanisms.

2.4.1 Electron spin resonance spectra

As mentioned above, the transfer of electron spin polarization from radical centres within the sample to nuclei of interest is dependent on many factors. One such aspect is the electron spin resonance (ESR) spectrum, which is specific to individual radical species,

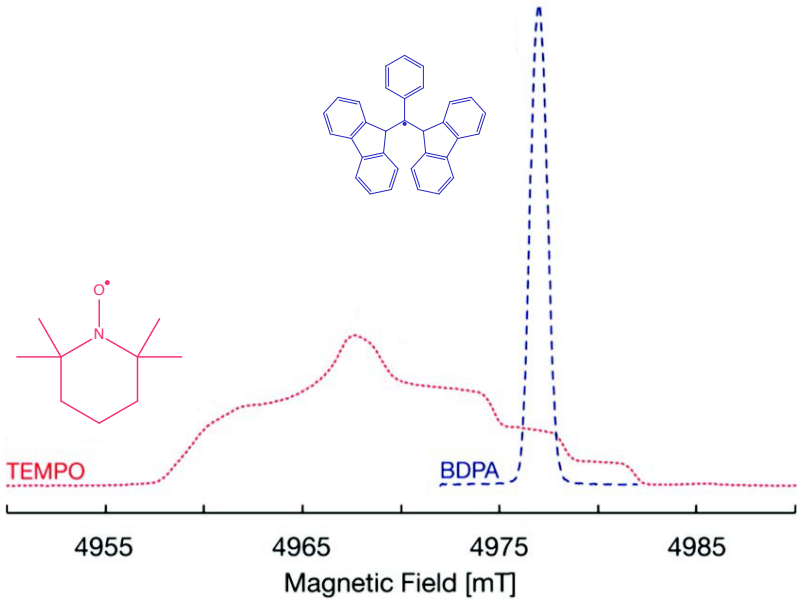

FIGURE 2.6: Echo-detected ESR spectra of BDPA (blue, dashed line) and TEMPO (red, dotted line) radicals at 140 GHz and 20 K. BDPA is a narrow line radical used for polarizing nuclei such as ^{13}C and ^{15}N, and has a linewidth of ∼40 MHz (full-width at half-maximum). TEMPO is a wide line radical and is predominantly used for polarizing protons. The linewidth of the TEMPO resonance is ∼400 MHz (full-width at half-maximum). Adapted from reference [100].

see figure 2.6. The resonance frequency of the ESR line indicates the energy at which the electron emits and absorbs radiation, and the lineshape of the ESR spectrum dictates the nature of the polarization transfer to different nuclei, i.e. the DNP mechanism. The choice of radical is therefore a vital consideration when aiming to hyperpolarize a particular nuclear species via DNP. The effects of preferred radicals on particular DNP mechanisms are discussed later.

At high magnetic field (>3.35 T) and low temperature ($\lesssim$4.2 K) the electron and nuclear resonances are well isolated ($\lesssim$200 GHz separation, nuclei and magnetic field dependent), i.e. the unpaired electron absorbs radiation which is γ_e/γ_n higher in frequency than the nuclei of the sample. It should be noted that the electron (linewidth $\lesssim$1 GHz) and nuclear (linewidth $\simeq$30 MHz) resonances do not overlap in the solid state. The severe difference in linewidth is related to the solid state interactions of electrons and nuclei, and the orientations of the unpaired radical species in the frozen medium. In this case, the linewidth of the NMR resonance for a nucleus at ∼4.2 K is governed predominantly by dipolar interactions with electrons and other nuclei, and is hence proportional to the concentration of nuclei within the sample.

For the electron spins, the shape and linewidth of the ESR line is a little more complicated as there are two effects responsible for the overall broadening of the ESR spectrum, both of which depend on the type of radical used to paramagnetically dope the sample. Homogeneous broadening is attributed to field-independent dipole-dipole interactions between electrons embedded within the sample [101], and can be controlled by optimizing the electron spin concentration. Inhomogeneous broadening is related to the hyperfine interaction and g-anisotropy of the electron [102, 103]. In this case, the individual electrons experience different magnetic fields throughout the sample. If the radical electron is located on a nucleus with non-zero spin, such as ^{14}N in TEMPO, a hyperfine coupling exisits between the electron and the nucleus, and the resulting ESR spectrum is split into individual components corresponding to the quantum number m_I of the nucleus. Splittings are often on the order of megahertz. The ESR spectrum of radicals frozen into the glassy matrix is additionally a superposition spectrum of individual electron moments at many different orientations with respect to the static magnetic field. The electron g-tensor allows a measure of the orientational dependence of the Zeeman interaction for electrons in the solid state, and the anisotropy of the g-tensor (g-anisotropy) partly specifies the inhomogeneous lineshape of the ESR line.

With the above information at hand, one can now design an efficient scheme for electron-nuclear polarization transfer, which is ultimately achieved by saturating the ESR line of the chosen radical species at a particular frequency.

2.4.2 Solid-effect DNP

Overhauser first suggested applying microwaves to materials in order to engage specific transitions involving simultaneous flip-flop processes of the electrons and nuclei [88]. In 1953, Carver and Slichter confirmed the SE by performing DNP experiments on lithium metal [104]. A few years later, preliminary descriptions of the solid-effect (SE) were provided by Jeffries [105]. Another key breakthrough was provided by Abragam and Proctor in 1958. The pair published work suggesting that by pumping microwaves at formally "forbidden" transition frequencies, coupled electron-nuclear population conversion could be induced [106]. The phenomenon was subsequently demonstrated by employing microwave irradiation at the frequencies $\omega_e \pm \omega_n$ in the presence of paramagnetic centres [107], and the solid-effect was born. Another important piece of evidence

for solid-effect DNP was reported in 1978 by Abragam and Goldman [108], in which the transfer of electron polarization to nuclei was found to be executed through dipolar interactions.

The solid-effect (SE) is the perhaps the simplest DNP mechanism to explain, and only concerns the interactions between a single electron-nuclear pair. The process is illustrated in more detail below, but a brief synopsis is given here:

1. **Microwaves off**. The bath of electrons is hyperpolarized at low temperatures, and nearly all electron spins are in the state $|\alpha_e\rangle$. Nuclei are initially poorly polarized.

2. **Microwaves on**. A microwave field of frequency $\omega_e - \omega_n$ is applied to the sample. An electron-nuclear pair in the state $|\alpha_e\beta_n\rangle$ undergoes a flip-flop transition. The new coupled spin state is $|\beta_e\alpha_n\rangle$.

3. **Relaxation**. The relaxation time of the electron T_{1e} (milliseconds) is significantly shorter than the relaxation time of the nucleus T_{1n} (minutes) at low temperature. The spin pair transforms into the state $|\alpha_e\alpha_n\rangle$.

4. **Repolarize**. Steps 2 and 3 may now be repeated several times and for other electron-nuclear pairs, eventually leading to the hyperpolarization of small pockets of nuclei within the sample.

The solid-effect (SE) is a 2-spin interaction, involving one nucleus and one electron, with external influences from an applied microwave field. In order for the SE to be valid, a narrow line radical must be implemented in the DNP process. Narrow line radicals have ESR linewidths which are narrower than the Larmor frequency of the nucleus to be polarized: $\Delta\omega_e < \omega_n$. Radicals such as BDPA, trityl and ox063 display narrow ESR lines, as these radicals are symmetric in molecular structure and do not possess strong electron-nuclear hyperfine couplings.

The efficiency of electron-nuclear polarization transfer can be investigated as a function of the microwave frequency, see figure 2.7. The x-axis represents the microwave frequency and the y-axis shows the ensuing enhancement of the NMR signal or "DNP signal". Maximum polarization enhancements are observed when the microwave condition $\omega_e \pm \omega_n$ is satisfied. The positive sign of the condition corresponds to the negative

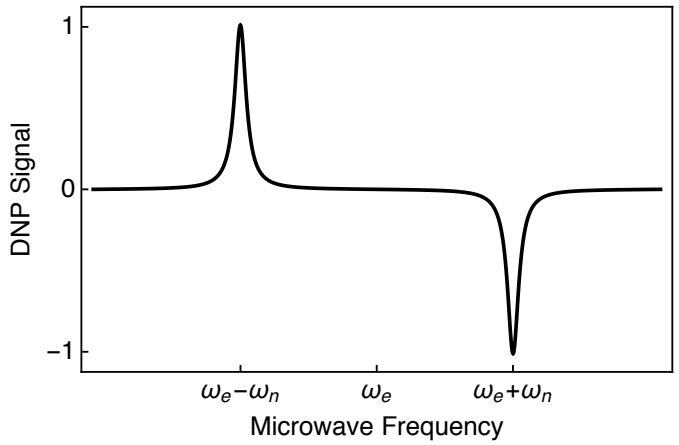

FIGURE 2.7: Microwave swept DNP enhancement (DNP spectrum) of a narrow line radical such as BDPA at 6.7 T and 1.4 K. A positive DNP enhancement is recorded at a microwave frequency of $\omega_e - \omega_n$, and a negative DNP enhancement is observed at $\omega_e + \omega_n$. The maximum enhancements have been normalized to ± 1, respectively. The flat region around ω_e and the distinct peaks at $\omega_e \pm \omega_n$ indicate a *well resolved* solid-effect.

lobe of the "DNP spectrum" and the negative sign corresponds to the positive lobe. The frequency of the microwave field is therefore chosen specifically to be $\omega_e \pm \omega_n$ to encourage the flow of polarization from the electrons to the nuclei. Microwave irradiation applied at any other frequency results in a reduced electron-nuclear polarization transfer efficiency. If a wide line radical is used for SE DNP, under the application of the same microwave field, competing contributions from the condition $\omega_e \pm \omega_n$ are simultaneously satisfied, and ultimately nullify the hyperpolarization of a particular spin state.

Consider the spin state of the electrons $|\alpha_e\rangle$ at high magnetic field (>3.35 T) and low temperature ($\lesssim$4.2 K). The magnetic moments of the electron bath are approximately 100% anti-aligned with the static magnetic field. The nuclei are poorly polarized under these conditions, and the polarization bias towards the preferential orientation is approximately 63 out of every 2000 spins for protons at 6.7 T and 4.2 K, i.e. the majority of nuclei possess no preferential alignment with the static magnetic field. To consider the effect of applying microwave irradiation at this frequency, one should consult a state population diagram, see figure 2.8. At thermal equilibrium ($\sim$4.2 K) the populations of the coupled electron-nuclear spin states are described by the Boltzmann distribution, see chapter 1. It should be noted that the state $|\alpha_e\rangle$ corresponds to an electron in anti-alignment with the static magnetic field, as the electron has a gyromagnetic ratio $\gamma_e < 0$. Consider the electron-nuclear pairs which are in the state $|\alpha_e\beta_n\rangle$, and turn on the microwave field. In this case, the frequency of the microwave irradiation is $\omega_e - \omega_n$.

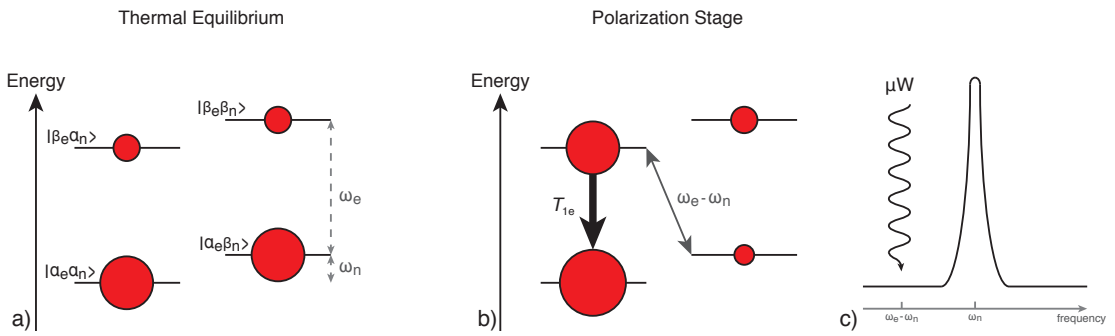

FIGURE 2.8: Schematic for solid-effect DNP at 6.7 T and ∼4.2 K. The grey arrow denotes flip-flop transitions, and the black arrow (T_{1e}) denotes longitudinal electron relaxation. a) At thermal equilibrium, the electron and nuclear spin populations are dictated by Boltzmann distribution. b) The populations are rearranged under the action of flip-flop transitions induced by the application of a microwave field with frequency $\omega_e - \omega_n$. Polarization is accrued in the ground state $|\alpha_e\alpha_n\rangle$ as the relaxation time of the electron T_{1e} is significantly shorter than the relaxation of the nuclei T_{1n}. c) Microwave irradiation condition $\omega_e - \omega_n$ for the solid effect.

The electrons in the $|\alpha_e\beta_n\rangle$ pairs which are subjected to the microwave irradiation experience a "flip-flop" transition with the coupled nucleus. This mechanism is only feasible if the nuclear spin is pointing in the opposite sense to the electron spin, since the flip-flop transition must conserve energy. The flip-flop transition induced by the microwave irradiation converts population from the $|\alpha_e\beta_n\rangle$ spin state to the $|\beta_e\alpha_n\rangle$ spin state.

Electron spins are known to relax quickly in most cases, and usually far more rapidly than the majority of nuclei. The rapid T_{1e} processes associated with the electron spins promptly deplete the $|\beta_e\alpha_n\rangle$ state of population as the electron spins return to thermal equilibrium. Population is consequently transferred to the ground state $|\alpha_e\alpha_n\rangle$, and a population difference is accrued across the states separated by ω_n. At low temperatures (∼4.2 K) the nuclear spin relaxation time T_{1n} is typically very long, and is usually on the order of minutes or hours. The nuclear population imbalance is therefore maintained, and the sample is said to be *hyperpolarized*. The short T_{1e} of the electron is a valuable asset for DNP, as the process can now be repeated several times and for other electron-nuclear pairs. In practice an electron can have many nuclear counterparts during the hyperpolarization stage. Hence, a high efficiency is realized for the solid-effect if the following condition is satisfied [109]:

$$\frac{N_n T_{1e}}{N_e T_{1n}} \ll 1, \tag{2.13}$$

where N_n and N_e are the number of nuclear and electron spins embedded within the

frozen sample, respectively. The ideal conditions for the solid effect are therefore high concentrations of nuclei with long relaxation times, comixed with a minimal amount of electron spins which relax rapidly.

The SE directly polarizes nuclei surrounding the unpaired electron. As previously touched upon, an additional process, known as *spin diffusion*, spreads the population imbalance throughout the sample bulk [110]. For spin diffusion to be effective, the bulk nuclei must be in dipolar contact with a polarized nucleus [111]. This is not the case for the core nuclei immediately surrounding the unpaired electron, as the paramagnetic centre shifts the resonance frequencies of the adjacent nuclei, in comparison to the bulk nuclei. The spin diffusion process is therefore quenched, and the nuclear hyperpolarization is trapped within a "DNP shell" [110]. The DNP shell is limited to a finite locus around each unpaired electron to due to distance dependent nature of the electron-nuclear hyperfine interaction [112]. Spin diffusion instead uses bulk nuclei outside of the DNP shell to extend the nuclear hyperpolarization to the rest of the sample. This is profitable for the hyperpolarization of the entire sample, as the nuclei are fixed within the lattice and may not undergo direct hyperpolarization via the solid-effect. It should be noted that the NMR signals available from the core nuclei are "bleached" due to the short nuclear T_{1n} attributed to the large hyperfine interaction with the nearby unpaired electron [113]. The enhanced NMR signal is therefore associated with the bulk nuclei which are hyperpolarized via the spin diffusion process.

2.4.3 Cross-effect DNP

The SE was extensively studied in crystals, but to obtain higher concentrations of nuclear spins a switch was made to frozen alcohols [114]. The ESR lines in these systems are inhomogeneously broadened due to the anisotropy of the g-factor. Dipole-dipole interactions between electrons also contribute to the ESR linewidth. This is analogous to the situation with wide line radical systems [115, 116]. As discussed in section 2.4.1, inhomogeneous effects can provide a larger distribution of ESR resonances than a Gaussian distribution. Such ESR spectra can therefore be thought of as containing individual "spin-packets" that act independently under the effects of microwave irradiation. It can be very difficult, but possible, to "burn a hole" in an inhomogeneously broadened

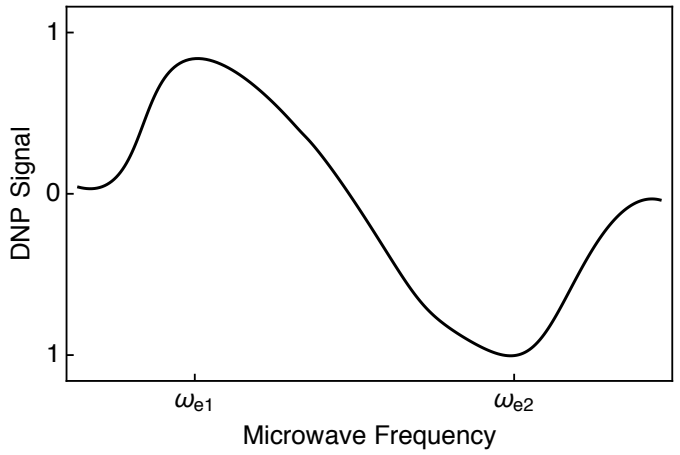

FIGURE 2.9: Microwave swept DNP enhancement (DNP spectrum) of a wide line radical such as TEMPO at 6.7 T and 1.4 K. The forbidden transitions $\omega_e \pm \omega_n$ begin to superimpose with the allowed transition ω_e. The maximum enhancement has been normalized to ± 1, respectively, with the maxima and minima separated by $\omega_{e1} - \omega_{e2}$.

ESR spectrum, by saturating spin packets at certain frequencies dictated by the applied microwave field. Upon continued microwave irradiation, off-resonant spin packets subsequently become saturated through a process known as *spectral diffusion*. Spectral diffusion is a phenomenon in which the individual spin-packets of an inhomogeneously broadened ESR line overlap as result of dipolar contact with neighbouring electrons, allowing energy to be transferred throughout the ESR spectrum. On first glance, this might appear to diminish the DNP effect, as the formally forbidden transitions $\omega_e \pm \omega_n$ begin to superimpose with the allowed ω_e transition and as such cannot be irradiated separately, see figure 2.9.

In 1963 Kessenikh and Manenkov proposed a 3-spin DNP process involving simultaneous spin flips between two electrons and a single nucleus, which is today known as the cross-effect (CE) [117–119]. Such transitions are allowed when the following matching condition for the microwave field is met: $\omega_{e1} - \omega_{e2} = \omega_n$, which is possible as both of the electrons can have different g-anisotropies. To facilitate the CE mechanism, wide line radicals should be impregnated into the glassy DNP matrix. Wide line radicals have ESR linewidths which are wider than the Larmor frequency of the nucleus to be polarized: $\Delta\omega_e > \omega_n$. Nitroxide radicals such as TEMPO and TEMPOL display wide ESR lines, as strong electron-nuclear hyperfine couplings and large g-anisotropies are present in these systems. Owing to the use of wide line radicals for cross-effect DNP, it is therefore sufficient to saturate an allowed transition corresponding to either electron spin, and hence the cross-effect is simultanesouly active for two spin packets separated

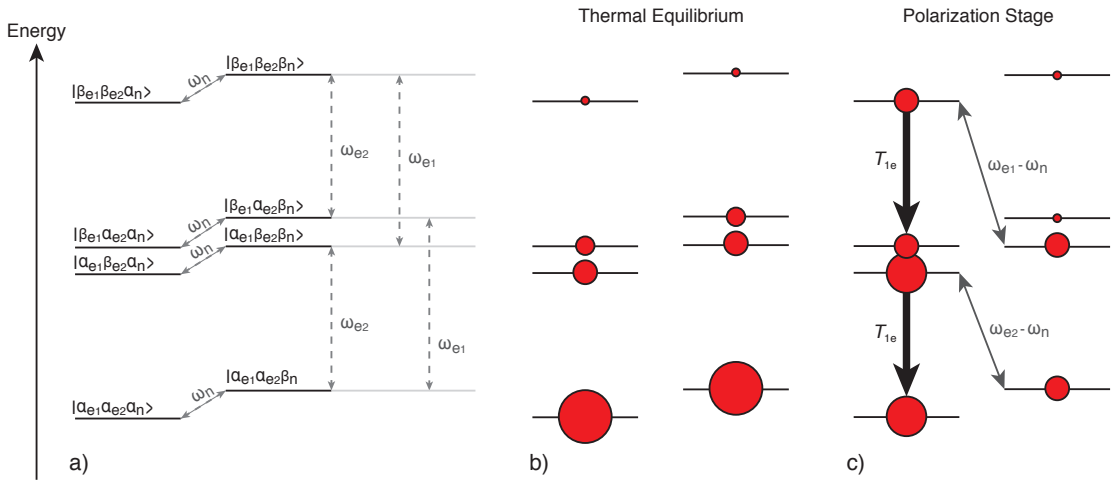

FIGURE 2.10: Schematic for cross-effect DNP at 6.7 T and ∼4.2 K. The grey arrow denotes flip-flop transitions, and the black arrow (T_{1e}) denotes longitudinal electron relaxation. a) Coupled energy level structure for the two-electron, one-nucleus spin system. b) Spin populations at thermal equilibrium are determined by the Boltzmann distribution. At lower temperatures ($\lesssim$10 K) electron spins are predominantly in the $|\alpha_e\rangle$ state, whilst nuclei are poorly polarized. c) The populations are redistributed by the three-spin cross-effect for electron-nuclear systems satisfying the condition $\omega_{e1} - \omega_{e2} = \omega_n$ under an applied microwave field of frequency $\omega_e - \omega_n$. Nuclear Zeeman polarization is accumulated in the $|\alpha_e\alpha_n\rangle$ state as T_{1e} relaxation is orders of magnitude shorter than the nuclear relaxation time T_{1n}.

by ω_n. In this regime, the cross-effect becomes a more efficient method of polarization transfer than the solid-effect.

Just as with the solid-effect, cross-effect DNP can be sufficiently described with the use of clear energy level diagrams, see figure 2.10. Consider the same initial conditions as in section 2.4.2, but this time note that the initial spin populations to be concerned with are $|\alpha_{e1}\alpha_{e2}\beta_n\rangle$ and $|\beta_{e1}\alpha_{e2}\beta_n\rangle$. Application of a microwave field with frequency $\omega_{e2} - \omega_n$ causes one of the electrons in the $|\alpha_{e1}\alpha_{e2}\beta_n\rangle$ and $|\beta_{e1}\alpha_{e2}\beta_n\rangle$ states to experience a "flip-flop" transition with the coupled nucleus. The flip-flop transition induced by the microwave irradiation converts population into the $|\alpha_{e1}\beta_{e2}\alpha_n\rangle$ and $|\beta_{e1}\beta_{e2}\alpha_n\rangle$ spin states, respectively, and polarization transfer is promoted between the electron pair and the lone nucleus. Note, the electron subjected to the flip-flop interaction must again be aligned in the opposite sense to the nucleus, with respect to the static magnetic field direction. The separated timescales of electron and nuclear spin relaxation processes allow an imbalance of population across states separated by ω_n, and hence an increased nuclear Zeeman polarization is obtainable through cross-effect DNP.

2.4.4 Thermal mixing DNP

Highly efficient cross-effect DNP can occasionally be present at low radical concentrations, and is sometimes observed alongside solid-effect DNP [120–125], despite the low orientation probabilities of finding two electrons separated by the nuclear Larmor frequency. Evidently, a great deal of spin-packets within the ESR line do not satisfy the cross-effect condition. A more involved theory of DNP, which takes into account all spin-spin and spectral diffusion processes, was developed by Redfield [126], Provotorov [127] and Borghini [128, 129], and is today known as thermal mixing. Thermal mixing is a thermodynamic model that describes the polarisation transfer between many electron and nuclear spins [130, 131], and is now recognized as an efficient DNP mechanism. Thermal mixing becomes dominant at lower temperatures when the electron T_{1e} is extended and the spin diffusion process finishes in less than one electron T_{1e}. The thermal mixing mechanism is additionally active in cases of homogeneously broadened electron systems, i.e. when the electron concentration is increased, as the microwave field uniformly saturates all ESR transitions. The solid-effect and cross-effect mechanisms become ineffective under these conditions.

2.5 Dissolution-dynamic nuclear polarization

Jan-Hendrik Ardenkjaer-Larsen and coworkers pioneered the dissolution-DNP approach in 2004, and their first experiments showed a >10,000-fold increase in liquid state polarization [71]. Recently, D-DNP has been directly applicable to *in vivo* research. The first in-patient study demonstrating the feasibility of hyperpolarized [1-^{13}C]pyruvate as a non-invasive marker of tumour metabolism was completed successfully [87]. Patients with prostate cancer were safely injected with hyperpolarized pyruvate in order to characterize rates of pyruvate-lactate conversion in localized tumours via real-time magnetic resonance imaging [132]. D-DNP has also been used to evaluate tumour grades [133] and to continuously monitor the treatment response of living organisms such as cancer cells [134].

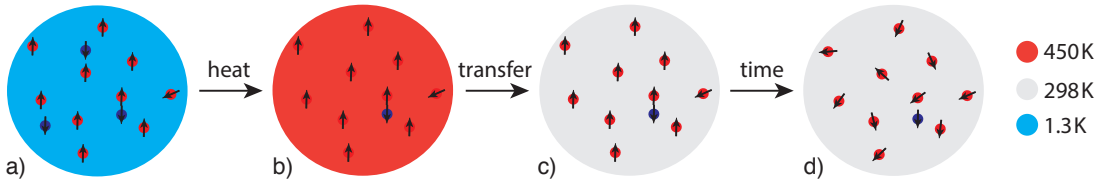

FIGURE 2.11: Overview of the dissolution-DNP process. Red spheres denote nuclei ($\gamma > 0$), blue spheres denote unpaired electrons. a) Sufficient time is allowed as to accrue maximum hyperpolarization of nuclear spins in the solid-state. b) The microwave field is removed and the frozen material undergoes a rapid melt by using a jet of warm solvent which is injected into the sample space. c) The warm, hyperpolarized liquid is rapidly transferred to an external, high-field NMR magnet under the pressure of helium gas. The sample voyage is engineered such that low-field relaxation from unpaired electrons is negligible. d) High-resolution NMR experiments are performed in the liquid state before relaxation processes return the hyperpolarized nuclear spin populations to thermal equilibrium.

2.5.1 Overview of the dissolution process

D-DNP is a batch-mode experiment, not a continuous operation, and so the largest achievable nuclear spin polarizations are required prior to dissolution in order to obtain the best possible results. Once the applied microwaves are removed, the nuclear hyperpolarization generated by DNP is lost by means of spin relaxation, which is attributed to nuclear-electron interactions. Furthermore, the cryostat is often pressurized and temperatures rise to ∼3-4 K, which in turn induces faster relaxation of the nuclear spins. The dissolution process, therefore, must be rapid in order to avoid further losses in the nuclear Zeeman polarization. A schematic of the dissolution-DNP process is shown in figure 2.11.

The dissolution process is a rather simple one, but is tricky to execute in practice. Experimental conditions must be compatible with the dissolution procedure, and so most dissolutions are performed at ∼4.2 K, which is convenient as an electron spin polarization approaching unity is achieved in the region of $\lesssim$10 K. Once the desired level of Zeeman polarization is amassed in the solid state, the frozen sample is rapidly heated with a jet (∼4-5 mL volume) of warm solvent (∼150°C temperature). The heated solvent is located in a bomb placed directly above the glassy matrix, radical and sample, and is injected into the sample cup under the pressure of helium gas. The DNP mixture melts rapidly upon contact with the warm solvent and the helium gas pushes the hyperpolarized liquid sample towards a separate NMR magnet, where the acquisition of a hyperpolarized NMR signal subsequently takes place. Accelerated relaxation is a potential concern in regions of low magnetic field along the sample path, but can mostly be negated by the use of a

magnetic tunnel [135]. In most cases, the high population imbalance established by DNP is maintained during the sample voyage between NMR instruments, despite the sample temperature equilibrating with room temperature by the time the hyperpolarized media reaches the liquid state device.

The typical result of a D-DNP experiment is a liquid state spectrum with level of sensitivity that can only usually be reproduced with thousands of individual signal summations. The enhancements recorded using D-DNP are typically larger than those observed for solid-state DNP (capped at γ_e/γ_n) due to the room temperature readout of the hyperpolarized spin order in the liquid state. Determining the level of signal enhancement depends on factors such as the presence of microwave irradiation, the state of the sample matter, the temperature and the number of transients used to record the reference spectrum. More details regarding DNP enhancements are given in chapter 4. The capability to transfer hyperpolarized media to high-resolution instruments also comes with a few advantages, namely, cheap microwave sources can be employed as samples can be polarized at lower magnetic fields.

As previously referred to, diffusion and translation of unpaired electron species within the dissolution solvent drives paramagnetic relaxation of the hyperpolarized nuclei during the sample voyage between polarization and detection magnets, with relaxation particularly prevalent at low magnetic fields [136]. This process can be countered with a fast, adiabatic dissolution, and the use of a magnetic tunnel [135]. Paramagnetic relaxation is additionally offset by co-freezing beads of ascorbate alongside the substance of interest. When the frozen beads are rapidly dissolved by the warm solvent jet, the ascorbate molecules scavenge the radical source. Upon radical quenching, ascorbyl radicals are formed which disproportionate from the bulk solution. Paramagnetic relaxation is therefore prevented as no unpaired electron species remain within the sample. Radical scavenging is currently the preferred option for D-DNP experiments as no fast mechanical radical filtering systems are available. Radicals may also be diluted by using an increased solvent volume, however, the sample concentration and spectral quality will consequently suffer.

Some disadvantages of dissolution-DNP remain a problem at present. D-DNP is a one-shot experiment, meaning that all the available polarization accrued by DNP in the solid state must be exploited in a single dissolution. Hyperpolarized spin order cannot

be continuously replenished by bubbling a source of high spin order into the sample volume, unlike some parahydrogen-based hyperpolarization experiments [137, 138]. One significant drawback of the D-DNP approach is the limited time available for signal acquisition. The resulting hyperpolarized signals cannot result from a series of summed acquisitions, as is the case for solid state DNP measurements or traditional signal summation experiments. The brief acquisition period is in essence down to the short T_1 for the substances of interest, which are often small molecules. The use of conventional relaxation times currently prevents D-DNP from producing high-performance results in alternative fields such as 2D-NMR spectroscopy. In the next section, the concept of longer-lived spin states, and the symmetry properties that ensure signal longevity, are explored.

2.6 Overview of long-lived states

The longitudinal relaxation time constant T_1 was traditionally seen as the limiting factor for the lifetime of NMR signals. After rf-perturbation, the original "memory" of the spin system is fully recoverable in a time of approximately $5 \times T_1$ [14]. The T_1 window, typically a matter of seconds, has already provided unique opportunities for NMR spectroscopists to probe processes such as diffusion, flow, and slow molecular motion [41, 139]. Nonetheless, the common time limit for an NMR experiment is governed by the return of longitudinal spin order towards thermal equilibrium. Hyperpolarization techniques for use in NMR spectroscopy and imaging are also hampered by the requirement of exploiting nuclear spin order within the T_1 time frame. Lengthening T_1 further usually requires chemical modification, such as isotopic labelling, which can be expensive. In this section, I will discuss an alternative form of *long-lived* spin order, the lifetime of which can far exceed that of ordinary magnetization.

Long-lived states (LLS) possess the capability to store nuclear spin order for durations which considerably exceed the T_1 time limit, providing a suitable approach to overcome the constraints on relaxation dynamics. The first discovery of a long-lived nuclear spin state occurred in the laboratory of Malcolm H. Levitt at the University of Southampton in 2004 [14]. Together with coworkers Marina Caravetta and Ole G. Johannessen, the proton pair in a molecule of 2,3-dibromothiophene was shown to reveal "dark" quantum states with singlet lifetimes exceeding T_1 by a factor of 7. As time progressed, a growing bank of molecules bearing long-lived singlet states emerged [20, 22, 23, 28, 30, 32, 34, 35, 54, 55, 140–148], along with the knowledge of what creates longevity for the nuclear spin order [16, 17, 26, 56, 149–155]. A key step in this process was the synthesis of singlet molecules with spin pairs subject to small symmetry breaking interactions [24], and consequently the development of rf-pulse schemes allowing coherent access to the nuclear singlet order [21, 31, 150, 156–160].

In more recent years, the phenomena of long-lived states has been developed and applied in an endeavour to overcome the issue of limited signal lifetimes in near chemically equivalent spin systems. Molecular systems have therefore been designed to coax out longer-lived singlet lifetimes, with small chemical shift differences specifically synthesised for this purpose. A long-lived state with a lifetime surpassing one hour in a room temperature solution has recently been achieved for a Napthalene derivative composed

of a sufficiently isolated ^{13}C spin-pair [35]. A lifetime for nuclear spin order exceeding 1 hour has only even been achieved previously in a gas phase NMR experiment [161]. The Naphthalene system embodies the majority of the current knowledge in the LLS community, and currently holds the world record for a long-lived singlet lifetime. Similar achievements have also been recorded independently by Giuseppe Pileio and Alexej Jerschow for a proton pair in a sample of dimethyl fumarate [29, 33, 145], which has a long-lived state lifetime of ∼10 minutes. The key fundamentals for long singlet lifetimes in spin-1/2 pairs are:

- strong coupling regime i.e. J-stabilization, small singlet leakage, [17, 24]
- inversion symmetry, [144]
- low-γ singlet nuclei, [146]
- isotopic substitution i.e. selective deuteration*, [22]
- no neighbouring magnetic nuclei. [28, 29, 33, 35, 145]

Other important considerations for extending nuclear singlet lifetimes are: a rigid molecular structure, the removal of paramagnetic relaxation sources i.e. O_2, and avoiding relaxation sinks i.e. nearby methyl groups. It is likely that a few of the above constraints cannot be met for the majority of LLS candidate molecules, but singlet lifetimes outlasting those of longitudinal magnetization are still achieved in the majority of cases. Furthermore, the NMR spectroscoper can also manipulate the spin system at hand in order to prolong the lifetime of the nuclear singlet order. The techniques of field-cycling and rf-suppression are typically used to preserve singlet lifetimes, as the symmetry properties and relaxation dynamics are favourable altered in certain circumstances.

*In the final chapter of this thesis, discussion of a "new" singlet relaxation mechanism is presented. This mechanism has been term singlet-scalar relaxation of the second kind (S-SR2K). In this case, selective deuteration considerably shortens the nuclear singlet lifetime. Singlet-SR2K could therefore be the rate limiting factor for long-lived states in systems already exhibiting substantial singlet lifetimes.

This work presented in this thesis concentrates predominantly on the relaxation behaviour of nuclear singlet states for coupled pairs of spin-1/2 nuclei. In this section, I

will convey the fundamental aspects of nuclear singlet states for 2-spin-1/2 systems, and how the properties of nuclear singlet states allows for long-lived relaxation behaviour.

2.7 Nuclear singlet and triplet states

As discussed in chapter 1, there are two eigenstates of the total angular momentum for a single spin-1/2 nucleus. The eigenstates are denoted $|\alpha\rangle$ and $|\beta\rangle$, and specify the absolute alignment of the intrinsic magnetic moment parallel $|\alpha\rangle$ or anti-parallel $|\beta\rangle$ to the static magnetic field. For a pair of spin-1/2 nuclei, the angular momentum couples in both a constructive and destructive manner. A composite spin system is formed with a total angular momentum of I=0 (destructive addition) or I=1 (constructive addition). Hence, there are four orthonormal eigenstates of the total angular momentum operator for a pair of spin-1/2 nuclei. The nature of these four eigenstates depends highly on the symmetry properties of the spin-pair at hand. Here I consider a pair of homonuclei (i and j) in an A_2 spin system connected via a scalar coupling J_{ij}, i.e. the two spins-1/2 are chemically equivalent at high magnetic field.

The four eigenstates of the total angular momentum operator for a pair of spin-1/2 nuclei are constructed by using products of the $|\alpha\rangle$ and $|\beta\rangle$ eigenstates, these are:

$$|\alpha\alpha\rangle\,, |\alpha\beta\rangle\,, |\beta\alpha\rangle\,, |\beta\beta\rangle\,. \tag{2.14}$$

The above eigenstates are often referred to as the Zeeman product states. The multiplicity of the constructive and destructive combinations of angular momentum allows one to speculate about the construction of the spin-0 and spin-1 eigenstates. The spin-1 configuration has three components of the angular momentum for a spin-1/2 pair: $m_I = 0, \pm 1$. Together these components form a spin-1 manifold consisting of three eigenstates referred to as the nuclear triplet states:

$$|T_{+1}\rangle = |1,+1\rangle = |\alpha\alpha\rangle\,, \tag{2.15}$$

$$|T_0\rangle = |1,0\rangle = \frac{1}{\sqrt{2}}(|\alpha\beta\rangle + |\beta\alpha\rangle), \tag{2.16}$$

$$|T_{-1}\rangle = |1,-1\rangle = |\beta\beta\rangle\,. \tag{2.17}$$

There is just one destructive combination of angular momentum for a pair of spin-1/2 nuclei, i.e. the spin-0 eigenstate has a multiplicity of 1, and is known as the nuclear singlet state:

$$|S_0\rangle = |0,0\rangle = \frac{1}{\sqrt{2}}(|\alpha\beta\rangle - |\beta\alpha\rangle). \tag{2.18}$$

In general, the nuclear singlet and triplet states are declared using the bra-ket notation: $|I, m_I\rangle$. Here I will introduce the shorthand notation "S" for the nuclear singlet state, and "T" for the three nuclear triplet states. For a spin-1/2 nuclear pair ij, the nuclear singlet and triplet states are eigenstates of the total $(\hat{I}_i + \hat{I}_j)^2$ and z-projection $\hat{I}_{iz} + \hat{I}_{jz}$ angular momentum operators:

$$(\hat{I}_i + \hat{I}_j)^2 |I, m_I\rangle = I(I+1)\hbar^2 |I, m_I\rangle , \tag{2.19}$$

$$(\hat{I}_{iz} + \hat{I}_{jz}) |I, m_I\rangle = m_I\hbar |I, m_I\rangle , \tag{2.20}$$

where the subscripts i and j indicate the nucleus of the spin pair upon which the angular momentum operator is acting. For the nuclear singlet state, which has a composite nuclear spin of 0, the solutions to the eigenequations 2.19 and 2.20 are therefore:

$$(\hat{I}_i + \hat{I}_j)^2 |S_0\rangle = 0 |S_0\rangle , \tag{2.21}$$

$$(\hat{I}_{iz} + \hat{I}_{jz}) |S_0\rangle = 0 |S_0\rangle , \tag{2.22}$$

and the nuclear singlet state is evidenced to act as a single, magnetically silent particle. Direct observation of the spin-0 singlet state is therefore not feasible with NMR, and detection of singlet spin order requires passage through the triplet manifold. The nuclear triplet states behave as the three eigenstates of a spin-1 particle, as shown by the eigenequations:

$$(\hat{I}_i + \hat{I}_j)^2 |T_{m_I}\rangle = 2\hbar^2 |T_{m_I}\rangle , \tag{2.23}$$

$$(\hat{I}_{iz} + \hat{I}_{jz}) |T_{m_I}\rangle = m_I\hbar |T_{m_I}\rangle , \tag{2.24}$$

where $m_I = 0, \pm 1$. In each case, the angular momentum operators $(\hat{I}_i + \hat{I}_j)^2$ and $\hat{I}_{iz} + \hat{I}_{jz}$ commute. It is therefore possible to know the eigenvalues to each eigenequation simultaneously, as the commuting operators share a common set of eigenfunctions. In which case, $\hat{I}_{iz} + \hat{I}_{jz}$ may be replaced with $\hat{I}_{ix} + \hat{I}_{jx}$ or $\hat{I}_{iy} + \hat{I}_{jy}$.

Combining the population operators for the nuclear singlet state $|S_0\rangle\langle S_0|$, and the nuclear triplet states $|T_{m_I}\rangle\langle T_{m_I}|$, allows one to construct an operator for the singlet-triplet population imbalance $\hat{Q}_{\mathrm{SO}}$:

$$\hat{Q}_{\mathrm{SO}} = |S_0\rangle\langle S_0| - \overline{|T_{m_I}\rangle\langle T_{m_I}|}, \tag{2.25}$$

where $\overline{|T_{m_I}\rangle\langle T_{m_I}|}$ is the mean population operator for the triplet manifold:

$$\overline{|T_{m_I}\rangle\langle T_{m_I}|} = \frac{1}{3}\sum_{m_I} |T_{m_I}\rangle\langle T_{m_I}| = \frac{(|T_{+1}\rangle\langle T_{+1}| + |T_0\rangle\langle T_0| + |T_{-1}\rangle\langle T_{-1}|)}{3}. \tag{2.26}$$

The population difference operator $\hat{Q}_{\mathrm{SO}}$ is a property of spin-1/2 pairs known as nuclear singlet order, and is a long-lived characteristic of singlet magnetic resonance experiments [150, 151]. The imbalance between the population of the nuclear singlet state and the mean population of the three nuclear triplet states is determined by the "expectation value" of the population difference operator $\hat{Q}_{\mathrm{SO}}$, see section 1.5.1. At room temperature, and in thermal equilibrium, the ratio of populations between the triplet and singlet manifolds is 3:1.

2.8 Symmetry properties of singlet order

It is the symmetry properties of the nuclear singlet and triplet states which enables the singlet order of spin-1/2 pairs to achieve extraordinary lifetimes, with respect the lifetime of ordinary magnetization. Consider the permutation operator $\hat{P}(m_i, m_j)$:

$$\hat{P}(m_i, m_j)\,|m_i, m_j\rangle = |m_j, m_i\rangle\,. \tag{2.27}$$

$\hat{P}(m_i, m_j)$ swaps the order of the two nuclei i and j, or equivalently exchanges the labels of two spins:

$$\hat{P}(m_i, m_j)\,|S_0\rangle = -\,|S_0\rangle\,, \tag{2.28}$$

$$\hat{P}(m_i, m_j)\,|T_{m_I}\rangle = +\,|T_{m_I}\rangle\,. \tag{2.29}$$

As can be seen from equations 2.15-2.18, the nuclear singlet wavefunction is antisymmetric with respect to spin exchange whilst the nuclear triplet wavefunctions are all

exchange-symmetric.

The exchange symmetry imposes strict transition rules for the nuclear singlet and triplet states under a fluctuating Hamiltonian. The fluctuating Hamiltonian is essentially a matrix containing transition probabilities between all spin states. The fluctuating Hamiltonian is required to be symmetric for a pair of spin-1/2 nuclei because the total energy of the system is invariant to the exchange of identical spins. A permutation-symmetric Hamiltonian $\hat{H}_{ij}$ is defined by:

$$\hat{\hat{P}}(m_i, m_j)\hat{H}_{ij} = \hat{H}_{ij}, \tag{2.30}$$

where $\hat{\hat{P}}(m_i, m_j)$ is the permutation superoperator [162], and is defined as:

$$\hat{\hat{P}}(m_i, m_j) = \hat{P}(m_i, m_j) \otimes \hat{P}(m_i, m_j)^{\dagger}. \tag{2.31}$$

The permutation operator $\hat{P}(m_i, m_j)$ can be shown to commute with the symmetric Hamiltonian $\hat{H}_{ij}$. Expanding equation 2.30 provides:

$$\hat{P}(m_i, m_j)\hat{H}_{ij}\hat{P}(m_i, m_j)^{\dagger} = \hat{H}_{ij}, \tag{2.32}$$

and by multiplying both sides of equation 2.32 with $\hat{P}(m_i, m_j)$, and suitably rearranging the result, yields the following commutivity relation:

$$[\hat{P}(m_i, m_j), \hat{H}_{ij}] = 0. \tag{2.33}$$

The application of $\hat{\hat{P}}(m_i, m_j)$ twice will recover the original form of $\hat{H}_{ij}$, hence simply acting as the identity operation:

$$\hat{P}(m_i, m_j)^{\dagger}\hat{P}(m_i, m_j) = \hat{\mathbb{1}}. \tag{2.34}$$

The above property permits a more careful examination of the matrix elements belonging to the symmetric Hamiltonian. Consider a matrix element of $\hat{H}_{ij}$ which links the nuclear singlet state $|S_0\rangle$ and the states of the triplet manifold $|T_{m_I}\rangle$, such as $\langle S_0| \hat{H}_{ij} |T_{m_I}\rangle$. Deliberate insertion of the identity operation (equation 2.34) returns:

$$\langle S_0| \hat{P}(m_i, m_j)^{\dagger}\hat{P}(m_i, m_j)\hat{H}_{ij}\hat{P}(m_i, m_j)^{\dagger}\hat{P}(m_i, m_j) |T_{m_I}\rangle . \tag{2.35}$$

By using the spin-exchange symmetry properties of the nuclear singlet and triplet states (equations 2.28 and 2.29), and the permutation commutation relation in equation 2.32, it may be shown that:

$$\langle S_0| \hat{H}_{ij} |T_{m_I}\rangle = -\langle S_0| \hat{H}_{ij} |T_{m_I}\rangle . \tag{2.36}$$

A permutation-symmetric Hamiltonian, therefore, cannot connect spin states of opposite exchange symmetry [139, 163, 164]:

$$\langle S_0| \hat{H}_{ij} |T_{m_I}\rangle = 0, \tag{2.37}$$

and singlet-triplet transitions are forbidden in the absence of symmetry-breaking nuclear spin interactions. The singlet-triplet population imbalance (and the associated singlet polarization) is hence a conserved property of the spin system. Therefore, once a population imbalance is established, coherent population interconversion is only possible via interactions which are themselves antisymmetric with respect to the spin exchange symmetry, or by uncorrelated local magnetic field fluctuations across the spin-1/2 pair. The three nuclear triplet states are connected by triplet-triplet transitions induced by a fluctuating Hamiltonian which is exchange-symmetric, and the matrix elements $\langle T_{m_I}| \hat{H}_{ij} |T_{m_I}\rangle$ may be non-zero:

$$\langle T_{m_I}| \hat{H}_{ij} |T_{m_I}\rangle \neq 0, \tag{2.38}$$

as the three nuclear triplet states posses the same exchange-symmetry. This property may be shown by replacing $\langle S_0|$ for $\langle T_{m_I}|$ in equation 2.36. The dominant relaxation process for 2-spins-1/2 in solution is the in pair dipole-dipole interaction, and is an exchange-symmetric interaction (see equation 1.162). Hence, the singlet state is immune to relaxation via the in pair dipole-dipole mechanism and has the following property:

$$\hat{H}^{ij}_{DD} |S_0\rangle = 0, \tag{2.39}$$

where $\hat{H}^{ij}_{DD}$ is the dipole-dipole Hamiltonian for spins i and j [19, 165]. In the absence of other antisymmetric NMR interactions the singlet-triplet population difference is infinitely long-lived. In realistic spin systems, a mixture of exchange-symmetric and exchange-antisymmetric NMR mechanisms are present. Singlet-triplet decoherence is

small but non-zero, and the decay of singlet order is slow compared to the decay of conventional magnetization, which is affected by magnetic interactions of all symmetries.

Singlet-triplet population interconversion is also governed by the key principle of angular momentum commutation. It may therefore be shown that a Hamiltonian which commutes with the total angular momentum operator $(\hat{I}_i + \hat{I}_j)^2$, or equally $\hat{I}_{iz} + \hat{I}_{jz}$, is unable to induce singlet-triplet transitions. Equation 1.157 states that the commutation between spherical tensor operators given by $\hat{T}^{ij}_{lm}$ is proportional to the matrix element: $\langle lm'| \hat{T}^{ij}_{lm} |lm\rangle$. Consider the case of the dipole-dipole Hamiltonian, which is represented by the spherical tensor operator $\hat{T}^{ij}_{2m}$, and its commutivity with nuclear singlet order $\hat{T}^{ij}_{00}$:

$$[\hat{T}^{ij}_{2m}, \hat{T}^{ij}_{00}] = 0. \tag{2.40}$$

The commutator bracket is equal to zero as the matrix elements $\langle lm'| \hat{T}^{ij}_{00} |lm\rangle$ are independent of the magnetic quantum number m for a given angular momentum quantum number l. Or simply put, the commutation of a spherical tensor operator with a scalar is always zero. Therefore any nuclear spin Hamiltonian which commutes with the total angular momentum operator $(\hat{I}_i + \hat{I}_j)^2$ must conserve the singlet and triplet eigenfunctions $|I, m_I\rangle$, as it is a requirement of commuting operators to share a common set of orthonormal eigenfunctions. Furthermore, by examining the commutators of the Liouville-von Neumann equation (1.99) it is clear that:

$$\frac{d}{dt}\hat{\rho} = 0 \quad \text{if } \hat{\rho} = \hat{T}^{ij}_{00}, \tag{2.41}$$

in the presence of exchange-symmetric interactions, and again one can see that $\hat{T}^{ij}_{00}$ is a conserved property of the spin system. The field of long-lived states is built upon identifying constants of motion, i.e. states, populations etc. which do not evolve under fluctuating NMR interactions, and hence this is a key result from this chapter. The only other constant of the motion in this case is the total number of nuclei present in the spin system. The states $|0, 0\rangle$ and $|1, m_1\rangle$ are hence disconnected and do not interconvert, unless the nuclear spin Hamiltonian does not commute with $(\hat{I}_i + \hat{I}_j)^2$. Under these conditions nuclear singlet order is not a conserved property of the spin system, and singlet-triplet relaxation is permitted.

2.9 Properties of the coherent Hamiltonian

At high magnetic field the coherent Hamiltonian is a combination of interactions between nuclear spins, and also interactions between spins and the magnetic field, as described by equation 1.161. A common scenario is the Zeeman interaction $\hat{H}_Z^{\mathrm{L}}$ dominating the Hamiltonian. Other interactions, such as scalar couplings $\hat{H}_J$, are also present but are often significantly smaller in size. For simplicity, the presence of a time-dependent rf-field is excluded from the Hamiltonian. The coherent Hamiltonian for a pair of scalar coupled spin-1/2 nuclei in solution includes the following terms:

$$\hat{H}_{\mathrm{coh}} = \hat{H}_Z^{\mathrm{L}} + \hat{H}_J. \tag{2.42}$$

The Zeeman Hamiltonian written in the laboratory frame L is given by:

$$\hat{H}_Z^{\mathrm{L}} = \omega_0(1+\delta_i)\hat{I}_{iz} + \omega_0(1+\delta_j)\hat{I}_{jz}, \tag{2.43}$$

where $\omega_0(1+\delta_i)$ is the chemically shifted nuclear Larmor frequency for nucleus i. The J-coupling Hamiltonian is given by:

$$\hat{H}_J = 2\pi J_{ij}\hat{I}_i \cdot \hat{I}_j, \tag{2.44}$$

where J_{ij} is the in pair scalar coupling. The scalar product of angular momentum vectors $\hat{I}_i$ and $\hat{I}_j$ in the Hamilontian $\hat{H}_J$ may be expanded in terms of the ladder operators $\hat{I}^+$ and $\hat{I}^-$:

$$\hat{I}_i \cdot \hat{I}_j = \hat{I}_{iz}\hat{I}_{jz} + \frac{1}{2}(\hat{I}_i^+\hat{I}_j^- + \hat{I}_i^-\hat{I}_j^+). \tag{2.45}$$

For the case of magnetically equivalent spins-1/2, i.e. $\delta_i = \delta_j$, the coherent Hamiltonian has the following matrix representation in the singlet-triplet eigenbasis:

$$\hat{H}_{ST} = \begin{array}{c} \\ |S_0\rangle \\ |T_{-1}\rangle \\ |T_0\rangle \\ |T_{+1}\rangle \end{array} \begin{array}{c} \begin{array}{cccc} \langle S_0| & \langle T_{-1}| & \langle T_0| & \langle T_{+1}| \end{array} \\ \begin{pmatrix} \frac{-3\pi J_{ij}}{2} & 0 & 0 & 0 \\ 0 & \omega_0(1+\frac{\delta_\Sigma^{ij}}{2}) + \frac{\pi J_{ij}}{2} & 0 & 0 \\ 0 & 0 & \frac{\pi J_{ij}}{2} & 0 \\ 0 & 0 & 0 & -\omega_0(1+\frac{\delta_\Sigma^{ij}}{2}) + \frac{\pi J_{ij}}{2} \end{pmatrix} \end{array} \tag{2.46}$$

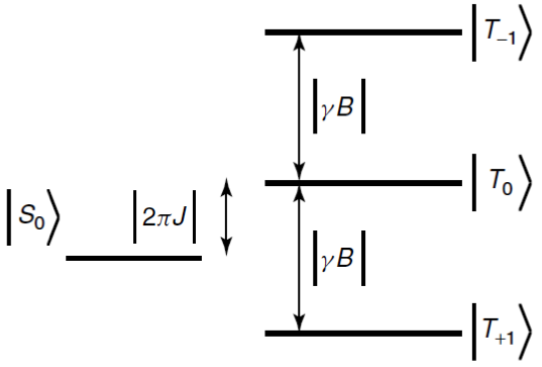

FIGURE 2.12: The energy level structure for a spin-1/2 nuclear pair as described by the matrix representation of the coherent Hamiltonian in the singlet-triplet eigenbasis. This schematic is correct for the case of magnetic equivalence and for $\gamma > 0$, $J > 0$. Taken from reference [26].

where δ_{Σ}^{ij} is the sum of chemical shift terms δ_i and δ_j. Employing a laboratory frame analysis allows one to determine the singlet-triplet energy level structure from the matrix representation of the coherent Hamiltonian, see figure 2.12. The triplet eigenstates are separated by $\hbar\omega_0$ (neglecting small chemical shift contributions), and are all additionally shifted by $\frac{\pi J_{ij}}{2}$. The singlet state is shifted by $\frac{-3\pi J_{ij}}{2}$ and hence is separated from the central triplet level by $2\pi J_{ij}$. The Zeeman term of the coherent Hamiltonian may be simplified for the purposes of facilitating this discussion by undergoing a transformation to the rotating frame. See appendix B for details regarding the rotating frame transformation. $\hat{H}_Z$ as written in the rotating frame is:

$$\hat{H}_Z = \Omega_i \hat{I}_{iz} + \Omega_j \hat{I}_{jz}, \tag{2.47}$$

where Ω_i is the offset frequency of spin i in the rotating frame. $\hat{H}_Z$ can be additionally restructured by using a more convenient formalism involving the sum Ω_{Σ}^{ij} and difference Ω_{Δ}^{ij} of the resonance offsets for spins i and j:

$$\hat{H}_Z = \frac{\Omega_{\Sigma}^{ij}}{2}(\hat{I}_{iz} + \hat{I}_{jz}) + \frac{\Omega_{\Delta}^{ij}}{2}(\hat{I}_{iz} - \hat{I}_{jz}). \tag{2.48}$$

For the case of $\Omega_i = \Omega_j$, the coherent Hamiltonian in equation 2.47 describes a magnetically equivalent spin pair, as there are no additional J-couplings to external nuclei and the exchange of labels i and j leaves $\hat{H}_{\text{coh}}$ invariant. This property can be shown by acting with the permutation superoperator described in equation 2.31 on $\hat{H}_{\text{coh}}$. In this case $\hat{H}_{\text{coh}}$ commutes with $(\hat{I}_i + \hat{I}_j)^2$, and nuclear eigenstates of differing exchange-symmetry are not permitted to interconvert, i.e. permutation symmetry is achieved in the case of

magnetic equivalence. Such a situation is found for the protons in dihydrogen or water, both of which constitute an A_2 spin system.

The matrix representation of the coherent Hamiltonian is divided into separate subspaces belonging to different projections of the spin quantum number m_I. There is a single 2×2 matrix of $m_I = 0$ states, and two one-dimensional $m_I = |1|$ subspaces, i.e. the populations belong to the states $|1, \pm 1\rangle$. The coherent Hamiltonian has the following matrix form in the singlet-triplet eigenbasis [16]:

$$\hat{H}_{\text{coh}}^{ST} = \begin{array}{c} \\ |S_0\rangle \\ |T_{+1}\rangle \\ |T_0\rangle \\ |T_{-1}\rangle \end{array} \begin{array}{c} \begin{array}{cccc} \langle S_0| & \langle T_{+1}| & \langle T_0| & \langle T_{-1}| \end{array} \\ \begin{pmatrix} \langle S_0| \hat{H}_{\text{coh}} |S_0\rangle & 0 & \langle S_0| \hat{H}_{\text{coh}} |T_0\rangle & 0 \\ 0 & \langle T_{+1}| \hat{H}_{\text{coh}} |T_{+1}\rangle & 0 & 0 \\ \langle S_0| \hat{H}_{\text{coh}} |T_0\rangle & 0 & \langle T_0| \hat{H}_{\text{coh}} |T_0\rangle & 0 \\ 0 & 0 & 0 & \langle T_{-1}| \hat{H}_{\text{coh}} |T_{-1}\rangle \end{pmatrix} \end{array}. \tag{2.49}$$

where $\langle i| \hat{H}_{\text{coh}} |j\rangle$ is a matrix element of $\hat{H}_{\text{coh}}$. The coherent Hamiltonian is shown to be block diagonal upon reordering of the basis eigenstates. $\hat{H}_{\text{coh}}$ contains a six-dimensional subspace of zero quantum operators, constructed from the four population operators $\langle i| \hat{H}_{\text{coh}} |j\rangle = \delta_{ij} |i\rangle \langle j|$ and the two singlet-central triplet coherences $\langle S_0|T_0\rangle$ and $\langle T_0|S_0\rangle$. More explicitly, the matrix representation of the coherent Hamiltonian (magnetic equivalence regime) in the singlet-triplet eigenbasis is:

$$\hat{H}_{\text{coh}}^{ST} = \begin{array}{c} \\ |S_0\rangle \\ |T_{+1}\rangle \\ |T_0\rangle \\ |T_{-1}\rangle \end{array} \begin{array}{c} \begin{array}{cccc} \langle S_0| & \langle T_{+1}| & \langle T_0| & \langle T_{-1}| \end{array} \\ \begin{pmatrix} \frac{-3\pi J_{ij}}{2} & 0 & 0 & 0 \\ 0 & \frac{\Omega_\Sigma^{ij}}{2} + \frac{\pi J_{ij}}{2} & 0 & 0 \\ 0 & 0 & \frac{\pi J_{ij}}{2} & 0 \\ 0 & 0 & 0 & -\frac{\Omega_\Sigma^{ij}}{2} + \frac{\pi J_{ij}}{2} \end{pmatrix} \end{array}, \tag{2.50}$$

where $\Omega_\Sigma^{ij} = \Omega_i + \Omega_j$ and is the sum of resonance offsets for spins i and j. Clearly the difference in resonance offsets is zero, as the two spins are defined to be magnetically equivalent. The coherent Hamiltonian in the singlet-triplet basis is strictly diagonal, and indeed there are no terms present which connect states of different angular momentum quantum number l. As discussed previously for a magnetically equivalent spin-1/2 pair, the exchange symmetry of the coherent Hamiltonian does not permit mixing of the nuclear singlet and triplet eigenstates, and the two manifolds are disconnected.

Nuclear singlet order, defined as the population imbalance between the mean populations of the singlet and triplet manifolds (equation 2.25), is only perturbed in the presence of exchange-antisymmetric NMR interactions. Access to the nuclear singlet order is therefore only possible if the coherent Hamiltonian does not posses permutation symmetry. In the case of a magnetically equivalent spins-1/2 pair, access to the nuclear spin order is unavailable due to the absence of off-diagonal terms in $\hat{H}_{\text{coh}}$. The presence of a symmetry-breaking interactions are required to provide access to the nuclear singlet order, and are necessary for the flow of nuclear spin populations between the nuclear singlet and triplet states. The later point is relevant for singlet NMR experiments, in which the population of the singlet state is slowly collected in the triplet manifold over time. Symmetry breaking in the style of chemical inequivalence is present for a desymmetrized spin pair, for example, in an asymmetric molecule. In practical cases, a small chemical shift difference is often synthetically engineered between the two singlet nuclei. Alternatively, magnetic equivalence is broken by inequivalent scalar couplings to nuclei outside of the spin pair. In this next section, I will focus on the case of a small chemical shift difference between the nuclei i and j which leads to the coupling of nuclear singlet and triplet states.

The eigenstates of the coherent Hamiltonian change if the chemical equivalence of the two nuclei is broken. As the singlet and triplet states are no longer the true eigenstates of the coherent Hamiltonian, a suitable matrix representation of the coherent Hamiltonian is visualized using the Zeeman product basis. The matrix representation of the coherent Hamiltonian using the Zeeman product basis is:

$$\hat{H}_{\text{coh}}^{ZP} = \begin{array}{c} \\ |\alpha\alpha\rangle \\ |\alpha\beta\rangle \\ |\beta\alpha\rangle \\ |\beta\beta\rangle \end{array} \begin{array}{c} \begin{array}{cccc} \langle\alpha\alpha| & \langle\alpha\beta| & \langle\beta\alpha| & \langle\beta\beta| \end{array} \\ \begin{pmatrix} \frac{\Omega_{\Sigma}^{ij}}{2} + \frac{\pi J}{2} & 0 & 0 & 0 \\ 0 & \frac{\Omega_{\Delta}^{ij}}{2} - \frac{\pi J}{2} & \pi J & 0 \\ 0 & \pi J & -\frac{\Omega_{\Delta}^{ij}}{2} - \frac{\pi J}{2} & 0 \\ 0 & 0 & 0 & -\frac{\Omega_{\Sigma}^{ij}}{2} + \frac{\pi J}{2} \end{pmatrix} \end{array}. \tag{2.51}$$

where $\Omega_{\Delta}^{ij} = \Omega_i - \Omega_j$ and is the difference between resonance offsets for spins i and j. The ladder operators $\hat{I}^+$ and $\hat{I}^-$ contribute to the off-diagonal elements in $\hat{H}_{ZP}$, the presence of which infers that the Zeeman product states are also not exact eigenstates of the coherent Hamiltonian. The parts of the coherent Hamiltonian proportional to $\hat{I}_{iz} + \hat{I}_{iz}$ contribute to the diagonal part of equation 2.51. The matrix representation

of the coherent Hamiltonian is dependent on the level of inequivalence between spins i and j. In the case of significant chemical inequivalence, the off-diagonal components are considerably smaller than the difference in terms which they connect, i.e. $\pi J_{ij} \ll \frac{\Omega_{\Sigma}^{ij}}{2}$. Under the secular approximation, the ladder operators may be omitted from the spin Hamiltonian, and the matrix representation of $\hat{H}_{\text{coh}}$ becomes diagonal. In this regime, the Zeeman product states are *approximate* eigenstates of the $\hat{H}_{\text{coh}}$.

One may convert the matrix representation of the coherent Hamiltonian from the Zeeman product basis to the singlet-triplet basis by using a conversion matrix $\hat{Q}_{PS}$:

$$\hat{Q}_{PS} = \begin{array}{c} \\ |\alpha\alpha\rangle \\ |\alpha\beta\rangle \\ |\beta\alpha\rangle \\ |\beta\beta\rangle \end{array} \begin{array}{c} \begin{array}{cccc} \langle T_{+1}| & \langle S_0| & \langle T_0| & \langle T_{-1}| \end{array} \\ \begin{pmatrix} 1 & 0 & 0 & 0 \\ 0 & \frac{1}{\sqrt{2}} & \frac{1}{\sqrt{2}} & 0 \\ 0 & \frac{-1}{\sqrt{2}} & \frac{1}{\sqrt{2}} & 0 \\ 0 & 0 & 0 & 1 \end{pmatrix} \end{array}. \tag{2.52}$$

$\hat{Q}_{PS}$ converts the representation of an approximate eigenstate $|P\rangle$ written in the Zeeman product basis P into the corresponding approximate eigenstate $|S\rangle$ written in the singlet-triplet basis S:

$$|S\rangle = \hat{Q}_{PS}\,|P\rangle\,. \tag{2.53}$$

Technically the conversion matrix $\hat{Q}_{PS}$ serves as the identity operator, meaning that any physical results are invariant of the chosen basis. An example would be the conversion of the term $\hat{I}_{iz} - \hat{I}_{jz}$. Initially, $\hat{I}_{iz}$ and $\hat{I}_{jz}$ are written in the Zeeman product basis, using natural units, as:

$$\hat{I}_{iz} = |\alpha\alpha\rangle\langle\alpha\alpha| - |\beta\alpha\rangle\langle\beta\alpha| + |\alpha\beta\rangle\langle\alpha\beta| - |\beta\beta\rangle\langle\beta\beta|\,, \tag{2.54}$$

$$\hat{I}_{jz} = |\alpha\alpha\rangle\langle\alpha\alpha| - |\alpha\beta\rangle\langle\alpha\beta| + |\beta\alpha\rangle\langle\beta\alpha| - |\beta\beta\rangle\langle\beta\beta|\,. \tag{2.55}$$

The difference in the $\hat{I}_{iz}$ and $\hat{I}_{jz}$ operators yields:

$$\hat{I}_{iz} - \hat{I}_{jz} = 2(|\alpha\beta\rangle\langle\alpha\beta| - |\beta\alpha\rangle\langle\beta\alpha|). \tag{2.56}$$

Apply the conversion matrix $\hat{Q}_{PS}$ to both components of $\hat{I}_{iz} - \hat{I}_{jz}$:

$$Q_{SP}^{\dagger}\,|\alpha\beta\rangle\langle\alpha\beta|\,Q_{SP} = \frac{1}{2}(|T_0\rangle\langle T_0| + |T_0\rangle\langle S_0| + |S_0\rangle\langle T_0| + |S_0\rangle\langle S_0|\,, \tag{2.57}$$

$$\hat{Q}_{SP}^{\dagger}\left|\beta\alpha\right\rangle\left\langle\beta\alpha\right|\hat{Q}_{SP}=\frac{1}{2}(\left|T_0\right\rangle\left\langle T_0\right|-\left|T_0\right\rangle\left\langle S_0\right|-\left|S_0\right\rangle\left\langle T_0\right|+\left|S_0\right\rangle\left\langle S_0\right|. \tag{2.58}$$

Hence, $\hat{I}_{1z}-\hat{I}_{2z}$ reported in the singlet-triplet basis is:

$$\hat{I}_{iz}-\hat{I}_{jz}=\left|T_0\right\rangle\left\langle S_0\right|+\left|S_0\right\rangle\left\langle T_0\right|. \tag{2.59}$$

After using the conversion matrix $\hat{Q}^{PS}$, one may formalize the coherent Hamiltonian in the singlet-triplet basis. $\hat{H}_{\text{coh}}$ is again decomposed into Zeeman (equation 2.48) and J-coupling (equation 2.45) terms:

$$\hat{H}_Z=\omega_0(\left|T_{+1}\right\rangle\left\langle T_{+1}\right|)-\left|T_{-1}\right\rangle\left\langle T_{-1}\right|), \tag{2.60}$$

$$\begin{aligned}\hat{H}_J=&\frac{\Omega_{\Sigma}^{ij}}{2}(\left|T_{+1}\right\rangle\left\langle T_{+1}\right|)-\left|T_{-1}\right\rangle\left\langle T_{-1}\right|)+\frac{\Omega_{\Delta}^{ij}}{2}(\left|T_0\right\rangle\left\langle S_0\right|)+\left|S_0\right\rangle\left\langle T_0\right|)\\&+\frac{1}{2}\pi J(\left|T_{+1}\right\rangle\left\langle T_{+1}\right|+\left|T_0\right\rangle\left\langle T_0\right|+\left|T_{-1}\right\rangle\left\langle T_{-1}\right|)-\frac{3}{2}\pi J(\left|S_0\right\rangle\left\langle S_0\right|).\end{aligned} \tag{2.61}$$

The singlet-triplet basis matrix representation of the coherent Hamiltonian is therefore:

$$\hat{H}_{\text{coh}}^{ST}=\begin{array}{c}\\ \left|S_0\right\rangle\\ \left|T_{+1}\right\rangle\\ \left|T_0\right\rangle\\ \left|T_{-1}\right\rangle\end{array}\begin{array}{c}\begin{array}{cccc}\left\langle S_0\right| & \left\langle T_{+1}\right| & \left\langle T_0\right| & \left\langle T_{-1}\right|\end{array}\\ \begin{pmatrix}\frac{-3\pi J_{ij}}{2} & 0 & \frac{\Omega_{\Delta}^{ij}}{2} & 0\\ 0 & \frac{\Omega_{\Sigma}^{ij}}{2}+\frac{\pi J_{ij}}{2} & 0 & 0\\ \frac{\Omega_{\Delta}^{ij}}{2} & 0 & \frac{\pi J_{ij}}{2} & 0\\ 0 & 0 & 0 & -\frac{\Omega_{\Sigma}^{ij}}{2}+\frac{\pi J_{ij}}{2}\end{pmatrix}\end{array}. \tag{2.62}$$

In the case of slight chemical inequivalence between nuclei i and j, i.e. $\pi J_{ij}\gg\frac{\Omega_{\Delta}^{ij}}{2}$, the presence of the off-diagonal terms $\frac{\Omega_{\Delta}^{ij}}{2}$ connects states spanning different manifolds of exchange-symmetry and allows weakly allowed transitions between the nuclear singlet and triplet states. These weakly allowed transitions are selectively pumped via carefully calibrated rf-pulse sequences, and are the point of access to the nuclear singlet order from the rapidly relaxing triplet states $\left|T_{m_I}\right\rangle$. The size of the chemical shift difference dictates the parameters of the singlet NMR pulse sequences, as described at the end of this chapter. The importance of the term $\frac{\Omega_{\Sigma}^{ij}}{2}$ may be mediated by external influences such as shuttling the sample to regions of low magnetic field [14], using strong continuous wave rf-irradiation [15, 149] or by employing chemical reactions [21, 55, 143]. Due to the immunity of the nuclear singlet order to the exchange-symmetric in pair dipole-dipole interaction, the interconversion between nuclear singlet and triplet states can often occur slowly i.e. with low probability. If the long-lived nuclear spin order is accessible via a

small chemical shift difference, the opportunity to encode information for times exceeding those provided by ordinary magnetization is possible [24].

In order to finish this section, I will attend to the case of two chemically equivalent spin-1/2 nuclei with inequivalent scalar couplings to other spins outside of the singlet pair. This regime is relevant for accessing the nuclear singlet order at low magnetic field [16] and in symmetric spin systems [21, 31, 160]. Consider the case of a chemically equivalent spin-1/2 pair with an in pair scalar coupling denoted J_{ij}. Now introduce a third magnetic nucleus (spin k, $I = 1/2$) to the spin system. The scalar couplings from the singlet spins i and j to the exterior nucleus are denoted J_{ik} and J_{ik}, with $J_{ik} \neq J_{jk}$. The coherent Hamiltonian $\hat{H}^{ijk}_{\text{coh}}$ is therefore written as:

$$\hat{H}^{ijk}_{\text{coh}} = 2\pi J_{ij}\hat{I}_i \cdot \hat{I}_j + 2\pi J_{ik}\hat{I}_{iz} \cdot \hat{I}_{kz} + 2\pi J_{jk}\hat{I}_{jz} \cdot \hat{I}_{kz}, \tag{2.63}$$

where the weak-coupling approximation has been used for the scalar couplings between spins i,j and spin k. The matrix representation of $\hat{H}^{ijk}_{\text{coh}}$ expressed in the following basis:

$$\mathbb{B}^{ijk} = \mathbb{B}^{ij}_{ST} \otimes \mathbb{B}^{k}_{ZP}, \tag{2.64}$$

where $\mathbb{B}^{N}_{M}$ represents the kets for the group of spins N in the eigenbasis M, is:

$$\hat{H}^{ST}_{\text{coh}} = \begin{array}{c} \\ |S_0\rangle \\ |T_{-1}\rangle \\ |T_0\rangle \\ |T_{+1}\rangle \end{array} \begin{array}{c} \begin{array}{cccc} \langle S_0| & \langle T_{-1}| & \langle T_0| & \langle T_{+1}| \end{array} \\ \begin{pmatrix} \frac{-3\pi J_{ij}}{2} & 0 & \frac{\pi J^{ijk}_{\Delta}}{2} & 0 \\ 0 & -\pi\frac{J^{ijk}_{\Sigma}}{2} + \frac{\pi J_{ij}}{2} & 0 & 0 \\ \frac{\pi J^{ijk}_{\Delta}}{2} & 0 & \frac{\pi J_{ij}}{2} & 0 \\ 0 & 0 & 0 & \pi\frac{J^{ijk}_{\Sigma}}{2} + \frac{\pi J_{ij}}{2} \end{pmatrix} \end{array}, \tag{2.65}$$

where $J^{ijk}_{\Delta} = J_{ik} - J_{jk}$, and $J^{ijk}_{\Sigma} = J_{ik} + J_{jk}$. The matrix representation of $\hat{H}^{ijk}_{\text{coh}}$ is presented in a subspace which contains the relevant spin dynamics, i.e. the kets corresponds to only $\mathbb{B}^{ij}_{ST} \otimes |\alpha\rangle^{k}_{ZP}$. The $|S_0\rangle$ and $|T_0\rangle$ states (singlet-triplet basis of spins i and j) are connected by the off-diagonal term $\frac{\pi J^{ijk}_{\Delta}}{2}$, and hence weakly allowed transitions are allowed between the $|S_0\rangle$ and $|T_0\rangle$ states. Even in the case of chemical equivalence, the term $\frac{\pi J^{ijk}_{\Delta}}{2}$ breaks the symmetry of the spin system and therefore provides the access route for polarization transfer between the two manifolds of differing exchange-symmetry. In cases where differential out-of-pair J-couplings are present, the singlet-triplet population imbalance may be probed for molecules with chemically equivalent spin-1/2 pairs.

2.10 Singlet polarization

Singlet NMR remains limited by the low polarization available from experiments performed at room temperature. Hyperpolarizable molecules with built-in long-lived states offer a promising gateway to alleviate such sensitivity issues, see chapter 4 for more details [147]. As with many hyperpolarization experiments, it is useful to quantify the level of nuclear Zeeman polarization reached as a result of the hyperpolarization process, see section 2.3. In the case of hyperpolarized singlet experiments, one may also desire to know the amount of nuclear singlet order contained within the spin density operator. At this point, it is useful to introduce the concept of *singlet polarization*. The singlet polarization p_{S} is the projection of the spin density operator $\hat{\rho}$ onto the operator $\hat{P}_{\mathrm{S}}$ (see appendix B for more details):

$$p_{\mathrm{S}} = \frac{\mathrm{Tr}[\hat{P}_{\mathrm{S}}^{\dagger}\hat{\rho}]}{\mathrm{Tr}[\hat{P}_{\mathrm{S}}^{\dagger}\hat{P}_{\mathrm{S}}]}, \tag{2.66}$$

where $\hat{P}_{\mathrm{S}}$ is the singlet polarization operator and is defined as:

$$\hat{P}_{\mathrm{S}} = \frac{3}{4}\hat{Q}_{\mathrm{SO}} = -\hat{I}_i \cdot \hat{I}_j = \sqrt{3}\,\hat{T}_{00}^{ij}. \tag{2.67}$$

The singlet polarization p_{S} is normalized to ensure that the maximum singlet-triplet population difference is +1, i.e. the singlet state $|S_0\rangle$ is entirely populated whilst the triplet manifold is fully depleted of population. In the opposite case, i.e. complete population of the triplet states $|T_{m_I}\rangle$, the singlet polarization p_{S} is -1/3. The bounds on the nuclear singlet polarization are therefore: $-1/3 < p_{\mathrm{S}} < +1$.

As is often the case in DNP experiments, the experimental desire is to shuttle the maximal amount of spin population to the $m_I = \pm 1$ nuclear triplet states, depending on the offset frequency of the applied microwaves. In this way, the maximum population difference, and hence singlet polarization, is accrued between the spin-0 and spin-1 manifolds. The maximum Zeeman polarization between the $m_I = \pm 1$ nuclear triplet states is established simultaneously. Estimates of the nuclear Zeeman polarization are easily obtainable, and can be used to provide the level of nuclear singlet polarization. Consider an ensemble of non-interacting, inequivalent spin-1/2 pairs (i and j) in the solid-state, the eigenstates of the coherent Hamiltonian at high magnetic field are given by the Zeeman product states. The populations of the Zeeman product states $p(\psi_i\psi_j)$

are combinations of the populations p_i and p_j for each spin:

$$p(\alpha_i\alpha_j) = (1+p_i)(1+p_j)/4, \quad (2.68)$$

$$p(\alpha_i\beta_j) = (1+p_i)(1-p_j)/4, \quad (2.69)$$

$$p(\beta_i\alpha_j) = (1-p_i)(1+p_j)/4, \quad (2.70)$$

$$p(\beta_i\beta_j) = (1-p_i)(1-p_j)/4, \quad (2.71)$$

where the factor of $1/4$ is included to ensure that: $p(\alpha_i\alpha_j)+p(\alpha_i\beta_j)+p(\beta_i\alpha_j)+p(\beta_i\beta_j) = 1$, i.e. the maximum polarization of the outer $|\alpha_i\alpha_j\rangle$ and $|\beta_i\beta_j\rangle$ states is ± 1. Assuming that the spins i and j are equally polarized by DNP at low temperatures: $p_i = p_j = p_{\mathrm{Z}}$, where p_{Z} is the Zeeman polarization of an individual nucleus and is orders of magnitude greater than the thermal equilibrium polarization. The nuclear Zeeman product state populations may therefore be rewritten as:

$$p(\alpha_i\alpha_j) = (1+2p_Z+p_{\mathrm{Z}}^2)/4, \quad (2.72)$$

$$p(\alpha_i\beta_j) = (1-p_{\mathrm{Z}}^2)/4, \quad (2.73)$$

$$p(\beta_i\alpha_j) = (1-p_{\mathrm{Z}}^2)/4, \quad (2.74)$$

$$p(\beta_i\beta_j) = (1-2p_Z+p_{\mathrm{Z}}^2)/4. \quad (2.75)$$

Consider the sequence of events during the *dissolution*-DNP process. After the microwaves are halted the solid mixture of sample, radical and glassy matrix is rapidly dissolved by a jet of superheated solvent before being adiabatically transferred to a high resolution NMR magnet in $\sim$10 s. If the sample of interest contains a pair of *nearly equivalent* spins-1/2 (i and j) satisfying the condition: $\Omega_{\Delta}^{ij} \ll J_{ij}$ for $J_{ij},\gamma_{i,j} > 0$, the liquid-state eigenstates of the coherent Hamiltonian at high magnetic field may be approximated by the nuclear singlet and triplet states:

$$p(\alpha_i\alpha_j) \rightarrow p(T_{+1}), \quad (2.76)$$

$$p(\alpha_i\beta_j) \rightarrow p(S_0), \quad (2.77)$$

$$p(\beta_i\alpha_j) \rightarrow p(T_0), \quad (2.78)$$

$$p(\beta_i\beta_j) \rightarrow p(T_{-1}). \quad (2.79)$$

The singlet polarization, defined by using the singlet polarization operator P_{S} in equation 2.67, is the normalized population difference across the singlet S_0 and triplet T_{m_I} manifolds:

$$p_{\mathrm{S}} = p(S_0) - \frac{(p(T_{+1}) + p(T_0) + p(T_{-1}))}{3}. \tag{2.80}$$

Inserting expressions from equations 2.72-2.79 into equation 2.80 yields a singlet polarization which is dependent on the nuclear Zeeman polarization. The singlet polarization p_{S} as a function of the nuclear Zeeman polarization p_{Z} is therefore:

$$p_{\mathrm{S}} = -\frac{p_{\mathrm{Z}}^2}{3}. \tag{2.81}$$

In the case that DNP succeeds in a total population of the $|T_{\pm 1}\rangle$ states, i.e. $p_{\mathrm{Z}}{=}\pm 1$, the corresponding singlet polarization is -1/3. The negative sign of the singlet polarization indicates a complete depletion of population from the $m_I = 0$ state, and hence a population deficit for the singlet state. Strong nuclear Zeeman polarization is therefore always accompanied by a strong singlet polarization for an ensemble of strongly coupled spin-1/2 pairs. As shown in chapter 4, the hyperpolarized singlet order has the potential to remain observable at long times after initially being polarized, in which time the hyperpolarized spin order available from the nuclear Zeeman polarization has decayed to thermal equilibrium with the characteristic time constant T_1.

2.11 Singlet methods

In the previous section, the fundamental properties of the nuclear singlet and triplet states for 2-spin-1/2 systems were presented. Nuclear singlet order, defined as the population imbalance between the two manifolds of differing exchange symmetry, was shown to be immune to relaxation from the in pair dipole-dipole coupling. Long-lived states were consequently proposed as a means to overcome the limited signal lifetimes available from longitudinal magnetization, and extraordinary singlet lifetimes far exceeding T_1 have previously been observed in a range of molecular systems [29, 33, 35]. Singlet order is a magnetically silent arrangement of spin isomers, and is undetectable in conventional NMR experiments. In order to access the long-lived spin order, alternative pulse sequences which interconvert population between the singlet and triplet manifolds are required. In this section, I discuss the two favoured pulse sequences for the preparation of nuclear singlet order, continuing the matrix representation formalism of the coherent Hamiltonian from section 2.9. The singlet-triplet conversion schemes used in this thesis are the spin-lock induced crossing (SLIC) and magnetization-to-singlet (M2S) pulse sequences. Each pulsed method contains inherent advantages and disadvantages, but are both efficient in creating strong population imbalances for spin-1/2 pairs.

2.11.1 Signal detection for spin-1/2 pairs

Before contemplating the pulse sequences used to observe and manipulate the nuclear singlet order, I would like to first recognize the effects that the NMR silent property of the nuclear singlet state has on the detection of ordinary magnetization. Consider a single spin i (I=1/2, $\gamma_i > 0$) in high magnetic field. Using Dirac notation, the quantum state of the system is represented by the ket vector $|I, m_I\rangle$, where I is the angular momentum quantum number and m_I is the spin projection quantum number. As discussed in chapter 1, the Zeeman effect lifts the degeneracy of the states $|I, m_I\rangle$ for a particle in a magnetic field and reveals a substructure identified by quantum numbers $m_I = -I, ..., +I$. In this case, the values of m_I are $\pm 1/2$, and the eigenvalues of the $\hat{I}_{iz}$ operator are $\hbar/2$ and $-\hbar/2$, respectively. In quantum mechanics, the ladder operators raise or lower the eigenvalues of another operator by the quantity $\hbar$. The raising $\hat{I}_i^+$ and

lowering $\hat{I}_i^-$ operators are defined as:

$$\hat{I}_i^+ \left|I, m_I\right\rangle = \hbar\sqrt{I(I+1) - m_I(m_I+1)}\left|I, m_I+1\right\rangle, \tag{2.82}$$

$$\hat{I}_i^- \left|I, m_I\right\rangle = \hbar\sqrt{I(I+1) - m_I(m_I-1)}\left|I, m_I-1\right\rangle. \tag{2.83}$$

The action of the operator $\hat{I}_i^+$ on the ket $|I, m_I\rangle$ raises the value of m_I to $m_I + 1$, corresponding to a state-to-state transition from $|I, m_I\rangle$ to $|I, m_I + 1\rangle$. The transition element $\langle I, m_I + 1| \hat{I}_i^+ |I, m_I\rangle$ for a lone spin-1/2 nucleus gives a coherence amplitude of $\hbar$, and hence the ladder operators for an individual spin-1/2 nucleus have the following matrix representations:

$$\hat{I}_i^+ = \begin{array}{c} \\ |\alpha\rangle \\ |\beta\rangle \end{array} \begin{array}{c} \begin{array}{cc} \langle\alpha| & \langle\beta| \end{array} \\ \begin{pmatrix} 0 & 1 \\ 0 & 0 \end{pmatrix} \end{array} \;\&\; \hat{I}_i^- = \begin{array}{c} \\ |\alpha\rangle \\ |\beta\rangle \end{array} \begin{array}{c} \begin{array}{cc} \langle\alpha| & \langle\beta| \end{array} \\ \begin{pmatrix} 0 & 0 \\ 1 & 0 \end{pmatrix} \end{array}. \tag{2.84}$$

Now consider a pair of spins i and j in high magnetic field. Assume that the two spins: 1. both have an angular momentum quantum number $I = 1/2$; 2. are heteronuclear; and 3. are chemically inequivalent ($\Omega_\Delta^{ij} \gg 0$). In this case, the eigenstates of the coherent Hamiltonian are given by the Zeeman product state states, see equation 2.14. It can be shown, by similar methods, that the matrix representation of the raising $\hat{I}_{ij}^+$ and lowering $\hat{I}_{ij}^-$ operators are:

$$\hat{I}_{ij}^+ = \begin{array}{c} \\ |\alpha\alpha\rangle \\ |\alpha\beta\rangle \\ |\beta\alpha\rangle \\ |\beta\beta\rangle \end{array} \begin{array}{c} \begin{array}{cccc} \langle\alpha\alpha| & \langle\alpha\beta| & \langle\beta\alpha| & \langle\beta\beta| \end{array} \\ \begin{pmatrix} 0 & 1 & 1 & 0 \\ 0 & 0 & 0 & 1 \\ 0 & 0 & 0 & 1 \\ 0 & 0 & 0 & 0 \end{pmatrix} \end{array} \;\&\; \hat{I}_{ij}^- = \begin{array}{c} \\ |\alpha\alpha\rangle \\ |\alpha\beta\rangle \\ |\beta\alpha\rangle \\ |\beta\beta\rangle \end{array} \begin{array}{c} \begin{array}{cccc} \langle\alpha\alpha| & \langle\alpha\beta| & \langle\beta\alpha| & \langle\beta\beta| \end{array} \\ \begin{pmatrix} 0 & 0 & 0 & 0 \\ 1 & 0 & 0 & 0 \\ 1 & 0 & 0 & 0 \\ 0 & 1 & 1 & 0 \end{pmatrix} \end{array}. \tag{2.85}$$

The matrices are represented using the same ordering of the Zeeman product basis as in equation 2.51. A typical pulse-acquire experiment probes single quantum (-1) transitions between spin states separated by the nuclear Larmor frequency. There are four single quantum (-1) transitions for a chemically inequivalent spin-1/2 pair, as shown in figure 1.10. The NMR signal intensity from the spins in the sample S_{sample} is proportional to the trace of the spin density operator $\hat{\rho}$ projected upon the lowering operator

$\hat{I}_{ij}^{-}$:

$$S_{sample} \propto \frac{\mathrm{Tr}[\hat{\rho}\hat{I}_{ij}^{-}]}{\mathrm{Tr}[\hat{I}_{ij}^{-}(\hat{I}_{ij}^{-})^{\dagger}]}, \tag{2.86}$$

where the inner product selects the relevant components of $\hat{\rho}$. A $(\pi/2)_{-y}$ pulse tilts the magnetization vector, originally aligned with static magnetic field, into the x-axis of the rotating frame. The spin density operator $\hat{\rho}$ transforms as follows: $\hat{\mathbb{1}} + \hat{I}_{iz} + \hat{I}_{jz} \rightarrow \hat{\mathbb{1}} + \hat{I}_{ix} + \hat{I}_{jx}$. In the Zeeman product basis, the matrix representation of the operator $\hat{I}_{ix} + \hat{I}_{jx}$ is:

$$\hat{I}_{ix} + \hat{I}_{jx} = \begin{array}{c} \\ |\alpha\alpha\rangle \\ |\alpha\beta\rangle \\ |\beta\alpha\rangle \\ |\beta\beta\rangle \end{array} \begin{array}{c} \begin{array}{cccc} \langle\alpha\alpha| & \langle\alpha\beta| & \langle\beta\alpha| & \langle\beta\beta| \end{array} \\ \begin{pmatrix} 0 & \frac{1}{\sqrt{2}} & \frac{1}{\sqrt{2}} & 0 \\ \frac{1}{\sqrt{2}} & 0 & 0 & \frac{1}{\sqrt{2}} \\ \frac{1}{\sqrt{2}} & 0 & 0 & \frac{1}{\sqrt{2}} \\ 0 & \frac{1}{\sqrt{2}} & \frac{1}{\sqrt{2}} & 0 \end{pmatrix} \end{array}. \tag{2.87}$$

By using equation 2.86, and the matrix representations of the operators $\hat{I}_{ij}^{-}$ and $\hat{I}_{ix}+\hat{I}_{jx}$, the signal intensity is determined to be: $S_{sample} \propto \frac{\hbar^2}{\sqrt{2}}$.

Now consider a second pair of spins i and j in high magnetic field, and assume the two are magnetically equivalent ($\Omega_{\Delta}^{ij} = 0$). In this case, the eigenstates of the coherent Hamiltonian are given by the nuclear singlet and triplet states. An example of the energy level structure for a pair of magnetically equivalent spins is shown in figure 2.12. For a magnetically equivalent spin system, only single quantum triplet-triplet transitions are relevant. No directly observable transitions occur between states with differing values of m_I. In order to make a direct comparison with the case of chemically inequivalent spin pairs the operators $\hat{I}_{ij}^{-}$ and $\hat{I}_{ix} + \hat{I}_{jx}$ require transformation into the singlet-triplet basis, which can be achieved using the transformation matrix in equation 2.52. The resulting operator matrix representations are as follows:

$$\hat{I}_{ij}^{-} = \begin{array}{c} \\ \langle S_0| \\ \langle T_{+1}| \\ \langle T_0| \\ \langle T_{-1}| \end{array} \begin{array}{c} \begin{array}{cccc} \langle S_0| & \langle T_{+1}| & \langle T_0| & \langle T_{-1}| \end{array} \\ \begin{pmatrix} 0 & 0 & 0 & 0 \\ 0 & 0 & 1 & 0 \\ 0 & 1 & 0 & 1 \\ 0 & 0 & 1 & 0 \end{pmatrix} \end{array} \quad \& \quad \hat{I}_{ix} + \hat{I}_{jx} = \begin{array}{c} \\ \langle S_0| \\ \langle T_{+1}| \\ \langle T_0| \\ \langle T_{-1}| \end{array} \begin{array}{c} \begin{array}{cccc} \langle S_0| & \langle T_{+1}| & \langle T_0| & \langle T_{-1}| \end{array} \\ \begin{pmatrix} 0 & 0 & 0 & 0 \\ 0 & 0 & 0 & 0 \\ 0 & \sqrt{2} & 0 & 0 \\ 0 & 0 & \sqrt{2} & 0 \end{pmatrix} \end{array}. \tag{2.88}$$

The matrices are represented using the same ordering of the singlet-triplet basis as in equation 2.46. Evaluating equation 2.86 in the singlet-triplet basis also returns

a signal intensity: $S_{sample} \propto \frac{\hbar^2}{\sqrt{2}}$. A notable outcome of this result are the identical signal intensities S_{sample} for different regimes of chemical and magnetic inequivalence, which is hardly surprising as the signal at time $t = 0$ does not depend on the form of the coherent Hamiltonian. It is interesting to note that in the singlet-triplet basis $\sim$75% of the spin ensemble are in states corresponding to $|T_{m_I}\rangle$, and hence $\sim$25% of the total population cannot undergo observable transitions with other $|T_{m_I}\rangle$ states. The operators $\hat{I}_{ij}^-$ and $\hat{I}_{ix} + \hat{I}_{jx}$ have matrix representations which are dependent on the chosen orthonormal basis, whilst the scalar $\mathrm{Tr}[\hat{\rho}\hat{I}_{ij}^-]$ is basis independent. These results demonstrate the robustness of detecting ordinary magnetization in regimes of magnetic equivalence, as the calculated signal intensity is not compromised by having $\sim$25% of the total population residing in the unobservable spin-0 state.

2.11.2 Singlet NMR experiments

The state of a nuclear ensemble, neatly represented by the spin density operator $\hat{\rho}$, evolves over time in accordance with the manipulations imposed on the closed system by the spectroscoper, the internal (J-couplings, chemical shifts etc.) and external (static magnetic field $\vec{B}_0$) interactions present throughout the experiment, and spin relaxation (the nuclear ensemble returning to thermal equilibrium). The spin density operator can additionally be engineered by the design of a suitable coherent Hamiltonian to attain a desired form of spin order. A typical singlet NMR experiment consists of three main parts:

1. **Prepare.** What is the state to be prepared? The pulse sequence employed in an NMR experiment ultimately depends on the target state of the spectroscoper. There are likely alternative methods of preparing the same state but the method of preparation is ultimately limited by the entities of interest.

2. **Evolve.** Once the state of choice has been prepared, time evolution is an advantageous tool for determining the relaxation properties of particular spin orders. The simplest examples are the inversion and saturation recovery experiments used to investigate the longitudinal relaxation time T_1.

3. **Reconvert.** The detection state of all NMR experiments is the same, and regardless of how the chosen state was prepared and consequently evolved, the detection

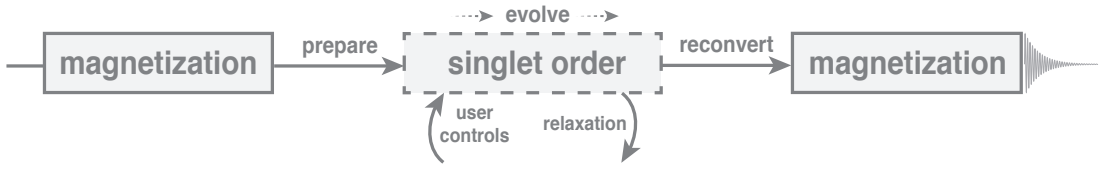

FIGURE 2.13: The three crucial stages of a singlet NMR experiment. Prepare: the spin system is engaged by incoming pulses from the spectrometer which encode the original magnetization as a more preferential form of spin order where relevant information is consequently stored. Evolve: the newly established spin order is propagated forward in time under the influence of coherent effects (including user defined control such as continuous wave rf-fields and pulsed field gradients) and incoherent relaxation phenomena. Reconvert: NMR experiment detect physical observables, such as the $\hat{I}^-$ operator, and as such reconversion to observable magnetization is required for monitoring the evolution and relaxation of the established spin order.

state must correspond to a physical observable. In this respect, singlet pulse sequences are often symmetric about the evolution period.

Each basic stage is depicted graphically, and in chronological order, in figure 2.13. Importantly, the preparation stage requires the ensemble to be placed in a magnetic field $\vec{B}_0$, which creates a small, but observable, population imbalance between nuclear spin states once thermal equilibrium is reached. The longitudinal magnetization obtainable from this process acts as the starting point for the preparation procedure to come [166, 167]. The preparation and detection stages of singlet NMR experiments will be the main points of focus in this section.

2.12 Spin-lock induced crossing

The spin-lock induced crossing (SLIC) pulse sequence has been the preferred method of accessing nuclear singlet order in this work. The approach was first developed by Rosen and coworkers in 2013 [157], and uses the small chemical shift difference between spin-1/2 nuclei to access to the long-lived singlet order. Other variants, such as the adiabatic SLIC [158, 159], also exist and achieve efficient triplet-singlet population interconversion. A schematic of the spin-lock induced crossing (SLIC) pulse sequence is illustrated in figure 2.14.

This SLIC pulse sequence operates as follows: after the initial 90° pulse, a radiofrequency field is applied with a 90° phase shift. The amplitude of this field is selected

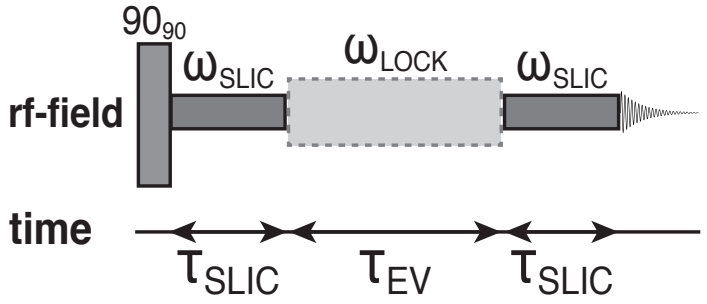

FIGURE 2.14: The spin lock induced crossing (SLIC) pulse sequence used for accessing the long-lived singlet order in near-equivalent pairs of spin-1/2 nuclei and measuring its resulting decay.

so that the nutation frequency $\omega_{\mathrm{SLIC}}/2\pi$ matches the J-coupling J_{ij}. This establishes a resonance which causes the spin-locked magnetization to be converted into nuclear singlet order through the action of the chemical shift difference, with the conversion complete in a time τ_{SLIC}, neglecting relaxation and other complications [157]. The dependence of τ_{SLIC} on the chemical shift difference Ω_{Δ}^{ij} is explored later. The preparation stage of the SLIC pulse sequence excites the maximum obtainable nuclear singlet order, in the case that the conversion rate is fast compared to relaxation. The nuclear singlet order is allowed to evolve for a variable interval τ_{EV}, occasionally in the presence of a larger-amplitude "spin-locking" rf field (nutation frequency $\omega_{\mathrm{LOCK}}/2\pi$), which suppresses singlet-triplet mixing [149]. A second SLIC pulse sequence converts the nuclear singlet order into transverse magnetization, and the induced NMR signal is detected, see figure 2.14. The decay of the long-lived nuclear singlet order is tracked by repeating the pulse sequence with different values of the singlet evolution interval τ_{EV}.

2.12.1 SLIC experiment for inequivalent spin-1/2 pairs

It is possible to examine the effects of a weak, transverse field applied to a spin-1/2 nuclear pair i and j. In such cases, the offset frequency of the weak rf-field is assumed to be equal to the mean resonance position of the two nuclei, i.e. $(\Omega_i + \Omega_j)/2$. In this section, it is convenient to define the basis using linear combinations of the Zeeman

product states:

$$|\phi_S\rangle = \cos(\frac{\theta_{ij}}{2})\,|\alpha\beta\rangle - \sin(\frac{\theta_{ij}}{2})\,|\beta\alpha\rangle\,, \tag{2.89}$$

$$|T_{-1}\rangle = |\beta\beta\rangle\,, \tag{2.90}$$

$$|\phi_T\rangle = \sin(\frac{\theta_{ij}}{2})\,|\alpha\beta\rangle + \cos(\frac{\theta_{ij}}{2})\,|\beta\alpha\rangle\,, \tag{2.91}$$

$$|T_{+1}\rangle = |\alpha\alpha\rangle\,, \tag{2.92}$$

where θ_{ij} is the arctangent of $2\pi J_{ij}/\Omega^{ij}_{\Delta}$, see equation 1.15. Only the m_I=0 states ($|\phi_S\rangle$ and $|\phi_T\rangle$) are connected via J_{ij} and can become mixed. As the mixing angle $\theta_{ij} \rightarrow \pi/2$ (regime of chemical equivalence) the nuclear singlet and triplet states become eigenstates of the coherent Hamiltonian $\hat{H}_{\text{coh}}$, and equations 2.15-2.18 are returned. In order to understand how the application of a weak, transverse field can lead to the augmentation of nuclear singlet order, I revisit the matrix representation of the coherent Hamiltonian $\hat{H}_{\text{coh}}$ at high magnetic field. In the case of slight chemical inequivalence between the two nuclei i and j, i.e. $\pi J_{ij} \gg \frac{\Omega^{ij}_{\Delta}}{2}$, the approximate eigenbasis for an ensemble of non-interacting spin-1/2 pairs is the singlet-triplet basis ($\theta_{ij} \lesssim \pi/2$). A transformation into the rotating frame simplifies the matrix representation of $\hat{H}^{ST}_{\text{coh}}$ as terms on the order of the nuclear Larmor frequency are removed. Diagonalization of $\hat{H}^{ST}_{\text{coh}}$ gives the eigenvalues in equations 1.17-1.21, and the corresponding matrix representation of $\hat{H}^{ST}_{\text{coh}}$ is shown in equation 2.62.

A low amplitude spin-locking field $\omega^{ij}_{\text{SLIC}}$ is applied at the average resonance frequency of the two nuclei $(\Omega_i + \Omega_j)/2$ creating off-diagonal terms which connect the three I=1 nuclear triplet states, i.e. the spin-locking pulse is applied on resonance with the triplet transitions. The I=0 nuclear singlet state remains disconnected from the triplet manifold, as only single-quantum triplet-triplet transitions are allowed. The coherent Hamiltonian in the presence of weak rf-irradiation $\hat{H}^{ST}_{\text{coh,rf}}$ is:

$$\hat{H}_{\text{coh,rf}} = \frac{\Omega^{ij}_{\Sigma}}{2}(\hat{I}_{iz} + \hat{I}_{jz}) + \frac{\Omega^{ij}_{\Delta}}{2}(\hat{I}_{iz} - \hat{I}_{jz}) + 2\pi J_{ij}\hat{I}_i \cdot \hat{I}_j + \omega^{ij}_{\text{SLIC}}(\hat{I}_{ix} + \hat{I}_{jx}), \tag{2.93}$$

and has the following matrix representation in the singlet-triplet eigenbasis:

$$\hat{H}^{ST}_{\text{coh,rf}} = \begin{array}{c} \\ |\phi_S\rangle \\ |T_{-1}\rangle \\ |\phi_T\rangle \\ |T_{+1}\rangle \end{array} \begin{array}{c} \begin{array}{cccc} \langle\phi_S| & \langle T_{-1}| & \langle\phi_T| & \langle T_{+1}| \end{array} \\ \begin{pmatrix} \frac{-3\pi J_{ij}}{2} & 0 & \frac{\Omega^{ij}_{\Delta}}{2} & 0 \\ 0 & \frac{\pi J_{ij}}{2} & \frac{\omega^{ij}_{\text{SLIC}}}{\sqrt{2}} & 0 \\ \frac{\Omega^{ij}_{\Delta}}{2} & \frac{\omega^{ij}_{\text{SLIC}}}{\sqrt{2}} & \frac{\pi J_{ij}}{2} & \frac{\omega^{ij}_{\text{SLIC}}}{\sqrt{2}} \\ 0 & 0 & \frac{\omega^{ij}_{\text{SLIC}}}{\sqrt{2}} & \frac{\pi J_{ij}}{2} \end{pmatrix} \end{array}, \tag{2.94}$$

where $\omega^{ij}_{\text{SLIC}}$ is the nutation frequency of the applied SLIC pulse. The off-diagonal terms are proportional to $\omega^{ij}_{\text{SLIC}}$ and Ω^{ij}_{Δ} with:

$$\Omega^{ij}_{\Delta} = \Omega_i - \Omega_j. \tag{2.95}$$

The duration of the SLIC pulse is typically on the order of milliseconds to seconds. Such pulse durations are approximately on the timescale of the spin system evolution controlled by the in pair scalar coupling J_{ij} and the chemical shift difference Ω^{ij}_{Δ}. Assuming a small but non-zero in pair scalar coupling, and a long spin-locking time relative to the nuclear Larmor period, allows the coherent Hamiltonian can be diagonalized for a second time. The diagonalized matrix representation of $\hat{H}^{ST}_{\text{coh,rf}}$ is:

$$\hat{H}^{ST}_{\text{coh,rf}} = \begin{array}{c} \\ |S_0\rangle \\ |\psi_{-1}\rangle \\ |\psi_0\rangle \\ |\psi_{+1}\rangle \end{array} \begin{array}{c} \begin{array}{cccc} \langle S_0| & |\psi_{-1}\rangle & |\psi_0\rangle & |\psi_{+1}\rangle \end{array} \\ \begin{pmatrix} \frac{-3\pi J_{ij}}{2} & \frac{\Omega^{ij}_{\Delta}}{2\sqrt{2}} & 0 & -\frac{\Omega^{ij}_{\Delta}}{2\sqrt{2}} \\ \frac{\Omega^{ij}_{\Delta}}{2\sqrt{2}} & \frac{\pi J_{ij}}{2} - \omega_{\text{SLIC}} & 0 & 0 \\ 0 & 0 & \frac{\pi J_{ij}}{2} & 0 \\ -\frac{\Omega^{ij}_{\Delta}}{2\sqrt{2}} & 0 & 0 & \frac{\pi J_{ij}}{2} + \omega_{\text{SLIC}} \end{pmatrix} \end{array}. \tag{2.96}$$

In the presence of continuous wave (CW) irradiation the mixing angle θ_{ij} is replaced by θ_{rf} (see appendix B for more details) and the mixing between the nuclear singlet and triplet states is governed by the nutation frequency of the CW pulse ω_{CW}:

$$\tan(\theta_{rf}) = \frac{2\omega_{\text{CW}}}{\Omega^{ij}_{\Delta}}. \tag{2.97}$$

Diagonalization of the coherent Hamiltonian $\hat{H}^{ST}_{\text{coh,rf}}$ provides four "SLIC" eigenstates:

$$|S_0\rangle = \frac{1}{\sqrt{2}}[\sqrt{2}\sin(\theta_{rf})\,|S_0\rangle - \cos(\theta_{rf})(|T_{+1}\rangle + |T_{-1}\rangle)], \tag{2.98}$$

$$|\psi_{-1}\rangle = \frac{1}{2}[\sqrt{2}\,|T_0\rangle - \sin(\theta_{rf})(|T_{+1}\rangle + |T_{-1}\rangle) - \sqrt{2}\cos(\theta_{rf})\,|S_0\rangle], \tag{2.99}$$

$$|\psi_0\rangle = \frac{1}{\sqrt{2}}(|T_{+1}\rangle - |T_{-1}\rangle), \tag{2.100}$$

$$|\psi_{+1}\rangle = \frac{1}{2}[\sqrt{2}\,|T_0\rangle + \sin(\theta_{rf})(|T_{+1}\rangle + |T_{-1}\rangle) + \sqrt{2}\cos(\theta_{rf})\,|S_0\rangle]. \tag{2.101}$$

In the limit of strong CW irradiation, i.e. $\omega_{\text{CW}} \gg \Omega^{ij}_{\Delta}$, the angle $\theta_{rf} \to \pi/2$, and the SLIC eigenstates are consequently simplified to:

$$|S_0\rangle = |S_0\rangle\,, \tag{2.102}$$

$$|\psi_{-1}\rangle = \frac{1}{2}(|T_{-1}\rangle + |T_{+1}\rangle) - \frac{1}{\sqrt{2}}\,|T_0\rangle\,, \tag{2.103}$$

$$|\psi_0\rangle = \frac{1}{\sqrt{2}}(|T_{+1}\rangle - |T_{-1}\rangle), \tag{2.104}$$

$$|\psi_{+1}\rangle = \frac{1}{2}(|T_{-1}\rangle + |T_{+1}\rangle) + \frac{1}{\sqrt{2}}\,|T_0\rangle\,, \tag{2.105}$$

which is the eigenbasis of the operator $\hat{I}_{ix} + \hat{I}_{jx}$. In cases of slight chemical inequivalence and no continuous wave irradiation, $\theta_{ij} \to \pi/2$ and the same eigenstates are found under the condition of weak spin-locking. The eigenstate $|S_0\rangle$ is maintained in the presence of the spin-lock pulse, whilst the states $|\psi_{m_I}\rangle$ become superpositions of the nuclear triplet states $|T_{m_I}\rangle$. The states $|S_0\rangle$ and $|\psi_0\rangle$ are separated by J_{ij} and do not depend on ω_{SLIC}, whilst the states $|\psi_{\pm1}\rangle$ are linearly dependent on ω_{SLIC}.

The final form of the SLIC eigenstates and coherent Hamiltonian $\hat{H}^{ST}_{\text{coh,rf}}$ showcase the inner workings of the SLIC pulse, and a clear route for triplet-singlet population interconversion. Suppose that the nutation frequency of the long SLIC pulse is set to match the in pair scalar coupling J_{ij} of the singlet spins i and j:

$$\omega_{\text{SLIC}} = 2\pi J_{ij}. \tag{2.106}$$

In this case, it is evident that the populations $|S_0\rangle\langle S_0|$ and $|\psi_{-1}\rangle\langle\psi_{-1}|$ are connected as the energies of the states $|S_0\rangle$ and $|\psi_{-1}\rangle$ are equal. A "level-crossing" [168–170] is therefore created by the application of a weak spin-locking field, and the off-diagonal elements $\frac{\Omega^{ij}_{\Delta}}{2\sqrt{2}}$ facilitate a population transfer between states $|S_0\rangle$ and $|\psi_{-1}\rangle$ in this regime.

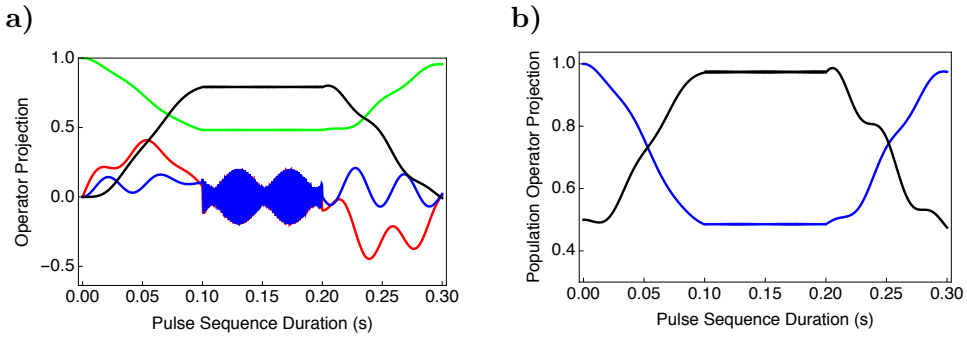

FIGURE 2.15: a) Simulated trajectories for the transfer of longitudinal magnetization $\hat{I}_{iz} + \hat{I}_{jz}$ into transverse magnetization $\hat{I}_{ix} + \hat{I}_{jx}$ (green), $\hat{I}_{iy} - \hat{I}_{jy}$ (red), and nuclear singlet order $-\frac{2\hat{I}_{iz}\cdot\hat{I}_{jz}+\hat{I}_i^+\cdot\hat{I}_j^-+\hat{I}_i^-\cdot\hat{I}_j^+}{2\sqrt{3}}$ (black) using the pulse sequence described in figure 2.14 for a pair of near-equivalent spin-1/2 nuclei. Residual longitudinal magnetization $\hat{I}_{iz} - \hat{I}_{jz}$ is shown by the blue trajectory. The simulation uses the following parameters: $J_{ij} = 11.7\,\text{Hz}$, $\Omega_\Delta^{ij} = 13.5\,\text{ppb}$, $\omega_{\text{SLIC}} = 2\pi 11.7\ \text{rads}^{-1}$, $\tau_{\text{SLIC}} = 100\,\text{ms}$, $\omega_{\text{LOCK}} = 500\,\text{Hz}$, $\tau_{\text{EV}} = 100\,\text{ms}$ and $\vec{B}_0 = 11.7\,\text{T}$. No relaxation is included in the simulation. b) Simulated trajectories of population difference operators $|T_{-1}\rangle\langle T_{-1}|$ - $|T_{+1}\rangle\langle T_{+1}|$ (blue) and $|\psi_{-1}\rangle\langle\psi_{-1}|$ - $|S_0\rangle\langle S_0|$ (black) under the action of the pulse sequence described in figure 2.14. The simulation parameters are the same as in a).

Simulated trajectories of the nuclear singlet order and the Cartesian product operators $\hat{I}_{ix} + \hat{I}_x$, $\hat{I}_{iy} - \hat{I}_{jy}$ and $\hat{I}_{iz} - \hat{I}_{jz}$ for the SLIC pulse sequence are shown in figure 2.15a).

The initial 90°_{90} pulse creates coherences between the $|\phi_0\rangle$ and $|T_{\pm 1}\rangle$ states, which corresponds to a population difference across the $|T_{\pm 1}\rangle$ states. Over the course of the spin-locking duration, the $|T_{\pm 1}\rangle$ population difference evolves into a population difference between the states $|\psi_{-1}\rangle$ and $|S_0\rangle$, see figure 2.15b). The rate of polarization transfer is modulated by the size of the chemical shift difference Ω_Δ^{ij}. As most J-synchronous transfers are oscillatory, population interconversion between the singlet and triplet states is predictable and controllable. The timescale for maximal polarization transfer is therefore:

$$\tau_{\text{SLIC}} = \frac{2\pi}{\sqrt{2}\Omega_\Delta^{ij}}, \tag{2.107}$$

which occurs at the halfway point of the polarization oscillation period $\frac{2\sqrt{2}\pi}{\Omega_\Delta^{ij}}$.

2.12.2 SLIC experiment for equivalent spin-1/2 pairs

As considered in section 2.9, a chemically equivalent spin-1/2 pair (i and j) scalar coupled to an external spin-1/2 nucleus (k) requires an alternative route of access to the nuclear

singlet order. In this case, the coherent Hamiltonian $\hat{H}^{ijk}_{\text{coh}}$ is given in equation 2.63. In the presence of a weak rf-field $\omega^{ij}_{\text{SLIC}}$ applied to spins i and j the coherent Hamiltonian $\hat{H}^{ijk}_{\text{coh,rf}}$ becomes:

$$\hat{H}^{ijk}_{\text{coh,rf}} = 2\pi J_{ij}\hat{I}_i \cdot \hat{I}_j + 2\pi J_{ik}\hat{I}_{iz} \cdot \hat{I}_{kz} + 2\pi J_{jk}\hat{I}_{jz} \cdot \hat{I}_{kz} + \omega^{ij}_{\text{SLIC}}(\hat{I}_{ix} + \hat{I}_{jx}). \tag{2.108}$$

The matrix representation of the coherent Hamiltonian $\hat{H}^{ijk}_{\text{coh,rf}}$ in a frame that diagonalizes the $\hat{I}_{ix} + \hat{I}_{kx}$ operators is:

$$\hat{H}^{ijk}_{\text{coh,rf}} = \begin{array}{c} \\ |S^{ijk}_0\rangle \\ |\psi^{ijk}_{-1}\rangle \\ |\psi^{ijk}_0\rangle \\ |\psi^{ijk}_{+1}\rangle \end{array} \begin{array}{c} \left\langle S^{ijk}_0 \right| \quad |\psi^{ijk}_{-1}\rangle \quad |\psi^{ijk}_0\rangle \quad |\psi^{ijk}_{+1}\rangle \\ \begin{pmatrix} \frac{-3\pi J_{ij}}{2} & -\frac{\pi J^{ijk}_{\Delta}}{2\sqrt{2}} & 0 & \frac{\pi J^{ijk}_{\Delta}}{2\sqrt{2}} \\ -\frac{\pi J^{ijk}_{\Delta}}{2\sqrt{2}} & \frac{\pi J_{ij}}{2} - \omega_{\text{SLIC}} & \frac{\pi J^{ijk}_{\Sigma}}{2\sqrt{2}} & 0 \\ 0 & \frac{\pi J^{ijk}_{\Sigma}}{2\sqrt{2}} & \frac{\pi J_{ij}}{2} & \frac{\pi J^{ijk}_{\Sigma}}{2\sqrt{2}} \\ \frac{\pi J^{ijk}_{\Delta}}{2\sqrt{2}} & 0 & \frac{\pi J^{ijk}_{\Sigma}}{2\sqrt{2}} & \frac{\pi J_{ij}}{2} + \omega_{\text{SLIC}} \end{pmatrix} \end{array}, \tag{2.109}$$

where the off-diagonal terms are proportional to:

$$J^{ijk}_{\Delta} = J_{ik} - J_{jk}, \tag{2.110}$$

$$J^{ijk}_{\Sigma} = J_{ik} + J_{jk}, \tag{2.111}$$

and the eigenvalues of the diagonalized coherent Hamiltonian $\hat{H}^{ijk}_{\text{coh,rf}}$ are:

$$|S^{ijk}_0\rangle = |S_0\rangle \otimes |I_k, M_{I_k}\rangle, \tag{2.112}$$

$$|\psi^{ijk}_{-1}\rangle = [\frac{1}{2}(|T_{-1}\rangle + |T_{+1}\rangle) - \frac{1}{\sqrt{2}}|T_0\rangle] \otimes |I_k, M_{I_k}\rangle, \tag{2.113}$$

$$|\psi^{ijk}_{0}\rangle = [\frac{1}{\sqrt{2}}(|T_{+1}\rangle - |T_{-1}\rangle)] \otimes |I_k, M_{I_k}\rangle, \tag{2.114}$$

$$|\psi^{ijk}_{+1}\rangle = [\frac{1}{2}(|T_{-1}\rangle + |T_{+1}\rangle) + \frac{1}{\sqrt{2}}|T_0\rangle] \otimes |I_k, M_{I_k}\rangle, \tag{2.115}$$

where $|I_k, M_{I_k}\rangle$ is the spin state of nucleus k. The matrix representation of the coherent Hamiltonian $\hat{H}^{ijk}_{\text{coh,rf}}$ shown in equation 2.109 is given in a subspace of $\hat{H}^{ijk}_{\text{coh,rf}}$ which contains all the relevant spin dynamics. The subspace consists of 4 states, out of a total of 8 states, with the chosen states corresponding to the $|\beta\rangle$ state of spin k.

Consider again the case of $\omega^{ij}_{\text{SLIC}}$ matched to $2\pi J_{ij}$. A level crossing is created between the states $|S^{ijk}_0\rangle$ and $\langle\psi^{ijk}_{-1}|$, and the off-diagonal terms $\frac{\pi J^{ijk}_{\Delta}}{2\sqrt{2}}$ allow a population transfer which gradually accumulates the nuclear singlet order. In contrast to the case of two inequivalent spins-1/2, the maximum triplet-singlet conversion efficiency is achieved

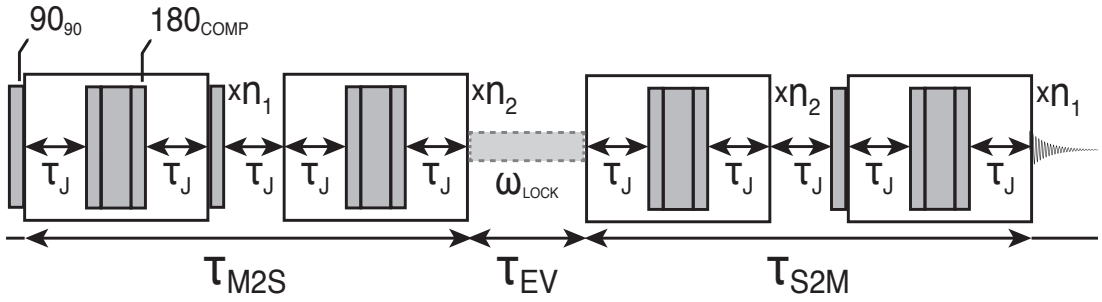

FIGURE 2.16: The magnetization-to-singlet-singlet-to-magnetization (M2SS2M) pulse sequence used for accessing the long-lived singlet order in near-equivalent pairs of spin-1/2 nuclei and measuring its resulting decay.

when:

$$\tau_{\mathrm{SLIC}}^{ijk} = \frac{\sqrt{2}}{J_{\Delta}^{ijk}}, \tag{2.116}$$

as the oscillatory transfer is modulated by the difference in out-of-pair scalar couplings J_{Δ}^{ijk} [21, 31, 157, 160].

2.13 Magnetization-to-singlet-singlet-to-magnetization

The small chemical shift difference between spin-1/2 nuclei allows coherent access to the nuclear singlet order, as demonstrated by the SLIC pulse sequence in section 2.12.1. An alternative pulse sequence which also operates effectively in the *near-equivalence* regime is the magnetization-to-singlet-singlet-to-magnetization (M2SS2M) [150, 156]. The M2SS2M pulse scheme was realized by Tayler and Levitt and was originally used as a method of accessing nuclear singlet order, before the SLIC sequence was available. Although not quite as simple as the SLIC, the M2SS2M does have its advantages and is presented in this thesis alongside D-DNP experiments. A comparison of the SLIC and M2SS2M pulse sequences is given in appendix B. In this section, an evaluation of the M2S pulse sequence is given.

The M2SS2M pulse sequence is built on two repeated blocks of J-synchronized echo (JSE) trains that, if applied in an appropriate manner, combine to produce a more sophisticated pulse sequence which has the ability to interconvert magnetization and singlet order. A schematic of the M2SS2M sequence is shown in figure 2.16. The spin

density operator description of the M2S pulse sequence (first half of the M2SS2M pulse sequence) for a pair of near-equivalent spin-1/2 nuclei (i and j) works as follows:

Considering that the nuclear singlet $|S_0\rangle$ and triplet $|T_{m_I}\rangle$ states have near identical populations at thermal equilibrium, the longitudinal spin order of the spin system is defined as the population difference between the outer triplet $m_I = \pm 1$ states ($|T_{-1}\rangle$ and $|T_{+1}\rangle$):

$$\hat{I}_{iz} + \hat{I}_{jz} \equiv |T_{+1}\rangle\langle T_{+1}| - |T_{-1}\rangle\langle T_{-1}|\,. \tag{2.117}$$

The application of an initial 90°_{90} radiofrequency pulse tilts the longitudinal magnetization $\hat{I}_{iz} + \hat{I}_{jz}$ into the xy-plane and creates transverse magnetization. The Cartesian product operator $\hat{I}_{ix} + \hat{I}_{jx}$ corresponds to triplet-triplet coherences between the outer $m_I = \pm 1$ triplet states $|T_{\pm 1}\rangle$ and the inner $m_I = 0$ triplet state $|T_0\rangle$:

$$\hat{I}_{ix} + \hat{I}_{jx} \equiv |T_{+1}\rangle\langle T_0| + |T_0\rangle\langle T_{+1}| + |T_0\rangle\langle T_{-1}| + |T_{-1}\rangle\langle T_0|\,. \tag{2.118}$$

The JSE unit is constructed from a composite 180°_0 pulse sandwiched by two delay periods of $\tau_J = 1/4J_{ij}$, see figure 2.16. Successive JSE units transform the single quantum coherences into triplet-singlet coherences between the outer m_I=$\pm$1 states $|T_{\pm 1}\rangle$ and the singlet state $|S_0\rangle$, which corresponds to the operator $\hat{I}_{iy} - \hat{I}_{jy}$ in the Cartesian product operator basis. Depending on whether the number of echoes n_1 is odd or even, the operator $\hat{I}_{iy} - \hat{I}_{jy}$ is expressed as:

$$\mathrm{n}_1\text{=odd:}\quad \hat{I}_{iy} - \hat{I}_{jy} \equiv i(|T_{+1}\rangle\langle S_0| + |S_0\rangle\langle T_{+1}| + |S_0\rangle\langle T_{-1}| + |T_{-1}\rangle\langle S_0|), \tag{2.119}$$

$$\mathrm{n}_1\text{=even:}\quad \hat{I}_{iy} - \hat{I}_{jy} \equiv i(|T_{+1}\rangle\langle S_0| + |S_0\rangle\langle T_{+1}| - |S_0\rangle\langle T_{-1}| - |T_{-1}\rangle\langle S_0|). \tag{2.120}$$

A shortcut would be to swap the states $|T_0\rangle$ and $|S_0\rangle$. The number of echoes n_1 exploited to switch the state $|T_0\rangle$ with $|S_0\rangle$ is dependent on the size of the chemical shift difference Ω^{ij}_{Δ}. The echo number n_1 is defined as:

$$\mathrm{n}_1 = \frac{\pi}{2\theta_{ij}}, \tag{2.121}$$

and in practice must be rounded to the nearest integer. As a rule of thumb, a smaller chemical shift difference Ω^{ij}_{Δ} with respect to the in pair scalar coupling J_{ij} indicates that more echoes are required to interconvert the state $|T_0\rangle$ with $|S_0\rangle$. In the near-chemical equivalence regime $\theta_{ij} \to 0$ and large numbers of echoes are required to exchange $|T_0\rangle$

with $|S_0\rangle$ in certain cases [54]. The following 90°_0 pulse rotates the transverse magnetization into $\hat{I}_{iz} - \hat{I}_{jz}$, i.e. a zero quantum coherence between the m_I=0 states. The 90°_0 rotation leaves the singlet state unperturbed whilst interconverting the $|T_{\pm1}\rangle$ and $|T_0\rangle$ state populations:

$$\pm(|T_{+1}\rangle + |T_{-1}\rangle) \quad \overset{90^\circ_0}{\longleftrightarrow} \quad \mp\frac{i}{\sqrt{2}}|T_0\rangle\,, \tag{2.122}$$

$$|S_0\rangle \quad \overset{90^\circ_0}{\longleftrightarrow} \quad |S_0\rangle\,. \tag{2.123}$$

Equations 2.119 and 2.120 transform under the application of the 90°_0 pulse in order to represent the operator $\hat{I}_{iz} - \hat{I}_{jz}$ [156]:

$$\text{n}_1\text{=odd:} \quad \hat{I}_{iz} - \hat{I}_{jz} \equiv \frac{1}{\sqrt{2}}(|T_0\rangle\langle S_0| - |S_0\rangle\langle T_0|), \tag{2.124}$$

$$\text{n}_1\text{=even:} \quad \hat{I}_{iz} - \hat{I}_{jz} \equiv \frac{1}{\sqrt{2}}(|T_0\rangle\langle S_0| + |S_0\rangle\langle T_0|). \tag{2.125}$$

The echo number n_1 is often chosen to be even since a second JSE train with half the number of pulses (n_2=$\text{n}_1/2$) is used later in the M2S sequence. In the case of n_1 = even, the effect of free evolution for a time $\tau_J = 1/4J_{ij}$ under an internal Hamiltonian governed by the in pair scalar coupling J_{ij} phase shifts the triplet-singlet coherences [25, 150]:

$$\text{n}_1\text{=even:} \quad \hat{I}_{iz} - \hat{I}_{jz} \equiv \frac{1}{\sqrt{2}}(|T_0\rangle\langle S_0| - |S_0\rangle\langle T_0|), \tag{2.126}$$

i.e. the coherences have opposite sign. The resulting coherences may now be converted to a population difference between the m_I=0 $|S_0\rangle$ and $|T_0\rangle$ states. A second JSE train, performed with half the number of echoes (n_2=$\pi/4\theta_{ij}$), transforms the singlet state $|S_0\rangle$ into a superposition of m_I=0 states:

$$|S_0\rangle \rightarrow \frac{|S_0\rangle + |T_0\rangle}{\sqrt{2}}, \tag{2.127}$$

and converts the coherences described in equations 2.124 and 2.125 into a singlet-triplet population difference $\hat{Q}_{\text{ST}}$ between the $m_I = 0$ states $|S_0\rangle$ and $|T_0\rangle$:

$$\text{n}_1\text{=even:} \quad \hat{Q}_{\text{ST}} \equiv \frac{1}{2}|S_0\rangle\langle S_0| - |T_0\rangle\langle T_0|\,. \tag{2.128}$$

The M2S sequence is therefore capable of performing the same task as the SLIC pulse,

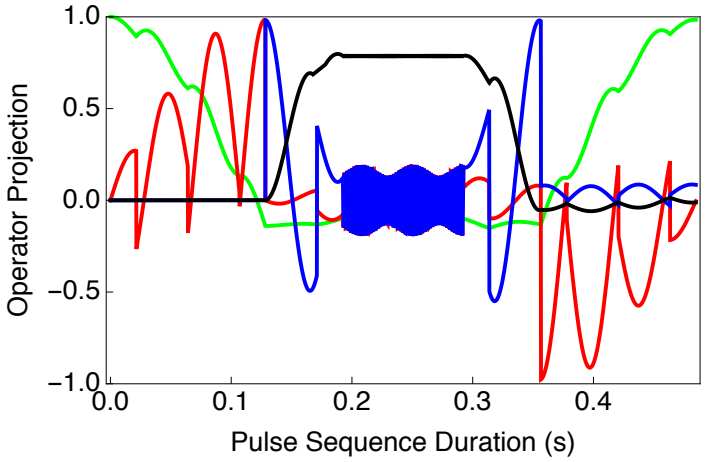

FIGURE 2.17: Simulated trajectories for the transfer of longitudinal magnetization $\hat{I}_{iz}+\hat{I}_{jz}$ into transverse magnetization $\hat{I}_{ix}+\hat{I}_{jx}$ (green), $\hat{I}_{iy}-\hat{I}_{jy}$ (red), and nuclear singlet order $-\frac{2\hat{I}_{iz}\cdot\hat{I}_{jz}+\hat{I}_i^+\cdot\hat{I}_j^-+\hat{I}_i^-\cdot\hat{I}_j^+}{2\sqrt{3}}$ (black) using the pulse sequence described in figure 2.16 for a pair of near-equivalent spin-1/2 nuclei. Residual longitudinal magnetization $\hat{I}_{iz}-\hat{I}_{jz}$ is shown by the blue trajectory. The simulation uses the following parameters: $J_{ij}=11.7\,\text{Hz}$, $\Omega_\Delta^{ij}=13.5\,\text{ppb}$, $n_1=3$, $n_2=1$, $\tau_J=21.4\,\text{ms}$, $\omega_{\text{LOCK}}=500\,\text{Hz}$, $\tau_{\text{EV}}=100\,\text{ms}$ and $\vec{B}_0=11.7\,\text{T}$. No relaxation is included in the simulation.

and as the name suggests convert longitudinal magnetization into nuclear singlet order (proportional to Q_{ST}, see later). It should be noted that the time reversal of the M2S sequence (applying the sequence in reverse chronological order) achieves the opposite transformation and converts nuclear singlet order into observable magnetization (the initial 90°_{90} pulse is ignored). The reverse pulse sequence is termed singlet-to-magnetization (S2M). The S2M pulse sequence employs the same parameters as the M2S pulse sequence. Simulated trajectories of the nuclear singlet order and the Cartesian product operators $\hat{I}_{ix}+\hat{I}_x$, $\hat{I}_{iy}-\hat{I}_{jy}$ and $\hat{I}_{iz}-\hat{I}_{jz}$ for the M2SS2M pulse sequence are shown in figure 2.17. The singlet-to-magnetization (S2M) pulse sequence is used in the context of this work to draw out the hyperpolarized singlet order from a pair of near-equivalent protons in a singly deuterated methyl group.

It is interesting to note the upper bound on the polarization transfer for the following transformation: magnetization → singlet order → magnetization. As previously discussed, the form of the spin density operator at the commencement of the evolution period τ_{EV} is proportional to $\hat{Q}_{\text{ST}}$ for two spins-1/2 (i and j). The singlet-central triplet population difference $\hat{Q}_{\text{ST}}$ prepared by the M2S sequence (equation 2.128) may be more

conveniently expressed as:

$$\begin{aligned} |S_0\rangle\langle S_0| - |T_0\rangle\langle T_0| \;\rightarrow\; & |S_0\rangle\langle S_0| - \frac{1}{3}(|T_{+1}\rangle\langle T_{+1}| + |T_0\rangle\langle T_0| + |T_{-1}\rangle\langle T_{-1}|) \\ + \;\; & \frac{1}{3}(|T_{+1}\rangle\langle T_{+1}| - 2\,|T_0\rangle\langle T_0| + |T_{-1}\rangle\langle T_{-1}|), \end{aligned} \tag{2.129}$$

where the first term (line 1) corresponds to the nuclear singlet order, i.e. the imbalance between the singlet and mean triplet populations [150, 151]. The second term (line 2) represents the perturbed nuclear triplet populations, which are currently out of thermal equilibrium due to the application of the M2S pulse sequence. Suppose now that $\hat{Q}_{\mathrm{ST}}$ is left to evolve for a time interval which is long with respect to the longitudinal relaxation time T_1 but short with respect to the singlet relaxation time T_{S}. Assuming that the nuclear triplet populations return to uniformity after a time period of $\sim 5 \times T_1$, with minimal decay of the nuclear singlet order, the singlet-central triplet population difference corresponds to $\hat{Q}_{\mathrm{SO}}$, see equation 2.25. The term relating to the longitudinal spin order of the singlet pair i and j becomes diminishingly small at long evolution times τ_{EV}, and is neglected. The resulting spin density operator may therefore be written as the sum of two orthogonal terms:

$$\begin{aligned} \hat{Q}_{\mathrm{SO}} \;\rightarrow\; & \frac{2}{3}\left(|S_0\rangle\langle S_0| - |T_0\rangle\langle T_0|\right) \\ + \;\; & \frac{1}{3}(|S_0\rangle\langle S_0| - |T_{+1}\rangle\langle T_{+1}| + |T_0\rangle\langle T_0| - |T_{-1}\rangle\,\langle T_{-1}|). \end{aligned} \tag{2.130}$$

The first term (line 1) is reconverted by the S2M pulse sequence into the operator $2/3(\hat{I}_{ix} + \hat{I}_{jx})$, i.e. 2/3 of the starting Zeeman polarization. The M2SS2M pulse sequence therefore has a maximum theoretical efficiency of 2/3 for the conversion scheme: magnetization → singlet order → magnetization. The SLIC pulse sequence possesses an identical maximum theoretical conversion efficiency. A more detailed approach to the bounds on polarization transfer is discussed by Sørensen [171] and Levitt [151, 172, 173]. In practice, efficiencies lower than 2/3 are observed due to the additional loss of nuclear spin order related to the effects of relaxation during pulse sequence execution, pulse imperfections, $\vec{B}_1$ magnetic field inhomogeneities and other complications. Other terms are also present in $\hat{Q}_{\mathrm{SO}}$ (line 2), but may be destroyed via singlet filtration techniques [54–56].

Chapter 3

Long-lived nuclear spin states in monodeuterated methyl groups

As previously discussed, long-lived states (LLS) are configurations of nuclear spins which are protected against relaxation in nuclear magnetic resonance (NMR) experiments [14–27, 35, 142, 144, 149, 150, 156–158]. In systems of spin-1/2 pairs, the LLS is called *singlet order*. This consists of the population imbalance between the spin-0 singlet state and the spin-1 triplet states [14–16]. The decay time constant of singlet order is denoted T_S. Access to the nuclear singlet order is provided by a chemical shift difference between the participating spins, or by differences in spin-spin couplings to spins outside the pair [23].

LLS have also been observed in the 3-spin-1/2 systems of rapidly rotating methyl groups in solution [141, 155, 174]. In this case the LLS is given by the imbalance in populations between spin states spanning different irreducible representations of the C_3 permutation group [175]. Some materials, such as γ-picoline, display quantum-rotor induced polarization (QRIP) effects, in which a large polarization of the methyl LLS is induced by dissolution of the material from cryogenic conditions [141, 176–178]. However, the hyperpolarized LLS only gives rise to observable NMR signals through an incoherent cross-relaxation mechanism involving a fourth nuclear spin, which greatly reduces the available signal enhancement [141, 155, 174].

Since methyl groups are ubiquitous in nature, the exploitation of methyl LLS is potentially attractive. In this chapter I show that, in certain cases, it is possible to achieve coherent access to a methyl LLS with a high conversion efficiency into observable

NMR signals. The conditions are: (i) the methyl group is monodeuterated, and therefore contains a proton pair; (ii) the local environment is chiral, and (iii) the three methyl rotamers have sufficiently different populations, so that a small chemical shift difference is induced between the CH_2D protons after averaging over all populated states. It is shown that the small chemical shift difference allows coherent (and therefore efficient) access to the long-lived singlet order of a proton spin pair, using known radiofrequency pulse techniques [150, 156–158].

In this chapter, the proton LLS in the N-CH_2D group of N-CH_2D-2-methylpiperidine is also presented, with the observed singlet lifetimes T_S found to be between 20 and 55 seconds (dependent on temperature). The ratio of the singlet relaxation time T_S to the longitudinal relaxation time T_1 was found to be remarkably constant over a wide range of conditions, and equal to 3.1 ± 0.1. The results suggest that a common underlying mechanism is responsible for the decay of longitudinal magnetization and nuclear singlet order. The singlet relaxation in this system is hence shown to be dominated by the dipolar interactions between the CH_2D protons and the CH_2D deuteron. The measured singlet relaxation times cannot be explained by a model in which the three hydrogen nuclei are localised at the vertices of an equilateral triangle, and a modified geometrical model is proposed which is consistent with the experimental data. This result shows that it is feasible to exploit methyl LLS without relying on weak cross-relaxation effects, in suitable cases.

3.1 Equilibrium isotope effects for CH_2D groups

The three protons of a methyl (CH_3) group are chemically equivalent from an NMR standpoint due to the rapid rotational motion of the methyl rotor. This gives rise to a single resonance in the NMR spectrum as the chemical shift of each proton is interchanged on a timescale which is shorter than the nuclear Larmor period. In the case of a monodeuterated methyl (CH_2D) group in a *chiral* molecule, the two CH_2D protons are diastereotopic and have distinct chemical shifts. A visible CH_2D proton chemical shift difference is much harder to observe however, and chemical inequivalence of CH_2D protons has only been observed in a small handful of molecules, most of which contain an N-CH_2D group in a chiral environment [56, 179–184].

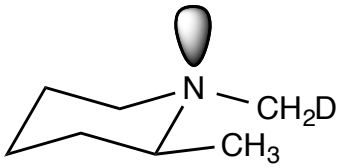

FIGURE 3.1: The dominant di-equatorial chair conformation [179] of N-CH_2D-2-methylpiperidine in solution at room temperature, showing the nitrogen lone pair which is implicated in the inequivalence of the two CH_2D protons.

An appreciable diastereotopic chemical shift difference between the two protons of a CH_2D group is most easily induced by two key components:

1. *A strong rotameric preference/aversion for a particular* CH_2D *group rotamer [185], i.e. a rotameric population asymmetry.*

2. *Distinct magnetic environments at each static site occupied by a* CH_2D *group proton.*

Prior studies suggest that a nitrogen lone pair neighbouring a CH_2D group can cause relatively large isotope effects on the conformational equilibria [186–188]. Based on such evidence, Anet and Kopelevich investigated the proton NMR spectrum of N-CH_2D-2-methylpiperidine, a chiral six-membered ring containing an N-CH_2D group, which displays an observable CH_2D proton chemical shift difference [56, 179, 181, 182, 184]. The chemical structure of N-CH_2D-2-methylpiperidine is given in figure 3.1 and is used extensively in CH_2D-based experiments throughout this thesis.

3.1.1 Vibrational spectroscopy

Before a discussion of symmetry breaking interactions and long-lived states in CH_2D groups can take place, the theory behind the equilibrium isotope effect (EIE) requires explanation. From a brief recapitulation of vibrational spectroscopy, all bonds have quantized vibrational energy levels. The vibrational energy levels E_n depend on; 1. the frequency of the bond stretch ν; and 2. the reduced mass of the two bonded atoms μ. The bond stretching frequency ν is written as:

$$\nu = \frac{1}{2\pi}\sqrt{\frac{k}{\mu}} \tag{3.1}$$

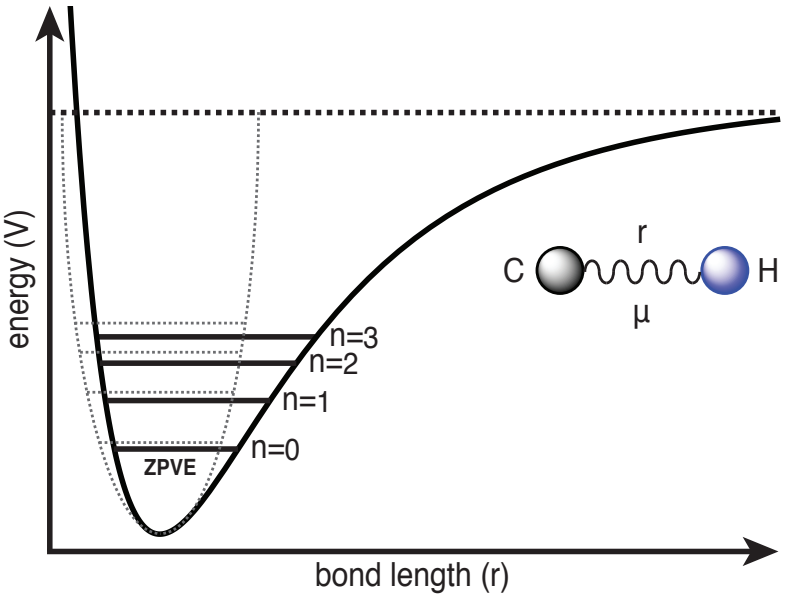

FIGURE 3.2: The vibrational energy levels of an anharmonic oscillator for integer values of n. The ZPVE (E_0) corresponds to the ground vibrational state n=0. The anharmonic potential (black, solid line) is given by the Morse potential (equation 3.3). A harmonic oscillator is represented by the parabolic potential (grey, dashed lines).

where k is the force constant. The reduced mass μ is given by:

$$\mu = \frac{m_1 m_2}{m_1 + m_2}, \tag{3.2}$$

where m_i is the mass of atom i. In a simplified version of events, the potential energy of a C-H bond as a function of nuclear separation is given by the Morse potential, see figure 3.2 [189, 190]. The Morse potential $V(\mathrm{r})$ is expressed as:

$$V(\mathrm{r}) = D_e(1 - e^{-\beta(\mathrm{r}-\mathrm{r}_0)})^2, \tag{3.3}$$

where D_e is the dissociation energy of the molecule, β provides a measure of curvature at the bottom of the well, and r_0 is the equilibrium bond length. The Morse potential represents an anharmonic potential as the restoring force of the "spring" has a non-linear response as a function of bond length r. However, anharmonic systems may be approximated as harmonic oscillators in the vicinity of a stable equilibrium point, with the anharmonic component acting as a small perturbation. The vibrational energy level structure of the harmonic oscillator therefore serves as a good approximation to the anharmonic oscillator for small vibrational displacements, at which point the restoring

force of the potential is approximately linear. I will hence assume a harmonic potential for the discussion of the equilibrium isotope effect (EIE) [191]. The vibrational states of a harmonic potential are given by:

$$\mathrm{E_n} = h\nu(\mathrm{n} + \frac{1}{2}), \tag{3.4}$$

where $\mathrm{n} \geq 0$. The zero point vibrational energy (ZPVE) is located at the bottom of the potential well and corresponds to the state n=0:

$$\mathrm{E_0} = \frac{h\nu}{2}. \tag{3.5}$$

The ZPVE ($\mathrm{E_0}$) is the ground vibrational state and is therefore susceptible to small vibrational perturbations.

3.1.2 Equilibrium isotope effects for deuterium

The deuterium isotope effect is one of the most studied isotope effects due to its large size [192, 193]. The percentage mass change between a proton and a deuteron is considerably greater than any other isotopic substitution. The equilibrium isotope effect (EIE) may be described by the ground vibrational state $\mathrm{E_0}$ of a potential minima as approximately 99.9% of C-H(D) bonds are in the n=0 state at room temperature [194]. In a simple model, where the bonded atoms can be considered as balls on springs, only the mass dependent properties of the system are disturbed, in this particular case, by the isotopic labelling of a deuteron for a proton. The increased mass of a deuteron compared to a proton adds to the overall reduced mass μ of the system, i.e. the C-H(D) bond. This in turn reduces the stretching frequency ν and the ZPVE of the C-H(D) bond, see equation 3.1.

3.1.3 Symmetry breaking interactions for CH_2D groups

In order to demonstrate how the EIE develops into a significant rotameric population asymmetry, the Newmann projections for the CH_2D group of N-CH_2D-2-methylpiperidine must be considered, see figure 3.3a). The notation for the three CH_2D rotamers of N-CH_2D-2-methylpiperidine is as follows:

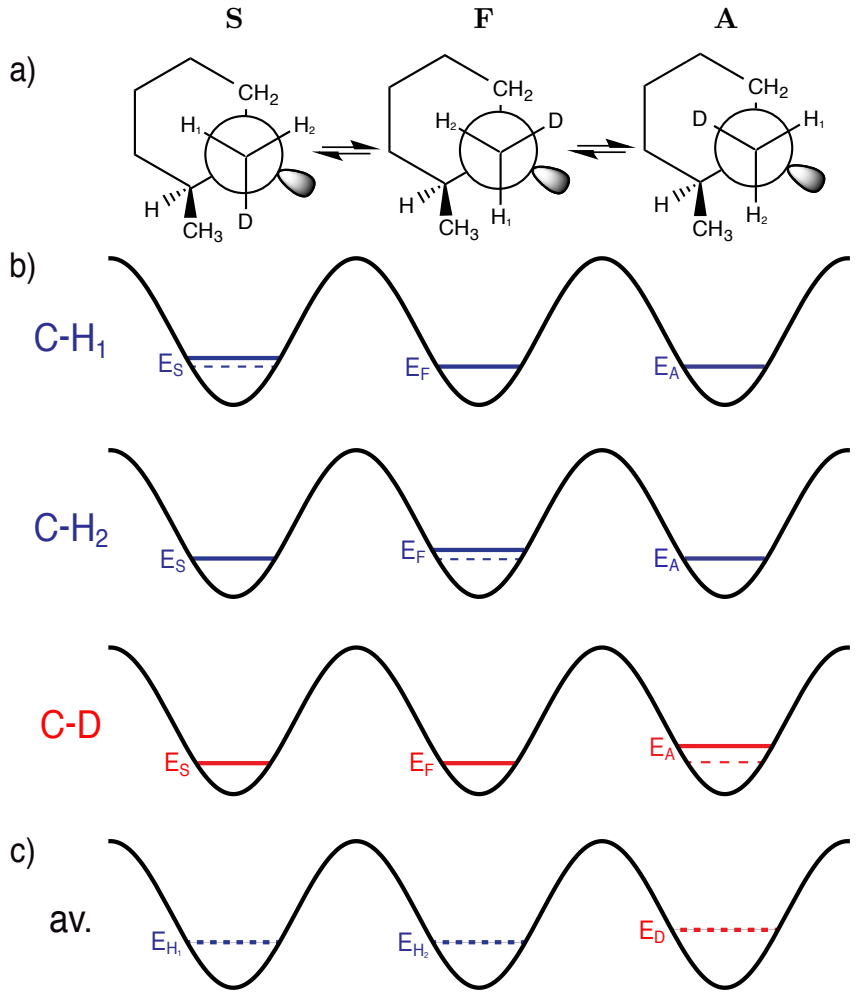

FIGURE 3.3: a) The three CH_2D rotamers of N-CH_2D-2-methylpiperidine. b) The zero point vibration energies (ZPVEs) of the C-H_1, C-H_2 and C-D bonds in each of the three rotamers. Dashed lines represent the ZPVE in the case of no nitrogen lone pair. c) The average ZPVE of each rotamer as a function of the ZPVEs for each C-H(D) bond.

- **S**. The deuteron is sterically interacting with the 2-position CH_3 group,
- **F**. The deuteron is free from interaction with the 2-position CH_3 group,
- **A**. The deuterium is *anti* to the lone pair of electrons on the nitrogen atom.

As discussed in section 3.1.2, the ZPVE of a C-D bond is lower than that of a C-H bond. This is evident for all three rotamers in figure 3.3b). However, the ZVPE of a C-H(D) bond is raised when the H(D) nucleus is *anti* to the lone pair of electrons on the nitrogen atom. This effect is greater for a deuteron in this location as $n-\sigma^*$ hyperconjugation involving the lone pair of electrons and the *anti* methyl C-D sigma bond is weaker for a C-D bond, compared with the corresponding effect for a C-H bond. As the *anti* bond

is weaker than the other two C-H(D) bonds, the molecule loses zero-point vibrational stabilization when deuterium partitions the **S** and **F** bonding positions. When the ZPVEs for the C-H(D) bonds are averaged across the three rotamers, the rotamer with the deuteron *anti* to the lone pair (**A**) has a higher average ZPVE, compared with the case of when a proton partitions the gauche bonds (rotamers **S** and **F**), see figure 3.3c). This is the primary origin of the equilibrium isotope effect for a CH_2D group, and provides a sufficient description of the appreciable population asymmetry generated between the three CH_2D group rotors. A distinguishable chemical shift for each proton is therefore also realized by considering the same example of the EIE for a CH_2D group.

3.1.4 Observable CH_2D proton chemical shift differences

The EIE discussed in section 3.1.3 is responsible for the observable chemical shift difference Ω_Δ^{12} between the two CH_2D protons (labelled 1 and 2) of N-CH_2D-2-methylpiperidine. The following procedure is used to determine the size of the proton chemical shift difference Ω_Δ^{12} for a CH_2D group in a *chiral* molecule:

1. Calculate ΔG_i and the relative populations P_i of the rotamers **S**, **F** and **A**.
2. Determine the chemical shift difference Ω_Δ^{12} between the protons of the rotamers **S**, **F** and **A**.
3. Weight the proton chemical shift differences Ω_Δ^{12} by the relative populations P_i.

The population P_i of a rotamer i is defined as:

$$P_i = \frac{e^{\frac{-\Delta G_i}{\kappa_B T}}}{Z}, \tag{3.6}$$

where ΔG_i is the difference in the Gibbs free energies between C-H and C-D bonds for the rotamer i [191], κ_B is the Boltzmann constant, T is the temperature, and Z is the partition function. The partition function is defined as:

$$Z = \sum_i e^{\frac{-\Delta G_i}{\kappa_B T}}, \tag{3.7}$$

i.e. the sum over all relative populations. The partition function normalizes the relative populations such that the total population is equal to 1. The chemical shift difference

between the CH_2D protons of the rotamer i is denoted $\Omega_{\Delta}^{12}(i)$. For example, if position **S** is occupied by the deuteron then protons are in positions **F** and **A**, and the chemical shift difference between the CH_2D protons of the rotamer **S** is given by: $\Omega_{\Delta}^{12}(\mathbf{S}) = \delta_{\mathbf{F}} - \delta_{\mathbf{A}}$, and hence $\Omega_{\Delta}^{12}(i)$ is allowed to be negative. The procedure described above leads to the following expression for the proton chemical shift difference Ω_{Δ}^{12} of a CH_2D group:

$$\Omega_{\Delta}^{12} = P_{\mathbf{S}}\Omega_{\Delta}^{12}(\mathbf{S}) + P_{\mathbf{F}}\Omega_{\Delta}^{12}(\mathbf{F}) + P_{\mathbf{A}}\Omega_{\Delta}^{12}(\mathbf{A}). \tag{3.8}$$

The proton chemical shift differences $\Omega_{\Delta}^{12}(i)$ are averaged across all populated CH_2D rotamers, which gives rise to an observable CH_2D chemical shift difference Ω_{Δ}^{12} in the ^{1}H NMR spectrum.

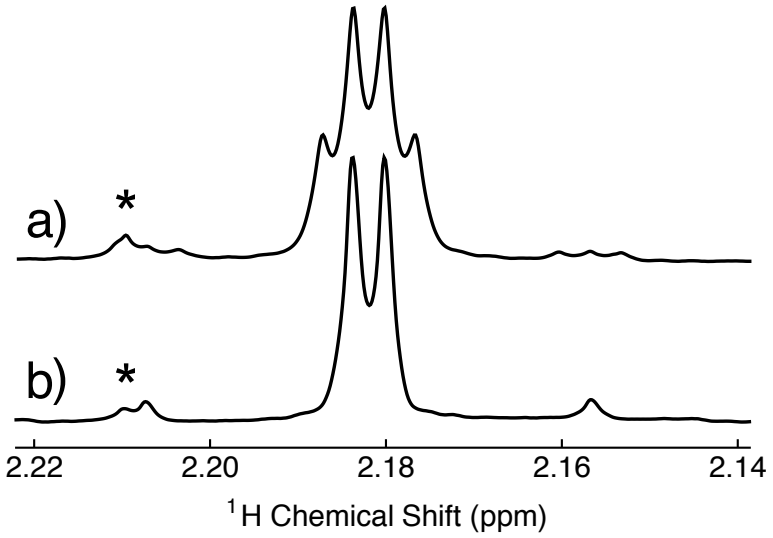

FIGURE 3.4: Part of the experimental ^{1}H spectrum of N-CH_2D-2-methylpiperidine in CD_2Cl_2 solution acquired at 11.7 T (500 MHz) and 25°C with a single transient. a) Spectrum without deuteron decoupling; b) Spectrum with deuteron decoupling (deuteron nutation frequency = 500 Hz). The asterisk indicates a small signal from a non-deuterated N-methyl-2-methylpiperidine impurity, shifted in frequency by a secondary isotope effect.

3.2 Experiments

3.2.1 Proton spectra

The methyl region of the proton NMR spectrum of N-CH_2D-2-methylpiperidine is shown in figure 3.4. This spectral region has a quartet-like appearance in the absence of deuteron decoupling (figure 3.4a). The characteristic AB spectral pattern of an inequivalent proton pair appears when a deuteron decoupling field is used to remove the $^2J_{\mathrm{HD}}$ splittings (figure 3.4b). This spectrum is consistent with a J-coupling of $\left|^2J_{\mathrm{HH}}\right|$ = 11.7 ± 0.2 Hz and a chemical shift difference of Ω^{12}_{Δ} = 13.5 ± 0.4 ppb between the CH_2D protons, as reported previously [179]. The existence of a small chemical shift difference has been attributed to (i) hyperconjugation between the nitrogen lone pair and the *anti*-methyl C-H(D) σ-bond, which allows the zero-point vibrational energies of the *anti* CH and CD bonds to influence the rotamer energies; as a result, the rotamer with the CD bond *anti* to the nitrogen lone pair is less populated than the other two rotamers in thermal equilibrium, and (ii) the chiral environment associated with the neighbouring methyl group, which causes a significant chemical shift difference between the two protons in each rotamer [179, 182]. In these circumstances, there remains a

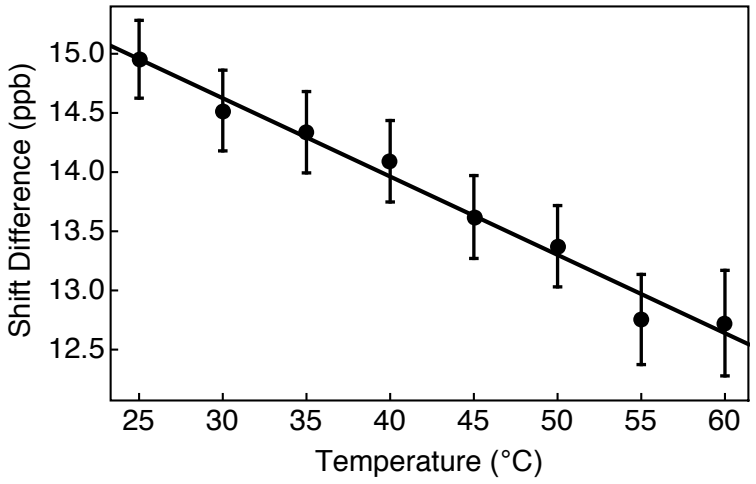

FIGURE 3.5: Chemical shift difference Ω_{Δ}^{12} between the CH_2D protons of N-CH_2D-2-methylpiperidine in C_6D_6 solution at 11.7 T (500 MHz) as a function of temperature.

significant chemical shift difference between the CH_2D protons after averaging over all methyl rotamers. The observed chemical shift difference decreases as the temperature is increased, as shown in figure 3.5. This is consistent with the Boltzmann populations of the three rotamers becoming more similar at higher temperatures.

3.2.2 Singlet NMR

The small chemical shift difference allows access to the long-lived singlet order between the CH_2D protons by using SLIC [157] pulse sequence, as shown in figure 3.6. The pulse sequence is described in detail in section 2.12.1. The experimental parameters were as follows: $\omega_{\mathrm{SLIC}}/2\pi = 11.7\,\mathrm{Hz}$, $\omega_{\mathrm{LOCK}}/2\pi = 300\,\mathrm{Hz}$, $\tau_{\mathrm{SLIC}} = 100\,\mathrm{ms}$ (500 MHz) and $\tau_{\mathrm{SLIC}} = 73\,\mathrm{ms}$ (600 MHz). The resonance offset was placed in the centre of the CH_2D peak at 2.18 ppm. The singlet state is a magnetically silent arrangement of nuclear spin configurations and is unperturbed by the presence of a T_{00} filter, which employs the optimized parameters shown in appendix B to remove signals deriving from residual magnetization. The maximum amplitude of the singlet-filtered ^{1}H NMR signal, relative to that induced by a single 90° pulse, was found to be 0.43, somewhat lower than the theoretical maximum of 2/3 [173], the loss being attributed to radiofrequency field imperfections and relaxation. A two-step phase cycle, in which the phase of the 90_{90} pulse and the receiver are simultaneously changed by 180° in successive transients, removes spurious signals generated by longitudinal magnetization accrued during the long SLIC pulses. An interval of 90 s was used between successive transients.

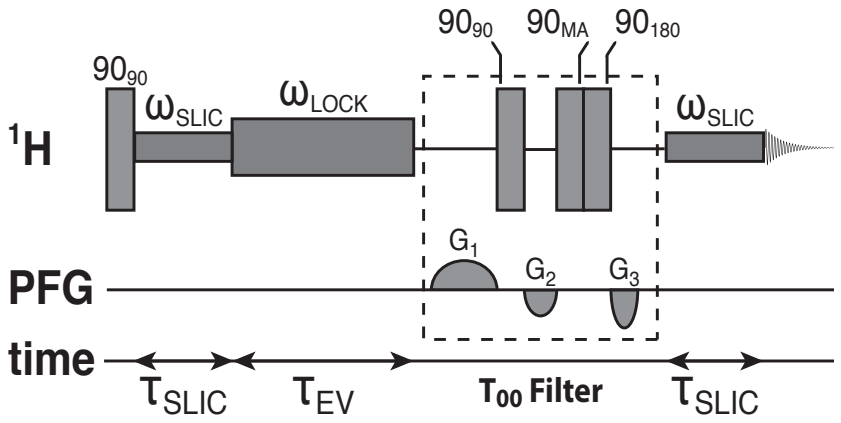

FIGURE 3.6: Pulse sequence used for accessing long-lived singlet order in monodeuterated methyl groups and measuring its decay. The experiments used the following nutation frequencies: $\omega_{\mathrm{SLIC}}/2\pi = 11.7\,\mathrm{Hz}$ and $\omega_{\mathrm{LOCK}}/2\pi = 300\,\mathrm{Hz}$. The duration of the SLIC pulse was 100 ms in the 500 MHz experiments and 73 ms in the 600 MHz experiments. Singlet order is allowed to evolve for a time τ_{EV}. The "T_{00} filter" sequence suppresses signals that do not pass through singlet order. "MA" denotes the "magic angle" (54.7°).

3.3 Results

A typical decay curve for singlet order is shown in figure 3.7. This shows a single exponential decay with time constant $T_S = 27.0 \pm 0.6\,\mathrm{s}$. This is approximately three times longer than the relaxation time for longitudinal magnetization $T_1 = 8.7 \pm 0.1\,\mathrm{s}$, as estimated from the inversion recovery curve, also shown in figure 3.7.

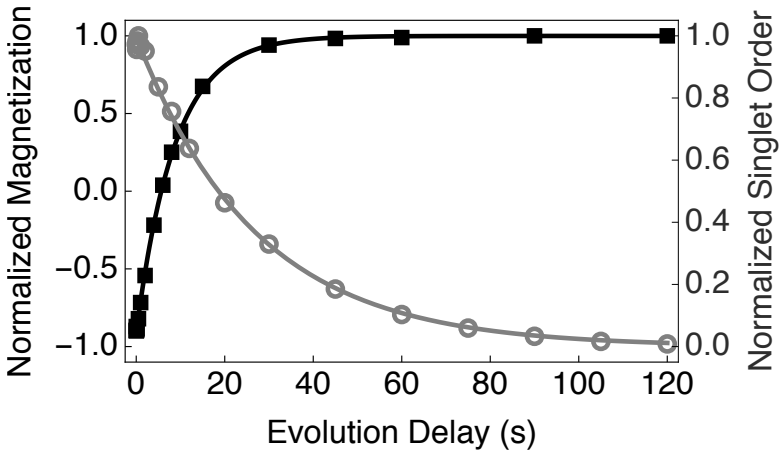

FIGURE 3.7: Experimental relaxation curves for 0.1 M N-CH_2D-2-methylpiperidine in degassed CD_2Cl_2 solvent (proton frequency = 500 MHz, temperature 25°C). Open symbols, grey line, and right-hand axis: Decay of singlet order measured by the pulse sequence in figure 3.6. Filled symbols, black line, and left-hand axis: Spin-lattice relaxation measured by inversion recovery. All signal amplitudes were normalized to the first point. The fitted curves have a single-exponential form.

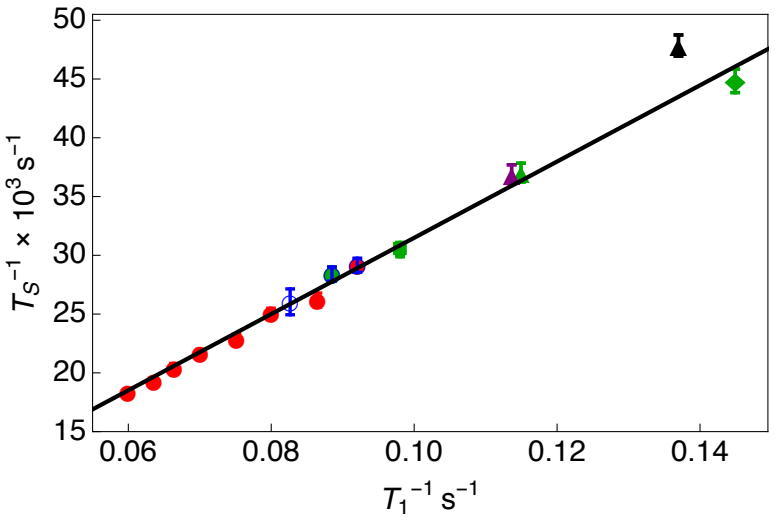

FIGURE 3.8: Longitudinal relaxation rate constants (T_1^{-1}) plotted against singlet relaxation rate constants (T_S^{-1}) for 0.1 M N-CH_2D-2-methylpiperidine over a wide range of solvents (degassed), temperatures and magnetic fields. The experimental conditions are as follows: (●) C_6D_6 solution, at temperatures increasing from 25°C (rightmost point) to 60°C (leftmost point) in 5°C increments, at a field of 14.1 T (600 MHz); (○) C_6D_6 solution, at magnetic fields increasing from 9.4 T (400 MHz, leftmost point) to 14.1 T (600 MHz, rightmost point) in 100 MHz increments, at a temperature of 25°C; (▲) CH_2Cl_2 solution at 25°C and 11.7 T (500 MHz); (●) C_6D_6 solution at 25°C and 11.7 T (500 MHz); (■) CD_3CN solution at 25°C and 11.7 T (500 MHz); (▲) CD_2Cl_2 solution at 25°C and 11.7 T (500 MHz); (◆) CD_3OD solution at 25°C and 11.7 T (500 MHz); (▲) CD_2Cl_2 solution of N-CH_2D-2-(CD_3)-piperidine at 25°C, 11.7 T (500 MHz). A constant ratio $T_S/T_1 = 3.1 \pm 0.1$ is observed over a wide range of experimental conditions.

Figure 3.8 shows a plot of T_1^{-1} against T_S^{-1} for a variety of solvents, temperatures and magnetic fields. The singlet relaxation time constants T_S increase with increasing temperature and decreasing solvent viscosity. The fit to a straight line with zero intercept and inverse slope $(3.1)^{-1} = 0.324$ is remarkably good. The ratio of T_S to T_1 is remarkably consistent and given by 3.1 ± 0.1 over a wide range of conditions. Measured relaxation time constants T_1 and T_S are presented for this disparate data set in table 3.1. The data shown in figure 3.8 were all obtained for N-CH_2D-2-methylpiperidine, except for a single point which was obtained for a compound with complete deuteration of the second methyl group, i.e. N-CH_2D-2-CD_3-piperidine (purple triangle). Clearly, deuteration of the second methyl group in N-CH_2D-2-methylpiperidine does not have a strong effect on the relaxation behaviour.

TABLE 3.1: The set of singlet relaxation times T_S and longitudinal relaxation times T_1 for the CH_2D group of 0.1 M N-CH_2D-2-methylpiperidine shown in figure 3.8.

Solvent*	Temp.	Magnetic Field	T_S/s	T_1/s	Symbol
C_6D_6	25°C	14.1 T (600 MHz)	34.3 ± 0.7	10.9 ± 0.2	● ○
C_6D_6	30°C	14.1 T (600 MHz)	38.2 ± 0.9	11.6 ± 0.2	●
C_6D_6	35°C	14.1 T (600 MHz)	39.9 ± 0.7	12.5 ± 0.3	●
C_6D_6	40°C	14.1 T (600 MHz)	43.8 ± 0.8	13.3 ± 0.2	●
C_6D_6	45°C	14.1 T (600 MHz)	46.1 ± 0.7	14.3 ± 0.3	●
C_6D_6	50°C	14.1 T (600 MHz)	48.9 ± 0.9	15.1 ± 0.3	●
C_6D_6	55°C	14.1 T (600 MHz)	52 ± 1	15.7 ± 0.3	●
C_6D_6	60°C	14.1 T (600 MHz)	55 ± 1	16.7 ± 0.3	●
C_6D_6	25°C	9.4 T (400 MHz)	38 ± 2	12.1 ± 0.4	○
C_6D_6	25°C	11.7 T (500 MHz)	35.2 ± 0.7	11.3 ± 0.3	○ ●
CD_3CN	25°C	11.7 T (500 MHz)	32.8 ± 0.6	10.2 ± 0.2	■
CD_2Cl_2	25°C	11.7 T (500 MHz)	27.0 ± 0.6	8.7 ± 0.1	▲
CD_3OD	25°C	11.7 T (500 MHz)	22.3 ± 0.5	6.9 ± 0.1	◆
CH_2Cl_2	25°C	11.7 T (500 MHz)	20.9 ± 0.8	7.3 ± 0.2	▲
CD_2Cl_2	25°C	11.7 T (500 MHz)	27.1 ± 0.6	8.8 ± 0.2	▲

The longitudinal relaxation times T_1 and singlet relaxation times T_S included in figure 3.8 for N-CH_2D-2-methylpiperidine are shown in table 3.1. The experimental conditions were as follows:

(●) 25-60°C temperature (5°C increment), 14.1 T (600 MHz), C_6D_6 solvent

(○) 9.4 T (400 MHz) - 14.1 T (600 MHz) magnetic field (2.35 T (100 MHz) increment), 25°C and C_6D_6 solvent

(●) C_6D_6, (■) CD_3CN, (▲) CD_2Cl_2 and (◆) MeOD solvent, 25°C and 11.7 T (500 MHz)

(▲) 25°C, 11.7 T (500 MHz) and CH_2Cl_2 solvent

(▲) N-CH_2D-2-(CD_3)-piperidine at 25°C, 11.7 T (500 MHz) and CD_2Cl_2 solvent.

*Samples were subjected to thorough degassing using multiple freeze-pump-thaw cycles to remove the majority of dissolved molecular oxygen present in solution. The singlet T_S and longitudinal T_1 lifetimes were measured via the aforementioned experimental methods after each degassing cycle until no further lengthening of the relaxation times were observed. This procedure was repeated for each individual sample and ensures that each sample was degassed as comprehensively as experimentally possible, at which point the effect of paramagnetic induced singlet and longitudinal relaxation from dissolved molecular oxygen in solution is negligible.

3.4 Discussion

The data show that the long-lived singlet order may be accessed coherently, and with high efficiency, for the proton pair of the monodeuterated methyl group in N-CH_2D-2-methylpiperidine. The singlet lifetime T_S is proportional to T_1 of the same protons, with the proportionality constant given by 3.1 ± 0.1, over a wide range of experimental conditions. In this section, an explanation for the constant ratio of T_S to T_1 is proposed, and the value of the proportionality constant is investigated.

3.4.1 Relaxation mechanisms

A large variety of relaxation mechanisms may contribute to the T_S and T_1 relaxation of the CH_2D protons. As well as the dipole-dipole interactions between the three magnetic nuclei of the CH_2D group, there are also chemical shift anisotropy contributions, magnetic dipole-dipole interactions with other nuclei in the same molecule, and intermolecular dipole-dipole interactions. The quadrupolar relaxation of the deuterium nuclei might also contribute to proton relaxation through mechanisms such as scalar relaxation of the second kind [152, 195]. Furthermore, spin-rotation relaxation is known to be significant for many rotating methyl groups [58–61], and contributes to the LLS relaxation of γ-picoline in solution [141, 155]. Singlet relaxation may also be caused by state mixing due to a finite chemical shift difference between the participating protons, or by asymmetric J-couplings to other magnetic nuclei ("singlet-triplet leakage") [24].

The excellent correlation between the T_S and T_1 values shown in figure 3.8 strongly supports the hypothesis that the longitudinal and singlet relaxation of the CH_2D proton pair is driven by a common mechanism, with a common correlation function. This suggests that the mechanisms that dominate the T_S and T_1 relaxation of the CH_2D protons are internal to the CH_2D group. This conclusion is supported by the following observations: (i) Deuteration of the 2-methyl group leads to only a small change in the relaxation times even though the protons of the 2-methyl group approach to within 229 pm of the CH_2D protons; (ii) a large change in the deuteration level of the solvent only has a small influence on the relaxation times, see figure 3.8 and table 3.1.

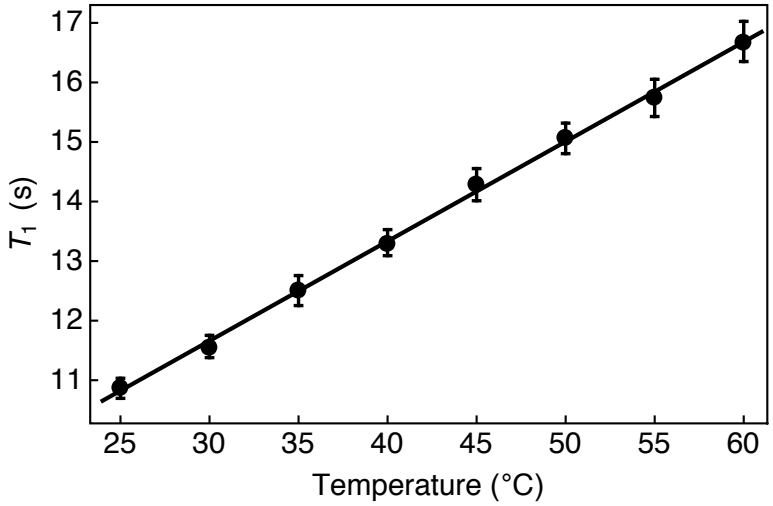

FIGURE 3.9: The longitudinal relaxation time T_1 of 0.1 M N-CH_2D-2-methylpiperidine plotted as a function of temperature. Experiments were performed in degassed C_6D_6 solution at 14.1 T (600 MHz).

In addition, one may discount major contributions from the spin-rotation, scalar relaxation, chemical shift anisotropy and singlet-triplet leakage mechanisms, for the following reasons:

1. *Spin-rotation.* The experimental finding that T_S increases with increasing temperature (figure 3.8) speaks strongly against a significant contribution from spin-rotation, since that mechanism usually increases in strength with increasing temperature [58–61]. Presumably, in the current case, the methyl rotation is too strongly hindered to permit a significant spin-rotation relaxation contribution. Data showing the temperature-dependence of the relaxation time constant T_1^{-1} are presented in figure 3.9. The increase in the value of T_1 with increasing temperature also supports the conclusion that spin-rotation relaxation is not significant in this case.

2. *Scalar relaxation of the second kind.* The existence of a resolved deuteron splitting in the proton spectrum (figure 3.4a), as well as direct measurements of deuteron relaxation (section 3.6.2) indicate that deuteron relaxation is too slow to induce significant scalar relaxation of the coupled protons. Furthermore, the two $^2J_{\mathrm{HD}}$ couplings are identical to a good approximation, which precludes a scalar contribution to singlet relaxation [152].

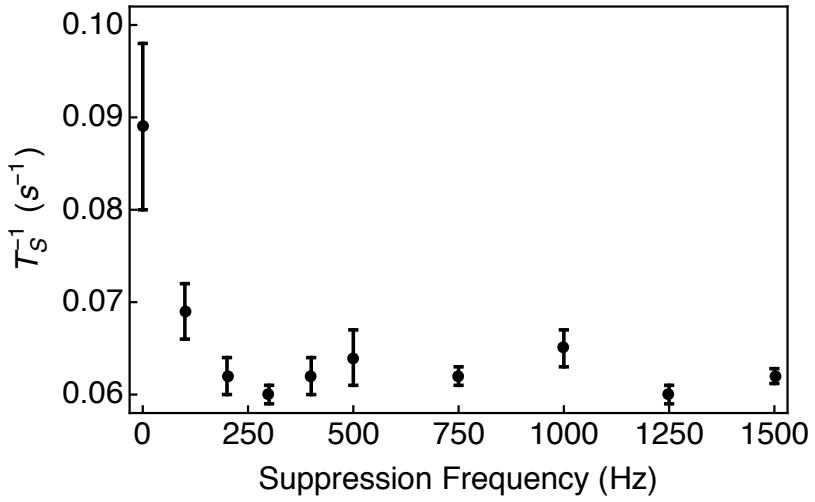

FIGURE 3.10: Experimental dependence of T_S^{-1} on the spin-locking rf-field strength for 0.1 M N-CH_2D-2-methylpiperidine in non-degassed CD_2Cl_2 solvent (proton frequency = 500 MHz, temperature 25°C). The sharp decrease in T_S^{-1} at low values of ω_{LOCK} is due to the suppression of singlet-triplet leakage by the applied rf-field.

3. *Chemical shift anisotropy.* The weak dependence of T_S and T_1 on magnetic field indicates a relatively small contribution from CSA.

4. *Singlet-triplet leakage.* Singlet-triplet leakage induced by the small chemical shift difference between the CH_2D protons can be a significant contribution to the singlet relaxation rate constant T_S^{-1} [24]. However, in the current experiments, this contribution is suppressed very effectively by the application of an on resonant radiofrequency field during the singlet relaxation interval. Data showing the dependence of T_S^{-1} on the spin-locking rf-field amplitude, expressed as the nutation frequency ω_{LOCK}, is shown in figure 3.10.

It is therefore postulated that both the singlet and longitudinal relaxation of the proton pair in the monodeuterated methyl group of N-CH_2D-2-methylpiperidine are dominated by the ^{1}H-^{1}H and ^{1}H-^{2}D dipole-dipole interactions within the methyl group itself, modulated by the internal rotation of the methyl group with respect to the rest of the molecule, and by the rotation of the molecule as a whole. A relaxation model is therefore constructed based on (i) a simplified description of the motion of the methyl group and the molecule as a whole, and (ii) a description of the vibrationally-averaged spin-spin interactions within the rotating methyl group.

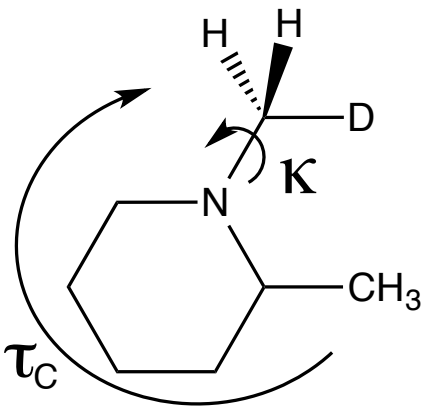

FIGURE 3.11: The relaxation of the CH_2D protons in N-CH_2D-2-methylpiperidine is governed by the three-fold jump rate κ and overall rotational correlation time τ_C.

3.4.2 Motional model

A plausible motional model for the monodeuterated methyl group in N-CH_2D-2-methylpiperidine consists of a hindered 3-fold rotor attached to a sphere undergoing isotropic rotational diffusion, see figure 3.11. Although the existence of a finite chemical shift difference between the CH_2D protons implies that the methyl rotamers have slightly unequal populations, this effect is ignored in the relaxation analysis, for the sake of simplicity. The thermally activated jumps between the methyl rotamers are assumed to be described by a rate constant κ, while the overall rotational diffusion of the molecule is described by a correlation time τ_C. Both κ and τ_C are in general temperature-dependent. It is also assumed that the correlation time τ_C is short enough relative to the nuclear Larmor period to invoke the extreme narrowing approximation [195].

3.4.3 Dipole-dipole interactions

The three magnetic nuclei in the CH_2D group interact by the magnetic dipole-dipole interaction. In general these dipole-dipole interactions are described by traceless second-rank tensors, and are subjected to averaging over local molecular vibrations and librations on a timescale fast compared to the methyl 3-fold jumps or the molecular tumbling. Spin relaxation is caused by the motional modulation of the vibrationally-averaged dipole-dipole interaction tensors.

In general, the vibrationally-averaged tensors differ, both in magnitude and in orientation, from tensors derived from a naive geometrical model, for which point-like

nuclei are located at the vertices of an equilateral triangle, with the magnitudes of the dipole-dipole interactions in exact proportion to the product of the gyromagnetic ratios, since the internuclear distances are all equal [196]. As discussed below, this naive equilateral model of the CH_2D group is inconsistent with the experimental results.

To maintain high generality, the relaxation theory is developed using three different interaction tensors for the vibrationally-averaged dipole-dipole interactions, leaving the magnitudes and orientations of the tensors as adjustable parameters. The two ^{1}H-^{2}D interaction tensors are assumed to have the same principal values, by symmetry. For the sake of simplicity, the vibrationally-averaged interaction tensors are assumed to be axially symmetric, with the unique principal axes perpendicular to the N-C rotor axis. The angle between the unique principal axes of the two vibrationally-averaged ^{1}H-^{2}D interaction tensors is denoted 2θ. This angle defines the cross-correlation of the two ^{1}H-^{2}D interaction tensors, and is therefore important for the proton singlet relaxation. By symmetry, the unique principal axis of the vibrationally-averaged ^{1}H-^{1}H interaction tensor is perpendicular to the bisector of the two ^{1}H-^{2}D principal axes. A point-nucleus equilateral geometry model would lead to the angle $2\theta = 60°$, but this value is not assumed in the following discussion.

3.5 Relaxation theory

In this section, the relaxation superoperators for the two protons and deuteron of the CH_2D group are constructed. The relaxation superoperators are used to determine the relaxation rate expressions for the singlet T_S^{-1} and longitudinal T_1^{-1} relaxation of the CH_2D group. Here I must praise Jean-Nicolas Dumez (CNRS, Gif-sur-Yvette) for his efforts in underpinning the theory behind long-lived state relaxation in monodeuterated methyl groups.

3.5.1 Coherent Hamiltonian

Consider a H_2D system, comprised by the two protons and the deuterium of a singly deuterated methyl group in solution. The two proton spins are labelled as 1 and 2, the deuteron spin as 3. The protons have spin $I = 1/2$ and the deuterium has spin $I = 1$, so there are $2 \times 2 \times 3 = 12$ Hilbert states in total. The relaxation properties of this

system may be analysed in Liouville space, which has dimension $12 \times 12 = 144$. In this chapter, the aim is to calculate the relaxation rates for the longitudinal magnetization of the protons, $\hat{I}_{1z} + \hat{I}_{2z}$, and of the deuterium, $\hat{I}_{3z}$, as well as the nuclear singlet order for the proton pair, $\hat{T}_{00}^{12}$.

Time-independent interactions that govern the evolution of a spin ensemble are contained within the coherent Hamiltonian. In isotropic solution, the two protons are separated in frequency space by a small chemical shift difference Ω_{Δ}^{12}. The coherent Hamiltonian $\hat{H}_{\text{coh}}$ is defined as follows:

$$\hat{H}_{\text{coh}} = \frac{\Omega_{\Delta}^{12}}{2}(\hat{I}_{1\text{z}} - \hat{I}_{2\text{z}}) + 2\pi\,|J_{\text{HH}}|\,\hat{I}_1 \cdot \hat{I}_2 + 2\pi\,|J_{\text{HD}}|\,(\hat{I}_{1\text{z}} \cdot \hat{I}_{3\text{z}} + \hat{I}_{2\text{z}} \cdot \hat{I}_{3\text{z}}), \tag{3.9}$$

where $|J_{\text{HH}}|$ and $|J_{\text{HD}}|$ are the proton-proton and proton-deuteron scalar couplings, respectively.

3.5.2 Fluctuating Hamiltonian

Nuclear spin relaxation is driven by fluctuations of incoherent interactions which are time- and orientation-dependent. The fluctuating Hamiltonian $\hat{H}_{\text{fluc}}$ is expressed using spherical tensors:

$$\hat{H}_{\text{fluc}} = \sum_{\lambda} \hat{H}_{\text{fluc}}^{\lambda} = \sum_{\lambda} c^{\lambda} \sum_{l=0}^{2} \sum_{m=-l}^{l} (-1)^m A_{lm}^{\lambda} \hat{T}_{l-m}^{\lambda}, \tag{3.10}$$

and is written as a sum over all spin interactions λ, and ranks l and tensor components m. c^{λ} is a real constant. A_{lm}^{λ} and T_{l-m}^{λ} are the spatial and spin tensors for the fluctuating Hamiltonian $\hat{H}_{\text{fluc}}$ in the laboratory frame. c^{λ}, $A_{lm}^{\lambda,P}$ and $\hat{T}_{l-m}^{\lambda}$ are given in table 3.2.

For the CH_2D system, the fluctuating interactions include; the dipole-dipole (DD) interactions between every spin pair, and the quadrupolar interaction (Q) for the deuterium spin. The free rotation of the CH_2D moiety can also induce the spin rotation relaxation mechanism, which is typically present for methyl groups, but is not included in this analysis. The chemical-shielding anisotropy (CSA) and other interactions are also ignored. For the dipole-dipole interaction, the fluctuating Hamiltonian $\hat{H}_{\text{DD}}$ is expressed as follows:

$$\hat{H}_{\text{DD}} = \sum_{i=1}^{2} \sum_{j=i+1}^{3} b_{ij} \sum_{m=-2}^{2} (-1)^m A_{2m}^{\text{DD}} \hat{T}_{2-m}^{ij}, \tag{3.11}$$

TABLE 3.2: Tensor components of the rank-2 interaction ($l = 2$): the dipole-dipole (DD) interaction for a spin pair ij and the quadrupolar (Q) interaction for a spin i. The $\hat{T}_{2m}$ tensor components are given in the laboratory frame and the A_{2m} tensor components are given in the principal axis system P of the interaction λ. r_{ij} is the internuclear distance between spin i and spin j, eQ_i is the quadrupole moment and eq_i is the electric field gradient for nucleus i, $\eta_{\lambda,i}$ is the biaxality of interaction λ.

λ	c^λ	m	$A_{2m}^{\lambda,P}$	$\hat{T}_{2m}^{\lambda}$
DD	$-\frac{\mu_0\gamma_i\gamma_j\hbar}{4\pi r_{ij}^3}$	0	$6^{1/2}$	$6^{-1/2}\left(3I_{iz}I_{jz} - I_i \cdot I_j\right)$
		±1	0	$\mp\left(1/2\right)\left(I_{i\pm}I_{jz} + I_{iz}I_{j\pm}\right)$
		±2	0	$\left(1/2\right)I_{i\pm}I_{j\pm}$
Q	$\frac{e^2q_iQ_i}{2I(2I-1)\hbar}$	0	$(3/2)^{1/2}$	$6^{-1/2}\left(3I_{iz}^2 - I(I+1)\right)$
		±1	0	$\mp\left(1/2\right)\left(I_{i\pm}I_{iz} + I_{iz}I_{i\pm}\right)$
		±2	$(1/2)\eta_i$	$\left(1/2\right)I_{i\pm}^2$

where the summation over the spin labels i and j accounts for the dipole-dipole interactions internal to the CH_2D group. The dipole-dipole coupling constant b_{ij} is defined in equation 1.163. Spins with $I > 1/2$ have a non-spherical charge density at the nucleus and possess an electric quadrupole moment. Interactions occur between the electric quadrupole moment and the electric field gradient tensor present at the nucleus. The fluctuating Hamiltonian for the quadrupole interaction is defined as follows:

$$\hat{H}_{\mathrm{Q}} = \omega_{\mathrm{Q}} \sum_{m=-2}^{2} (-1)^m A_{2m}^{\mathrm{Q}} \hat{T}_{2-m}^{3}, \tag{3.12}$$

where ω_{Q} is the nuclear quadrupolar coupling constant and is defined in equation 1.176. $\hat{T}_{2m}^{3}$ is the quadrupolar spin tensor for the fluctuating Hamiltonian of spin 3. Deuterium carries a nuclear spin $I = 1$, and therefore the expression for the nuclear quadrupole coupling constant ω_{Q} simplifies to:

$$\omega_Q = \frac{e^2qQ}{2\hbar}. \tag{3.13}$$

3.5.3 Spectral densities

The spectral density of an interaction λ describes the intensity of motion at a frequency ω. The spectral densities $J_{m,m'}^{\lambda,\lambda'}$ are written:

$$J_{m,m'}^{\lambda,\lambda'}(\omega) = \int_0^\infty d\tau\, G_{m,m'}^{\lambda,\lambda'}(\tau)\, e^{i\omega\tau}, \tag{3.14}$$

with the corresponding autocorrelation functions $G^{\lambda,\lambda'}_{m,m'}(\tau)$:

$$G^{\lambda,\lambda'}_{m,m'}(\tau) = \langle A^{\lambda *}_{lm}(t) A^{\lambda'}_{lm'}(t-\tau)\rangle. \tag{3.15}$$

See appendix B for more details regarding spectral densities and autocorrelation functions. The spectral densities for the dipole-dipole and quadrupolar interactions (λ) are derived from a sequence of rotations from the principal axis system P of the interaction λ to a common rotor frame R, then to a molecular frame M, and finally to the laboratory frame L:

$$A^{\lambda}_{2m}(t) = \sum_{m_1}\sum_{m_2}\sum_{m_3} A^{\lambda,P}_{2m_3} D^2_{m_3m_2}(\Omega^{\lambda}_{PR}) D^2_{m_2m_1}(\Omega_{RM}(t)) D^2_{m_1m}(\Omega_{ML}(t)), \tag{3.16}$$

$D^2_{m_im_j}$ is a component of the Wigner matrix of rank 2; Ω^{Q}_{PR} is the set of Euler angles that describes the transformation from the independent principal axis systems of the dipole-dipole and quadrupolar interactions P to the rotor frame R fixed with respect to the CH_2D group and with its z-axis aligned with the local 3-fold symmetry axis. The z-axis of the laboratory frame L is defined to be parallel to the static magnetic field $\vec{B}_0$. For the dipole-dipole interaction, only the component m=0 is non-zero. For the quadrupolar interaction of the deuterium nucleus, the biaxality of the ^{2}H quadrupole coupling tensor is small (axially symmetric tensor) and is neglected. Hence only the m=0 rank-2 component of the spatial tensor $A^{\mathrm{Q},P}_{2m}$ (written in the principal axis system P of the quadrupolar interaction for the deuterium nucleus) is included when considering transformations to the axis system of the rotor frame R, and also in consecutive frame transformations. With these assumptions, $A^{\lambda,P}_{20}$ is the only non-zero component of the rank-2 spatial tensor $A^{\lambda,P}_{2m}$ in the principal axis systems of both the dipole-dipole and quadrupolar interactions for the CH_2D group:

$$A^{\lambda}_{2m}(t) = A^{\lambda,P}_{20} \sum_{m_1}\sum_{m_2} D^2_{0m_2}(\Omega^{\lambda}_{PR}) D^2_{m_2m_1}(\Omega_{RM}(t)) D^2_{m_1m}(\Omega_{ML}(t)). \tag{3.17}$$

Using equation 3.17, the autocorrelation functions for the dipole-dipole and quadrupolar interactions may be written as follows:

$$\begin{aligned} G^{\lambda,\lambda'}_{m,m'}(\tau) \;=\; & A^{\lambda,P}_{20} A^{\lambda',P}_{20} \sum_{m_1,m_1'}\sum_{m_2,m_2'} D^{2*}_{0m_2}(\Omega^{\lambda}_{PR}) D^2_{0m_2'}(\Omega^{\lambda'}_{PR}) \\ & \times \langle D^{2*}_{m_2m_1}(\Omega_{RM}(0)) D^2_{m_2'm_1'}(\Omega_{RM}(\tau)) D^{2*}_{m_1m}(\Omega_{ML}(0)) D^2_{m_1'm'}(\Omega_{ML}(\tau))\rangle. \end{aligned} \tag{3.18}$$

Assuming that the rapid isotropic rotational diffusion of the CH_2D group and the overall reorientation of the molecule are uncorrelated, the autocorrelation functions for the dipole-dipole and quadrupolar interactions become:

$$\begin{aligned} G^{\lambda,\lambda'}_{m,m'}(\tau) &= A^{\lambda,P}_{20} A^{\lambda',P}_{20} \sum_{m_1,m'_1} \sum_{m_2,m'_2} D^{2*}_{0m_2}(\Omega^{\lambda}_{PR}) D^{2}_{0m'_2}(\Omega^{\lambda'}_{PR}) \\ &\quad \times \langle D^{2*}_{m_2m_1}(\Omega_{RM}(0)) D^{2}_{m'_2m'_1}(\Omega_{RM}(\tau)) \rangle \langle D^{2*}_{m_1m}(\Omega_{ML}(0)) D^{2}_{m'_1m'}(\Omega_{ML}(\tau)) \rangle. \end{aligned} \tag{3.19}$$

An expression of the relaxation superoperator may be derived in the standard semi-classical treatment of spin relaxation [195]. Internal motion is described with a 3-site jump model, with jump rate κ, and a spherical top is assumed for overall motion, with correlation time τ_C. For a spherical top, the contribution of overall tumbling to the autocorrelation function is [61]:

$$\langle D^{2*}_{m_1m}(\Omega_{ML}(0)) D^{2}_{m'_1m'}(\Omega_{ML}(\tau)) \rangle = \frac{1}{5} \delta_{m_1m'_1} \delta_{mm'} e^{-\frac{\tau}{\tau_C}}, \tag{3.20}$$

where the rotational correlation time τ_C describes the rapid isotropic rotational diffusion of the N-CH_2D-2-methypiperidine molecule in solution. The frame transformation from the principal axis system P of the dipole-dipole interaction to the axis system of the rotor frame R corresponds to a single rotation around the symmetry axis of the methyl group. The Euler angles create the following rotation matrix:

$$D^{2}_{m_2m_1}(\alpha^{DD}_{PR} = 0, \beta^{DD}_{PR} = 0, \gamma^{DD}_{PR}) = \delta_{m_2m_1} e^{-im_1\gamma}. \tag{3.21}$$

The rotation matrix for the frame transformation from the principal axis system P of the quadrupolar interaction to the axis system of the rotor frame R is created from the following Euler angles:

$$D^{2}_{m_2m_1}(\alpha^{Q}_{PR} = -\pi, \beta^{Q}_{PR} = -\pi, \gamma^{Q}_{PR} = 0) = e^{im_2\pi} d^{2}_{m_2m_1}(-\pi). \tag{3.22}$$

For a hindered methyl group, a three-site jump model is sufficient as to describe the internal CH_2D dynamics. I hence recall the model proposed by Woessner [49]. The model is a simple combination of an overall reorientational motion (isotropic small-step rotational diffusion) with the internal rotation of the methyl group described by thermally activated 3-fold jumps around a single molecule-fixed axis (methyl group symmetry axis). The jumps are between equivalent or near-equivalent sites, which correspond to

the rotamers of the CH_2D group presented in section 3.1.3. The diffusion of the spin-spin axis around the methyl group symmetry axis is assumed to have no influence on the internuclear separation of the CH_2D constituents. A rigorous derivation of the spectral density function for a 3-fold jump model is given in reference [197] and the result is used in the remainder of this chapter without further discussion. It should be noted that other, more complicated expressions for the spectral density of a methyl group are also presented in reference [49]. Therefore, for a methyl group undergoing thermally activated jumps between three equivalent sites, the contribution of internal motion to the correlation function is:

$$\langle D^{2*}_{m_2 m_1}(\Omega_{RM}(0)) D^{2}_{m'_2 m'_1}(\Omega_{RM}(\tau))\rangle = \delta_{m_1 m_2}\delta_{m'_1 m'_2}\delta_{m_2 m'_2}\delta_{m_1 m'_1} e^{-3\epsilon_{m_2}\kappa\tau}, \tag{3.23}$$

By combining equations 3.19, 3.20 and 3.23, the spectral densities $J^{\lambda,\lambda'}_{m,m'}(\omega)$ in equation 3.14 become:

$$\begin{aligned} J^{\lambda,\lambda'}_{mm'}(\omega) &= \delta_{mm'}\frac{1}{5}A^{\lambda,P}_{20}A^{\lambda',P}_{20}\sum_{m_2} D^{2*}_{0m_2}(\Omega^{\lambda}_{PR}) D^{2}_{0m'_2}(\Omega^{\lambda'}_{PR}) \\ &\quad \times \int_0^\infty d\tau\, e^{-3\epsilon_{m_2}\kappa\tau}\, e^{-\tau/\tau_C}\, e^{i\omega\tau}, \end{aligned} \tag{3.24}$$

with the spectral density at zero frequency, relevant in the extreme narrowing regime, becoming:

$$J^{\lambda,\lambda'}_{mm'}(0) = \delta_{mm'}\frac{1}{5}A^{\lambda,P}_{20}A^{\lambda',P}_{20}\sum_{m_2}\frac{\tau_C}{1+3\epsilon_{m_2}\kappa\tau_C} D^{2*}_{0m_2}(\Omega^{\lambda}_{PR}) D^{2}_{0m'_2}(\Omega^{\lambda'}_{PR}). \tag{3.25}$$

where

$$\epsilon_0 = 0 \quad \text{and} \quad \epsilon_{\pm 1} = \epsilon_{\pm 2} = 1. \tag{3.26}$$

3.5.4 Relaxation superoperators

The double commutation relaxation superoperator for the dipole-dipole and quadrupolar interactions may be written [49, 155]:

$$\hat{\hat{\Gamma}} = -\sum_{l=2}\sum_{\lambda,\lambda'} c^{\lambda}c^{\lambda'}\sum_{m,m'}(-1)^m J^{\lambda,\lambda'}_{m,m'}(0)\hat{\hat{T}}^{\lambda}_{lm}\hat{\hat{T}}^{\lambda'}_{l-m'}, \tag{3.27}$$

see section 1.6.6 for more details. This general expression can be used to calculate all auto-correlation and cross-correlation terms for the dipole-dipole and quadrupole interactions. Contributions to the relaxation superoperator from auto-correlation terms have $\lambda = \lambda'$ and cross-correlation terms have $\lambda \neq \lambda'$. A secularization step is additionally performed for the dipole-dipole and quadrupolar relaxation superoperators which removes all terms modulated at the difference in ^{1}H-^{2}H Larmor frequencies in the laboratory frame.

3.5.4.1 Dipole-dipole relaxation superoperator

The dipole-dipole relaxation superoperator may be constructed by considering for the form of the fluctuating dipole-dipole Hamiltonian in equation 3.11:

$$\hat{\hat{\Gamma}}_{\mathrm{DD}} = -\sum_{i,k=1}^{2}\sum_{j,l=i+1,k+1}^{3} b_{ij}b_{kl}\, J^{\mathrm{DD,DD}}_{m,m'}(0) \sum_{m,m'} (-1)^m \hat{\hat{T}}^{ij}_{2m}\hat{\hat{T}}^{kl}_{2-m'}. \tag{3.28}$$

Combining equations 3.25 and 3.28, and by using the value of $A^{\mathrm{DD},P}_{20}$ from table 3.2, the dipole-dipole relaxation superoperator may be expressed as:

$$\begin{aligned}\hat{\hat{\Gamma}}_{\mathrm{DD}} = -\sum_{i,k=1}^{2}\sum_{j,l=i+1,k+1}^{3} \frac{6}{5}\, b_{ij}\, b_{kl}\, \frac{\tau_{\mathrm{C}}}{1+3\epsilon_{m_2}\kappa\tau_{\mathrm{C}}} \sum_{m_2,m_2'} D^{2*}_{0m_2}(\Omega^{\mathrm{DD}}_{PR}) D^{2}_{0m_2'}(\Omega^{\mathrm{DD}}_{PR}) \\ \times \sum_{m} (-1)^m \hat{\hat{T}}^{ij}_{2m}\hat{\hat{T}}^{kl}_{2-m}.\end{aligned} \tag{3.29}$$

3.5.4.2 Quadrupole relaxation superoperator

The quadrupolar relaxation superoperator takes a similar form to the relaxation superoperator used to describe dipole-dipole relaxation:

$$\hat{\hat{\Gamma}}_{\mathrm{Q}} = -\omega_{\mathrm{Q}}^2\, J^{\mathrm{Q,Q}}_{m,m'}(0) \sum_{m,m'} (-1)^m \hat{\hat{T}}^{3}_{2m}\hat{\hat{T}}^{3}_{2-m'}. \tag{3.30}$$

Combining equations 3.25 and 3.30, and by using the value of $A_{20}^{\mathrm{Q},P}$ from table 3.2, the quadrupolar relaxation superoperator may written more explicitly:

$$\hat{\hat{\Gamma}}_{\mathrm{Q}} = -\frac{3}{10}\,\omega_{\mathrm{Q}}^2\,\frac{\tau_{\mathrm{C}}}{1+3\epsilon_{m_2}\kappa\tau_{\mathrm{C}}}\sum_{m_2,m_2'} D^{2*}_{0m_2}(\Omega^{\mathrm{Q}}_{PR})D^{2}_{0m_2'}(\Omega^{\mathrm{Q}}_{PR}) \times\sum_m (-1)^m \hat{\hat{T}}^3_{2m}\hat{\hat{T}}^3_{2-m}. \tag{3.31}$$

3.5.5 Rate expressions

Using the relaxation superoperators formulated in section 3.5.4, relaxation rates may be calculated as follows for the ^{1}H and ^{2}H longitudinal magnetization and for the ^{1}H singlet order:

$$T_1^{-1} = \frac{(\hat{I}_{1z}+\hat{I}_{2z}|\hat{\hat{\Gamma}}_{\mathrm{DD}}|\hat{I}_{1z}+\hat{I}_{2z})}{(\hat{I}_{1z}+\hat{I}_{2z}|\hat{I}_{1z}+\hat{I}_{2z})}, \tag{3.32}$$

$$T_{1\mathrm{D}}^{-1} = \frac{(\hat{I}_{3z}|\hat{\hat{\Gamma}}_{\mathrm{Q}}|\hat{I}_{3z})}{(\hat{I}_{3z}|\hat{I}_{3z})}, \tag{3.33}$$

$$T_{\mathrm{S}}^{-1} = \frac{(\hat{T}^{12}_{00}|\hat{\hat{\Gamma}}_{\mathrm{DD}}|\hat{T}^{12}_{00})}{(\hat{T}^{12}_{00}|\hat{T}^{12}_{00})}. \tag{3.34}$$

The contribution of the dipole-dipole interaction to ^{2}H longitudinal relaxation was found to be negligible, and was ignored.

In the regime of isotropic extreme-narrowing, the matrix elements $(\hat{T}_{ij}|\hat{\hat{\Gamma}}|\hat{T}_{ij})$ can be easily calculated for a superoperator with a block-diagonal matrix structure. The singlet and longitudinal spin order of the singlet pair (spins 1 and 2) are each identified by a single spherical tensor operator, and the relaxation rate is therefore given by a diagonal element of $\hat{\hat{\Gamma}}$. For the dipole-dipole relaxation of singlet order, the singlet relaxation rate constant T_{S}^{-1} is given by:

$$T_{\mathrm{S}}^{-1} = -\frac{6}{5}\sum_{i,k=1}^{2}\sum_{j,l=i+1,k+1}^{3} b_{ij}b_{kl}\,\frac{\tau_{\mathrm{C}}}{1+3\epsilon_{m_2}\kappa\tau_{\mathrm{C}}}\sum_{m_2,m_2'} D^{2*}_{0m_2}(\Omega^{\mathrm{DD}}_{PR})D^{2}_{0m_2'}(\Omega^{\mathrm{DD}}_{PR}) \times\sum_m (-1)^m \frac{(\hat{T}^{12}_{00}|\hat{\hat{T}}^{ij}_{2-m}\hat{\hat{T}}^{kl}_{2m}|\hat{T}^{12}_{00})}{(\hat{T}^{12}_{00}|\hat{T}^{12}_{00})}. \tag{3.35}$$

The relaxation rate expression for T_{S}^{-1} can be simplified by using the following relation, in the case that ij=kl:

$$(\hat{T}_{00}^{12}|\hat{\hat{T}}_{2m}^{ij,\dagger}\hat{\hat{T}}_{2m}^{kl}|\hat{T}_{00}^{12}) = \|\hat{\hat{T}}_{2m}^{ij}|\hat{T}_{00}^{12})\|^2, \tag{3.36}$$

where $(-1)^m\hat{\hat{T}}_{2-m}^{ij} = \hat{\hat{T}}_{2m}^{ij,\dagger}$. In chapter 2, I demonstrated that an important property of the nuclear singlet order was an immunity to the in pair dipole-dipole relaxation mechanism:

$$\hat{\hat{T}}_{2m}^{ij}|\hat{T}_{00}^{12}) = 0, \tag{3.37}$$

which is valid for the case of ij=12. Inserting equation 3.36 into equation 3.35, and accounting for the result in equation 3.37, leads to the following dipole-dipole auto-relaxation rate expression T_{S}^{-1} for the spin-1/2 protons of the CH_2D group:

$$T_{\mathrm{S}}^{-1} = -\frac{6}{5}\sum_{i=1}^{2} b_{\mathrm{i}3}^2 \frac{\tau_{\mathrm{C}}}{1+3\epsilon_{m_2}\kappa\tau_{\mathrm{C}}} \sum_{m_2,m_2'} D_{0m_2}^{2*}(\Omega_{PR}^{\mathrm{DD}}) D_{0m_2'}^{2}(\Omega_{PR}^{\mathrm{DD}}) \sum_{m} \frac{\|\hat{\hat{T}}_{2m}^{i3}|\hat{T}_{00}^{12})\|^2}{\|\hat{T}_{00}^{12}\|^2}. \tag{3.38}$$

Only dipole-dipole interactions of spins 1 and 2 with the deuteron (spin 3) were found to significantly relax the nuclear singlet order.

For the dipole-dipole relaxation of longitudinal order, any terms denoting coupled rank-1 spin order, e.g. $(\hat{I}_1^-\hat{I}_2^+ - \hat{I}_1^+\hat{I}_2^-)/\sqrt{2}$, may be neglected as these terms are disconnected from the single spin longitudinal operators, and hence the longitudinal relaxation rate constant T_1^{-1} is given by the sum of single spin longitudinal operators:

$$\begin{aligned} T_1^{-1} = & -\frac{6}{5}\sum_{i,k=1}^{2}\sum_{j,l=i+1,k+1}^{3} b_{ij}b_{kl}\frac{\tau_{\mathrm{C}}}{1+3\epsilon_{m_2}\kappa\tau_{\mathrm{C}}} \sum_{m_2,m_2'} D_{0m_2}^{2*}(\Omega_{PR}^{\mathrm{DD}}) D_{0m_2'}^{2}(\Omega_{PR}^{\mathrm{DD}}) \\ & \times \sum_{m}(-1)^m \frac{(\hat{T}_{10}^{i}+\hat{T}_{10}^{j}|\hat{\hat{T}}_{2-m}^{ij}\hat{\hat{T}}_{2m}^{kl}|\hat{T}_{10}^{i}+\hat{T}_{10}^{j})}{(\hat{T}_{10}^{i}+\hat{T}_{10}^{j}|\hat{T}_{10}^{i}+\hat{T}_{10}^{j})}. \end{aligned} \tag{3.39}$$

In chapter 1, I demonstrated that spherical tensor operators possess the following property:

$$\hat{\hat{T}}_{2m}^{ij}|\hat{T}_{10}^{i}+\hat{T}_{10}^{j}) = -m|\hat{T}_{2m}^{ij}). \tag{3.40}$$

and hence the rate expression for longitudinal relaxation (equation 3.39) can be simplified by using the relation:

$$\|\hat{\hat{T}}_{2m}^{ij}|\hat{T}_{10}^{i}+\hat{T}_{10}^{j})\|^2 = m^2\|\hat{T}_{2m}^{ij}\|^2. \tag{3.41}$$

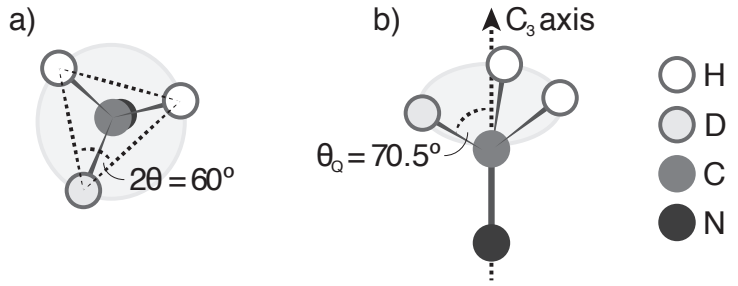

FIGURE 3.12: Schematic of a point-particle model with an equilateral triangle geometry a) perpendicular to and b) in the plane of the CH_2D group. The light grey disk denotes the plane of the CH_2D group. $2\theta = 60°$ and $\theta_Q = 70.5°$ for an equilateral triangle geometry.

Inserting equation 3.41 into equation 3.39 leads to the following dipole-dipole auto-relaxation rate expression T_1^{-1} for the longitudinal order of the spin-1/2 protons in the CH_2D group:

$$T_1^{-1} = -\frac{6}{5}\sum_{i=1}^{2}\sum_{j=i+1}^{3} b_{ij}^2 \frac{\tau_{\mathrm{C}}}{1+3\epsilon_{m_2}\kappa\tau_{\mathrm{C}}} \sum_{m_2,m_2'} D_{0m_2}^{2*}(\Omega_{PR}^{\mathrm{DD}}) D_{0m_2'}^{2}(\Omega_{PR}^{\mathrm{DD}}) \sum_{m>0} m^2 \frac{\|\hat{T}_{2m}^{ij}\|^2}{\|\hat{T}_{10}^{i}+\hat{T}_{10}^{j}\|^2}. \tag{3.42}$$

The sum over m does not include terms corresponding to $m = 0$ as these terms do not contribute to the auto-relaxation rate ($ij = kl$) of spins 1 and 2 in this case. Similar can be shown for the quadrupolar auto-relaxation rate of spin 3.

The motional and intra-methyl interaction models described in section 3.4.2 lead to the following expressions for the proton longitudinal and singlet relaxation rate constants:

$$T_1^{-1} = \frac{(4+3\kappa\tau_{\mathrm{C}})}{24\,(1+3\kappa\tau_{\mathrm{C}})}\left(16\omega_{\mathrm{HD}}^2 + 9\omega_{\mathrm{HH}}^2\right)\tau_C, \tag{3.43}$$

$$T_{\mathrm{S}}^{-1} = \frac{8\sin^2 2\theta}{1+3\kappa\tau_{\mathrm{C}}}\omega_{\mathrm{HD}}^2\tau_C, \tag{3.44}$$

where the dipolar coupling constants for the vibrationally-averaged proton-proton interaction and proton-deuteron interactions are denoted ω_{HH} and ω_{HD}, respectively. In practice, the relevant matrix elements were calculated analytically using the *Mathematica*-based symbolic package *SpinDynamica* [198]. Figure 3.12 shows the relevant angles for the relaxation rates given in equations 3.43, 3.44 and 3.46. The second Euler angle β_{PR} is equal to $\pi/2$ for the three dipole-dipole interactions. The third Euler angle γ_{PR}

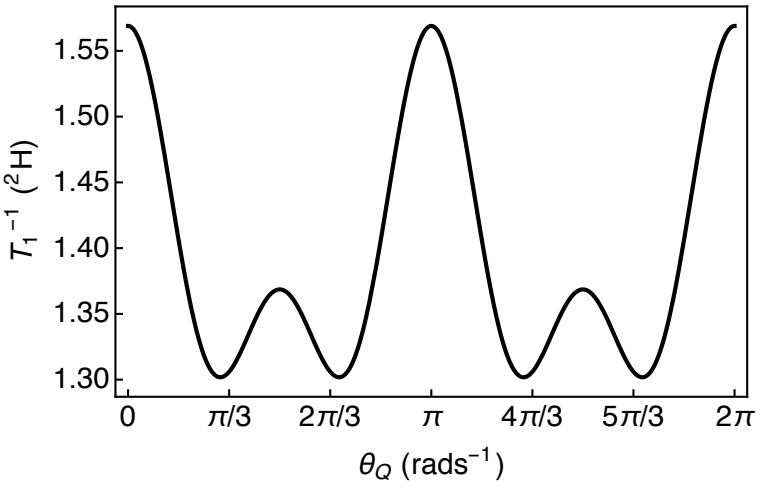

FIGURE 3.13: Plot of the longitudinal relaxation rate constant $T_1^{-1}(^2\mathrm{H})$ for the deuteron of the CH_2D group as a function of θ_Q. $\theta_Q = 70.5°$ for an equilateral triangle geometry.

is θ for the H_1D interaction and $-\theta$ for the H_2D interaction. For the quadrupolar interaction, the dominant principal axis of the ^{2}D electric field gradient tensor is assumed to be along the CD bond vector, so that $\beta_{PR} = \theta_Q$, where θ_Q is the angle formed between the 3-fold jump axis and the CD bond.

The following expressions apply to the relaxation of the ^{13}C nuclei in the CH_N groups on the six-membered ring (with $N = 1$ or 2), and for the ^{2}H relaxation of the deuteron in the monodeuterated methyl group:

$$T_1^{-1}(^{13}\mathrm{C}) = \mathrm{N}\omega_{\mathrm{CH}}^2\tau_{\mathrm{C}}, \tag{3.45}$$

$$T_1^{-1}(^2\mathrm{H}) = \frac{3\left(32 + 33\kappa\tau_{\mathrm{C}} + 9\kappa\tau_{\mathrm{C}}\left(4\cos(2\theta_{\mathrm{Q}}) + 3\cos(4\theta_{\mathrm{Q}})\right)\right)}{64\left(1 + 3\kappa\tau_{\mathrm{C}}\right)}\omega_{\mathrm{Q}}^2\tau_{\mathrm{C}}. \tag{3.46}$$

where N is the number of attached protons, ω_{CH} is the dipole-dipole coupling constant for the interaction between the proton and carbon nuclei, and ω_Q is the quadrupole coupling frequency of the deuteron. Figure 3.13 shows a plot of $T_1^{-1}(^2\mathrm{H})$ as a function of θ_Q. For a tetragonal geometry of the CH_2D group:

$$T_1^{-1}(^2\mathrm{H}) = \frac{(3 + \kappa\tau_{\mathrm{C}})}{2\left(1 + 3\kappa\tau_{\mathrm{C}}\right)}\omega_{\mathrm{Q}}^2\tau_{\mathrm{C}}. \tag{3.47}$$

These equations assume rigid-body rotational diffusion of the whole molecule (including the ring) and 3-fold jumps of the methyl group, with ^{13}C-^{1}H dipolar and quadrupolar

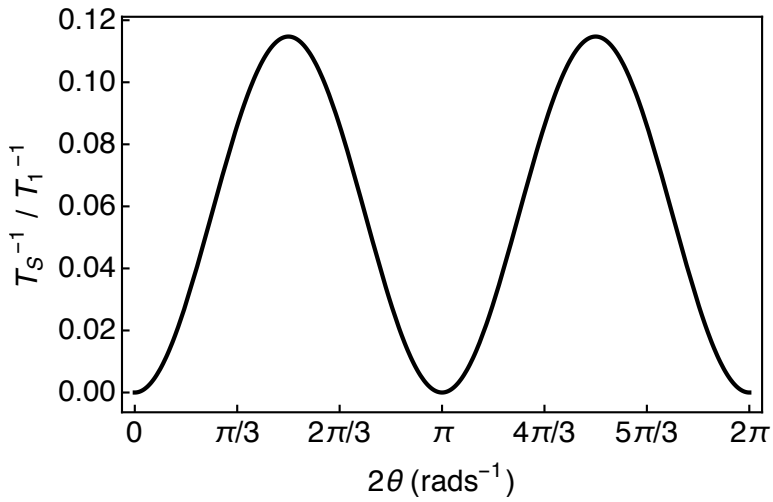

FIGURE 3.14: Plot of the relaxation rate ratio $T_{\mathrm{S}}^{-1}/T_{!}^{-1}$ for the protons of the CH_2D group as a function of 2θ. $2\theta = 60°$ for an equilateral triangle geometry.

relaxation dominating the ^{13}C and ^{2}D relaxation, respectively. For the simple case of point nuclei (ignoring vibrational averaging), the coupling constants are defined as follows:

$$\omega_{\mathrm{CH}} = -\left(\mu_0/4\pi\right)\gamma(^1\mathrm{H})\gamma(^{13}\mathrm{C})\hbar r_{\mathrm{CH}}^{-3}, \tag{3.48}$$

$$\omega_Q = \frac{e^2qQ}{2\hbar}, \tag{3.49}$$

where r_{HC} is the internuclear distance, Q is the electric quadrupolar moment of the deuterium nucleus, and eq is the electrical field gradient at the deuterium nucleus [199]. This relaxation model leads to the following expression for the ratio of T_S to T_1:

$$\frac{T_S}{T_1} = (4 + 3\kappa\tau_{\mathrm{C}})\,\frac{16\omega_{\mathrm{HD}}^2 + 9\omega_{\mathrm{HH}}^2}{192\omega_{\mathrm{HD}}^2 \sin^2 2\theta}. \tag{3.50}$$

Figure 3.14 shows a plot of T_S^{-1}/T_1^{-1} as a function of 2θ. In general the ratio T_S/T_1 depends on the jump rate κ and rotational correlation time τ_{C}, and is expected to depend on temperature, solvent, and other factors. However, in the "slow-jump regime" $\kappa\tau_{\mathrm{C}} \ll 1$, the ratio of T_S to T_1 becomes independent of κ and τ_{C}, and only depends on interaction parameters within the CH_2D group:

$$\frac{T_S}{T_1} \simeq \frac{16\omega_{\mathrm{HD}}^2 + 9\omega_{\mathrm{HH}}^2}{48\omega_{\mathrm{HD}}^2 \sin^2 2\theta} \simeq \frac{3\omega_{\mathrm{HH}}^2}{16\omega_{\mathrm{HD}}^2 \sin^2 2\theta}. \tag{3.51}$$

TABLE 3.3: ^{13}C longitudinal relaxation times T_1 for the ring ^{13}C nuclei of 0.1 M N-CH_2D-2-methylpiperidine in degassed CD_2Cl_2 solution at 11.7 T (500 MHz) and 25°C.

Site	$T_1(^{13}C)$/s
2	10.2 ± 0.3
3	6.3 ± 0.5
4	6.2 ± 0.2
5	6.5 ± 0.3
6	6.9 ± 0.4

The fact that the ^1H-^1H dipolar couplings are about 6 times stronger than the ^1H-^2D dipolar couplings (at equal distances) has been invoked in the last approximation. The observed direct proportionality of T_S to T_1 is consistent with the validity of the slow-jump regime over the explored range of experimental conditions.

3.6 Supporting relaxation data

The T_1 values for the ring ^{13}C sites and the CH_2D deuteron are reported for the case of 0.1 M N-CH_2D-2-methylpiperidine in degassed CD_2Cl_2 solution at 11.7 T (500 MHz) and 25°C.

3.6.1 Carbon-13 NMR

The measured ^{13}C T_1 values for N-CH_2D-2-methylpiperidine are shown in table 3.3 with the ^{13}C numbering scheme shown in figure 3.15. The ring CH_2 sites have similar ^{13}C relaxation time constants T_1 of 6.5 ± 0.3 s, with the ring CH site displaying a longer ^{13}C relaxation time constant of 10.2 ± 0.3 s. These relaxation times were measured by inversion recovery with 0.5 kHz ^1H decoupling.

3.6.2 Deuterium NMR

Under the same conditions, the ^2H spin-lattice relaxation time constant, given by $T_1(^2H)$, for the CH_2D deuteron was measured by inversion recovery to be 0.75 ± 0.01 s.

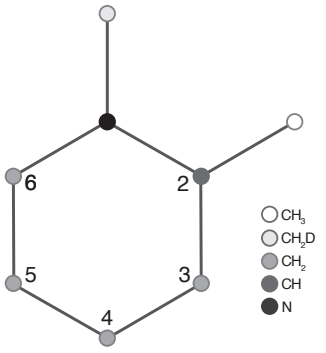

FIGURE 3.15: Structure of N-CH_2D-2-methylpiperidine, showing the numbering of ^{13}C sites on the piperidine ring.

3.7 Relaxation analysis

The ^{13}C and ^{2}H relaxation data allow an estimate of the rotational correlation time τ_C and the 3-fold jump rate κ. The following analysis refers to the data obtained on 0.1 M N-CH_2D-2-methylpiperidine in degassed CD_2Cl_2 solution, at 11.7 T (500 MHz) and 25°C.

3.7.1 Rotational correlation time

The overall rotational correlation time τ_C was estimated by analysing the experimental $T_1(^{13}C)$ relaxation time constants for ^{13}C nuclei in the CH_N groups on the six-membered ring, using equation 3.45 which applies for extreme-narrowing isotropic rotational tumbling, dominated by the ^{13}C-^{1}H dipolar relaxation mechanism [49]. By assuming an internuclear ^{13}C-^{1}H distance of 108.9 pm, which corresponds to a dipole coupling constant of $\omega_{CH}/2\pi = -23.4$ kHz, the following estimate of the rotational correlation time is obtained: $\tau_C = 3.8 \pm 0.6$ ps.

3.7.2 Thermally activated jump rate

The 3-fold jump rate constant κ may be estimated from the ^{2}D T_1 relaxation time constant, by using equation 3.46. The deuteron quadrupole coupling constant $\omega_Q/2\pi = 83.5$ kHz has been estimated by solid-state NMR [200, 201]. The unique principal axis of the deuteron quadrupole coupling tensor is assumed to be along the C-D bond, at an

angle of 70.5° with respect to the 3-fold jump axis. From comparing the experimental relaxation time $T_1(^2\mathrm{H}) = 0.75 \pm 0.01\,\mathrm{s}$ with equation 3.46, which was derived for the case of a hindered 3-fold rotor attached to a molecule undergoing isotropic rotational diffusion, and assuming that the quadrupolar mechanism dominates the deuteron relaxation, an estimate of the upper limit on the 3-fold jump rate is obtained: $\kappa \lesssim 3.2 \times 10^{10}\,\mathrm{s}^{-1}$.

3.8 Geometrical models

The product of the rotational correlation time and the 3-fold jump rate constant is therefore given by $\kappa\tau_\mathrm{C} \lesssim 0.12$, which supports the validity of the slow-jump regime and hence equation 3.51. Now consider the case where the three hydrogen nuclei of the CH_2D group are considered to be points, located at the vertices of an equilateral triangle. In this case $2\theta = 60°$, the internuclear distances are all equal, and the dipolar couplings are in the ratio of the gyromagnetic ratios $\omega_\mathrm{HH}/\omega_\mathrm{HD} = \gamma(^1\mathrm{H})/\gamma(^2\mathrm{D}) = 6.51$. This "equilateral triangle model" predicts the following relaxation time ratio: $\left(T_S/T_1\right)_\triangle = 10.6$. However, the observed value is quite different: $\left(T_S/T_1\right)_\mathrm{obs} = 3.1 \pm 0.1$.

How can this discrepancy be explained? One approach would be to call into question the intra-methyl relaxation model: However, as discussed above, the evidence for the dominance of intra-CH_2D interactions in the ^{1}H and ^{2}D relaxation is very strong. An alternative approach is to maintain the local intra-methyl relaxation model, but to modify the relative magnitudes and geometries of the dipole-dipole interactions within the rotating CH_2D group, to take into account differential vibrational averaging on a faster timescale than the molecular rotation or 3-fold jumps.

A detailed analysis of the effect of rapid vibrational motions on the dipolar interaction tensors in the CH_2D group would be a major project. For the sake of simplicity a naive picture is employed, in which the nuclei are still regarded as localized points, but with the ^{2}D nucleus displaced from its original position, in order to account for differential vibrational averaging of the ^{2}D and ^{1}H interactions. In order to maintain symmetry, we consider a model in which the ^{2}D nucleus is moved in the CH_2D plane along the line bisecting the ^{1}H-^{1}H vector (figure 3.16a). This adjustment changes the internuclear distances as well as the angle θ. The dependence of the theoretical relaxation rate ratio T_S/T_1 on the deuterium displacement is shown in figure 3.16b). There is

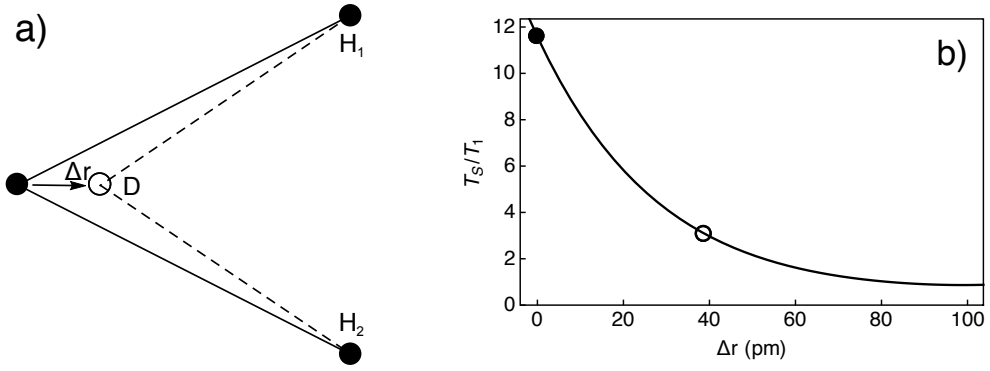

FIGURE 3.16: a) Adjustment of the effective geometry of the CH_2D group to account for the observed relaxation rate ratio $T_S/T_1 = 3.1$. The three nuclei are initially at the vertices of an equilateral triangle of side length 179.6 pm (black circles). The deuterium nucleus is displaced towards the original centre of the triangle (open circle) by a distance Δr. (b) Dependence of the relaxation rate ratio T_S/T_1 on the displacement Δr. The open circle shows the displacement needed for consistency with the observed rate ratio $T_S/T_1 = 3.1$. The black circle shows the predicted rate ratio from an equilateral triangle geometry. The calculations assume a rotational correlation time $\tau_C = 3.8\,\text{ps}$ and a thermally activated jump rate constant $\kappa = 1.7 \times 10^{10}\,\text{s}^{-1}$.

a strong sensitivity to the deuterium displacement, with the observed ratio $T_S/T_1 = 3.1$ being consistent with a displacement of 38.7 pm towards the original centre of the equilateral triangle. This represents a contraction in both ^{1}H-^{2}D distances by about 18%, and a change in the angle 2θ from 60° to 75.1°. A sketch of the adjusted geometry is shown in figure 3.16a).

This degree of geometrical distortion is probably unrealistic. It is more likely that differential vibrational averaging of the ^{1}H-^{1}H and ^{1}H-^{2}D dipolar interactions is responsible for the observed T_S/T_1 ratio. Vibrational motion out of the CH_2D plane is likely to be particularly effective. For example, the larger vibrational amplitudes of the ^{1}H nuclei relative to the more massive ^{2}D nucleus would reduce the ^{1}H-^{1}H dipolar interaction more than the ^{1}H-^{2}D dipolar interactions. This effect would lead to a correction in the right direction. A more sophisticated analysis of vibrational effects on the interaction parameters has not been attempted.

It is also possible to estimate the contribution of the chemical shift anisotropy mechanism to the proton singlet and longitudinal relaxation rates. Using the expressions given in reference [24], and the reported values of the ^{1}H CSA ($\sigma^H = -5\,\text{ppm}$), provides estimates of $T_S^{-1}(\text{CSA}) = 0.69 \pm 0.09 \times 10^{-3}\,\text{s}^{-1}$ and $T_1^{-1}(\text{CSA}) = 0.24 \pm$

$0.03 \times 10^{-3}\,\mathrm{s}^{-1}$. Clearly the chemical shift anisotropy mechanism does not significantly contribute to the CH_2D group singlet and longitudinal relaxation of N-CH_2D-2-methylpiperidine.

3.9 Rapidly rotating CH_2D groups

In the previous section it was demonstrated that the finite value of Ω_{Δ}^{12} in N-CH_2D-2-methylpiperidine allows access to the CH_2D nuclear singlet order [56]. A relatively low relaxation time ratio $T_S/T_1 \simeq 3.1$ was observed in this case. This was attributed to slow rotational jumps of the CH_2D moiety between three rotational conformers, which was supported indirectly by the ^{13}C and ^{2}H relaxation data, combined with a non-equilateral effective geometry for the two protons and the deuteron [56]. A much larger ratio of T_S to T_1 is expected in the case of rapid CH_2D rotation [183]. However, it has been unclear whether rapid CH_2D rotation is compatible with a sufficiently large chemical shift difference $\Delta\delta$, required for access to the nuclear singlet order.

Chemical inequivalence between CH_2D protons has only been described so far in three chemical compounds [179, 180, 182]. Of these, the one expected to provide rapid CH_2D rotation is (α-deuterio-*o*-chlorotoluene)chromium tricarbonyl (**I**), see figure 3.17. In this section, I show that rapid CH_2D rotation is not *a priori* incompatible with a finite chemical shift difference, and that long-lived nuclear singlet order is accessed in this rapidly-rotating CH_2D system, and displays a relatively large relaxation time ratio, $T_S/T_1 \simeq 11.3$.

3.9.1 Experiments

3.9.1.1 Proton spectra

The relevant portion of the proton NMR spectrum of **I**, in the presence of deuteron decoupling (nutation frequency = 500 Hz), is shown in figure 3.17. The two central peaks of the AB spectral pattern are unresolved, and the weak outer components are only just visible, indicating a very small value of the chemical shift difference relative to the J-coupling. A small chemical shift difference between the CH_2D protons is observed in this compound, and is attributed to a significant interaction between the orbitals of the

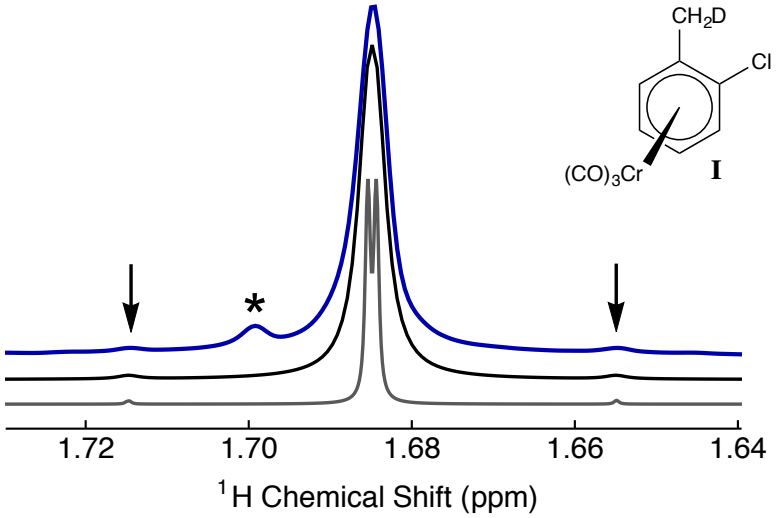

FIGURE 3.17: Part of the experimental ^{1}H spectrum of (α-deuterio-*o*-chlorotoluene)chromium tricarbonyl (**I**) in C_6D_6 solution acquired at 11.7 T (500 MHz) with 16 transients, in the presence of deuteron decoupling (500 Hz nutation frequency). Blue line: experimental proton spectrum; Black line: simulation ($|J_{HH}| = 14.7$ Hz, $\Omega^{12}_{\Delta} = 8.0$ ppb), using Lorentzian line broadening (half-width at half-height = 1.5 Hz); Grey line: simulation ($|J_{HH}| = 14.7$ Hz, $\Omega^{12}_{\Delta} = 8.0$ ppb), using Lorentzian line broadening (half-width at half-height = 0.3 Hz). The intensity of the grey spectrum has been artificially reduced. The inner splitting of the grey spectrum is 0.6 Hz. The asterisk indicates a small signal from a non-deuterated impurity, shifted in frequency by a secondary isotope effect. The small outer components of the AB spectral pattern are indicated by arrows. Inset: structure of **I**, indicating the out-of-plane chromium complex.

chromium centre and those of the CH_2D carbon, combined with the chiral environment provided by the *ortho*-Cl substituent [180]. The spectrum may be simulated by using the following parameters: $|J_{HH}| = 14.7 \pm 0.3$ Hz, $\Delta\delta = 8.0 \pm 0.4$ ppb. These are consistent with the literature [180].

3.9.1.2 Singlet NMR

The small chemical shift difference allows access to the long-lived singlet order of the CH_2D protons, by using radiofrequency pulse techniques which operate in the near-equivalence regime [150, 156–158]. In the current study, the SLIC (Spin-Lock Induced Crossing) method was used [157], as shown in figure 3.6. The parameters of the SLIC pulse sequence were chosen to maximise triplet-singlet population conversion: $\omega_{SLIC}/2\pi = 14.7$ Hz, $\omega_{LOCK}/2\pi = 0$ Hz and $\tau_{SLIC} = 170$ ms. An interval of 360 s was used between successive transients. The maximum amplitude of the singlet-filtered ^{1}H NMR signal, relative to that induced by a single 90° pulse, was found to be 0.28. The loss relative

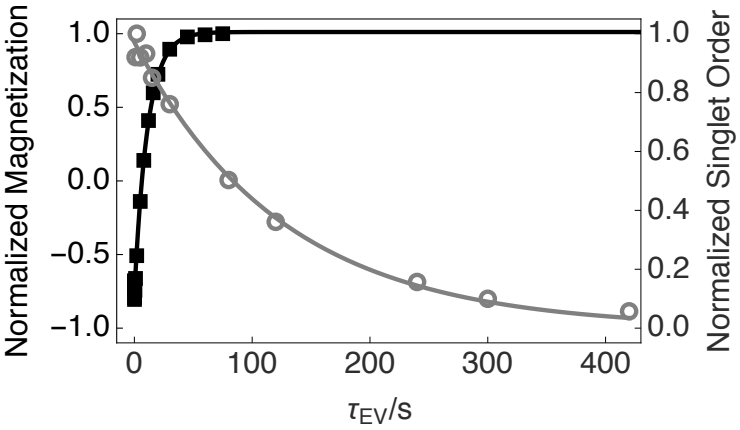

FIGURE 3.18: Experimental relaxation curves for the CH_2D protons in 0.1 M **I** in degassed C_6D_6 solvent (proton frequency = 500 MHz, temperature = 25°C). Open symbols, grey line, and right-hand axis: Decay of long-lived nuclear singlet order measured using the pulse sequence in figure 3.6. Filled symbols, black line, and left-hand axis: Spin-lattice relaxation measured by inversion recovery. All signal amplitudes were normalized to the first point. The fitted curves have a single-exponential form.

to the theoretical maximum of 2/3 [173] is not yet fully understood but is attributed to radiofrequency field imperfections and relaxation.

3.9.2 Results

A decay curve for CH_2D proton singlet order is shown in figure 3.18. This shows a single exponential decay with time constant $T_S = 126 \pm 6$ s. This is more than eleven times longer than the relaxation time for the longitudinal magnetization of the CH_2D protons, $T_1 = 11.2 \pm 0.6$ s, as estimated from the inversion recovery curve, also shown in figure 3.18. Without degassing, $T_S = 21.9 \pm 0.8$ s and $T_1 = 5.1 \pm 0.3$ s. Measurements of T_S and T_1 values for the CH_2D protons in **I** at several temperatures between 25°C and 55°C are shown in table 3.4. The ratio T_S/T_1 remains reasonably constant over this temperature range. Temperature is therefore an implicit parameter of T_1 and T_S.

TABLE 3.4: Relaxation times for the CH_2D protons in 0.1 M **I** in degassed C_6D_6 solution at 11.7 T (500 MHz), for a range of temperatures.

Temperature/°C	T_1/ s	T_S/ s	T_S/T_1
25	11.2 ± 0.6	126 ± 6	11.3 ± 0.8
35	12.6 ± 0.4	131± 10	10.4 ± 0.9
45	14.1 ± 0.5	141 ± 6	10.0 ± 0.6
55	15.6 ± 0.7	144 ± 7	9.3 ± 0.6

3.9.3 Discussion

The observed relaxation time ratio $T_S/T_1 \simeq 11.3$ is much larger than that found for the case of N-CH_2D-2-methylpiperidine, where a ratio of 3.1 was observed [56]. This may be attributed to much faster rotational diffusion of the CH_2D group in **I** around the approximate 3-fold axis. This is physically reasonable since the site adjacent to the CH_2D group in **I** is a sp^2-hybridized carbon, while the adjacent site in the N-CH_2D piperidine derivative is a sp^3-hybridized nitrogen, whose lone pair engages in a hyperconjugation interaction with the deuterated methyl group [179]. Neutron spectroscopy of methyl rotors show that sp^3 hybridization of the neighbouring atom is almost always associated with strong hindering of the methyl rotation, and therefore a small or absent tunnelling splitting [202]. It is therefore plausible that the CH_2D group has much greater rotational freedom in **I**, as compared to the N-CH_2D piperidine derivative studied in sections 3.2-3.8.

The torsional potential energy function for a methyl group adjacent to a sp^2 carbon is known to contain periodic components with both 6-fold and 3-fold symmetry [203]. The 3-site jump model for proton singlet relaxation developed in section 3.4.2 is therefore not appropriate to the case of compound **I**. In the discussion below, a model in which the CH_2D rotor performs free rotational diffusion is used, with correlation time τ_R, while the overall rotational diffusion of the molecule in solution is described by a correlation time τ_C. A model of this kind was used to treat methyl long-lived states and quantum-rotor-induced polarization in γ-picoline [141, 155]. As in section 3.4.3, the linear relationship of T_S and T_1 (table 3.4) indicates a common correlation time for these processes, and it is assumed that the proton relaxation in the CH_2D group is dominated by the local dipolar interactions between the protons and the deuteron. These local dipolar interactions are averaged on a fast timescale by rapid vibrational or librational motion, so it is not possible in general to assume that the nuclei can be treated as point dipoles at the vertices of an equilateral triangle [56].

3.9.4 Spectral densities for rapidly rotating CH_2D groups

For a freely diffusing methyl group, the contribution of internal motion to the correlation function is [61, 155]:

$$\langle D^{2*}_{m_2 m_1}(\Omega_{RM}(0)) D^{2}_{m'_2 m'_1}(\Omega_{RM}(\tau))\rangle = \delta_{m_1 m_2}\delta_{m'_1 m'_2}\delta_{m_2 m'_2}\delta_{m_1 m'_1} e^{-m_2^2 \frac{\tau}{\tau_R}}, \tag{3.52}$$

The spectral densities for the dipole-dipole and quadrupolar interactions therefore become:

$$\begin{aligned} J^{\lambda,\lambda'}_{mm'}(\omega) &= \delta_{mm'}\,\frac{1}{5} A^{\lambda,P}_{20} A^{\lambda',P}_{20} \sum_{m_2} D^{2*}_{0m_2}(\Omega^{\lambda}_{PR}) D^{2}_{0m'_2}(\Omega^{\lambda'}_{PR}) \\ &\quad \times \int_0^\infty d\tau\, e^{-m_2^2 \frac{\tau}{\tau_R}}\, e^{-\tau/\tau_C}\, e^{i\omega\tau}, \end{aligned} \tag{3.53}$$

with the spectral density at zero frequency, relevant in the extreme narrowing regime, becoming:

$$J^{\lambda,\lambda'}_{mm'}(0) = \delta_{mm'}\,\frac{1}{5} A^{\lambda,P}_{20} A^{\lambda',P}_{20} \sum_{m_2} \frac{\tau_C \tau_R}{m_2^2 \tau_C + \tau_R} D^{2*}_{0m_2}(\Omega^{\lambda}_{PR}) D^{2}_{0m'_2}(\Omega^{\lambda'}_{PR}). \tag{3.54}$$

In extreme narrowing, the isotropic rotational diffusion model leads to the following expressions for the T_1 and T_S relaxation rate constants for the CH_2D protons:

$$T_1^{-1} = \frac{(\tau_R + \tau_C)}{6\,(\tau_R + 4\tau_C)} \left(16\omega^2_{HD} + 9\omega^2_{HH}\right) \tau_C, \tag{3.55}$$

$$T_S^{-1} = \frac{8\tau_R \sin^2 2\theta}{(\tau_R + 4\tau_C)} \omega^2_{HD} \tau_C. \tag{3.56}$$

The CH_2D deuteron relaxation is assumed to be dominated by the electric quadrupole mechanism, with a rate constant given by:

$$\begin{aligned} T_1^{-1}(^2\mathrm{H}) = \frac{3}{16}\Big(\frac{1}{2}\,(1 + 3\cos 2\theta)^2 + \frac{6\tau_R \sin^4\theta}{(\tau_R + 4\tau_C)} \\ + \frac{6\tau_R \sin^2 2\theta}{(\tau_R + \tau_C)}\Big)\omega_Q^2 \tau_C, \end{aligned} \tag{3.57}$$

where a tetrahedral effective geometry is assumed. These are similar to the expressions given in section 3.5.5 (equations 1-4 of reference [56]) for the 3-site jump model of CH_2D relaxation.

3.9.5 Relaxation analysis

^{13}C and ^{2}D relaxation times were measured in degassed C_6D_6 solution at 11.7 T (500 MHz) and 25°C. The ^{2}D T_1 of the CH_2D group was 1.2 ± 0.1 s. The ^{13}C T_1 values for the CH sites of the *o*-chlorotoluene moiety were 5.3 ± 0.4 s.

The experimentally determined T_1 relaxation times for the aromatic ring ^{13}C sites were found to be consistent with a rigid-body rotational diffusion model, and by comparing with equation 3.45 lead to the following estimate of the overall rotational correlation time at 25°C: $\tau_C = 9.0 \pm 0.6$ ps. From comparing the experimental T_1 relaxation time constant of the CH_2D deuteron with equation 3.57, an estimate of the correlation time for free rotational diffusion of the CH_2D methyl rotor is obtained: $\tau_R = 2.8 \pm 0.3$ ps. In this case the product $\tau_C \tau_R^{-1} > 1$. This confirms that the CH_2D group in **I** undergoes local rotational diffusion which is more rapid than the overall rotational tumbling of the molecule. This is different from the case of N-CH_2D-2-methylpiperidine, where the 3-fold jumps of the CH_2D group are slow relative to the overall molecular tumbling, see section 3.7.2 [56].

The rotational diffusion model leads to the following expression for the relaxation time ratio T_S/T_1:

$$\frac{T_S}{T_1} = \left(1 + \frac{\tau_C}{\tau_R}\right) \frac{16\omega_{HD}^2 + 9\omega_{HH}^2}{48\omega_{HD}^2 \sin^2 2\theta} \tag{3.58}$$

$$\simeq \left(1 + \frac{\tau_C}{\tau_R}\right) \frac{3\omega_{HH}^2}{16\omega_{HD}^2 \sin^2 2\theta}. \tag{3.59}$$

using the approximation $|\omega_{HD}|^2 \ll |\omega_{HH}|^2$. The simplest model of *intra*-CH_2D interactions assumes that the proton and deuteron nuclei are fixed as points on the vertices of an equilateral triangle. Since all internuclear distances are equal, the angle between the unique principal axes of the two HD dipolar coupling tensors is given by $2\theta = \pi/3$. The estimated correlation times $\tau_C = 9.0 \pm 0.6$ ps and $\tau_R = 2.8 \pm 0.3$ ps lead to a predicted relaxation time ratio $T_S/T_1 = 47 \pm 4$. This is far larger than the observed ratio of ∼11.3.

In the case of N-CH_2D-2-methylpiperidine, a good agreement with the observed relaxation time ratio was obtained by adjusting the effective geometry of the CH_2D group to take differential vibrational averaging into account, see section 3.8. Moving the effective position of the deuteron by 38.7 pm towards the centre of the CH_2D triangle

generated good agreement with experiment [56]. In the current case, the same adjustment of effective geometry leads to a predicted relaxation time ratio $T_S/T_1 = 14.1 \pm 0.4$. This is in better agreement with the experimental result $T_S/T_1 \simeq 11.3$, although a significant discrepancy remains. The remaining discrepancy could be associated with deviations from the free rotational diffusion model, in the direction of a discrete jump model. Additional relaxation mechanisms could also be involved, such as interactions with neighbouring nuclei and spin-rotation interactions. This is plausible since small additional contributions can have a large proportionate effect on the small value of T_S^{-1}. This issue has not been investigated further.

3.10 Conclusions

It is possible to populate the long-lived nuclear singlet order in the proton pairs of monodeuterated methyl groups, under suitable conditions. This requires non-uniformity in the rotamer populations as well as a local chiral environment in order to induce a small isotropic chemical shift difference between the CH_2D protons. Both conditions are fulfilled for the CH_2D group in N-CH_2D-2-methylpiperidine, where a hyperconjugation effect involving the nitrogen lone pair perturbs the vibrational energies and hence the rotamer populations, while the neighbouring methyl group provides a chiral environment; and (α-deuterio-*o*-chlorotoluene)chromium tricarbonyl, where the small chemical shift difference observed is associated with the asymmetry of the complex coupled with the selective C-H(D) bond weakening induced by the $Cr(CO)_3$ moiety [33, 34]. Coordination of metals to arenes is known to result in a dramatic withdrawal of electron density from the arene [204] and produce a significant interaction between the orbitals of the chromium centre and those of the CH_2D carbon. The chiral environment is provided by the *ortho*-Cl substituent [180].

In the N-CH_2D-2-methylpiperidine system, the ratio of the singlet relaxation time T_S to the longitudinal relaxation time T_1 was found to be 3.1 ± 0.1 over a wide range of conditions, with the longest observed value of T_S approaching 1 minute at elevated temperature. The observation of a constant ratio of T_S to T_1 supports a relaxation model in which dipolar interactions between the CH_2D protons and deuteron dominate the singlet relaxation. However, a naive model in which the ^1H and ^2D nuclei of the CH_2D group are viewed as point-like magnetic dipoles fixed at the vertices of an equilateral

triangle predicts a much larger ratio of T_S to T_1. The effects of a geometric distortion in which the ^{2}D nucleus is displaced towards the centre of the triangle was explored and it was found that a displacement of 38.7 pm was needed to explain the experimental data. This adjustment should not be viewed as a realistic structural proposal, but as a crude attempt to represent the differential effects of vibrational averaging and nuclear wavefunction delocalization within a simplistic point-nucleus geometric model.

The observed relaxation time ratio of $T_S/T_1 \simeq 3.1$ is probably too small for most feasible applications. However, it should be noted that equation 3.51 permits a much larger ratio of T_S/T_1 in the case of fast 3-fold jumps, i.e. $\kappa\tau_C \gtrsim 1$. This does not occur in N-CH_2D-2-methylpiperidine, where the rotational barrier appears to be relatively large but does arise in other compounds displaying inequivalence of the CH_2D proton pair, such as in (α-deuterio-*o*-chlorotoluene)chromium tricarbonyl, where a free rotor rotational diffusion model was used in the relaxation analysis of the singlet relaxation time constant T_S. Rapid CH_2D rotation was found to extend the proton singlet relaxation time of monodeuterated methyl groups, and in the case of (α-deuterio-*o*-chlorotoluene)chromium tricarbonyl the time constant T_S was more than 10 times longer than T_1, and was consistently longer than 2 minutes. Furthermore, at least in this case, a sufficient differential was maintained between rotamer populations while still having a sufficiently low rotational barrier as to permit rapid CH_2D rotation. As a result, the chemical shift difference between the CH_2D protons was not completely quenched, and the nuclear singlet state remained experimentally accessible, as well as being long-lived. These results are encouraging for the future applications of long-lived singlet states in monodeuterated methyl groups.

Attempts to observe long-lived singlet states in other chiral CH_2D systems, such as derivatives of 3-^{2}D-lactic acid, and also N-CH_2D-3-methylpiperidine (similar to the substance used above, but with a more remote CH_3 group) were unsuccessful. Access to the CH_2D singlet state in both of these cases presumably failed because the chemical inequivalence of the CH_2D protons is too small to exploit. Apart from unusual circumstances [180], hyperconjugation between a lone pair on a neighbouring atom (such as N) and the methyl C-H(D) bonds seems to be a requirement for obtaining a sufficient chemical shift difference of a few ppb or more. At the time of writing this thesis experiments have not been attempted on other chiral compounds containing a X-CH_2D moiety, where X is an atom other than N possessing a lone pair, such as P, O or S.

It should be noted that many interesting chiral molecules do contain a tetrahedral N-methyl group of suitable type. Examples include the psychoactive agents lysergic acid, codeine, morphine, cocaine, heroin, and methamphetamine. It is not yet known whether the methyl-monodeuterated versions of these systems possess an accessible long-lived singlet state.

Chapter 4

Direct hyperpolarization and coherent readout of long-lived proton singlet order

Conventional nuclear magnetic resonance (NMR) experiments are limited by low sensitivity and weak signals. Hyperpolarization techniques such as dissolution-DNP (dynamic nuclear polarization) [71] enhance solution-state NMR signals by orders of magnitude [71, 205–207]. The large NMR signal enhancements have a range of important applications including ligand-binding, drug transport and metabolic tracing [87, 116, 208–210], and wide-ranging implications such as the characterization of cancer in human patients [87].

However, the range of applications for hyperpolarized NMR is strongly restricted by the finite lifetime of the enhanced magnetization, which is usually limited to the characteristic relaxation time T_1. This limitation is especially severe for protons, which tend to have short values of T_1, due to their relatively strong nuclear magnetism. Most applications of D-DNP have involved weakly magnetic isotopes such as ^{13}C, even though the ubiquitous protons give stronger NMR signals. This is because the short spin-lattice relaxation times of protons usually lead to a large loss in polarization during the transfer from the polarizer to the point of use.

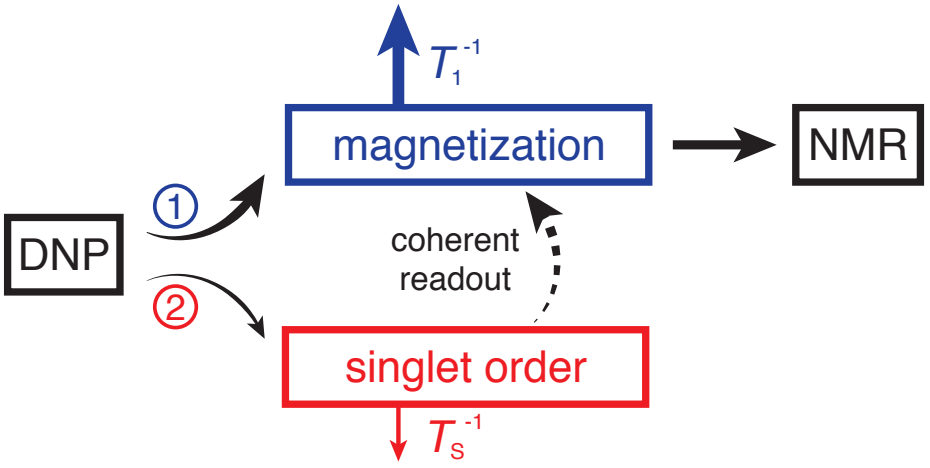

FIGURE 4.1: The significant NMR signal enhancements afforded by DNP may be harnessed by two approaches. ① DNP leads to hyperpolarized nuclear magnetization, which decays with the relatively large rate constant T_1^{-1}. ② In the case of spin-1/2 pairs, DNP also gives rise to hyperpolarized singlet order, which may be converted into observable magnetization by a coherent radiofrequency pulse sequence. Although the degree of singlet hyperpolarization is less than that of magnetization, the decay rate constant T_S^{-1} is much smaller than T_1^{-1}. The hyperpolarized signals may be larger at long times, when the singlet route is taken.

The use of LLS offers a promising means to transcend the limitation of hyperpolarized magnetization decaying rapidly in solution [14–16, 20, 21, 23, 28, 29, 31–33, 140, 142, 143, 146, 183, 208]. LLS are protected against intra-molecular dipole-dipole relaxation and other symmetric decay mechanisms, and typically have extended lifetimes $T_S > T_1$, see figure 4.1. The combination of LLS phenomena with hyperpolarization techniques is particularly promising, and applications of nuclear singlet order to hyperpolarized NMR experiments have been proposed [21, 28, 32, 34, 71, 87, 143, 145, 146, 208].

In this chapter, it is shown that this limitation may be overcome by (1) exploiting near-equivalent proton pairs; (2) direct hyperpolarization of long-lived proton singlet states in those proton pairs by using D-DNP, and (3) coherent and efficient conversion of the hyperpolarized proton singlet order into observable magnetization.

4.1 Introduction

Consider the protons (i and j) in the N-CH_2D group of N-CH_2D-2-methylpiperidine. If the chemical shift difference between the members of the spin pair is sufficiently small, the spins are termed *near-equivalent* [24]. The condition for near-equivalence is $\left|\Omega_\Delta^{ij}\right| << \left|2\pi J_{ij}\right|$, where Ω_Δ^{ij} is the chemical shift difference between the spins i and

j, and J_{ij} is the scalar coupling between the members of the spin pair. When this condition is satisfied, the energy eigenstates are approximately equal to the nuclear singlet and triplet states, and the nuclear singlet order is stable at high magnetic field without intervention. If the near-equivalence condition is not met, on the other hand, the nuclear singlet order must be maintained by applying an on resonant radiofrequency field [149], or by shuttling the sample to a region of sufficiently low magnetic field [16].

DNP generates a high nuclear Zeeman polarization p_Z, which may be associated with a very low nuclear spin temperature, on the order of milliKelvin. If the spin temperature is assumed to be uniform, a nuclear singlet polarization p_S is also generated, given by [25]:

$$p_S = -\frac{1}{3}p_Z^2. \tag{4.1}$$

A derivation of equation 4.1 is shown in section 2.10. The direct generation of hyperpolarized singlet order by DNP was first demonstrated for the case of [1,2-$^{13}C_2$]pyruvic acid [25]. However, in that case, the large chemical shift difference between the ^{13}C sites caused rapid singlet decay in high magnetic field, and no significant advantage could be demonstrated over conventional Zeeman polarization. The direct generation of nuclear singlet order by DNP was also demonstrated in magnetically-equivalent systems [55, 143] but in these systems chemical reactions or inefficient cross-relaxation processes are required to generate weakly observable NMR signals [55, 143].

In this section it is demonstrated that the use of *near-equivalent* proton pairs allows the long lifetime of hyperpolarized singlet order to be exploited in high magnetic field, while still providing an efficient, coherent route for conversion of the nuclear singlet order into enhanced NMR signals. Under these circumstances, the "singlet route" (②, lower part of figure 4.1) may provide stronger, longer-lasting, hyperpolarized NMR signals than the "Zeeman route" (①, upper part of figure 4.1).

As a proof of concept, the CH_2D protons of N-CH_2D-2-methylpiperidine were chosen as the near-equivalent spin pair for these experiments. The CH_2D protons have a 14 ppb chemical shift difference due to the chiral environment generated by the nearby methyl substituent, see figure 3.4 [56, 179, 184]. The structure of N-CH_2D-2-methylpiperidine is shown in figure 3.1. Coherent readout of the long-lived spin order is achieved, after hyperpolarization with D-DNP, by applying a singlet-to-magnetisation (S2M) pulse sequence [150, 156]. The bulk of the nuclear singlet order is converted to

magnetization, obviating the need for chemical reactions or weak cross-relaxation processes [55, 141, 143, 147, 155]. This procedure allows strongly enhanced proton NMR signals to be observed more than one minute after dissolution, by which time the hyperpolarized magnetization has completely disappeared, i.e. enhanced proton NMR signals are observed even when the hyperpolarized magnetization has completely vanished.

4.2 D-DNP methods

Solutions of 0.375 M N-CH_2D-2-methylpiperidine in the glass-forming mixture D_2O:glycerol-d_8 (50:50 v/v) were doped with 25 mM TEMPOL (**II**). The solution was sonicated for 2 minutes. Ten frozen pellets of **II** (10 μL volume per pellet) were inserted into a home-built polarizer. The sample polarized in a magnetic field of 6.7 T and at a temperature of ∼4.2 K for ∼48 minutes by applying frequency-modulated microwave irradiation at 188.3 GHz frequency and 100 mW power [211, 212]. The microwave modulation frequency and amplitude were 10 kHz and 50 MHz, respectively. The polarized pellets were dissolved with 5 mL CD_3CN solvent (degassed via bubbling with nitrogen gas for 5 minutes) preheated to 410 K at a pressure of 10 bar. The liquid sample was transferred in 10.7 s to a 11.7 T (500 MHz) NMR magnet by pushing with helium gas at 6 bar through a PTFE tube (1.5 mm inner diameter) running inside a magnetic tunnel (0.91 T, 5 m length) [135]. 1 s was taken for sample injection and bubble dissipation.

4.3 Solid-state polarization

Zeeman polarization p_Z^{solid} was accumulated in the solid-state for a sample of **II** in a magnetic field of 6.7 T and at a temperature of ∼4.2 K under the action of negative dynamic nuclear polarization (DNP) [212]. A Zeeman polarization of $p_Z^{solid} = -59 \pm 5\,\%$ was achieved in ∼48 minutes, see figure. 4.2a). The solid state enhancement ϵ_Z^{solid} was approximately -360±20 compared to a spectrum recorded with the microwaves off, see figure 4.2b). The thermal equilibrium spectrum was acquired after a 1 hour equilibration period at ∼4.2 K.

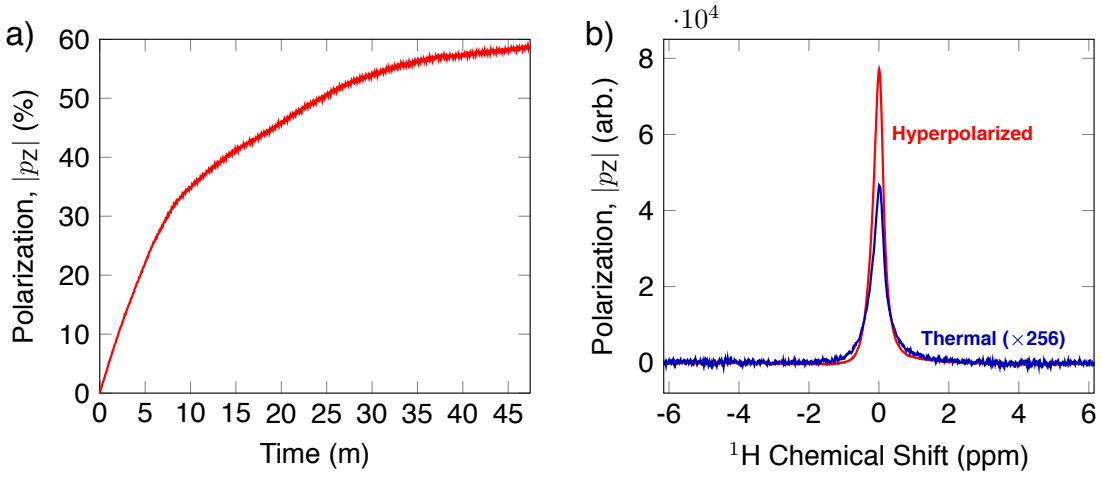

FIGURE 4.2: a) Build up of Zeeman polarization p_Z^{solid} in the solid state for a sample of **II** in a magnetic field of 6.7 T and at a temperature of ∼4.2 K. A Zeeman polarization of $p_Z^{solid} = -59 \pm 5\,\%$ was reached after ∼48 minutes. b) Solid state hyperpolarized (red) and thermal equilibrium (blue) spectra. The enhancement in the solid state is $\epsilon_Z^{solid} \simeq -360 \pm 20$.

4.4 Singlet order vs. magnetization

The enhanced NMR signals from the hyperpolarized magnetization and the nuclear singlet order are compared by using the procedure sketched in figure 4.3a). A sample of **II** has been prepared as described in section 4.2. The hyperpolarized sample is dissolved in deuterated acetonitrile solvent preheated to 410 K (pressure ∼10 bar) and transferred into a 11.7 T NMR magnet through a ∼0.9 T "magnetic tunnel" in transport time of ∼10 s [135]. After a variable high field waiting time τ_{HF}, a $\pi/2$ pulse is applied and the NMR signal is acquired (blue). Note that the single pulse and signal acquisition leaves any DNP-generated singlet order unperturbed, to a good approximation. The nuclear singlet order is read out by applying a T_{00} filter sequence, followed by a S2M pulse sequence, with a combined duration of ∼2 s [55, 56, 150, 156]. The T_{00} filter quenches all NMR signals not originating from the nuclear singlet order, and the S2M pulse sequence converts hyperpolarized singlet order into transverse magnetization, leading to a second NMR signal (red). The T_{00} filter is described in more detail in appendix B and references [54–56]. The time-reversal of the S2M sequence (M2S) is described in more detail in section 2.13. The parameters of the S2M pulse sequence were as follows: τ_J = 21.4 ms, $n_1 = 3$ and $n_2 = 1$. The sample is allowed to rest in the 11.7 T magnet for an additional 300 s in order to achieve thermal equilibrium, and a third NMR signal is acquired using a $\pi/2$ pulse (black). Fourier transformation of this signal provides the

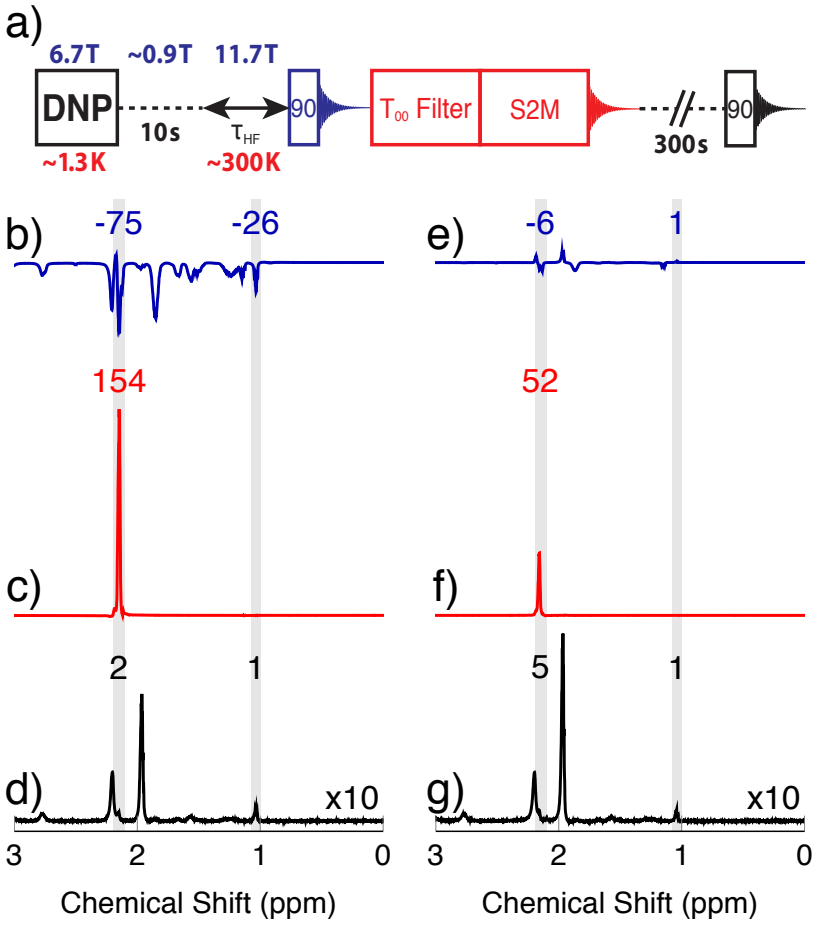

FIGURE 4.3: a) Timing sequence for acquiring spectra from the hyperpolarized magnetization, the hyperpolarized singlet order, and in thermal equilibrium, from the same sample. (b-d) Spectra obtained from a sample of **II** dissolved in degassed CD_3CN solution, hyperpolarized in the negative sense by DNP, and with a waiting interval τ_{HF} = 15 s after arrival in the high field magnet. b) Spectrum from hyperpolarized magnetization showing negatively enhanced signals; c) Spectrum from the nuclear singlet order converted into magnetization by the S2M sequence, showing a strongly enhanced CH_2D signal; d) Thermal equilibrium spectrum. (e-g) Similar spectra obtained on a second hyperpolarized sample of **II** dissolved in degassed CD_3CN solution, using a waiting interval τ_{HF} = 35 s after arrival in the high field magnet.

thermal equilibrium spectrum.

Figures 4.3(b-d) show the spectra obtained with a delay of τ_{HF} = 15 s. Relevant spectral ranges are shaded in grey and the integrals across these ranges are given above the spectra. All integrals are normalized to the intensity of the fully protonated methyl group at 1.09 ppm in the thermal equilibrium spectrum. The signal originating from the CH_2D group is at 2.20 ppm, and is partially obscured by a water impurity signal at 2.24 ppm. The acetonitrile solvent resonance is at 1.98 ppm. The spectrum generated by the initial $\pi/2$ pulse is shown in figure 4.3b), and displays enhancements of -75 and -26 for the CH_2D and CH_3 spectral regions, respectively. These signals originate

TABLE 4.1: Chemical shift of the water impurity for different volumes of co-mixed N-CH_2D-2-methylpiperidine, glass-forming D_2O:glycerol-d_8 (50:50 v/v) and TEMPOL (**II**) dissolved in 0.5 mL degassed CD_3CN solvent at 11.7 T (500 MHz) and 25°C. Chemical shifts were referenced with respect to the CD_3CN solvent peak.

Volume/μL	Chemical shift/ppm
2	2.217
5	2.297
10	2.389

from the hyperpolarized magnetization, with the negative sign reflecting the sense of the DNP. The signal obtained from the directly hyperpolarized singlet order is shown in figure 4.3c), and clearly exceeds the signal from the hyperpolarized magnetization, displaying an enhancement of +154. Only the CH_2D signal appears in figure 4.3c), since the T_{00} sequence suppresses signals which do not pass through the nuclear singlet order of the CH_2D protons.

The advantage of using hyperpolarized singlet order over hyperpolarized magnetization is even more pronounced at longer high field waiting times τ_{HF}. Spectra obtained with $\tau_{HF} = 35\,s$ are displayed in figures 4.3(e-g) and show only weak traces of signals from the hyperpolarized magnetization. The signal obtained from hyperpolarized singlet order at $\tau_{HF} = 35\,s$, on the other hand, still gives an enhancement of more than 50 relative to thermal equilibrium.

4.5 Water impurity

The resonance position of the impurity, thought to originate from residual water [213], was found to be dependent on the volume of **II** dissolved in degassed CD_3CN solvent, see table 4.1. At higher concentrations of **II**, the water impurity was shifted sufficiently far downfield such that the CH_2D resonance was unobscured in the proton NMR spectrum. For example, at a 10 μL volume of **II** the CH_2D peak was observed at 2.389 ppm. For volumes of **II** <2 μL, such as those achieved after dissolution, the CH_2D peak was obscured by a more intense water resonance. The resonance shift of the water impurity as a function of the volume of **II** is approximately linear, but is not currently understood. A plausible mechanism would be an exchange interaction between the -OH protons of the TEMPOL radical with those of the residual protonated water belonging to the glassy matrix. Such an exchange interaction could simultaneously lead to a downfield peak

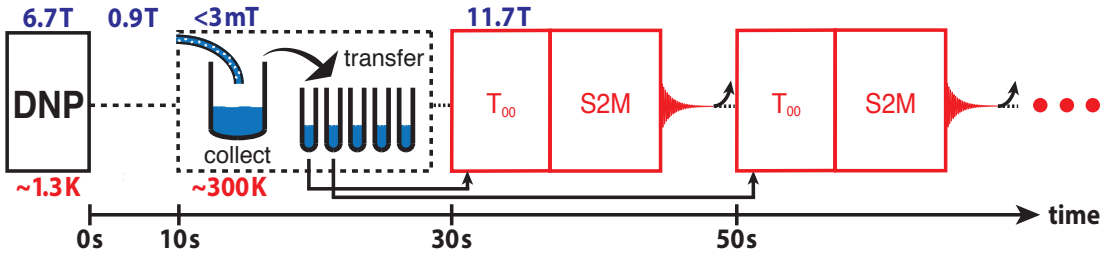

FIGURE 4.4: The procedure for monitoring the decay of the hyperpolarized singlet order. Hyperpolarized N-CH_2D-2-methylpiperidine is collected after dissolution at low magnetic field ($\leq$3 mT) in a flask preloaded with 2 mL degassed CD_3CN solvent. The solution is pipetted (at low magnetic field) into 5 separate 0.5 mL NMR tubes. The first tube is inserted into the 11.7 T magnet, a T_{00} filter sequence is applied to select out NMR signals passing through the nuclear singlet order [150, 156], and the S2M pulse sequence converts the hyperpolarized proton singlet order into observable magnetization for detection [55, 56]. Within the following 20 s the sample is ejected and the next NMR tube is injected; this procedure is repeated for all five NMR tubes. The curved arrow after each signal acquisition represents the ejection of the NMR tube.

shift for the water resonance and broader NMR lines. It is not yet known whether there are any previous reports of similar phenomena in the literature.

4.6 Decay of hyperpolarized singlet order

The hyperpolarized T_S is estimated by using the procedure sketched in figure 4.4. A hyperpolarized sample of **II** is flushed out of the cryostat using hot acetonitrile solvent and collected in a flask preloaded with 2 mL degassed acetonitrile solution in the stray field of a 11.7 T NMR magnet ($\leq$3 mT). The solution is divided into aliquots in the ambient magnetic field of the lab bench. The first 0.5 mL aliquot is loaded into an NMR tube and inserted into the 11.7 T NMR magnet. NMR signals are obtained from the hyperpolarized singlet order by applying a T_{00} filter sequence followed by a S2M pulse sequence [150, 156]. The tube is then ejected and a second tube is inserted that had been filled in the meantime. The delay between the measurements on the two tubes is 20 s. This process is repeated for a total of five tubes.

The signal enhancement factors in a Zeeman hyperpolarization experiment and a singlet hyperpolarization experiment are denoted by ϵ_Z and ϵ_S, respectively. These are given by the spectral integrals of the CH_2D peak relative to thermal equilibrium, i.e. $\epsilon_Z = I_Z/I_{eq}$ and $\epsilon_S = I_S/I_{eq}$, where I_Z and I_S are the integrals for the direct Zeeman and singlet hyperpolarization experiments, respectively. In practice, the intensity I_{eq} of the thermal-equilibrium CH_2D peak was estimated by multiplying the CH_3 peak intensity

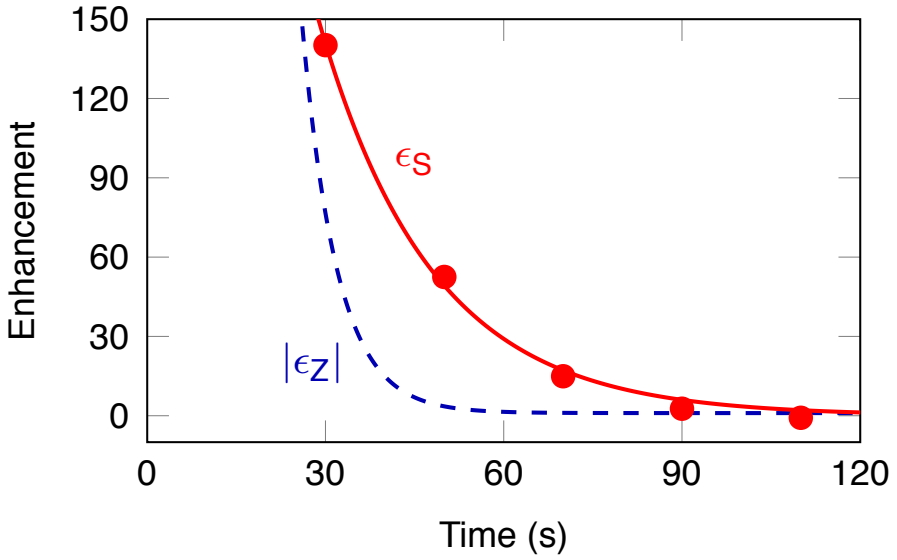

FIGURE 4.5: Filled circles: Experimental values of the signal enhancement factor in a singlet NMR experiment $\epsilon_S(t)$, as a function of the elapsed time t after dissolution. Solid line: Exponential decay curve given by $\epsilon_S(t) = \epsilon_S(0)\exp\{-t/T_S\}$, with initial enhancement $\epsilon_S(0) = 680$ and time constant $T_S = 19.0$ s. Dashed blue line: Magnitude of the signal enhancement in a Zeeman polarization experiment, as inferred from the data: $|\epsilon_Z(t)| = |\epsilon_Z(0)|\exp\{-t/T_1\}$, with $\epsilon_Z(0) = -14\,750$ and $T_1 = 5.9$ s.

by 2/3, in order to avoid complications caused by the overlap of the CH_2D peak with a water impurity peak.

The experimental signal enhancement factors $\epsilon_S(t)$ are shown by the filled symbols in figure 4.5. The time coordinate t of each point is given by the total elapsed time since dissolution, including the transport of the sample out of the polarizer, the waiting time in low magnetic field (different for each aliquot), the insertion into the high field magnet and any waiting time for stabilization before application of the pulse sequence shown in figure 4.4. The data fit well to a mono-exponential decay with a time constant $T_S = 19 \pm 3$ s, and an initial enhancement $\epsilon_S(0) = 680 \pm 126$.

A direct comparison with the signal enhancement from Zeeman polarization is not straightforward, since the Zeeman polarization decays rapidly and the spectral analysis is complicated by the peak overlap. The dashed blue curve in figure 4.5 shows an indirect estimate of $\epsilon_Z(t)$ which was inferred as follows: (i) The Zeeman polarization level was estimated by comparing the DNP-enhanced solid-state NMR signal at ∼1.3 K with a thermal equilibrium signal measured at ∼4.2 K (both signals were measured in the polarizer). This comparison gave the following estimate of the Zeeman polarization level in the solid state, prior to dissolution: $p_Z^{\text{solid}} = -59 \pm 5\,\%$; (ii) It was assumed that

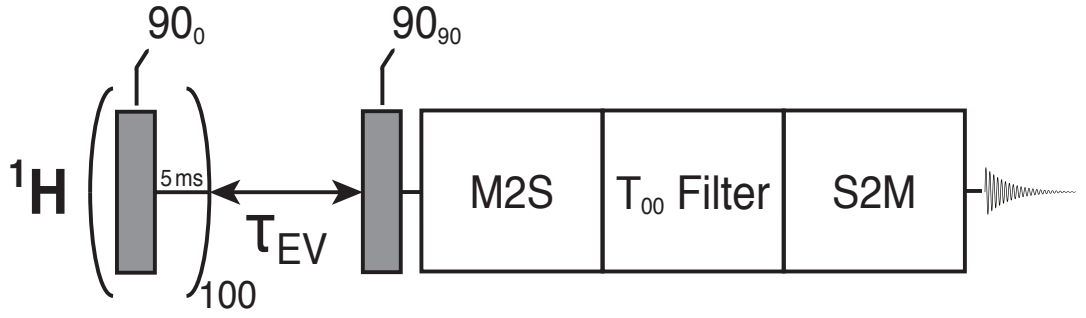

FIGURE 4.6: Pulse sequence for estimating the longitudinal relaxation time of the obscured CH_2D resonance.

the Zeeman polarization is substantially preserved throughout the dissolution process, so that $p_Z(0) \simeq p_Z^{\text{solid}}$, where $p_Z(0)$ is the Zeeman polarization immediately after dissolution; (iii) The thermal equilibrium Zeeman polarization for protons in a magnetic field of 11.7 T and a temperature of ∼300 K is governed by the Boltzmann distribution, and is given by $p_Z^{\text{eq}} = \hbar\gamma B^0/2k_BT = 39.8 \times 10^{-6}$, see section 2.2 for more details. Combining these results gives the following best estimate for the initial signal enhancement factor in the Zeeman-polarized experiment: $\epsilon_Z(0) = p_Z(0)/p_Z^{\text{eq}} = -14\,750$. The dashed blue line in figure 4.5 shows the curve $|\epsilon_Z(t)| = |\epsilon_Z(0)| \exp\{-t/T_1\}$, where $T_1 = 5.9$ s as estimated by separate saturation-recovery experiments. Figure 4.5 therefore shows that the singlet-polarization experiment yields larger signals than the Zeeman-polarized experiment, for elapsed times of greater than 30 s after dissolution.

4.7 Singlet-filtered saturation-recovery experiments

The pulse sequence for measuring the ^{1}H T_1 of the CH_2D peak obscured by the suspected water impurity is shown in figure 4.6. The scheme commences with a "saturation comb" $(90^\circ_0$ - delay$)_{100}$ which crushes all observable magnetization. The delay between 90°_0 pulses was 5 ms. After an evolution period τ_{EV}, ordinary magnetization is accrued and converted into nuclear singlet order by the M2S (magnetization to singlet) pulse sequence [150, 156]. The T_{00} filter destroys all signals not originating from the proton singlet order [55, 56], solely selecting the CH_2D singlet signal, which is subsequently back-converted into observable magnetization by the S2M pulse sequence. NMR spectra were acquired as a function of τ_{EV} and the CH_2D T_1 of 5.9 ± 0.7 s was determined from the integrals of the resulting signal resonances.

4.8 Estimate of S2M efficiency

In the current study, the combination of a T_{00} filter and the S2M (singlet-to-magnetization) pulse sequence are used to retrieve the nuclear singlet order generated directly from DNP. In order to determine the efficiency of the S2M sequence η_{S2M} the Zeeman magnetization of a thermally polarized sample was converted to nuclear singlet order, and subsequently reconverted, by using the M2SS2M (magnetization-to-singlet singlet-to-magnetization) pulse sequence, see section 2.13 for more details. The M2S pulse sequence converts the hyperpolarized transverse magnetization into hyperpolarized singlet order, any remaining magnetization is quenched by using a T_{00} filter, and lastly the nuclear singlet order is back-converted to magnetization using the S2M pulse sequence. The signal was recorded and compared to a separate signal which was acquired following an excitation with a 90°_{0} pulse. The ratio of the two signals was found to be 0.4. The efficiency of the S2M pulse sequence is therefore: $\eta_{\mathrm{S2M}} = 0.4^{1/2} = 0.63 \pm 0.02$, which is close to the theoretical maximum of $\sqrt{2/3}$ [173]. The experiment was carried out on a sample of 5 μL **II** in 0.5 mL CD_3CN solvent.

4.9 Discussion

4.9.1 Singlet polarization levels

The singlet polarization p_{S} in the solution state, immediately after dissolution, may be deduced from the signal enhancement factor $\epsilon_{\mathrm{S}}(0)$ through the equation:

$$\left|p_{\mathrm{S}}(0)\right| = \epsilon_{\mathrm{S}}(0)\frac{\left|p_{\mathrm{Z}}^{\mathrm{eq}}\right|}{\eta_{\mathrm{S2M}}}, \tag{4.2}$$

where $p_{\mathrm{Z}}^{\mathrm{eq}}$ is the thermal equilibrium Zeeman polarization in high magnetic field, and η_{S2M} is the conversion factor for nuclear singlet order into Zeeman order using the S2M pulse sequence. The triplet-singlet-triplet conversion was found to have an experimental efficiency of $\eta_{\mathrm{S2M}} = 0.63 \pm 0.02$ for N-CH_2D-2-methylpiperidine under the relevant experimental conditions, see section 4.8. From the thermal equilibrium Zeeman polarization $p_{\mathrm{Z}}^{\mathrm{eq}} = 39.8 \times 10^{-6}$ and the enhancement factor $\epsilon_{\mathrm{S}}(0) = 680 \pm 126$ (see above), the following estimate for the initial singlet polarization, immediately after dissolution, was determined to be: $\left|p_{\mathrm{S}}(0)\right| = 4.3 \pm 0.8\%$.

It is instructive to compare this figure with that deduced from the DNP-induced Zeeman polarization by using equation 4.1. As described above, the best estimate of the Zeeman polarization level in the solid state is $p_{\mathrm{Z}}^{\mathrm{solid}} = -59 \pm 5\,\%$. Application of equation 4.1 gives the following estimate of the DNP-induced singlet polarization: $p_{\mathrm{S}} = -12 \pm 2\,\%$.

The best estimate of the singlet polarization, as deduced from the solid-state Zeeman polarization, is therefore ∼3 times larger than the best estimate of the same quantity measured in solution after dissolution. There are many possible reasons for this discrepancy, including the following: (i) The nuclear singlet state is an approximate eigenstate, and thermalization between the Zeeman and singlet reservoirs is incomplete at the time of dissolution, limiting the applicability of equation 4.1; (ii) The violation of the high-temperature approximation (section 1.5.3) may introduce spin order that is manifest neither as magnetization nor as nuclear singlet order; (iii) The concept of a uniform spin temperature under DNP may not be valid; (iv) The estimate of Zeeman polarization is associated with multiple sources of uncertainty, including the bleaching effects of radicals on the solid-state NMR signals [113] and the temperature-dependence of the detection electronics; (v) The spin dynamics during the dissolution process are not well understood, and as such a loss in the level of the nuclear singlet order during the dissolution process may not be ruled out; (vi) Any possible dependence of relaxation times on magnetic field was not accounted for. Given these major sources of uncertainty, the highly qualitative agreement between the estimates of the DNP-induced singlet order from the solid-state and solution-state NMR measurements is satisfactory.

4.9.2 Singlet lifetime

The lifetime of the hyperpolarized singlet order was found to be ∼3.1 times longer than that belonging to longitudinal magnetization, in agreement with the previous study in chapter 3. In prior experiments, the chemical inequivalence at high magnetic field was suppressed by an on resonant spin-locking field, which is assumed to be equivalent to storing the hyperpolarized singlet order in a ≤3 mT magnetic field. The reported singlet lifetime of 0.2 M N-CH_2D-2-methylpiperidine in degassed CD_3CN solvent at 11.7 T and 25°C is: $T_{\mathrm{S}} = 32.8 \pm 0.6$ s, see section 3.3 [56]. Discrepancies between the reported singlet

lifetimes are attributed to the presence of paramagnetic oxygen and radicals dissolved in solution.

4.10 Conclusions

Proton singlet order may be generated directly from a sample polarized strongly by dynamic nuclear polarization. In near-equivalent systems, the directly-generated singlet order is stable in high magnetic field without further intervention, and may be converted into observable magnetization by known techniques. It has been shown that such signals may be stronger than those associated with the nuclear Zeeman polarization, since the hyperpolarized singlet order decays more slowly than magnetization. This procedure does not require a chemical reaction to break the symmetry and does not exploit inefficient cross-relaxation phenomena. The study described here also shows that much remains to be done in understanding the behaviour of nuclear spins during the DNP and dissolution processes.

Chapter 5

Singlet-scalar relaxation of the second kind in the regime of slow quadrupolar relaxation

In this chapter, an important relaxation mechanism for the nuclear singlet order, which involves a difference between the scalar couplings of the spins-1/2 to a third nucleus which has an independent decay mechanism, such as nuclear quadrupolar relaxation, is presented. This new relaxation mechanism is a variant of the scalar relaxation of the second kind (SR2K) mechanism. Unlike the corresponding mechanism for longitudinal nuclear relaxation, which requires very rapid third-spin relaxation, the singlet-SR2K mechanism is significant for slow third-spin relaxation.

In the following sections, theoretical singlet-SR2K rate expressions are provided for the case of a spin-1/2 pair scalar coupled to a third nucleus exhibiting an intrinsic relaxation mechanism. It is shown that the singlet-SR2K mechanism may be suppressed by applying on resonant radiofrequency irradiation to the singlet spins or to the third nucleus. These phenomena are demonstrated experimentally for the ^{13}C singlet pair in the 4-spin system of a ^{13}C,^{2}H-labelled fumarate diester. The singlet relaxation time constants T_{S} were found to increase with increasing ^{13}C and ^{2}H spin-locking rf-field amplitudes, and the longest observed value of T_{S} approached 30 seconds. The experimental data are compared with the theoretical rate expressions.

5.1 Introduction

Pairs of spin-1/2 nuclei can form magnetically "silent" configurations which decay with extended lifetimes [14–20, 22–27, 56, 142, 144, 149, 150, 156–158, 183]. The relaxation time constant for the long-lived state (LLS) is denoted T_S and often transcends the traditional limit of signal observation for the nuclear magnetization, set by the conventional longitudinal relaxation time T_1, by a large factor [21, 28, 29, 33, 34, 143, 144, 146, 208]. There is great potential in the pairing of LLS phenomena with hyperpolarization methodology. Dissolution-dynamic nuclear polarization (D-DNP) in particular is a hyperpolarization technique which affords significant NMR signal enhancements compared to thermal equilibrium [71]. This promising combination has far-reaching applications, such as studies of hyperpolarized transport and MRI in which the behaviour of cancerous tissue may be characterized [87]. The current scope of hyperpolarized experiments is restricted by T_1. The LLS relaxation time T_S, which is often much longer than T_1, offers an encouraging means to overcome the limited observation window provided by hyperpolarized magnetization.

For spin-1/2 pairs in the near-equivalence regime, the singlet order is known to be sheltered from the motional modulation of the in-pair dipole-dipole interaction in solution [14–16, 26]. However, many other relaxation mechanisms remain active and can drive efficient singlet relaxation, attenuating the value of T_S. These may be summarized as follows:

1. Out-of-pair dipole-dipole interactions. Nuclei in close proximity to the spin-pair can shorten singlet lifetimes via dipole-dipole couplings [24]. The strength of the dipole-dipole coupling is dependent on the internuclear distance and participating nuclear isotopes [22]. Intermolecular dipole-dipole interactions with other molecules in solution and solvent molecules are also present but are often weaker in magnitude [56, 153].

2. Chemical shift anisotropy. Motional modulation of CSA tensors in solution can provide strong singlet relaxation [24, 145]. As the relaxation rate is sensitive to the difference in chemical shielding tensors at the two nuclear sites involved, molecular agents exhibiting singlet states are typically designed to only partially violate local symmetry [24]. A locally centrosymmetric naphthalene derivative with a singlet lifetime beyond 1 hour at room temperature was based on this principle [35].

3. Coherent leakage terms. Differences in chemical shift, and differences in scalar

couplings to out-of-pair nuclei, are known to cause singlet relaxation in solution [17, 24]. Advantageously, singlet-triplet leakages are suppressed by on resonant radiofrequency irradiation which simultaneously extends singlet lifetimes [56, 149]. In other instances, field cycling is required to remove large chemical shift differences which would otherwise dominate singlet relaxation [20].

4. Other interactions. Mechanisms including spin rotation, observed for the 3-spin systems of rapidly rotating methyl groups in solution [60, 141, 155], and relaxation via molecular oxygen, and other paramagnetic impurities dissolved in solution, can additionally relax the singlet state [145, 214].

Scalar relaxation of the second kind (SR2K) has long been established as a mechanism of T_1 relaxation [195, 215]. A nucleus i, scalar coupled to a quadrupolar spin Q of near identical nuclear Larmor frequency ($\omega_0^i \simeq \omega_0^Q$), relaxes via the SR2K mechanism if the quadrupolar longitudinal relaxation rate T_1^{-1} is on the order of ω_0^i. The cases of ^{13}C nuclei scalar coupled to ^{79}Br/^{81}Br and ^{14}N nuclei have been studied in detail [216–220]. Prior work on singlet-SR2K (S-SR2K) examines the limit where the T_1 of the external quadrupolar nucleus is on the timescale of the nuclear Larmor frequency [152], and does not predict the behaviour of the S-SR2K mechanism in the presence of radiofrequency fields applied to the spin-1/2 pair or the external quadrupolar nucleus. In this chapter, the S-SR2K mechanism in the slow quadrupolar relaxation regime is examined. The conditions for an efficient S-SR2K mechanism in the regime of slow quadrupolar relaxation are: (i) the quadrupolar nucleus external to the spin-pair has a longitudinal relaxation rate approximately the same order of magnitude as the in-pair scalar coupling, and (ii) there is a finite difference between the two out-of-pair scalar couplings.

5.2 Theory

At this point I must thank Giuseppe Pileio (University of Southampton) for his assistance in developing the theory of singlet-scalar relaxation of the second kind.

5.2.1 Model 3-spin-1/2 system

In this section, a general discussion of the S-SR2K mechanism in the limit of slow third-spin relaxation is presented for the case of a spin-1/2 pair coupled to a single

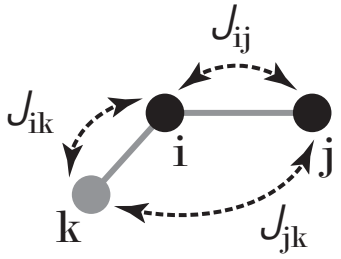

FIGURE 5.1: Model 3-spin-1/2 system and scalar coupling constant pattern. J_{ij} is the scalar coupling between spins i and j, shown in black. J_{ik} and J_{jk} are the scalar couplings between spins i and k and j and k, respectively. The third spin k is shown in grey.

external nucleus. The spin system under consideration consists of 3-spin-1/2 nuclei whose coupling scheme is shown in figure 5.1. The spins labelled as i and j are the two spins involved in the singlet pair. For simplicity, the singlet spins are considered to have an identical chemical shift frequency, i.e. $\Omega_{\Delta}^{ij} = 0$. The mutual scalar coupling constant between spins i and j is indicated here as J_{ij}. The singlet pair is also coupled to a third, external spin k via a scalar mechanism with J_{ik} and J_{jk} coupling constants. In order to isolate the phenomenon of singlet relaxation induced by a scalar mechanism of the second kind, there are no additional relaxation mechanisms acting directly on spins i and j. Spin k has a relaxation mechanism of its own, i.e. the longitudinal and transverse relaxation of the magnetization for spin k, described by the characteristic decay rates $R_1^{(k)}$ and $R_2^{(k)}$, respectively.

5.2.2 Spin dynamics

5.2.2.1 Hamiltonians

The coherent Hamiltonian $\hat{H}_{\text{coh}}$ for the 3-spin-1/2 system is conveniently written as:

$$\hat{H}_{\text{coh}} = \hat{H}_{in} + \hat{H}_{out} \tag{5.1}$$

with the coherent Hamiltonian for the *in* pair scalar coupling expressed as:

$$\hat{H}_{in} = 2\pi J_{ij}\, \hat{I}_i \cdot \hat{I}_j, \tag{5.2}$$

and with the coherent Hamiltonian for the *out* of pair scalar couplings written as:

$$\hat{H}_{out} = \pi \left(J_{\Sigma}^{ijk} + J_{\Delta}^{ijk} \right) \hat{I}_{iz} \hat{I}_{kz} + \pi \left(J_{\Sigma}^{ijk} - J_{\Delta}^{ijk} \right) \hat{I}_{jz} \hat{I}_{kz}. \tag{5.3}$$

The terms J_{Σ}^{ijk} and J_{Δ}^{ijk} are expressed as:

$$J_{\Sigma}^{ijk} = J_{ik} + J_{jk}, \tag{5.4}$$

$$J_{\Delta}^{ijk} = J_{ik} - J_{jk}. \tag{5.5}$$

The coherent Hamiltonian $\hat{H}_{\mathrm{coh}}$ is chosen to be time dependent since the use of applied radiofrequency fields will be exploited to influence the relaxation behaviour, see section 5.2.7.

5.2.2.2 Phenomenological relaxation superoperator

In the case of a 3-spin-1/2 system, as discussed in section 5.2.1, the relaxation superoperator is determined by the fluctuations of microscopic incoherent spin interactions acting on a single spin only (the external third nucleus, k). The incoherent part of the Liouvillian superoperator can easily be built in a phenomenological way by assuming that all terms involving longitudinal magnetization on spin k (i.e. terms containing the spin operator $\hat{I}_{kz}$) relax with the rate $R_1^{(k)}$, and all terms involving transverse magnetisation on spin k (i.e. terms involving the spin operators $\hat{I}_{kx}$ or $\hat{I}_{ky}$) relax with the rate $R_2^{(k)}$. Therefore, a phenomenological relaxation superoperator $\hat{\hat{\Gamma}}_k^{\mathrm{ph}}$ may be constructed, with matrix elements built as:

$$(\hat{Q}_r|\hat{\hat{\Gamma}}_k^{\mathrm{ph}}|\hat{Q}_s) = \left\{ \begin{array}{cc} -R_1^{(k)} & \mathrm{for}: \hat{Q}_r = \hat{Q}_s = \hat{I}_{kz} \\ -R_2^{(k)} & \mathrm{for}: \hat{Q}_r = \hat{Q}_s = \hat{I}_{kx}, \hat{I}_{ky} \\ 0 & \mathrm{for}: \hat{Q}_r = \hat{Q}_s \neq \hat{I}_{kx}, \hat{I}_{ky}, \hat{I}_{kz} \\ 0 & \mathrm{for}: \hat{Q}_r \neq \hat{Q}_s \end{array} \right\}. \tag{5.6}$$

5.2.2.3 Liouvillian

The dynamics of the model 3-spin-1/2 system presented in section 5.2.1 are described by the Liouville-von Neumann equation:

$$\frac{d}{dt}\hat{\rho}(t) = \hat{\hat{L}}(t)\hat{\rho}(t), \tag{5.7}$$

where the Liouvillian superoperator $\hat{\hat{L}}$ represents the superposition of coherent and incoherent influences on the spin system, and is written as:

$$\hat{\hat{L}} = -i\hat{\hat{H}}_{\text{coh}} + \hat{\hat{\Gamma}}^{\text{ph}}, \tag{5.8}$$

where $\hat{\hat{H}}_{\text{coh}}$ is the commutation superoperator of the coherent Hamiltonian $\hat{H}_{\text{coh}}$ and $\hat{\hat{\Gamma}}^{\text{ph}}$ is the phenomenological relaxation superoperator for spin k, see section 1.6.6 for more details. The Liouvillian superoperator $\hat{\hat{L}}$ has a set of N^2 eigenvalue/eigenoperator pairs $\{\Lambda_q, \hat{Q}_q\}$ where N indicates the dimension of the Hilbert space, i.e. the number of spin states. These pairs can be found by solving the following eigenequation:

$$\hat{\hat{L}}\hat{Q}_q = \Lambda_q\hat{Q}_q. \tag{5.9}$$

Because the Liouvillian superoperator $\hat{\hat{L}}$ is, in general, non-Hermitian, its eigenvalues may be complex, i.e.:

$$\Lambda_q = -\lambda_q + i\omega_q, \tag{5.10}$$

where λ_q and ω_q are both real. All eigenoperators with $\omega_q \neq 0$ correspond to coherences which decay at a rate λ_q and oscillate at a frequency ω_q. All eigenoperators with real eigenvalues, i.e. eigenvalues for which $\omega_q = 0$, correspond to the populations of particular spin state configurations which decay at a rate λ_q. The Liouvillian always has at least one trivial eigenvalue equal to zero ($\Lambda_0 = 0$) which represents the sum of populations for all states and is an invariant in a closed system.

5.2.3 Singlet order

The four eigenfunctions of the coherent Hamiltonian, i.e. the nuclear singlet and triplet states, for a system containing a pair of mutually coupled and magnetically equivalent

spin-1/2 nuclei are discussed rigorously in section 2.7. In such systems, the Liouvillian superoperator $\hat{\hat{L}}$ has another non-trivial zero eigenvalue if the relaxation superoperator contains only incoherent dipole-dipole interactions. The associated eigenoperator is the nuclear singlet order, and is represented by the population difference operator $\hat{Q}_{\mathrm{SO}}$ discussed in section 2.10. In this case, it is convenient to represent the nuclear singlet order of spins i and j as:

$$\hat{Q}_{\mathrm{SO}} = -\frac{2}{3}(\hat{I}_i^+\hat{I}_j^- + \hat{I}_i^-\hat{I}_j^+ + 2\hat{I}_{iz}\hat{I}_{jz}), \tag{5.11}$$

see section 2.10 for more details. In this chapter, it is claimed that the eigenvalue associated with the nuclear singlet order of spins i and j is different from zero when the spin-1/2 pair is coupled to a third nucleus that has a relaxation mechanism of its own. It is also proposed that this term becomes significant when the relaxation decay rate for the longitudinal order of the third nucleus is slow compared to the inverse of the scalar coupling between the 2-spin-1/2 nuclei in the singlet pair. In the following sections, I will discuss the details of this phenomenon using a simplified 3-spin-1/2 model system. The strategy adopted includes the following steps: i) derive the Liouvillian for the system; ii) write down its explicit matrix representation in a suitable operator basis; and iii) find the corresponding eigenvalues by using second order perturbation theory for finite matrices.

5.2.4 Basis functions

A convenient operator basis for the problem at hand is formulated as follows: i) define the following set of operators for the k-th spin:

$$\mathbb{B}_k = \left\{\hat{\mathbb{1}}_k, \hat{I}_{kz}, \hat{I}_k^+, \hat{I}_k^-\right\}, \tag{5.12}$$

and; ii) build the operator basis for the whole spin system by taking the direct product of $\mathbb{B}_k$ with the basis operators for spins i and j:

$$\mathbb{B} = \mathbb{B}_i \otimes \mathbb{B}_j \otimes \mathbb{B}_k^T, \tag{5.13}$$

with the operator basis of spin k tilted such that:

$$\mathbb{B}_k^T = \hat{\hat{R}}_y\left(\frac{\pi}{2}\right)\mathbb{B}_k = \hat{R}_y\left(\frac{\pi}{2}\right)\mathbb{B}_k\,\hat{R}_y^\dagger\left(\frac{\pi}{2}\right), \tag{5.14}$$

$$= \left\{\hat{\mathbb{1}}_k, \hat{I}_{kx}, i\hat{I}_{yz} - \hat{I}_{kz}, -i\hat{I}_{ky} - \hat{I}_{kz}\right\}, \tag{5.15}$$

where $\hat{\hat{R}}_y\left(\frac{\pi}{2}\right)$ is a rotation superoperator that rotates the spin operators for spin k by the angle $\pi/2$ about the y-axis. The convenience of rotating the spin operators for spin k will become clear below, see section 5.2.7.

The operator basis in equation 5.13 is conveniently reordered according to the coherence orders of spins i and j. Through such a basis reconstruction, 24 operators of coherence order zero for spins i and j are identified. These represent all populations and zero quantum coherences for this sub-set of spins, thus including the nuclear singlet order. Because spin operators with different coherence orders do not interact, the discussion that follows is therefore limited to the zero quantum subspace spanned by these 24 spin operators. The set of zero quantum operators that span this subspace is indicated as $\mathbb{B}_{ZQ}$.

5.2.5 Second order perturbation treatment of Liouvillian eigenvalues

With regards to spins i and j, consider the zero quantum operator block in the matrix representation of the Liouvillian superoperator $\hat{\hat{L}}$ expressed in the operator basis $\mathbb{B}_{ZQ}$. Analytical diagonalization would yield the decay rates for the nuclear singlet order and all other population operators and coherences which are zero order with respect to spins i and j. However, analytical diagonalization is not trivial and it is better to proceed with a second order perturbation treatment. A second order perturbation treatment of the Liouvillian eigenvalues requires identification and isolation of the perturbed part of the Liouvillian superoperator $\hat{\hat{L}}$. In order to do so, the Liouvillian superoperator in equation 5.8 is rewritten as:

$$\hat{\hat{L}} = \hat{\hat{L}}_0 + \hat{\hat{L}}_1 \tag{5.16}$$

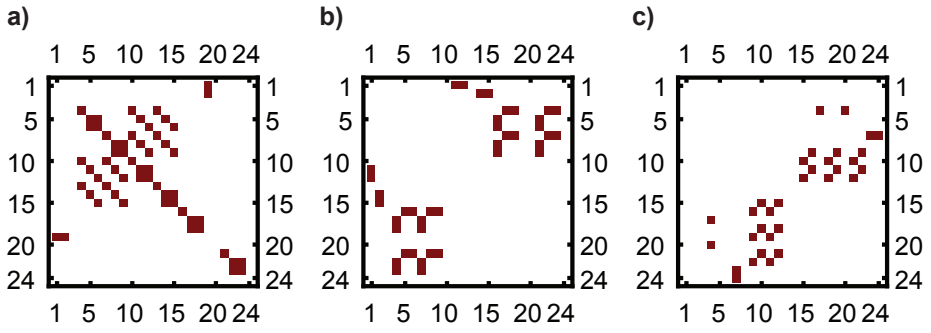

FIGURE 5.2: a) Matrix plot of $\hat{\hat{L}}_0$ in the zero quantum subspace $\mathbb{B}_{ZQ}$; b) matrix plot of $\hat{\hat{L}}_1$ in the zero quantum sub-basis $\mathbb{B}_{ZQ}$; and c) matrix plot of $\hat{\hat{L}}_1$ in the eigenbasis of $\hat{\hat{L}}_0$.

with the unperturbed and perturbed parts of the Liouvillian superoperator, $\hat{\hat{L}}_0$ and $\hat{\hat{L}}_1$, respectively, expressed as:

$$\hat{\hat{L}}_0 = \hat{\hat{\Gamma}}_k^{\text{ph}} + \hat{\hat{H}}_{in}, \tag{5.17}$$

$$\hat{\hat{L}}_1 = \hat{\hat{H}}_{out}, \tag{5.18}$$

where $\hat{\hat{H}}_{in}$ and $\hat{\hat{H}}_{out}$ are the commutation superoperators of the Hamiltonians $\hat{H}_{in}$ and $\hat{H}_{out}$, respectively. The matrix plots of $\hat{\hat{L}}_0$ and $\hat{\hat{L}}_1$ in the zero quantum subspace $\mathbb{B}_{ZQ}$ are shown in figure 5.2(a-b).

The matrix representation of $\hat{\hat{L}}_0$ in the zero quantum sub-basis $\mathbb{B}_{ZQ}$, whose generic element will be indicated here as $\left[\hat{\hat{L}}_0\right]_{rs}^{\mathbb{B}_{ZQ}}$, can be analytically diagonalized to yield a set of unperturbed, first order eigenvalue/eigenoperator pairs $\{\Lambda_q^{(1)}, \hat{Q}_q^{(1)}\}$. The set of eigenoperators is indicated as $\mathbb{B}_{ZQ}^D$. The first ten eigenoperators of interest in the set $\mathbb{B}_{ZQ}^D$ are shown:

$$\mathbb{B}_{ZQ}^D = \Bigg\{ \underset{①}{\frac{\hat{\mathbb{1}}}{2\sqrt{2}}}, \underset{②}{\frac{\hat{I}_{iz}+\hat{I}_{jz}}{2}}, \underset{③}{\sqrt{2}\hat{I}_{iz}\hat{I}_{jz}}, \underset{④}{\frac{\hat{I}_i^-\hat{I}_j^+ + \hat{I}_i^+\hat{I}_j^-}{2}}, \underset{⑤}{-\frac{\hat{I}_{kz}}{\sqrt{2}}}, \underset{⑥}{-2\sqrt{2}\hat{I}_{iz}\hat{I}_{jz}\hat{I}_{kz}}, \underset{⑦}{-\hat{I}_i^-\hat{I}_j^+\hat{I}_{kz} - \hat{I}_i^+\hat{I}_j^-\hat{I}_{kz}}, \underset{⑧}{-\hat{I}_{iz}\hat{I}_{kz} - \hat{I}_{jz}\hat{I}_{kz}}, \underset{⑨}{\frac{i\hat{I}_{ky}}{\sqrt{2}}}, \underset{⑩}{\frac{\hat{I}_{kx}}{\sqrt{2}}} \Bigg\}. \tag{5.19}$$

The following eigenvalue/eigenoperator pairs are of special interest:

$$\{\Lambda^{(1)}_{\textcircled{3}}, \hat{Q}^{(1)}_{\textcircled{3}}\} = \left\{0, \sqrt{2}\hat{I}_{iz}\hat{I}_{jz}\right\}, \tag{5.20}$$

$$\{\Lambda^{(1)}_{\textcircled{4}}, \hat{Q}^{(1)}_{\textcircled{4}}\} = \left\{0, \frac{1}{2}(\hat{I}^{+}_{i}\hat{I}^{-}_{j} + \hat{I}^{-}_{i}\hat{I}^{+}_{j})\right\}, \tag{5.21}$$

$$\{\Lambda^{(1)}_{\textcircled{5}}, \hat{Q}^{(1)}_{\textcircled{5}}\} = \left\{-R^{(k)}_{1}, \frac{-\hat{I}_{kz}}{\sqrt{2}}\right\}, \tag{5.22}$$

$$\{\Lambda^{(1)}_{\textcircled{9}}, \hat{Q}^{(1)}_{\textcircled{9}}\} = \left\{-R^{(k)}_{2}, \frac{i\hat{I}_{ky}}{2\sqrt{2}}\right\}, \tag{5.23}$$

$$\{\Lambda^{(1)}_{\textcircled{10}}, \hat{Q}^{(1)}_{\textcircled{10}}\} = \left\{-R^{(k)}_{2}, \frac{\hat{I}_{kx}}{2\sqrt{2}}\right\}. \tag{5.24}$$

These eigenvalue/eigenoperator pairs correspond to the two components of the nuclear singlet order, see equation 5.11, and the longitudinal and transverse relaxation rates of spin k. The zero value found for the decay rates simply indicates that the singlet-scalar relaxation of the second kind mechanism does not affect the nuclear singlet order to first order approximation. The decay rates of the spin operators $\hat{I}_{kx}$, $\hat{I}_{ky}$ and $\hat{I}_{kz}$ are shown for comparison. It is worth noting that the eigenoperator $\hat{Q}^{(1)}_{\textcircled{2}}$ corresponds to the longitudinal order of spins i and j and is unaffected by the singlet-SR2K mechanism, i.e. has a zero eigenvalue ($\Lambda^{(1)}_{\textcircled{2}} = 0$).

5.2.6 Decay rates for singlet-scalar relaxation of the second kind

In order to find the second order contributions to the eigenvalues corresponding to the two eigenoperators $\hat{Q}^{(2)}_{\textcircled{3}}$ and $\hat{Q}^{(2)}_{\textcircled{4}}$ it is first necessary rewrite the perturbation $\hat{\hat{L}}_1$ in the eigenbasis of $\hat{\hat{L}}_0$ ($\mathbb{B}^{D}_{ZQ}$) obtaining $\hat{\hat{L}}^{T}_{1}$, see figure 5.2c). $\hat{\hat{L}}_0$ is diagonal in its own eigenbasis. One can immediately observe that the eigenoperator ④, representing the flip-flop part of the nuclear singlet order, is only connected to eigenoperators ⑰ and ⑳. These three terms form an independent sub-block that contains all the relevant spin dynamics. The explicit form of this zero order sub-block is:

$$\begin{array}{c} \\ ④ \\ ⑰ \\ ⑳ \end{array} \begin{array}{c} \begin{array}{ccc} ④ & ⑰ & ⑳ \end{array} \\ \begin{pmatrix} 0 & \frac{i\mathbf{J}^{ijk}_{\Delta}}{2\sqrt{2}} & \frac{i\mathbf{J}^{ijk}_{\Delta}}{2\sqrt{2}} \\ \frac{i\mathbf{J}^{ijk}_{\Delta}}{2\sqrt{2}} & -R^{k}_{1} - i\mathbf{J}_{ij} & 0 \\ \frac{i\mathbf{J}^{ijk}_{\Delta}}{2\sqrt{2}} & 0 & -R^{k}_{1} + i\mathbf{J}_{ij} \end{pmatrix} \end{array}, \tag{5.25}$$

where the following shorthand notation has been introduced in order to simplify the resulting matrix elements:

$$\mathbf{J}_{ij} = 2\pi J_{ij}, \tag{5.26}$$

$$\mathbf{J}^{ijk}_{\Delta} = 2\pi J^{ijk}_{\Delta}. \tag{5.27}$$

The application of the second order perturbation equation for finite matrices to equation 5.25:

$$\Lambda^{(2)}_q = -\left[\hat{\hat{L}}_0\right]^{\mathbb{B}_{ZQ}}_{qq} - \sum_{r\neq q} \frac{\left[\hat{\hat{L}}^T_1\right]^{\mathbb{B}_{ZQ}}_{rq}\left[\hat{\hat{L}}^T_1\right]^{\mathbb{B}_{ZQ}}_{qr}}{\left[\hat{\hat{L}}_0\right]^{\mathbb{B}_{ZQ}}_{qq} - \left[\hat{\hat{L}}_0\right]^{\mathbb{B}_{ZQ}}_{rr}}, \tag{5.28}$$

yields the following eigenvalue/eigenoperator pair:

$$\{\Lambda^{(2)}_{\textcircled{4}}, \hat{Q}^{(2)}_{\textcircled{4}}\} = \left\{ \frac{R^{(k)}_1 (\mathbf{J}^{ijk}_{\Delta})^2}{4\left((R^{(k)}_1)^2 + \mathbf{J}^2_{ij}\right)}, \frac{1}{2}(\hat{I}^+_i \hat{I}^-_j + \hat{I}^-_i \hat{I}^+_j) \right\}. \tag{5.29}$$

Note also that the eigenoperators $\sqrt{2}\hat{I}_{iz}\hat{I}_{jz}$ have no connections with any other spin operators in figure 5.2c) and therefore $\Lambda^{(1)}_{\textcircled{3}}$ is identically null at any higher order. Only the flip-flop part of the nuclear singlet order is affected by the scalar coupling relaxation mechanism of the second kind, and the approximated second order decay rate is given by $\Lambda^{(2)}_{\textcircled{4}}$. The nuclear singlet order term involving the $\sqrt{2}\hat{I}_{iz}\hat{I}_{jz}$ spin operator is unaffected by this mechanism and therefore the experimentally measured singlet decay rate has a characteristic biexponential shape, as shown in figure 5.3.

Equation 5.29 relates to the case in which the exterior spin k is a spin-1/2 nucleus, and can be generalized to a generic spin I through multiplication with a factor of $4I(I+1)/3$ in order to obtain:

$$\{\Lambda^{(2)}_{\textcircled{4}}, Q^{(2)}_{\textcircled{4}}\} = \left\{ \frac{I(I+1)R^{(k)}_1 (\mathbf{J}^{ijk}_{\Delta})^2}{3\left((R^{(k)}_1)^2 + \mathbf{J}^2_{ij}\right)}, \frac{1}{2}(\hat{I}^+_i \hat{I}^-_j + \hat{I}^-_i \hat{I}^+_j) \right\}. \tag{5.30}$$

The validity of equation 5.30 has been tested by repeating the procedure described above for the cases of $I = 1$ and $I = 3/2$. It should be noted that the decay rate for the nuclear singlet order in equation 5.30 has the form of a Lorentzian spectral density function $\mathcal{J}(\mathbf{J}_{ij})$ sampled at $2\pi J_{ij}$, where the overall rotational correlation time is $T^{(k)}_1$.

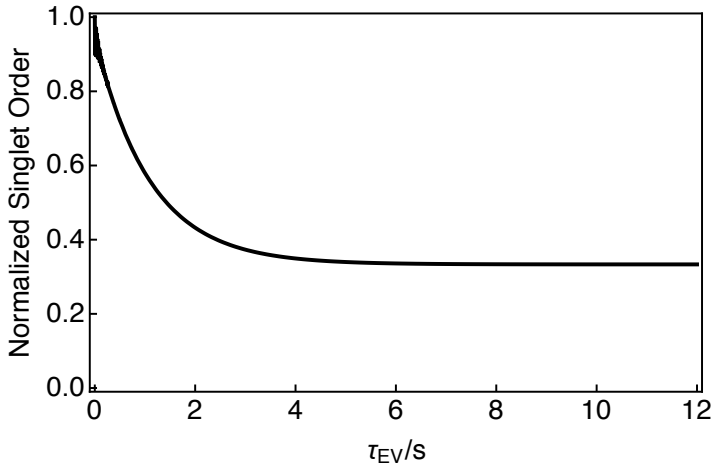

FIGURE 5.3: Simulated biexponential decay of the nuclear singlet order for spins i and j in the case that the singlet-SR2K mechanism is the sole relaxation source. In this case, the decay of the nuclear singlet order plateaus at a value of 1/3, as the term involving the $\sqrt{2}\hat{I}_{iz}\hat{I}_{jz}$ spin operator is unaffected by the singlet-SR2K mechanism. The simulation includes the scalar coupling network shown in figure 5.1 and phenomenological relaxation on the third spin k. The parameters used in the simulation were as follows: $J_{ij} = 71\,\text{Hz}$, $J_{\Delta}^{ijk} = 26\,\text{Hz}$, and $R_1^{(k)} = 5.952\,\text{s}^{-1}$.

Equation 5.30 is therefore rewritten as:

$$\{\Lambda^{(2)}_{\textcircled{4}}, Q^{(2)}_{\textcircled{4}}\} = \left\{ \frac{I(I+1)}{3}(\mathbf{J}_{\Delta}^{ijk})^2 \mathcal{J}(\mathbf{J}_{ij}), \frac{1}{2}(\hat{I}_i^+ \hat{I}_j^- + \hat{I}_i^- \hat{I}_j^+) \right\}, \tag{5.31}$$

where the Lorentzian spectral density function $\mathcal{J}(\mathbf{J}_{ij})$ is expressed as:

$$\mathcal{J}(\mathbf{J}_{ij}) = \frac{R_1^{(k)}}{(R_1^{(k)})^2 + \mathbf{J}_{ij}^2}. \tag{5.32}$$

5.2.7 Suppression of singlet-scalar relaxation via an applied rf-field

Equation 5.25 displays another interesting feature regarding the singlet-SR2K mechanism under investigation. The mixing of the nuclear singlet order term represented by ④ with the spin operators ⑰ and ⑳ is due to the out-of-diagonal terms $i\mathbf{J}_{\Delta}^{ijk}/2\sqrt{2}$, see figure 5.2c). It may therefore be possible to minimise the relaxation contribution from singlet-SR2K by applying an on resonant radiofrequency field acting on spin k only (or alternatively on spins i and j only).

To demonstrate this prediction, a radiofrequency field with an amplitude corresponding to the frequency ω_{LOCK} is added to the coherent Hamiltonian $\hat{H}_{\mathrm{coh}}$ in equation 5.1. This term has the following form, in the rotating frame:

$$\hat{H}_{\mathrm{CW}} = \omega_{\mathrm{LOCK}} \hat{I}_{kx}. \tag{5.33}$$

The rotating frame Liouvillian for the 3-spin-1/2 system becomes:

$$\hat{\hat{L}}_{\mathrm{CW}} = \hat{\hat{L}}_{0,\mathrm{CW}} + \hat{\hat{L}}_{1}, \tag{5.34}$$

with the new, unperturbed radiofrequency field containing portion of the Liouvillian superoperator $\hat{\hat{L}}$ rewritten as:

$$\hat{\hat{L}}_{0,\mathrm{CW}} = \hat{\hat{L}}_{0} + \hat{\hat{H}}_{\mathrm{CW}}, \tag{5.35}$$

where $\hat{\hat{H}}_{\mathrm{CW}}$ is the commutation superoperator of the radiofrequency Hamiltonian $\hat{H}_{\mathrm{CW}}$. In this case, the term J_{Σ}^{ijk} contained within the Hamiltonian $\hat{H}_{out}$ was found to have no affect on the outcome of applying second order perturbation theory to the Liouvillian superoperator $\hat{\hat{L}}_{\mathrm{CW}}$, and may therefore be ignored for simplicity.

The matrix representation of the new Liouvillian superoperator $\hat{\hat{L}}_{0,\mathrm{CW}}$ in the zero quantum subspace $\mathbb{B}_{ZQ}$ has all terms proportional to ω_{LOCK} on the diagonal as a result of the $\pi/2$ rotation about the y-axis of the spin operators for spin k used in building the basis $\mathbb{B}$ and, by consequence, the basis $\mathbb{B}_{ZQ}$. However, the unperturbed Liouvillian $\hat{\hat{L}}_{0,\mathrm{CW}}$, which includes $\hat{\hat{\Gamma}}^{\mathrm{ph}}$, is not *normal*, i.e. it does not commute with its Hermitian adjoint, due to complex off-diagonal elements outside of the zero quantum subspace. *Non-normal* matrices, such as the matrix representation of $\hat{\hat{L}}_{0,\mathrm{CW}}$ in the basis $\mathbb{B}_{ZQ}$, i.e. $\left[\hat{\hat{L}}_{0,\mathrm{CW}}\right]^{\mathbb{B}_{ZQ}}$, are not necessarily diagonalizable. Indeed, it was not possible to find all eigenvalues and eigenoperators of $\left[\hat{\hat{L}}_{0,\mathrm{CW}}\right]^{\mathbb{B}_{ZQ}}$.

The matrix $\hat{\hat{L}}_{0,\mathrm{CW}}$ in the basis $\mathbb{B}_{ZQ}$ can be made *normal*, a requirement of second order perturbation theory, by using the approximation $|\omega_{\mathrm{LOCK}}| \gg |R_1^{(k)} - R_2^{(k)}|/4$ or the case of $R_1^{(k)} = R_2^{(k)}$, i.e. the off-diagonal terms are ignored. This is a reasonable approximation since: 1) $R_1^{(k)} \simeq R_2^{(k)}$ in the limit of isotropic extreme narrowing, and as such the value of the off-diagonal elements are small compared to the difference between

the values of the diagonal terms; and 2) relaxation of the third spin k is slow, i.e. $T_1^{(k)}$ and $T_2^{(k)}$ are on the order of ∼100 ms, and hence applying a continuous wave (CW) decoupling field with a nutation frequency $\gtrsim$100 Hz should be sufficient as to actively decouple the singlet-SR2K mechanism. Assuming, for example, that $|\omega_{\mathrm{LOCK}}| \gg |R_1^{(k)} - R_2^{(k)}|/4$, and applying the second order perturbation equation for finite matrices (section 5.2.6) yields the eigenvalue corresponding to the eigenoperator ④:

$$\Lambda^{(2)}_{④,\mathrm{CW}} = \frac{(R_1^{(k)} + R_2^{(k)})[(R_1^{(k)} + R_2^{(k)})^2 + 4(\mathbf{J}_{ij}^2 + \omega_{\mathrm{LOCK}}^2)](\mathbf{J}_\Delta^{ijk})^2}{2[(R_1^{(k)} + R_2^{(k)})^2 + 4(\mathbf{J}_{ij}^2 + \omega_{\mathrm{LOCK}}^2)][(R_1^{(k)} + R_2^{(k)})^2 + 4(\mathbf{J}_{ij}^2 - \omega_{\mathrm{LOCK}}^2)]}, \tag{5.36}$$

which reduces to equation 5.29 ($\Lambda^{(2)}_{④}$) in the case that $\omega_{\mathrm{LOCK}} = 0$ and $R_1^{(k)} = R_2^{(k)}$. As above, equation 5.36 can be generalized to a generic third spin of angular momentum quantum number I:

$$\Lambda^{(2)}_{④,\mathrm{CW}} = \frac{2I(I+1)(R_1^{(k)} + R_2^{(k)})[(R_1^{(k)} + R_2^{(k)})^2 + 4(\mathbf{J}_{ij}^2 + \omega_{\mathrm{LOCK}}^2)](\mathbf{J}_\Delta^{ijk})^2}{3[(R_1^{(k)} + R_2^{(k)})^2 + 4(\mathbf{J}_{ij}^2 + \omega_{\mathrm{LOCK}}^2)][(R_1^{(k)} + R_2^{(k)})^2 + 4(\mathbf{J}_{ij}^2 - \omega_{\mathrm{LOCK}}^2)]}. \tag{5.37}$$

In the case of $R_1^{(k)} = R_2^{(k)}$, a condition that holds in the fast motion limit (FML), equation 5.37 simplifies further to:

$$\Lambda^{(2),FML}_{④,\mathrm{CW}} = \frac{I(I+1)R_1^{(k)}[(R_1^{(k)})^2 + \mathbf{J}_{ij}^2 + \omega_{\mathrm{LOCK}}^2](\mathbf{J}_\Delta^{ijk})^2}{3[(R_1^{(k)})^2 + (\mathbf{J}_{ij} - \omega_{\mathrm{LOCK}})^2][(R_1^{(k)})^2 + (\mathbf{J}_{ij} + \omega_{\mathrm{LOCK}})^2]}. \tag{5.38}$$

The rate $\Lambda^{(2),FML}_{④,\mathrm{CW}}$ for $I = 1/2$ is plotted against $R_1^{(k)}$ (the longitudinal relaxation rate constant of spin k) in figure 5.4 for the parameter set in table 5.1 and a range of nutation frequencies $\omega_{\mathrm{LOCK}}/2\pi$. The rate $\Lambda^{(2),FML}_{④,\mathrm{CW}}$ is maximized when $R_1^{(k)} = 2\pi J_{ij}$. A perturbation is only caused if the values of the off-diagonal terms are larger than the difference in the values of the diagonal terms. In the present case, this difference is on the order of $-R_1^{(k)} + i\mathbf{J}_{ij}$. This means that the singlet-SR2K mechanism is relevant when the relaxation rate of the third nucleus k (the inverse of its T_1) is of the order of J_{ij} or, more precisely, when $|\mathbf{J}_\Delta^{ijk}| \geq |i\mathbf{J}_{ij} - R_1^{(k)}|$. The S-SR2K mechanism is therefore effectively suppressed in the case that $\omega_{\mathrm{LOCK}} \gg 2\pi J_{ij}$, and is accelerated in the case that $\omega_{\mathrm{LOCK}} \simeq 2\pi J_{ij}$. A similar result is also predicted if an on resonant radiofrequency field is applied to spins i and j.

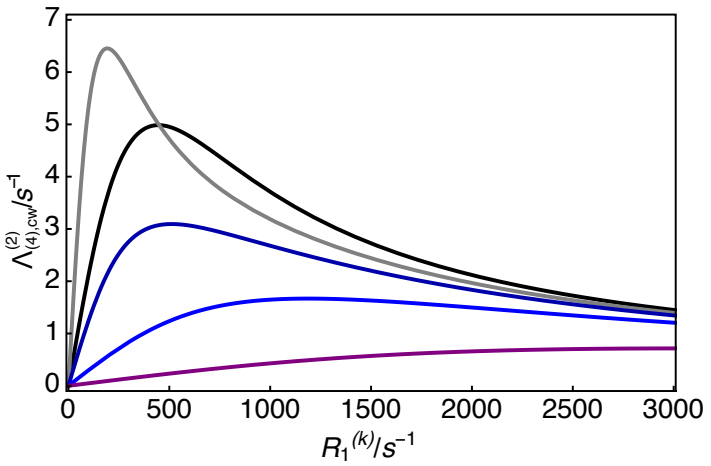

FIGURE 5.4: A plot of the decay rate $\Lambda_4^{(2),FML}$ in equation 5.36 versus $R_1^{(k)}$ using the parameters reported in table 5.1 and a range of nutation frequencies $\omega_{\mathrm{LOCK}}/(2\pi)$. The simulations used the following nutation frequencies: black curve: $\omega_{\mathrm{LOCK}}/2\pi = 0\,\mathrm{Hz}$; grey curve: $\omega_{\mathrm{LOCK}}/2\pi = 100\,\mathrm{Hz}$; dark blue curve: $\omega_{\mathrm{LOCK}}/2\pi = 140\,\mathrm{Hz}$; blue curve: $\omega_{\mathrm{LOCK}}/2\pi = 225\,\mathrm{Hz}$; purple curve: $\omega_{\mathrm{LOCK}}/2\pi = 500\,\mathrm{Hz}$.

5.2.8 The case of 2-spin-1/2 nuclei coupled to a spin-1 nucleus

In the following sections, I am interested in the specific case of a single $^{13}\mathrm{C}$ pair coupled to a deuterium spin ($I = 1$) via a scalar coupling mechanism. In such a system, the deuterium has a strong relaxation mechanism of its own provided by its quadrupolar moment. According to the Redfield relaxation theory and assuming, for simplicity, that the fast motional limit applies, the quadrupolar contribution to the longitudinal relaxation rate of spin k is given by [49]:

$$R_1^{(k)} = \frac{1}{10}(2I-1)(2I+3)\omega_Q^2(3+\eta_Q^2)\tau_{\mathrm{C}}. \tag{5.39}$$

For the case of $I = 1$, equation 5.40 simplifies to:

$$R_1^{(k)} = \frac{1}{2}\omega_Q^2(3+\eta_Q^2)\tau_{\mathrm{C}}, \tag{5.40}$$

with the nuclear quadrupole coupling constant expressed as:

$$\omega_Q = \frac{e^2qQ}{2I(2I-1)\hbar}, \tag{5.41}$$

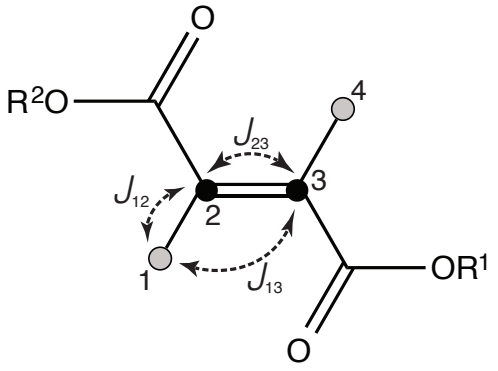

FIGURE 5.5: Molecular structure, labelling scheme and scalar coupling constant pattern of **III**. Black circles denote ^{13}C nuclei, grey circles denote ^{2}H nuclei. $R^1 = CD_2CD_2CD_3$ and $R^2 = CD_2CD_3$.

where Q is the electric quadrupolar moment of the deuterium nucleus, eq is the electrical field gradient at the deuterium nucleus, η_Q is the biaxality for the quadrupolar interaction of the deuterium nucleus, and τ_C is the overall rotational correlation time [199]. This value of the relaxation rate can be used in equation 5.36 with $I = 1$ to obtain the contribution of the scalar coupling to the nuclear singlet order decay rate when a singlet pair interacts with a single, slowly relaxing quadrupolar spin.

5.3 Experiments

5.3.1 Fumarate

The molecular structure of the sample used in this study is shown in figure 5.5. The material is a diester of 1-(ethyl-d_5) 4-(propyl-d_7)(*E*)-but-2-enedioate-2,3-$^{13}C_2$-d_2 (**III**) which contains a central 4-spin system comprising of two ^{13}C nuclei and two ^{2}H nuclei over a trans double bond. The 2-spin-1/2,2-spin-1 system displays a local centre of inversion, midway between the two ^{13}C nuclei. The asymmetric ester groups R^1 and R^2 are not important in the context of the work and are deuterated in order to reduce the relaxation contribution from dipole-dipole couplings. The complex 4-spin system of the deuterated fumarate diester in solution is a suitable spin system for the observation of singlet-SR2K. It is a difficult task to find a 3-spin system in which the chemical shift difference of the spin-1/2 pair does not dominate singlet relaxation via singlet-triplet mixing [24].

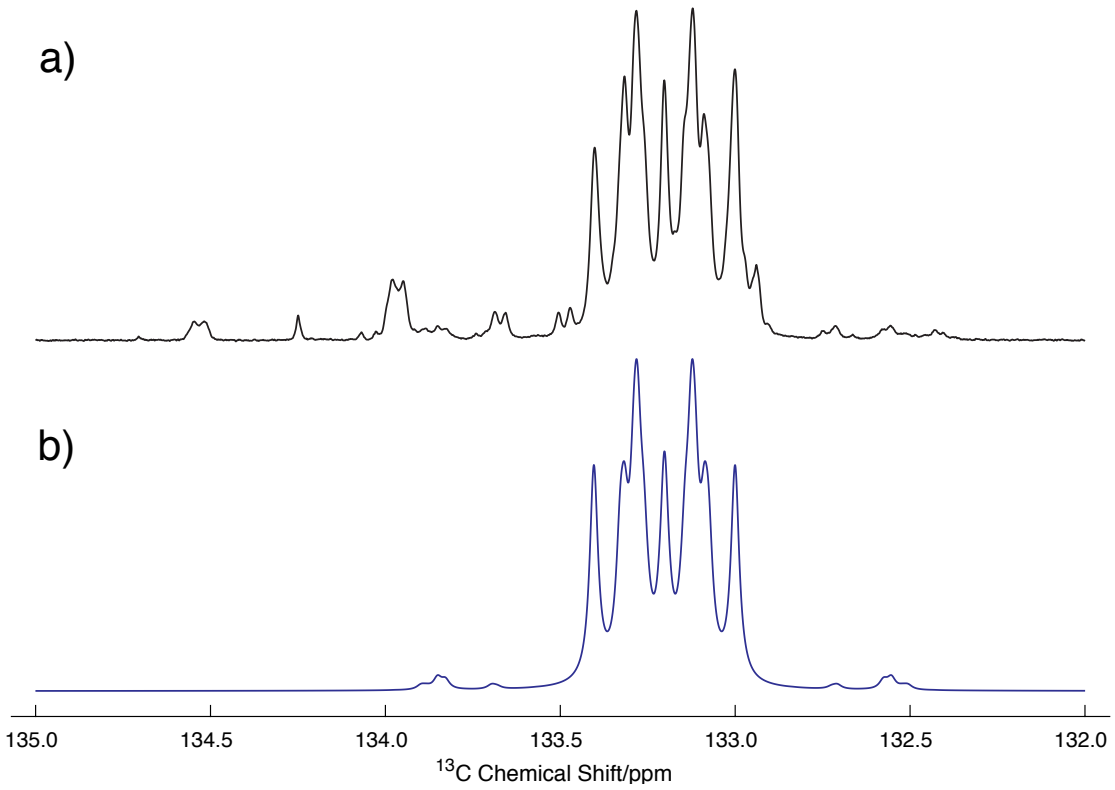

FIGURE 5.6: Part of the experimental ^{13}C spectrum of **III** in $CDCl_3$ solution acquired at 11.7 T and 25°C with 64 transients. a) Black curve: experimental carbon-13 spectrum; b) blue curve: simulated carbon-13 spectrum. Small signals from synthetic impurities are observed beyond 133.5 ppm.

5.3.2 Carbon-13 spectrum

The relevant portion of the experimental ^{13}C NMR spectrum of **III** is shown in figure 5.6. The experimental ^{13}C spectrum was fitted using the *MatLab*-based NMR software package *Spinach* [221]. Simulated scalar couplings (and differences) for **III** in $CDCl_3$ at 25°C are given in table 5.1. The molecular labelling scheme and scalar coupling constant pattern of **III** are shown in figure 5.5. The spin system in is the near-equivalence regime as the difference in scalar couplings $|J_{12} - J_{13}| = J_{\Delta}^{231}$ is less than half J_{23}.

TABLE 5.1: Spin system parameters for **III** in $CDCl_3$ at 25°C. Labels 2 and 3 indicate ^{13}C nuclei, labels 1 and 4 indicate ^{2}H nuclei. Scalar couplings (and differences) were obtained by fitting the experimental ^{13}C spectrum with the *MatLab*-based NMR software package *Spinach*. J_{Δ}^{231} is defined as: $|J_{12} - J_{13}|$.

Parameter	Value/2π
J_{23}	71.5 ± 0.9 Hz
$J_{12} = J_{34}$	25.9 ± 0.3 Hz
$J_{13} = J_{24}$	-0.5 ± 0.1 Hz
J_{Δ}^{231}	26.4 ± 0.3 Hz

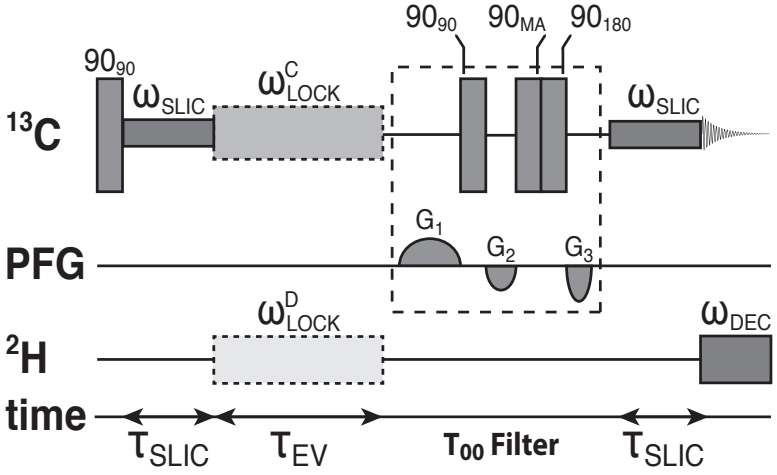

FIGURE 5.7: Pulse sequence for preparing long-lived nuclear singlet order in **III** and monitoring its decay. The experiments used the following parameters: $\omega_{\mathrm{SLIC}}/2\pi = 71\,\mathrm{Hz}$ and $\tau_{\mathrm{SLIC}}/2\pi = 27\,\mathrm{ms}$. The "$T_{00}$ filter" selects out signals that do not pass through the nuclear singlet order. "MA" denotes the "magic angle" (54.7°). The grey boxes denote larger-amplitude "spin-locking" rf-fields, with nutation frequencies $\omega^{\mathrm{C,D}}_{\mathrm{LOCK}}$, which are active during the singlet evolution delay τ_{EV}. The superscripts C and D denote the ^{13}C and ^{2}H spin-locking rf-fields, respectively. An interval of 150 s was used between successive transients when ^{13}C or ^{2}H spin-locking rf-fields were applied.

5.3.3 Singlet NMR

Symmetry-breaking interactions, such as small differences in chemical shift between the participating spins, or differential scalar couplings to other magnetic nuclei outside of the singlet pair are required for coherent access to the nuclear singlet order [23]. In this case, the differential out-of-pair scalar couplings allow coherent access to the ^{13}C nuclear singlet order, by using known radiofrequency pulse techniques which operate in the near-equivalence regime [150, 156–158]. Warren and coworkers were the first to demonstrate such access to nuclear singlet states via out-of-pair scalar couplings in AA'XX' spin systems [23, 31, 160]. In the current study, the spin-lock induced crossing (SLIC) method [157] was used, as shown in figure 5.7. The SLIC pulse sequence has been described extensively in section 2.12.1. A sequence of radiofrequency pulses and pulsed field gradients (known as a "T_{00} filter") destroys NMR signals that do not pass through the nuclear singlet order [54–56]. The parameters of the "T_{00} filter" are found in appendix B. The parameters of the SLIC pulse were chosen to maximise triplet-singlet population conversion: $\omega_{\mathrm{SLIC}}/2\pi = 71\,\mathrm{Hz}$ and $\tau_{\mathrm{SLIC}} = 27\,\mathrm{ms}$, i.e. the conversion was complete in a time: $\tau_{\mathrm{SLIC}} \simeq 2^{-1/2} J^{231}_{\Delta}$. A WALTZ-16 decoupling sequence (deuteron nutation frequency = 300 Hz) was applied on the ^{2}H channel during the ^{13}C observation

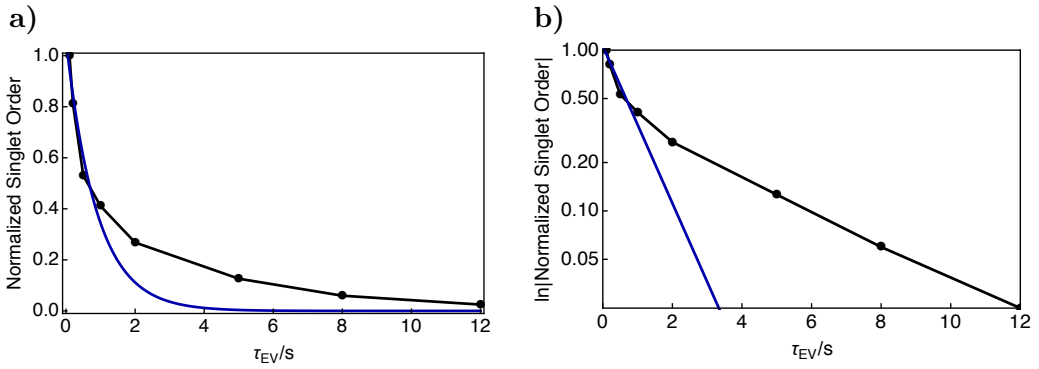

FIGURE 5.8: a) Experimental relaxation curve for the ^{13}C nuclear singlet order of 0.2 M **III** in degassed $CDCl_3$ solvent (magnetic field 11.7 T, temperature 25°C). Filled, black symbols: decay of the ^{13}C nuclear singlet order measured by the pulse sequence in figure 5.7; blue curve: single exponential fit of the experimental data. All experimental signal amplitudes were normalized to the first point. b) Logarithmic decay curve for the ^{13}C nuclear singlet order under the same conditions.

in order to collapse the NMR spectrum into a single peak [222]. The lock level was held whilst the ^{2}H decoupling was active. Nutation frequencies $\omega^{\mathrm{D}}_{\mathrm{LOCK}}$ and ω_{DEC} were calibrated relative to a high power 90° pulse of known duration by using the "pulse" algorithm inside the *Bruker TopSpin 3.2* software package. Pulse calibrations were performed on the ^{2}H channel of our *Bruker Avance III* spectrometer, which is equipped with a 5 mm TBO probe. All calculated nutation frequencies were verified against nutation frequency experiments, and no non-linearity was found in our ^{2}H amplifier. The maximum amplitude of the singlet-filtered ^{13}C NMR signal, relative to that induced by a single 90° pulse, was found to be 0.17. The loss relative to the theoretical maximum of 1/3 (AA′XX′ spin systems) is not yet fully understood but is attributed to radiofrequency field imperfections and relaxation.

5.4 Results

5.4.1 Carbon-13 NMR

A biexponential decay curve for the ^{13}C nuclear singlet order of **III** is shown in figure 5.8a). A single exponential fit of the initial decay (first 4 data points) provides a relaxation time: $T_{\mathrm{S}} = 0.9 \pm 0.2$ s. A logarithmic decay curve for the ^{13}C nuclear singlet order is displayed in figure 5.8b). The two linear regions are clearly visible and are indicative of a biexponential decay. The ^{13}C longitudinal relaxation time $T_1(^{13}\mathrm{C})$

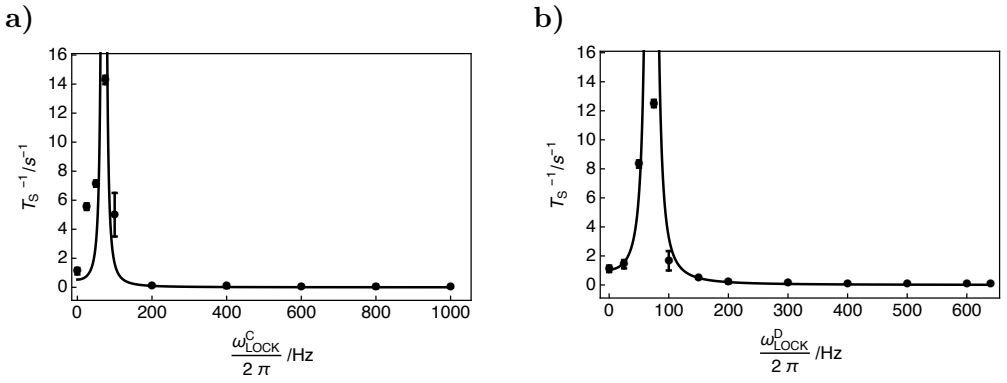

FIGURE 5.9: Experimental dependence of T_S^{-1} on a) ^{13}C and b) ^{2}H spin-locking rf-field amplitudes for 0.2 M **III** in degassed $CDCl_3$ solvent (magnetic field 11.7 T, temperature 25°C). Black circles: experimental data points; black curve: theoretical dependence of T_S^{-1} on ^{13}C and ^{2}H spin-locking rf-field amplitudes. The black curve reaches a maximum at $\omega^{C,D}_{LOCK}/2\pi = J_{23} = 71$ Hz but is not shown for clarity.

was estimated experimentally by using the inversion recovery pulse sequence. Under the same conditions, the resulting relaxation curve shows a single exponential recovery with a longitudinal ^{13}C relaxation time: $T_1(^{13}C) = 14.0 \pm 0.5$ s. The singlet relaxation time is therefore ~16 times smaller than that of longitudinal magnetization. See appendix B for further details regarding ^{13}C inversion recovery experiments, data fitting and uncertainty estimations.

5.4.2 Deuterium NMR

The longitudinal ^{2}H relaxation time $T_1(^{2}H)$ was estimated experimentally by using the inversion recovery pulse sequence. For the case of degassed $CDCl_3$ solution at 11.7 T and 25°C, the experimental relaxation curve shows a single exponential recovery with a longitudinal ^{2}H relaxation time for **III** given by: $T_1(^{2}H) = 168 \pm 7$ ms.

5.4.3 Suppression of singlet-scalar relaxation via applied rf-fields

The experimental singlet relaxation rate constants T_S^{-1} as a function of spin-locking rf-field amplitude, expressed as the nutation frequencies $\omega^C_{LOCK}/2\pi$ and $\omega^D_{LOCK}/2\pi$, are shown in figures 5.9(a-b), respectively. The measured singlet relaxation times T_S included in figures 5.9(a-b) for a range of ^{13}C and ^{2}H spin-locking rf-field amplitudes are given in table 5.2. The theoretical singlet relaxation rate constants T_S^{-1} as a function of ^{13}C and ^{2}H spin-locking rf-field amplitudes are also shown in figures 5.9(a-b).

TABLE 5.2: The set of experimental singlet relaxation times T_S for 0.2 M **III** in degassed $CDCl_3$ solvent (magnetic field 11.7 T, temperature 25°C) measured as a function of ^{13}C and ^{2}H spin-locking rf-field amplitudes, as shown in figures 5.9(a-b).

ω^{C}_{LOCK}/Hz	ω^{D}_{LOCK}/Hz	T_S/s
0	0	0.9 ± 0.2
25	0	0.18 ± 0.04
50	0	0.14 ± 0.03
75	0	0.07 ± 0.02
100	0	5.2 ± 0.4
200	0	9.6 ± 0.6
400	0	14.1 ± 1.8
600	0	16.0 ± 1.5
800	0	18.7 ± 2.3
1000	0	23.0 ± 1.6
0	25	0.7 ± 0.2
0	50	0.12 ± 0.03
0	75	0.08 ± 0.02
0	100	0.9 ± 0.2
0	200	5.3 ± 0.4
0	300	7.9 ± 0.4
0	400	8.9 ± 0.4
0	500	9.6 ± 0.3
0	600	10.8 ± 0.4
0	640	11.7 ± 0.4

In both cases, the experimental singlet relaxation rate constants T_S^{-1} increase dramatically, and reach a maximum, as ω^{C}_{LOCK} and $\omega^{D}_{LOCK}/2\pi$ approach $J_{23} = 71$ Hz. The theoretical dependence of T_S^{-1} on ^{13}C and ^{2}H spin-locking rf-field amplitudes also predicts a maximum at: $\omega^{C}_{LOCK}/2\pi = \omega^{D}_{LOCK}/2\pi = J_{23}$, but has a considerably larger value. The profile of the experimental and theoretical singlet relaxation curves are in reasonable agreement, although this discrepancy remains. It is therefore reasonable to assume that the approximations introduced in section 5.2.7 may not hold in the case of $\omega_{LOCK} \simeq 2\pi J_{23}$, or that higher-order correctional terms are necessary in order to account for this discrepancy. These results demonstrate that the model developed in section 5.2.7, and hence equation 5.38, are only valid in the regime of sufficiently large CW nutation frequencies, i.e. $\omega_{LOCK} \gg 2\pi J_{23}$. It is also plausible that the additional contributions of other interactions to the ^{13}C singlet relaxation can have a large proportionate effect on the value of T_S^{-1}. These issues have not been investigated further. Beyond ∼150 Hz spin-locking rf-field amplitude, in the regime of sufficiently large CW nutation frequencies, the experimental singlet relaxation rate constants T_S^{-1} decrease with increasing spin-locking rf-field amplitude during the singlet evolution period τ_{EV}.

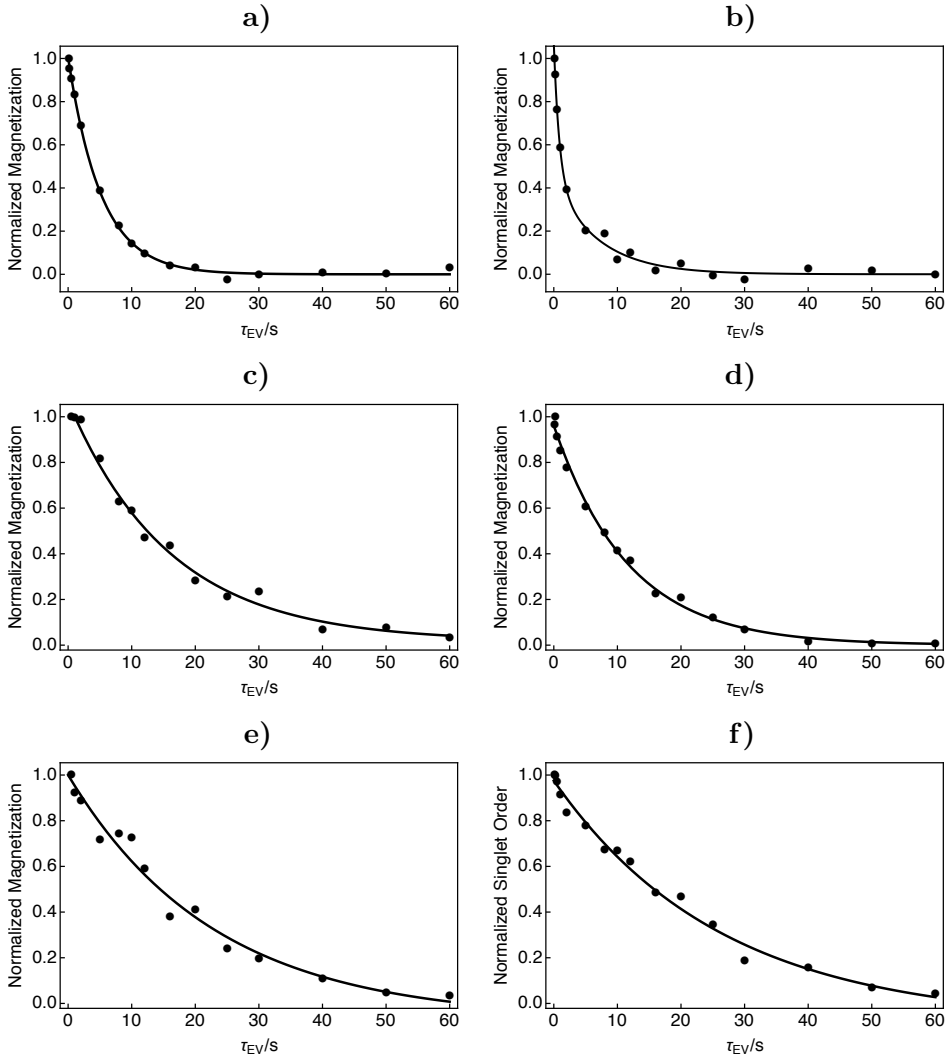

FIGURE 5.10: Experimental relaxation curves of ^{13}C nuclear singlet order for 0.2 M **III** in degassed $CDCl_3$ solvent (magnetic field 11.7 T, temperature 25°C). The decay of ^{13}C nuclear singlet order was measured by the pulse sequence in figure 5.7 in the presence of ^{13}C and ^{2}H spin-locking rf-fields during the singlet evolution delay τ_{EV}. The following nutation frequencies were used for experiments: a: $\omega^{C}_{LOCK}/2\pi = 100$ Hz; b: $\omega^{D}_{LOCK}/2\pi = 100$ Hz; c: $\omega^{C}_{LOCK}/2\pi = 600$ Hz; d: $\omega^{D}_{LOCK}/2\pi = 640$ Hz; e: $\omega^{C}_{LOCK}/2\pi = 1$ kHz; f: $\omega^{C}_{LOCK}/2\pi = 1$ kHz and $\omega^{D}_{LOCK}/2\pi = 640$ Hz. The singlet relaxation times are: a: $T_S = 5.2 \pm 0.4$ s; b: $T_S = 0.9 \pm 0.2$ s; c: $T_S = 16 \pm 2$ s; d: $T_S = 11.7 \pm 0.4$ s; e: $T_S = 23 \pm 2$ s; f: $T_S = 26 \pm 3$ s. All the fitted curves have a single-exponential form, except b) which shows a biexponential decay. All signal amplitudes were normalized to the first point.

It is likely that as the singlet-SR2K mechanism is gradually removed via coherent rf-irradiation an additional relaxation mechanism (which is not affected by the on resonant decoupling field) becomes increasingly dominant, and the curve plateaus. Singlet relaxation is effectively suppressed as ω^{C}_{LOCK} approaches 1 kHz nutation frequency and ω^{D}_{LOCK} approaches 640 Hz nutation frequency.

Decay curves for the ^{13}C nuclear singlet order in the presence of spin-locking fields with nutation frequencies $\omega_{\mathrm{LOCK}}^{\mathrm{C,D}}$ are shown in figure 5.10. Figure 5.10a) shows the decay of ^{13}C nuclear singlet order with a coherent CW field of $\omega_{\mathrm{LOCK}}^{\mathrm{C}} = 100\,\mathrm{Hz}$ nutation frequency applied during the singlet evolution delay τ_{EV}. The singlet decay is single exponential and has a relaxation time: $T_{\mathrm{S}} = 5.2 \pm 0.4\,\mathrm{s}$. Conversely, the case of $\omega_{\mathrm{LOCK}}^{\mathrm{D}} = 100\,\mathrm{Hz}$ nutation frequency is shown in figure 5.10b). In this case, the decay of ^{13}C nuclear singlet order is biexponential and has a singlet lifetime: $T_{\mathrm{S}} = 0.9 \pm 0.2\,\mathrm{s}$, which is equal to the singlet relaxation time determined at $\omega_{\mathrm{LOCK}}^{\mathrm{C}} = \omega_{\mathrm{LOCK}}^{\mathrm{D}} = 0\,\mathrm{Hz}$ nutation frequency. Figures 5.10c) and 5.10d) compare the decay of ^{13}C nuclear singlet order in the presence of spin-locking rf-fields with nutation frequencies: $\omega_{\mathrm{LOCK}}^{\mathrm{C}} = 600\,\mathrm{Hz}$ and $\omega_{\mathrm{LOCK}}^{\mathrm{D}} = 640\,\mathrm{Hz}$, respectively. The respective singlet relaxation times $T_{\mathrm{S}} = 16 \pm 2\,\mathrm{s}$ and $T_{\mathrm{S}} = 11.7 \pm 0.4\,\mathrm{s}$ imply that CW irradiation applied to the ^{13}C nuclei is approximately twice as effective in suppressing the singlet-SR2K mechanism than the case of CW irradiation applied to the deuterium nuclei, in agreement with theory (see figure 5.9). This phenomena is mirrored by the theoretical curves of the singlet relaxation rate constant T_{S}^{-1}, see figure 5.9. The curve in figure 5.10e) shows the decay of ^{13}C nuclear singlet order in the presence of a CW rf-field with an amplitude: $\omega_{\mathrm{LOCK}}^{\mathrm{C}} = 1\,\mathrm{kHz}$. The singlet relaxation curve is fitted with a single exponential decay, and has a singlet relaxation time: $T_{\mathrm{S}} = 23 \pm 2\,\mathrm{s}$. Figure 5.10f) shows the decay of ^{13}C nuclear singlet order in the presence of simultaneous CW rf-fields with nutation frequencies: $\omega_{\mathrm{LOCK}}^{\mathrm{C}} = 1\,\mathrm{kHz}$ and $\omega_{\mathrm{LOCK}}^{\mathrm{D}} = 640\,\mathrm{Hz}$. In this case, the singlet relaxation time was found to be: $T_{\mathrm{S}} = 26 \pm 3\,\mathrm{s}$. T_{S} is extended by a factor of 30, compared to the case of $\omega_{\mathrm{LOCK}}^{\mathrm{C}} = \omega_{\mathrm{LOCK}}^{\mathrm{D}} = 0\,\mathrm{Hz}$, and the ratio of T_{S} to T_1 is $\sim$2. The combination of simultaneous CW irradiation on both ^{13}C and ^{2}H nuclei is very effective at suppressing the singlet-SR2K mechanism. Clearly the application of spin-locking rf-fields during the singlet evolution delay τ_{EV} has a strong effect on the relaxation behaviour.

5.5 Discussion

In this section, the experimental data are compared with the theoretical expressions derived in section 5.2.6. In the absence of CW irradiation, the singlet lifetime was found to be approximately 0.9 s for the fumarate diester system, approximately 16 times shorter than the longitudinal relaxation time T_1. However, T_{S} was found to be long-lived

in cases where strong ^{13}C (and ^{2}H) spin-locking rf-fields were applied during the singlet evolution delay τ_{EV}. The largest observed ratio of the singlet relaxation time to the longitudinal relaxation time was approximately 2.

By using equation 5.29, which applies for extreme-narrowing isotropic rotational tumbling, the estimate of the longitudinal relaxation time for the ^{2}H nucleus, and the spin system parameters obtained from fitting the experimental ^{13}C NMR spectrum, the following estimate of the singlet-SR2K relaxation rate constant is obtained: $T_{\mathrm{S}}^{-1}(\mathrm{S2RK}) = 1.06 \pm 0.07\,\mathrm{s}^{-1}$. The longitudinal relaxation rate of the deuterium nucleus $R_1^{(k)}$ was doubled to account for the presence of the second deuteron. A monoexponential fitting of the initial decay for the ^{13}C nuclear singlet order (figure 5.8, blue curve) provides a singlet relaxation rate constant: $T_{\mathrm{S}}^{-1} = 1.1 \pm 0.2\,\mathrm{s}^{-1}$. The initial decay rate of the ^{13}C nuclear singlet order is in excellent agreement with the theoretically predicted value. It is therefore confirmed that the singlet-SR2K mechanism is the dominant relaxation source for the ^{13}C nuclear singlet order in **III**.

Equation 5.38 predicts the singlet relaxation rate constant T_{S}^{-1} in the presence of an on resonant radiofrequency field applied continuously to either the carbon-13 or deuterium nuclei throughout the singlet evolution delay τ_{EV}. By using equation 5.36, which also applies for extreme-narrowing isotropic rotational tumbling, the estimate of the longitudinal relaxation time for the ^{2}H nucleus, and the spin system parameters obtained from fitting the experimental ^{13}C NMR spectrum, the following estimate of the singlet relaxation rate constant in the presence of CW irradiation focussed on the deuterium spins with a 640 Hz nutation frequency is obtained: $T_{\mathrm{S}}^{-1}(\mathrm{CW}) = (13.6 \pm 0.7) \times 10^{-3}\,\mathrm{s}^{-1}$. The estimated singlet decay rate is not in good agreement with the experimentally determined rate: $T_{\mathrm{S}}^{-1} = (85 \pm 3) \times 10^{-3}\,\mathrm{s}^{-1}$. A similar discrepancy is observed for $T_{\mathrm{S}}^{-1}(\mathrm{CW})$ in the case of a spin-locking rf-field applied to the ^{13}C spins with a nutation frequency of 1 kHz. The discrepancy is likely to be attributed to other relaxation mechanisms which are present and accelerate the singlet relaxation, such as ^{13}C-^{2}H dipole-dipole couplings between the carbon-13 nuclei and the adjacent deuterons. It is also possible that the small, long range ^{13}C-^{2}H couplings to the deuterated ester groups could contribute to singlet relaxation via the singlet-SR2K mechanism. Relaxation effects of this kind may have already appeared in the literature, and could be the limiting factor of the singlet lifetimes achieved for the systems presented in the following references [28, 35, 145].

5.6 Conclusions

Since fumarates are a ubiquitous cellular substance, the extension of singlet lifetimes through chemical substitution is an important consideration. However, exchanging the adjacent protons for deuterons has been shown to introduce the singlet-scalar relaxation of the second kind (S-SR2K) mechanism, which drastically shortens the singlet lifetime. In this chapter, it has been successfully demonstrated that singlet-SR2K can significantly shorten the singlet relaxation time T_S of deuterated spin systems, under suitable conditions. This requires a difference in the scalar couplings from the singlet nuclei to an exterior quadrupolar nucleus, and the in pair scalar coupling to be comparable to the longitudinal relaxation rate of the quadrupolar spin. These conditions are satisfied for a 4-spin deuterated fumarate diester. In the current case, T_S is approximately 16 times shorter than T_1. The short value of T_S supports a relaxation model in which the dominant singlet interaction is S-SR2K. It is shown that the singlet-SR2K mechanism is steadily quenched by the application of ^{13}C (and ^{2}H) spin-locking rf-fields, in the case that the amplitude of the suppression field is considerably greater than the in pair scalar coupling. The maximum value of the singlet relaxation time was found to be: $T_S = 26 \pm 3\,s$, a factor of $\sim$2 greater than T_1.

It should be noted that other interesting molecules may also exhibit singlet-SR2K. Systems comprising of $H_2C{=}CD\text{-}CO_2R$ substructures, such as styrene-d_1, are of suitable type. However, the S-SR2K mechanism may only be isolated through implementing field cycling experiments as the large proton chemical shift difference introduces relaxation contributions from singlet-triplet leakage. It is also not yet known whether the proton singlet state of $H_2C{=}CX\text{-}CO_2R$ systems, where X is a quadrupolar nucleus relaxing on the timescale of the proton nuclear Larmor frequency, such as Br or Cl, display observable singlet-SR2K. Investigations into this effect are feasible on molecular systems such as bromoacrylates and bromothiophenes but would require detailed computational modelling or molecular dynamics, and also a measurement of the quadrupolar X-atom T_1.

Chapter 6

An outlook for hyperpolarized singlet NMR

6.1 Conclusions of this work

The previous three chapters of this thesis contain some of the findings which my colleagues and I have contributed to the field of hyperpolarized singlet state NMR. The demonstrated effects are, to the best of our knowledge, all novel and show that previously cemented techniques may still be used to generate new knowledge of hyperpolarized singlet NMR. The work was divided into three sections: long-lived states in CH_2D groups, direct generation and coherent readout of hyperpolarized singlet order, and singlet-scalar relaxation of the second kind. Experimental results from chapters 3, 4 and 5 were examined theoretically with analytical expressions for singlet relaxation or polarization, with the theory outlined in chapters 1 and 2 intended to facilitate the discussion of the experimental findings. A summary of the essential results of each chapter is given in the bullet points below.

Long-lived nuclear spin states in monodeuterated methyl groups

This thesis was intended to focus on the two limiting factors of nuclear magnetic resonance experiments: (1) short signal lifetimes; and (2) low signal sensitivity. The issue of (1) was addressed, in part, by the use of long-lived nuclear spin states [14, 15]. Long-lived spin states commonly exhibit relaxation times which outstrip those corresponding to ordinary magnetization [16, 20, 26, 55, 144, 146, 150, 151, 156]. The non-magnetic

nature of the nuclear singlet state preserves the spin order for a pair of coupled spins against symmetric NMR relaxation mechanisms. A singlet relaxation time exceeding 1 hour in room temperature solution has been observed [35], and a T_S/T_1 ratio greater than 50 has also been realized for a pair of strongly coupled protons [29, 33].

Chapter 3: Summary

- Singlet order is accessible in monodeuterated methyl groups.
- Experimental demonstrations were provided for N-CH_2D-2-methylpiperidine and (α-deuterio-*o*-chlorotoluene)chromium tricarbonyl.
- Singlet pulse sequences access the nuclear singlet order even when chemical shift differences are unresolved.
- The ratio of T_S to T_1 was found to be constant over a wide range of temperatures, solvents, and magnetic fields.
- The longest observed value of T_S approaches 2 1/2 minutes.
- A modified model of the CH_2D geometry was proposed to explain the observed relaxation time ratio.

Direct hyperpolarization and coherent readout of long-lived proton singlet order

The poor signal-to-noise levels (2), ultimately a limiting factor for observing NMR signals at long times after the encodement of nuclear spin order, was partially overcome by dissolution-dynamic nuclear polarization techniques [71]. DNP, and other hyperpolarization methods, drastically improve the initial Zeeman polarization for a sample in a magnetic field by increasing the net alignment of nuclear spins. Coupled with dissolution apparatus, the sample may be dissolved and rapdily transferred to a high resolution NMR magnet where more intricate spin manipulations may be performed.

Chapter 4: Summary

- Singlet order may be polarized directly by DNP.
- The effect is demonstrated on the inequivalent protons of a CH_2D group in a chiral molecule.

- In near-equivalent systems, the singlet order is long-lived in high magnetic field.
- Observable hyperpolarized signals may be generated coherently from the singlet order with high conversion efficiency.
- At long times, >1 minute after dissolution, singlet polarization has advantages over Zeeman polarization.

Singlet scalar relaxation of the second kind in the regime of slow quadrupolar relaxation
Over the past decade, it has been established that singlet lifetimes often exceed the longitudinal relaxation time T_1 by an order of magnitude [28, 144–146, 150, 156]. However, singlet lifetimes are not infinite and are intrinsically limited to some extent. In some cases, this may be attributed to dipole-dipole relaxation with remote protons, and hence deuteration is the favoured approach for attenuating this particular relaxation contribution. After an exhaustive study of all the singlet relaxation mechanisms which have been observed in a variety of candidate systems [24, 152, 153], another possibility remains. A variant of the scalar relaxation of the second kind mechanism, which involves a difference between the scalar couplings of the nuclear spins-1/2 to a third nucleus which has an independent relaxation mechanism, such as nuclear quadrupolar relaxation, has been experimentally observed for the first time. This new found relaxation mechanism could presently be the limiting step in the quest to extend singlet relaxation times to an even greater extent.

Chapter 5: Summary

- Singlet-scalar relaxation of the second kind has been identified as an important relaxation mechanism.
- The singlet SR2K mechanism is significant in the regime of slow quadrupolar relaxation.
- Relaxation rate expressions describing the behaviour of the S-SR2K mechanism were presented.
- An experimental demonstration was provided for a ^{13}C,^{2}H-labelled fumarate diester.

- The S-SR2K mechanism may be suppressed by applying on resonant radiofrequency fields.

6.2 Future endeavours and perspectives

I hope that the discoveries presented in this thesis have been interesting for the reader and have shown the story of my time as a PhD student over the last few years. Interesting possibilities for singlet NMR remain to be investigated, and I believe that the lifetime of nuclear singlet order can be extended still further. As previous discussed, a doubly labelled $^{13}C_2$-naphthalene derivative currently holds the world record for the longest singlet lifetime [35]. The results presented in chapter 5 of this thesis demonstrate that additional, previously unconsidered relaxation mechanisms may set the limit for singlet lifetimes, even in systems already display remarkable lifetimes [29, 33, 35]. The S-SR2K mechanism exists in systems where the singlet spins are scalar coupled to a slowly relaxing quadrupolar nucleus. Modulations of the scalar couplings between a ^{13}C spin pair and the neighbouring deuterons were shown to be the strongest singlet relaxation mechanism in a deuterated fumarate diester. Continuous wave irradiation is one route to suppressing the S-SR2K mechanism, but CW fields are not suitable for *in vivo* studies [223]. Whether the spectroscoper likes it or not, simply removing the surrounding protons via deuteration may not be the most effective route to lengthening singlet lifetimes. Entire deuteration of a molecular system may therefore not be entirely sufficient, and instead all magnetic nuclei surrounding the singlet pair should be evacuated, and replaced with magnetically silent isotopes (ignoring the small percentages of magnetic nuclei which are present at natural abundance). The advanced knowledge of singlet order decay will aid the design and construction of singlet pairs in molecular candidates with fewer and less effective relaxation mechanisms. A long-lived spin state in a pair of ^{15}N nuclei with a lifetime exceeding that of naphthalene has yet to be demonstrated, but a simple argument of the gyromagnetic ratios infers that the lifetime could be quite spectacular, and possibly exceed 4 hours in solution at room temperature.

The long lifetimes of hyperpolarized singlet order present an excellent opportunity to study biologically relevant processes *in vivo* using magnetic resonance imaging [224]. Delays between the hyperpolarizing device and point of use (possibly a human patient) will potentially be minimized by the exceptional lifetime of singlet spin order, even in

the presence of paramagnetic radicals. One potential avenue of long-lived states is the tracking of endogenous metabolites, or even exogenous substances which are injected into a human patient and dissolved in the bloodstream, over considerable timescales to monitor molecular transport to a site of interest. Experiments of this kind could potentially be used to validate drug delivery methods, and monitor cellular necrosis and the response of cancerous tissue to treatment [64, 133]. An alternative, and potentially more promising route, at least initially, could be to develop contrast agents using the extended lifetimes of singlet states [159]. Work of this kind has already been presented by the group of Bodenhausen in the context of drug screening, where a change in the ratio of T_S/T_1 provided ample constrast for the detection of ligand-binding and dissociation [206, 208, 225]. A major breakthrough would be the regular synthesis and demonstration of singlet molecules which are sensitive to their environmental conditions. The lifetime of the nuclear singlet order could hence be controlled as a function of pH, temperature and the presence uv light, even stretching or compressing the surroundings could have an impact on singlet lifetimes [226].

The dissolution-dynamic nuclear polarization experiments presented in chapter 4 have potentially intriguing implications for the future conduction of hyperpolarized singlet experiments. The results shown in this thesis demonstrate that, for strongly-coupled spin-1/2 pairs, the nuclear singlet order permits larger hyperpolarized signals to be observed at longer times after dissolution, compared with those of ordinary magnetization. Whilst the phenomenon is currently specific to systems which display near-magnetic-equivalence, such systems are relatively common, and are found, for example, in the side chains and glycine residues of peptides [156], and in sugars [227], and might also be exploited in the context of "singlet tagging" [148]. Another exciting development in the field of DNP is the "bullet" setup pioneered by Meier [228]. In contrast to classical D-DNP experiments [71], the hyperpolarized medium is transported as a solid and is ejected from the hyperpolarizer at speeds exceeding $100\,\mathrm{ms}^{-1}$ towards the point of use. The method has the potential to preserve the high levels of nuclear alignment throughout the short transfer period which, if used in conjunction with the direct generation of nuclear singlet order, would lead to impressive obtainable levels of singlet polarization in the liquid state. Translation of this methodology to clinical MRI would represent a major step forward in the application of DNP to medical diagnostics, and would provide an opportunity to showcase the advantages of using hyperpolarized long-lived states.

Appendix A

Syntheses

A.1 N-(CH_2D)-2-methylpiperidine

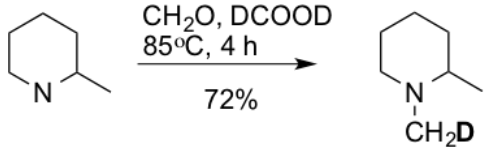

FIGURE A.1: Synthetic route to 2-methyl-1-(methyl-d)piperidine.

To 2-methylpiperidine (844 mg, 1 mL, 8.51 mmol) was added formaldehyde (37 wt.% in H_2O, 767 mg, 2.07 mL, 25.53 mmol, 3 equiv.) followed by careful addition of formic acid-d_2 (95% in D_2O, 1.72 g, 1.41 mL, 34.04 mmol, 4 equiv.), and the reaction heated at 85°C (using a water bath) for 3 h. The reaction was cooled to room temperature, water (2 mL) added and the acidic aqueous reaction was extracted with pet. ether. The aqueous layer was basified to pH 12 using 6 M NaOH and extracted with Et_2O (x5). The combined Et_2O extractions were dried ($MgSO_4$) and concentrated on a rotary evaporator with no vacuum (bath temp = 40°C) to give a pale yellow oil. Purification by Kugelrohr distillation (oven temperature 150°C - 160°C) to gave the title compound as a clear oil (696 mg, 6.09 mmol, 72%).

Sample preparation. Solutions were prepared in Wilmad low pressure/vacuum NMR tubes with a 5 mm OD. 6.2 μL of (N-CH_2D)-2-methylpiperidine was dissolved in 0.5 mL of choice solvent at a concentration of 0.1 M. Samples were subjected to thorough

degassing using 6 standard freeze-pump-thaw cycles to remove the majority of dissolved molecular oxygen.

A.1.1 1-(methyl-d)-2-(methyl-d$_3$)piperidine

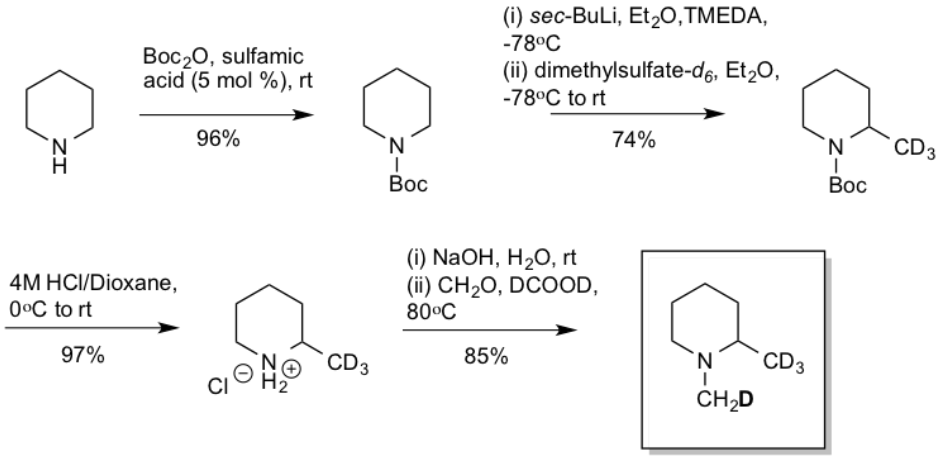

FIGURE A.2: Synthetic route to 1-(methyl-d)-2-(methyl-d$_3$)piperidine.

tert-Butyl piperidine-1-carboxylate:

Boc anhydride (6.78 g, 31.0 mmol) and sulfamic acid (150 mg, 1.5 mmol, 5 mol%) were mixed together neat and warmed to 28°C - 30°C to melt the $(Boc)_2O$. Piperidine (3.2 mL, 2.77 g. 32.0 mmol) was added and the resulting mixture was stirred at room temperature for 15 minutes. The reaction was diluted with Et_2O, washed with H_2O (x 2) and brine (x 2) and dried ($MgSO_4$). Removal of the solvents in vacuo (no heat) gave the title product as a pale yellow oil (5.51 g, 29.8 mmol, 96%).

tert-Butyl 2-(methyl-d3)piperidine-1-carboxylate:

A solution of tert-butyl piperidine-1-carboxylate (2.5 g, 13.51 mmol) in Et_2O (30 mL) was cooled to -78°C and treated with TMEDA (2.63 mL, 17.56 mmol) dropwise over 10 minutes. sec-BuLi (1.4 M in cyclohexane, 12.5 mL, 17.56 mmol) was added dropwise over 20 minutes. The pale yellow mixture was stirred for 5 h at -78°C. and then treated with a solution of dimethyl sulfate-d_6 (3.20 g, 24.32 mmol) in Et_2O (12 mL). The mixture was warmed to room temperature and stirred for 12 h. The reaction was concentrated in vacuo to give a crude colourless oil which was purified by column chromatography on silica gel eluting with 2% - 5% Et_2O: pet. ether. This afforded the title product as a clear oil (2.03 g, 10.0 mmol, 74%).

2-(methyl-d_3)piperidin-1-ium chloride:
To tert-butyl 2-(methyl-d_3)piperidine-1-carboxylate (1.0 g, 5.0 mmol) at 0°C was added 4 M HCl in dioxane (4 mL, 16 mmol) and the reaction stirred at room temperature for 30 minutes. Et_2O (20 mL) was added producing a white solid. The reaction was concentrated in vacuo and Et_2O (20 mL) added, the resultant white solid was filtered and washed with Et_2O (2 x 10 mL) and dried in vacuo to give the desired white salt (0.67 g, 4.84 mmol, 97%) which was used directly in the next reaction.

1-(methyl-d)-2-(methyl-d_3)piperidine:
2-(methyl-d_3)piperidin-1-ium chloride (0.63 g, 4.55 mmol) was dissolved in a solution of sodium hydroxide (182 mg, 4.55 mmol) in H_2O (2 mL) and stirred for 10 minutes at room temperature. To this mixture was added formaldehyde (37 wt.% in H_2O, 410 mg, 1.10 mL, 13.65 mmol, 3 equiv.) resulting in a cloudy white solution. Formic acid-d_2 (95% in D_2O, 0.86 mL, 22.75 mmol, 5 equiv.) was carefully added and the reaction heated at 85°C (using a water bath) for 4 h. The reaction was cooled to room temperature, water (2 mL) added and the acidic aqueous reaction was extracted with pet. ether. The aqueous layer was basified to pH 12 using 6 M NaOH and extracted with Et_2O (x5). The combined Et_2O extractions were dried ($MgSO_4$) and concentrated on a rotary evaporator with no vacuum (bath temp = 40°C) to give the title compound as a clear oil (455 mg, 3.89 mmol, 85%).

Sample preparation. Solutions were prepared in Wilmad low pressure/vacuum NMR tubes with a 5 mm OD. 6.2 μL of (N-CH_2D)-2-methylpiperidine was dissolved in 0.5 mL of CD_2Cl_2 solvent at a concentration of 0.1 M. Samples were subjected to thorough degassing using 6 standard freeze-pump-thaw cycles to remove the majority of dissolved molecular oxygen.

A.2 (α-deuterio-*o*-chlorotoluene)chromium tricarbonyl

Reduction of 2-chlorobenzyl bromide utilising sodium borodeuteride in DMSO-d_6 as a source of nucleophilic deuteride afforded 1-chloro-2-(methyl-*d*)benzene (**1**). Refluxing $Cr(CO)_6$ and chlorobenzene **1** in a mixture of dibutyl ether and THF (9:1) for 36 h

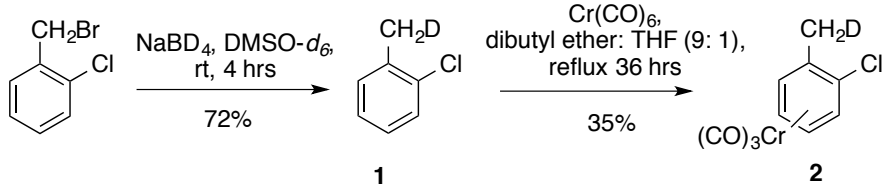

FIGURE A.3: Synthetic route to tricarbonyl (1-chloro-2-(methyl-*d*)benzene)-chromium (0) (**2**)

provided tricarbonyl (1-chloro-2-(methyl-*d*)benzene)-chromium (0) (**2**) as a yellow solid.

A.2.1 1-Chloro-2-(methyl-*d*)benzene (1)

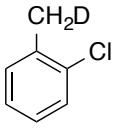

FIGURE A.4: Chemical structure of 1-chloro-2-(methyl-*d*)benzene (**1**)

To 2-chlorobenzyl bromide (2.00 g, 9.73 mmol) in DMSO-d_6 (6 mL) at 0°C was added sodium borodeuteride (0.82 g, 19.46 mmol) portion-wise. The reaction formed a white solid that was stirred for 4 h at room temperature. The reaction was quenched with methanol (0.75 mL), Et_2O was added and the organic layer washed with H_2O (x3), brine and then dried ($MgSO_4$). The solvent was removed in vacuo at room temperature. The resultant oil was purified by Kugelrohr distillation to give the title compound as a colourless oil (0.89 g, 6.98 mmol, 72%). Boiling point: 157-159°C.

^{1}H NMR (400 MHz, $CDCl_3$): δ = 7.36 (dd, J = 7.1 Hz, 1.7 Hz, 1H), 7.27 - 7.12 (m, 3H), 2.41 - 2.37 (t, J_{HD} = 7.1 Hz, 2H).

^{13}C NMR (101 MHz, $CDCl_3$): δ = 135.97, 134.35, 130.92, 129.03, 127.06, 126.53, 19.73 (t, J_{CD} = 19.8 Hz).

GC-MS (EI) m/z (100%) 126.8 $C_7H_6DCl^{+\bullet}$, 91.9 $C_7H_6D^{+\bullet}$.

A.2.2 Tricarbonyl (1-chloro-2-(methyl-*d*)benzene)-chromium (0) (2)

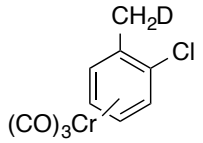

FIGURE A.5: Chemical structure of tricarbonyl (1-chloro-2-(methyl-*d*)benzene)-chromium (0) (**2**)

1-Chloro-2-(methyl-*d*)benzene (**1**, 0.38 g, 3.0 mmol) and chromium (0) hexacarbonyl (0.33 g, 1.5 mmol) in dibutyl ether/THF (9:1, 7.5 mL) was heated at reflux for 36 h. The reaction was allowed to cool, Et_2O was added and the solution passed through a short column of alumina, eluting with Et_2O. The solvent was removed in vacuo and the crude yellow solid recrystallized from Et_2O/pentane and the yellow crystals washed with cold pentane. The title compound was obtained as a yellow crystalline solid (0.28 g, 1.06 mmol, 35%). Melting point: 100-102°C.

^{1}H NMR (400 MHz, C_6D_6): $\delta = 4.75$ (br d, J = 6.2 Hz, 1H), 4.30 (br d, J = 6.0 Hz, 1H), 4.18 (br t, J = 6.1 Hz, 1H), 4.07 (br t, J = 6.1 Hz, 1H), 1.71 (br s, 2H).

^{13}C NMR (101 MHz, C_6D_6): δ = 112.04, 106.27, 93.87, 93.29, 91.01, 90.42, 18.98 (t, J_{CD} = 19.9 Hz).

GC-MS (EI) m/z (100%) 126.8 $C_7H_6DCl^{+\bullet}$.

Sample preparation. Solutions were prepared in Wilmad low pressure/vacuum NMR tubes with a 5 mm OD. 12.58 mg of **I** was dissolved in 0.5 mL of C_6D_6 at a concentration of 0.1 M. Samples were subjected to thorough degassing using 4 standard freeze-pump-thaw cycles to remove the majority of dissolved molecular oxygen.

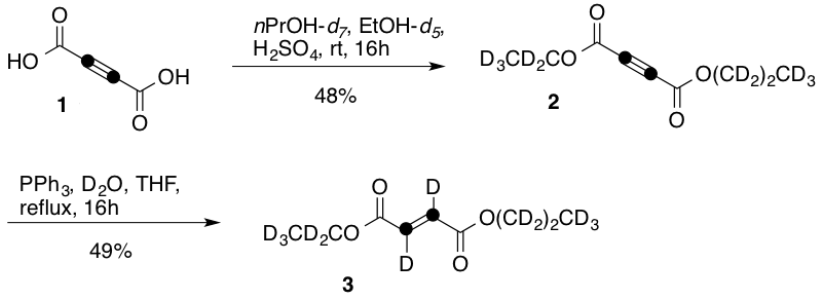

FIGURE A.6: Synthetic route to ethyl-d_5 (propyl-d_7) fumarate-2,3-$^{13}C_2$-d_2.

A.3 Ethyl-d_5 (propyl-d_7) fumarate-2,3-$^{13}C_2$-d_2

Ethyl-d_5 (propyl-d_7) fumarate-2,3-$^{13}C_2$-d_2 **3** was synthesised from commercially available acetylene-2,3-$^{13}C_2$ dicarboxylic acid (**1**) in two steps (figure A.6). Thus, treatment of acetylene-2,3-$^{13}C_2$ dicarboxylic acid (**1**) with ^{n}PrOH-d_7, EtOH-d_5 and H_2SO_4 at room temperature for 16 h afforded the mixed ester **2** in 48% yield. This ester **2** was used directly in a reduction reaction with PPh_3 and D_2O in THF to afford **3** in 49% yield (24% overall yield from **1**), the other major product isolated from this reaction was ethyl-d_5 (propyl-d_7) maleate-2,3-$^{13}C_2$-d_2 (35%).

Experimental

General experimental details:

All air/moisture sensitive reactions were carried out under an inert atmosphere (N_2 or Ar), using oven or flame-dried glassware. THF (from Na/benzophenone) was distilled before use. All other solvents and reagents were used as received from standard chemical suppliers unless otherwise stated. TLC was performed on aluminium plates pre-coated with silica gel 60 with an F254 indicator; visualized under UV light (254 nm) and/or by staining with $KMnO_4$. Flash column chromatography was performed with Merck Kieselgel 60 silica gel. ^{1}H and ^{13}C NMR spectra were recorded in $CDCl_3$ solutions using Bruker DPX400, Bruker AVII-400 or AVIIIHD-400 (400 and 100 MHz respectively) spectrometers. Chemical shifts are reported in δ units using $CHCl_3$ (δ 7.27 ppm ^{1}H, δ 77.0 ppm ^{13}C) as an internal standard. Coupling constants (J) are reported in Hz. For ^{13}C labelled compounds, only the signals corresponding to the labels are reported in the ^{13}C NMR data. MS were recorded using positive ion electrospray ionization (ESI+) obtained using a Micromass platform mass analyzer with an electrospray ion source.

1-(Ethyl-d_5) 4-(propyl-d_7)- but-2-ynedioate-2,3-$^{13}C_2$ dicarboxylate (**2**):
To a suspension of acetylene-2,3-$^{13}C_2$ dicarboxylic acid (**1**) (400 mg, 3.45 mmol) in 1-propanol-1,1,2,2,3,3,3-d_7 (0.78 mL, 10.35 mmol, 3.0 equiv.) and ethanol-1,1,2,2,2-d_5 (0.61 mL, 10.35 mmol, 3.0 equiv.) was added conc. H_2SO_4 (551 μL, 10.35 mmol, 3.0 equiv.). The reaction was allowed to stir at room temperature for 16 h and then diluted with Et_2O and H_2O. The aqueous layer was re-extracted with Et_2O (3 × 10 mL) and the combined organic layers washed with sat. aq. $NaHCO_3$, brine and dried (Na_2SO_4) and concentrated *in vacuo*. The residue purified by chromatography on silica gel (Et_2O:hexane 1:99) to afford the title compound 1-(ethyl-d_5) 4-(propyl-d_7)-but-2-ynedioate-2,3-$^{13}C_2$ dicarboxylate (**2**) as a colourless oil (327 mg, 1.65 mmol, 48%). Data for labelled but-2-ynedioate: ^{13}C NMR (100 MHz, $CDCl_3$) δ 76.6; MS (ESI+) m/z 221.0 [M + Na]+.

Ethyl-d_5 (propyl-d_7) fumarate-2,3-$^{13}C_2$-d_2 (**3**):
To 1-(ethyl-d_5) 4-(propyl-d_7)-but-2-ynedioate-2,3-$^{13}C_2$ dicarboxylate (**2**) (230 mg, 1.16 - mmol) was dissolved in anhydrous THF (3.0 mL) at 0°C was added D_2O (21 μL, 1.16 mmol). Triphenylphosphine (305 mg, 1.16 mmol) in anhydrous THF (3.0 mL) was then added dropwise and the reaction stirred at room temperature for 30 mins followed by heating at reflux for 16 h. The reaction was allowed to cool, concentrated in vacuo and the residue purified by chromatography on silica gel (Et_2O:hexane 1:99 to 1:24) to afford the title compound ethyl-d_5 (propyl-d_7) fumarate-2,3-$^{13}C_2$-d_2 (**3**) as a colourless oil (115 mg, 0.57 mmol, 49%). Data for unlabelled fumarate: ^{1}H NMR (400 MHz, $CDCl_3$) δ 6.86 (s, 2H), 4.26 (q, J = 7.1 Hz, 2H), 4.16 (t, J = 6.7 Hz, 2H), 1.76 - 1.64 (m, 2H), 1.32 (t, J = 7.1 Hz, 3H), 0.97 (t, J = 7.3 Hz, 3H); ^{13}C NMR (100 MHz, $CDCl_3$) δ 165.1, 165.0, 133.6, 133.6, 66.9, 62.3, 21.9, 14.1, 10.3; MS (ESI+) m/z 187.3 [M + H]+. Data for labelled fumarate: ^{13}C NMR (100 MHz, $CDCl_3$) δ 133.6 - 133.0 (m, 2C); MS (ESI+) m/z 241.3 [M + K]+.

Sample preparation. Solutions were prepared in Wilmad low pressure/vacuum NMR tubes with a 5 mm OD. 21 mg of ethyl-d_5 (propyl-d_7) fumarate-2,3-$^{13}C_2$-d_2 was dissolved in 0.5 mL of $CDCl_3$ solvent at a concentration of 0.207 M. Samples were subjected to thorough degassing using 6 standard freeze-pump-thaw cycles to remove the majority of dissolved molecular oxygen.

Appendix B

Mathematical tools

B.1 Longitudinal relaxation

During the discussion of longitudinal relaxation in chapter 1, the solution to the following Bloch equation was reported:

$$\frac{dM_z(t)}{dt} = -R_1 \left(M_z(t) - M_{z,equil} \right). \tag{B.1}$$

In this section I will provide the derivation of this result. The negative sign in the above expression denotes the decay of non-equilibrium z-magnetization reapproaching thermal equilibrium after rf-perturbation. The timescale on which this process takes place is governed by the longitudinal relaxation rate constant R_1. At a time $t = 0$ the initial z-magnetization is given by $M_z(0)$. The motion of z-magnetization returning to thermal equilibrium is revealed by rearranging and integrating equation B.1:

$$\int \frac{1}{M_z(t) - M_{z,equil}} dM_z(t) = -\int R_1 dt. \tag{B.2}$$

The left and right hand sides of equation B.2 are integrated with respect to the variables M_z and t, respectively:

$$\ln|M_z(t) - M_{z,equil}| = -R_1 t + c, \tag{B.3}$$

where c is the constant of integration. $M_{z,equil}$ and R_1 are also constants. At a time $t = 0$ equation B.3 can be used to find the value of c:

$$c = \ln|M_z(0) - M_{z,equil}|, \tag{B.4}$$

which may be resubsituted back into equation B.3:

$$\ln|M_z(t) - M_{z,equil}| = -R_1 t + \ln|M_z(0) - M_{z,equil}|. \tag{B.5}$$

By eye one can inspect that:

$$-R_1 t = \ln|\frac{M_z(t) - M_{z,equil}}{M_z(0) - M_{z,equil}}|, \tag{B.6}$$

and by taking the exponential of both sides of equation B.6:

$$e^{-R_1 t} = \frac{M_z(t) - M_{z,equil}}{M_z(0) - M_{z,equil}}, \tag{B.7}$$

and finally rearranging equation B.7:

$$\vec{M}_z(t) = M_{z,equil} + (M_z(0) - M_{z,equil})e^{-R_1 t}, \tag{B.8}$$

one arrives at the result presented in chapter 1. Equation B.8 states that the rate of change of z-magnetization is larger if the initial z-magnetization $M_z(0)$ is further way from thermal equilibrium initially, and that the time taken to reach thermal equilibrium after rf-perturbation is shorter if the relaxation rate constant R_1 is larger.

B.2 Propagation of a time dependent Hamiltonian

In the case of a time dependent Hamiltonian, there is no explicit expression for the time propagator. A solution is therefore approximated by dividing the total time into infinitesimal time steps Δt, and propagating over each infinitesimal time step:

$$\lim_{\Delta t \to 0} \hat{U}_i(t_b, t_a) = e^{-i\hat{H}(t_b)\Delta t} e^{-i\hat{H}(t_b - \Delta t)\Delta t} e^{-i\hat{H}(t_b - 2\Delta t)\Delta t} \ldots e^{-i\hat{H}(t_a)\Delta t}, \tag{B.9}$$

i.e. the limit of a time-ordered product of Hamiltonian operators. The Dyson time ordering superoperator $\hat{\hat{T}}$ is used to achieve this solution, and allows the infinitesimal time-propagator $\hat{U}_i(t_b, t_a)$ in equation B.9 to be expressed as:

$$\hat{U}_i(t_b, t_a) = \hat{\hat{T}} exp[-i \int_{t_a}^{t_b} dt' \hat{H}(t')]. \tag{B.10}$$

The Dyson time ordering superoperator applied to a set of Hamiltonians $\hat{H}(t_i)$ at different times t_i orders the Hamiltonians such that:

$$\hat{\hat{T}}(\hat{H}(t_b), \hat{H}(t_a)) = \hat{H}(t_b)\hat{H}(t_a), \tag{B.11}$$

for $t_b > t_a$.

B.3 Tensor transformations

Consider a 3×3 tensor $\left[C^{\lambda}_{mm'}\right]^P$ in the principle axis frame P of the interaction λ. In the frame P, the tensor is strictly diagonal:

$$\left[C^{\lambda}_{mm'}\right]^P = \begin{bmatrix} C^{\lambda}_{xx} & 0 & 0 \\ 0 & C^{\lambda}_{yy} & 0 \\ 0 & 0 & C^{\lambda}_{zz} \end{bmatrix}, \tag{B.12}$$

and has principal components: C^{λ}_{xx}, C^{λ}_{yy}, C^{λ}_{zz}. Define the z-axis of the static magnetic field to be parallel with the z-axis of the laboratory frame L. The relative orientation of the interaction tensor $C^{\lambda}_{mm'}$ in the frame P with respect to the laboratory frame L is specified by the set of Euler angles: $\Omega^{\lambda}_{PL} = \{\alpha^{\lambda}_{PL}, \beta^{\lambda}_{PL}, \gamma^{\lambda}_{PL}\}$. The matrix representation of the tensor in the laboratory frame L is as follows:

$$\left[C^{\lambda}_{mm'}\right]^L = D(\Omega^{\lambda}_{PL}) \left[C^{\lambda}_{mm'}\right]^P D(\Omega^{\lambda}_{PL})^{-1}. \tag{B.13}$$

As is often the case in NMR, an intermediate frame, usually the molecular frame M, is required to manage the relative frame transformations from the principle axis frame P of interaction λ to the laboratory frame L. The interaction tensor $C^{\lambda}_{mm'}$ has a fixed orientation with respect to the molecular axis system M, in which the molecule is also oriented with respect to the static magnetic field. The relative orientation of frame P

with respect to frame M is specified by using the Euler angles Ω^{λ}_{PM}, and the relative orientation of frame M with respect to frame L is specified by using the Euler angles Ω^{λ}_{ML}. Therefore, $D(\Omega^{\lambda}_{PL})$ is written by "chaining" Wigner rotation matrices:

$$D(\Omega^{\lambda}_{PL}) = D(\Omega^{\lambda}_{PM})D(\Omega^{\lambda}_{ML}). \tag{B.14}$$

Consider the a single term in the rotation matrix $\mathbf{R}(\Omega^{\lambda}_{PL})$, such as $\mathbf{R}_{zx}(\Omega^{\lambda}_{PL})$, which is interpreted by using rotation operators as follows:

$$\hat{R}_{zx}(\Omega^{\lambda}_{PL}) = \hat{R}_{zx}(\Omega^{\lambda}_{PM})\hat{R}_{xx}(\Omega^{\lambda}_{ML}) + \hat{R}_{zy}(\Omega^{\lambda}_{PM})\hat{R}_{yx}(\Omega^{\lambda}_{ML}) + \hat{R}_{zz}(\Omega^{\lambda}_{PM})\hat{R}_{zx}(\Omega^{\lambda}_{ML}), \tag{B.15}$$

where each component is specified by the rotation matrix given in equation 1.130. Chaining Wigner rotation matrices makes consecutive rotations over multiple interaction frames between the axis systems P and L considerably easier. Additional reference frames, such as a rotor axis system R, are often required in solid-state NMR and in the relaxation analysis of rotating methyl groups in solution. The rotor frame R rotates about a fixed axis with respect to the molecular frame M. The chain of Wigner rotation matrices in equation B.14 becomes:

$$D(\Omega^{\lambda}_{PL}) = D(\Omega^{\lambda}_{PR})D(\Omega^{\lambda}_{RM})D(\Omega^{\lambda}_{ML}). \tag{B.16}$$

where $D(\Omega^{\lambda}_{PR})$ defines the relative orientation of the principle axis system with respect to the rotor frame for an interaction λ, and $D(\Omega^{\lambda}_{RM})$ defines the relative orientation of the rotor frame with respect to the molecular frame. For further information, see reference [229].

B.4 Motional averaging

Complicated nuclear spin Hamiltonians may be simplified to a "motionally averaged" Hamiltonian, due to the rapid tumbling of molecules in isotropic liquids (and gases). If a molecule undergoes fast reorientation the interactions associated with the molecule will fluctuate in time. If the interactions fluctuate sufficiently fast a "motionally averaged" interaction strength may be used. The situation is made even simpler as some interactions may have zero time-averages, and can be neglected. Unless molecular motion is

slow a "motionally averaged" Hamiltonian is usually a good approximation to the full nuclear spin Hamiltonian.

The motionally averaged Hamiltonian depends on the type of motion averaging the interaction strengths. Rotations of a molecule in solution inherently suggest a change in the overall molecular orientation. Rotations are detectable by NMR because these motions alter the nuclear spin Hamiltonian, such as the coupling magnitudes for the anisotropic dipole-dipole and chemical shift anisotropy interactions. In general, three angles are required to define a rotation in space, these will be substituted by Θ, which is assumed to be time-dependent.

The time-dependent, secular Hamiltonian expressed as $\hat{H}^0(\Theta(t))$ may be written as the time-average secular Hamiltonian by taking into account motional averaging:

$$\overline{\hat{H}}^0(\Theta) = \tau^{-1} \int_0^\tau dt\, \hat{H}^0(\Theta(t)). \tag{B.17}$$

For large values of τ the *ergodic hypothesis* may be invoked as the molecule is likely to have sampled all molecular orientations. An integral over time is therefore considered as an integral over molecular orientation:

$$\overline{\hat{H}}^0(\Theta) = \int d\Theta P(\Theta) \hat{H}^0(\Theta), \tag{B.18}$$

where $P(\Theta)$ is the probability density of a molecule having a particular molecular orientation. In isotropic liquids (and gases) all orientations are equally likely, and the probability density is the same for all orientations. In cases of anisotropic media, such as liquid crystals, all orientations are not equally probable as molecular orientations aligned with the liquid crystal director are most preferable. The isotropic motionally averaged secular Hamiltonian is therefore written as:

$$\overline{\hat{H}}^0_{iso}(\Theta) = N^{-1} \int d\Theta \hat{H}^0(\Theta), \tag{B.19}$$

where N is a normalization constant, chosen so that the total probability is 1:

$$N = \int d\Theta. \tag{B.20}$$

B.5 Multipole expansion

Consider a charge q_i at position $\vec{r_i}$ defined by: $\rho(\vec{r}) = q_i\delta(\vec{r} - \vec{r_i})$. One can define an electronic potential such that: $E(\vec{r}) = -\nabla\phi(\vec{r})$, where:

$$\phi(\vec{r}) = \frac{1}{4\pi\epsilon_0}\int_V dV\frac{\rho(\vec{r})}{|\vec{r} - \vec{r_i}|}. \tag{B.21}$$

In the case where $\vec{r_i} \gg \vec{r}$, the multipole expansion of $\frac{1}{\vec{r}+\vec{r_i}}$ is valid:

$$\frac{1}{\vec{r} + \vec{r_i}} = \sum_{n=0}^{N}\frac{1}{n!}(\vec{r_i}\cdot\vec{\nabla}_r)^n\frac{1}{r}. \tag{B.22}$$

Therefore, the electric potential $\phi(\vec{r})$ becomes:

$$\phi(\vec{r}) = \frac{1}{4\pi\epsilon_0}\int_V dV\rho(\vec{r})\left[\frac{1}{r} + \frac{\vec{r_i}\cdot\vec{r}}{r^3} + \frac{3(\vec{r_i}\cdot\vec{r})^2 - r_i^2r^2}{2r^5} + ...\right]. \tag{B.23}$$

Thus, expanding equation B.23 via a Taylor series, the multipole expansion is complete:

$$\phi(\vec{r}) = \frac{1}{4\pi\epsilon_0}\left[\frac{Q}{r} + \frac{p_i\cdot r_i}{r^3} + \frac{1}{2}\sum_{ij}\frac{r_ir_j}{r^5}Q_{ij}\right], \tag{B.24}$$

where Q_{ij} (third term in the multipole expansion) represents the quadrupole moment. Q_{ij} is defined as:

$$Q_{ij} = \int_V dV(3r_i\cdot r_j - r_ir_j\delta_{ij})\rho\vec{r}. \tag{B.25}$$

This parameter is used to describe the effective shape of an ellipsoid representing a nuclear charge distribution.

B.6 Rotating frame transformation

In order to treat the presence of radiofrequency pulses the necessary evil of transforming between laboratory and rotating frames is required. As the resonant component of an rf-field rotates at a constant frequency in the rotating frame the spin Hamiltonian appears to be time-independent if one views the spins from a frame which "rotates with the rf-field", i.e. the on resonant component of the rf-field appears to be static in

the rotating frame. This mathematical trick greatly simplifies many problems within magnetic resonance.

Consider a laboratory reference frame with axes denoted: $\{ \mathbf{e}_x, \mathbf{e}_y, \mathbf{e}_z \}$. The rotating frame has axes: $\{ \mathbf{e}'_x, \mathbf{e}'_y, \mathbf{e}'_z \}$. The two frames are related by:

$$\mathbf{e}'_x = \mathbf{e}_x \cos(\phi(t)) + \mathbf{e}_y \sin(\phi(t)), \tag{B.26}$$

$$\mathbf{e}'_y = \mathbf{e}_y \cos(\phi(t)) - \mathbf{e}_y \sin(\phi(t)), \tag{B.27}$$

$$\mathbf{e}'_z = \mathbf{e}_z, \tag{B.28}$$

where $\phi(t)$ is a time-dependent angle given by:

$$\phi(t) = \omega_{\text{res}} t + \varphi(t), \tag{B.29}$$

where ω_{res} is the resonant part of the rf-field, and $\varphi(t)$ is a constant phase factor. Consider a spin in a magnetic field with an eigenstate $|\psi\rangle$ precessing at a Larmor frequency ω_{res} about the z-axis of the laboratory frame. For simplicity, assume that the spin polarization vector is oriented in the xy-plane. The eigenstate $|\psi\rangle$ evolves with the following form:

$$|\psi'\rangle = \hat{R}_z(\phi(t)) \, |\psi\rangle \, . \tag{B.30}$$

In the rotating frame, the angle between the spin polarization vector and the $\mathbf{e}_x$ and $\mathbf{e}_y$ axes is fixed, and hence the eigenstate would not appear to evolve:

$$|\tilde{\psi}\rangle = |\psi\rangle \, . \tag{B.31}$$

The "tilde" denotes the view from the rotating frame. The relationship between an eigenstate in the laboratory and rotating frame is therefore:

$$|\tilde{\psi}'\rangle = \hat{R}_z(-\phi(t)) \, |\psi'\rangle \, . \tag{B.32}$$

The equation of motion for eigenstates as viewed from the rotating frame derives from the Schrödinger equation:

$$-i\hat{\tilde{H}} \, |\tilde{\psi}'\rangle = \frac{d}{dt} \, |\tilde{\psi}'\rangle \, . \tag{B.33}$$

Using equation B.32 and the chain rule of differentiation, the right hand side of equation B.33 becomes:

$$\frac{d}{dt}\left[\hat{R}_z(-\phi(t))\,|\psi'\rangle\right] = \frac{d}{dt}\hat{R}_z(-\phi(t))\cdot|\psi'\rangle + \hat{R}_z(-\phi(t))\cdot\frac{d}{dt}\,|\psi'\rangle\,. \tag{B.34}$$

By substituting for the rotation operator $\hat{R}_z(-\phi(t))$ (see chapter 1, section 1.7.1) and solving for its time derivative:

$$\frac{d}{dt}e^{i\phi(t)\hat{I}_z}\,|\psi'\rangle = i\omega_{\rm res}\hat{I}_z\hat{R}_z(-\phi(t))\,|\psi'\rangle\,, \tag{B.35}$$

and using the relation: $\frac{d}{dt}\phi(t) = \omega_{\rm res}\frac{d}{dt}\phi(t)$, equation B.33 becomes:

$$-i\hat{\tilde{H}}\,|\tilde{\psi}'\rangle = i\omega_{\rm res}\hat{I}_z\hat{R}_z(-\phi(t))\,|\psi'\rangle - i\hat{R}_z(-\phi(t))\hat{H}\,|\psi'\rangle\,. \tag{B.36}$$

The rotating frame spin Hamiltonian is therefore written as:

$$\hat{\tilde{H}}\,|\tilde{\psi}'\rangle = \hat{R}_z(-\phi(t))\hat{H}\hat{R}_z(\phi(t))\,|\tilde{\psi}'\rangle - \omega_{\rm res}\hat{I}_z\,|\tilde{\psi}'\rangle\,. \tag{B.37}$$

The rotating frame Hamiltonian contains two terms. The first is a rotation of the laboratory frame Hamiltonian about the z-axis through the time dependent angle $\phi(t)$. This term implies that static spin operators move backwards in the rotating frame. The second term is a non-linear motion correction to the spin dynamics and arises simply because the frame is rotating.

B.7 Projection superoperators

As discussed in chapter 1, a quantum state $|\psi\rangle$ may be expanded as a linear combination of ket vectors $|\psi_i\rangle$:

$$|\psi\rangle = \sum_i c_i\,|\psi_i\rangle\,, \tag{B.38}$$

where $c_i = \langle\psi_i|\psi\rangle$, which ensures the relation:

$$\sum_i |\psi_i\rangle\langle\psi_i| = 1. \tag{B.39}$$

The projection superoperator ascertains the amount of an operator $\hat{N}$ within another operator $\hat{M}$, such as the level of singlet order $\hat{Q}_{\mathrm{SO}}$ within the spin density operator $\hat{\rho}$. The projection superoperator $\hat{\hat{p}}_{MN}$ is defined as:

$$\hat{\hat{p}}_{MN} = \frac{\mathrm{Tr}[\hat{M}^{\dagger}\hat{N}]}{\mathrm{Tr}[\hat{M}^{\dagger}\hat{M}]}, \tag{B.40}$$

and the application of the projection superoperator to an operator $\hat{N}$ is:

$$\hat{\hat{p}}_{MN}\hat{N} = \frac{\mathrm{Tr}[\hat{M}^{\dagger}\hat{N}]}{\mathrm{Tr}[\hat{M}^{\dagger}\hat{M}]}\hat{M} = \alpha_M \hat{M}. \tag{B.41}$$

The coefficient α_M is the measure of the operator $\hat{N}$ within the operator $\hat{M}$. The maximum value of $\alpha_M = 1$ as $\hat{\hat{p}}_{MN}$ is normalized by $\mathrm{Tr}[\hat{M}^{\dagger}\hat{M}]$.

B.8 Zeeman polarization as a hyperbolic tangent function

In chapter 2 the Zeeman polarization p_Z was expressed by using the following tangent function:

$$p_Z = \tanh\left(\frac{\hbar\gamma B_0}{2\kappa_B T}\right). \tag{B.42}$$

In this section, I will give the shortcuts to this expression of p_Z. Lets begin with the definition of the Zeeman polarization:

$$p_Z = \frac{p(\alpha) - p(\beta)}{p(\alpha) + p(\beta)}, \tag{B.43}$$

where $p(\alpha)$ is the $|\alpha\rangle$ state population and $p(\beta)$ is the $|\beta\rangle$ state population. The ratio between the populations of the $|\alpha\rangle$ and $|\beta\rangle$ states is defined by the Boltzmann distribution:

$$\frac{p(\alpha)}{p(\beta)} = e^{\left(\frac{\hbar\gamma B_0}{\kappa_B T}\right)}, \tag{B.44}$$

where ω_0 is the nuclear Larmor frequency, κ_B is the Boltzmann constant (1.38×10^{-23} JK^{-1}) and T is the temperature. The ratio of nuclear spin populations allows the Zeeman polarization to be expressed as follows:

$$p_Z = \frac{p(\beta)e^{\left(\frac{-\hbar\omega_0}{\kappa_B T}\right)} - p(\beta)}{p(\beta)e^{\left(\frac{-\hbar\omega_0}{\kappa_B T}\right)} + p(\beta)} = \frac{e^{\left(\frac{-\hbar\omega_0}{\kappa_B T}\right)} - 1}{e^{\left(\frac{-\hbar\omega_0}{\kappa_B T}\right)} + 1}, \tag{B.45}$$

upon cancelling $p(\beta)$. Now include a multiplicative constant of $exp\{\hbar\omega_0/2\kappa_B T\}$, and rearrange the resulting expression accordingly:

$$p_Z = \frac{e^{\left(\frac{-\hbar\omega_0}{\kappa_B T}\right)} - 1}{e^{\left(\frac{-\hbar\omega_0}{\kappa_B T}\right)} + 1} \cdot \frac{e^{\left(\frac{\hbar\omega_0}{2\kappa_B T}\right)}}{e^{\left(\frac{\hbar\omega_0}{2\kappa_B T}\right)}} = \frac{e^{\left(\frac{-\hbar\omega_0}{2\kappa_B T}\right)} - e^{\left(\frac{\hbar\omega_0}{2\kappa_B T}\right)}}{e^{\left(\frac{-\hbar\omega_0}{2\kappa_B T}\right)} + e^{\left(\frac{\hbar\omega_0}{2\kappa_B T}\right)}}. \tag{B.46}$$

The Zeeman polarization p_Z is clearly a hyperbolic tangent function and can readily be expressed in the following form:

$$p_Z = \tanh\left(\frac{\hbar\gamma B_0}{2\kappa_B T}\right). \tag{B.47}$$

Expressing p_Z in this manner allows the temperature and magnetic field dependencies of p_Z to be examined more explicitly.

B.9 Singlet order and rf-fields

In chapter 2, I briefly outlined the effects of applying a continuous wave (CW) field to a nuclear spin pair i and j during the evolution period τ_{EV} between encoding the nuclear singlet order and the subsequent reconversion to observable magnetization. In this section, I provide more details regarding this phenomenon. Details regarding the evolution of the nuclear singlet order (and the singlet-central triplet population imbalance) are found in references [16, 149, 150].

As is often the case for measurements of singlet relaxation time constants, the finite chemical shift difference which exists between the coupled spins of interest acts to attenuate the lifetime of the nuclear singlet order. This mechanism is termed "singlet-triplet leakage" and is discussed further in chapter 3. The singlet-triplet leakage mechanism is coherent and may therefore be removed (to good approximation) by the presence of an on resonant radiofrequency field. Consider the case of continuous wave (CW) irradiation with a pulse amplitude ω_{CW} applied at the average resonance frequency of the two singlet nuclei. Assume that ω_{CW} satisfies the following condition:

$$\omega_{\mathrm{CW}} \gg \Omega_{\Delta}^{ij}, \tag{B.48}$$

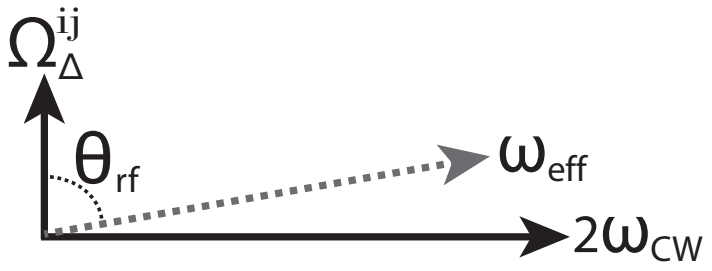

FIGURE B.1: The effective magnetic field axis (grey, dashed arrow) in the limit of strong continuous wave rf-irradiation, i.e. $\omega_{\mathrm{CW}} \gg \Omega_\Delta^{ij}$. θ_{rf} indicates the angle of the effective magnetic field with respect to the static magnetic field $\vec{B}_0$ and ω_{eff} denotes the amplitude of the effective magnetic field.

in which case the coherent Hamiltonian in the presence of CW irradiation $\hat{H}_{\mathrm{coh,CW}}$ is expressed in the rotating frame as:

$$\hat{H}_{\mathrm{coh,CW}} = \frac{\Omega_\Sigma^{ij}}{2}(\hat{I}_{iz} + \hat{I}_{jz}) + \frac{\Omega_\Delta^{ij}}{2}(\hat{I}_{iz} - \hat{I}_{jz}) + 2\pi J_{ij}\hat{I}_i \cdot \hat{I}_j + \omega_{\mathrm{CW}}(\hat{I}_{ix} + \hat{I}_{jx}). \tag{B.49}$$

The Zeeman term $\hat{I}_{iz} - \hat{I}_{jz}$ does not commute with the term from the coherent CW irradiation $\hat{I}_{1x} + \hat{I}_{2x}$ but may be neglected in the case that equation B.48 is fulfilled. The coherent Hamiltonian $\hat{H}_{\mathrm{coh,CW}}$ therefore simplifies to:

$$\hat{H}_{\mathrm{coh,CW}} = 2\pi J_{ij}\hat{I}_i \cdot \hat{I}_j + \omega_{\mathrm{CW}}(\hat{I}_{ix} + \hat{I}_{jx}), \tag{B.50}$$

and remains an exchange-symmetric Hamiltonian with respect to the permutation of nuclear spins i and j. $\hat{Q}_{\mathrm{SO}}$ is therefore a conserved property of $\hat{H}_{\mathrm{coh,CW}}$, see chapter 2 for more details. The singlet spin-1/2 nuclei experience an effective magnetic field due to the existence of the CW radiofrequency field, which is typically provided by the rf-coils of the probehead and is applied in a perpendicular direction to the static magnetic field, see figure B.1. The angle of the effective magnet field tilt (experienced by both spins i and j) is given by a tangent function of ω_{CW} and Ω_Δ^{ij}:

$$\tan(\theta_{rf}) = \frac{2\omega_{\mathrm{CW}}}{\Omega_\Delta^{ij}}, \tag{B.51}$$

with the effective magnetic field amplitude, defined to be co-axial with the z-axis of the effective magnetic field frame, expressed as:

$$\omega_{\text{eff}} = \left[\left(\frac{\Omega_{\Delta}^{ij}}{2} \right)^2 + \omega_{\text{CW}}^2 \right]^{\frac{1}{2}}. \tag{B.52}$$

The transformation from the rotating frame to the effective magnetic field frame for the Cartesian operators which constitute the coherent Hamiltonian $\hat{H}_{\text{coh,CW}}$ is given by:

$$\begin{bmatrix} \hat{I}'_{ix} + \hat{I}'_{jx} \\ \hat{I}'_{iy} + \hat{I}'_{jy} \\ \hat{I}'_{iz} + \hat{I}'_{jz} \end{bmatrix} = \begin{bmatrix} \cos\theta_{rf} & 0 & -\sin\theta_{rf} \\ 0 & 1 & 0 \\ \sin\theta_{rf} & 0 & \cos\theta_{rf} \end{bmatrix} \times \begin{bmatrix} \hat{I}_{ix} + \hat{I}_{jx} \\ \hat{I}_{iy} + \hat{I}_{jy} \\ \hat{I}_{iz} + \hat{I}_{jz} \end{bmatrix}, \tag{B.53}$$

where the primed ($'$) operators are specified in the effective magnetic field frame. For sufficient suppression of the coherent singlet-triplet leakage mechanism, the applied CW field must have a nutation frequency which substantially exceeds the chemical shift difference, i.e. $\omega_{\text{CW}} \gg \Omega_{\Delta}^{ij}$. In the limit of strong CW irradiation $\theta_{rf} \to \pi/2$, and the trigonometric elements of the transformation matrix simplify as follows; $\sin\theta_{rf} \to 1$ and $\cos\theta_{rf} \to 0$.

The transformation matrix enabling the nuclear singlet order to be expressed in the effective magnetic field frame is:

$$\hat{Q}_{CS} = \begin{array}{c} \\ |S_0\rangle \\ |T_{-1}\rangle \\ |T_0\rangle \\ |T_{+1}\rangle \end{array} \begin{array}{c} \begin{array}{cccc} |\hat{\mathbb{1}}\rangle & \left\langle \Sigma I'_{x,y} \right| & \left\langle I'_{iz} + I'_{jz} \right| & \left\langle I'_{iz} \cdot I'_{jz} \right| \end{array} \\ \begin{pmatrix} \frac{1}{4} & 0 & -\frac{1}{2} & -1 \\ \frac{1}{4} & -\frac{1}{2} & \frac{1}{2} & 0 \\ \frac{1}{4} & 0 & -\frac{1}{2} & 1 \\ \frac{1}{4} & \frac{1}{2} & \frac{1}{2} & 0 \end{pmatrix} \end{array} \tag{B.54}$$

where $\Sigma I'_{x,y} = \hat{I}'_{ix} \cdot \hat{I}'_{jx} + \hat{I}'_{iy} \cdot \hat{I}'_{jy}$. This transformation is equivalent to the following relabelling of the Cartesian operators $\hat{I}'_{iz} \leftrightarrow \hat{I}_{ix}$ and $\hat{I}'_{ix} \leftrightarrow \hat{I}_{iz}$ (identical transformations are present for spin j) which results in the following transformation matrix:

$$\hat{Q}_{CS} = \begin{array}{c} \\ |S_0\rangle \\ |T_{-1}\rangle \\ |T_0\rangle \\ |T_{+1}\rangle \end{array} \begin{array}{c} \begin{array}{cccc} |\hat{\mathbb{1}}\rangle & \langle \Sigma I_{z,y}| & \langle I_{ix} + I_{jx}| & \langle I_{ix} \cdot I_{jx}| \end{array} \\ \begin{pmatrix} \frac{1}{4} & 0 & -\frac{1}{2} & -1 \\ \frac{1}{4} & -\frac{1}{2} & \frac{1}{2} & 0 \\ \frac{1}{4} & 0 & -\frac{1}{2} & 1 \\ \frac{1}{4} & \frac{1}{2} & \frac{1}{2} & 0 \end{pmatrix} \end{array} \tag{B.55}$$

The transformation to the effective magnetic field frame described in equation B.55 demonstrates that the population of the nuclear singlet state expressed in the Cartesian product operator basis of the effective magnetic field frame remains as [75, 150, 151]:

$$|S_0\rangle \langle S_0| = \frac{\mathbb{1}}{4} - \hat{I}_i \cdot \hat{I}_j = \frac{\mathbb{1}}{4} - (\hat{I}_{ix} \cdot \hat{I}_{jx} + \hat{I}_{iy} \cdot \hat{I}_{jy} + \hat{I}_{iz} \cdot \hat{I}_{jz}). \tag{B.56}$$

The nuclear singlet order ($\hat{Q}_{\mathrm{SO}}$) additionally remains invariant to an effective magnetic field frame transformation, with $\hat{Q}_{\mathrm{SO}}$ expressed in the effective magnetic field frame as:

$$\hat{Q}_{\mathrm{SO}} = \frac{-1}{2\sqrt{3}} \left(\hat{I}_i^+ \cdot \hat{I}_j^- + \hat{I}_i^- \cdot \hat{I}_j^+ + 2\hat{I}_{iz} \cdot \hat{I}_{jz} \right). \tag{B.57}$$

B.10 SLIC vs. M2SS2M

The SLIC and M2SS2M pulse sequences are discussed in depth at the end of chapter 2. The advantages and disadvantages of each sequence are detailed in table B.1.

TABLE B.1: Comparison for the properties of the SLIC and M2SS2M pulse sequences used to interconvert longitudinal magnetization and the nuclear singlet order.

Property	SLIC	M2SS2M
generation of $\hat{Q}_{\mathrm{SO}}$	immediate	during n_2 JSE train
max $\hat{Q}_{\mathrm{SO}}$ efficiency	2/3	2/3
power requirements	$\sim$10 μW	$\sim$10 W
sequence duration	$\sim$100 ms	$\sim$100 ms
offset dependence	selective	broadband

Each pulse sequence operates effectively in the near-equivalence regime and displays obvious strengths and weaknesses. For example, the SLIC sequence consists of a single pulse dictated by two parameters which are easily optimized [156]. However, sufficiently low nutation frequencies are difficult to generate for the weak spin-locking

pulses below an intrinsic limit set by the amplifier of the spectrometer. The M2SS2M sequence (also simple to optimize and governed by two parameters) is comprised of echo trains positioned back-to-back. If large numbers of JSE trains are required to retrieve the nuclear singlet order, the hard (short) pulses which are readily synthesised by the spectrometer can occasionally trigger sample heating. On the other hand, the M2SS2M pulse sequence is used effectively in cases where the one-dimensional spectra of the singlet isotope is severely crowded, as the M2S portion of the pulse sequence efficiently selects the key singlet resonance. Furthermore, the SLIC pulse sequence is able to use experimental parameters which are exactly matched to the spin system parameters, whereas for the M2SS2M sequence the number of JSE trains n_1 must be rounded to an integer, limiting the experimental transfer efficiency. Finally, the π inversion pulses belonging to the M2SS2M pulse sequence are sensitive to inhomogeneous $\vec{B}_0$ fields. Composite π pulses are instead used to improve the off-resonance performance of the singlet-triplet interconversion.

B.11 Optimized T_{00} filter parameters

The T_{00} filter is implemented to suppress all signals not originating from the singlet state. NMR signals passing through spherical tensors of rank 1 or 2 are destroyed. Details of the T_{00} filter are also given in references [55, 56].

TABLE B.2: Optimized parameters of the T_{00} filter.

PFG	Shape	Strength	Duration
G1	SINE.100	5.0 Gcm^{-1}	4.4 ms
G2	SINE.100	-5.0 Gcm^{-1}	2.4 ms
G3	SINE.100	-7.5 Gcm^{-1}	2.0 ms

B.12 Autocorrelation functions

Molecules dissolved in solution do not behave as static objects, and are continuously undergoing molecular vibrations and librations. Other motions attributed to the reorientation of molecular groups or the molecule as a whole include; rotations, translations and diffusion. In turn, the molecular frame (imprinted on the molecular geometry) is not

time-independent and undergoes the same motional dynamics. The molecular frame is therefore seen to tumble in synchrony with the molecule with respect to the laboratory frame [49].

From the thorough treatment of nuclear spin relaxation discussed in chapter 3, it has been shown that: 1. frame transformations $R \rightarrow M$ and $M \rightarrow L$ are uncorrelated in the case that the isotropic rotational diffusion of the internal group and the overall reorientation of the molecule in solution posses suitably different timescales; and 2. molecular reorientations (frame $A \rightarrow$ frame B) across an interval τ are quantifiable by an autocorrelation function $G^{\lambda,\lambda'}_{m,m'}(\tau)$ such that:

$$\langle D^{2*}_{m_2 m_1}(\Omega^{\lambda}_{AB}(0)) D^{2}_{m'_2 m'_1}(\Omega^{\lambda}_{AB}(0))\rangle \times G^{\lambda,\lambda'}_{m,m'}(\tau) = \langle D^{2*}_{m_2 m_1}(\Omega^{\lambda}_{AB}(0)) D^{2}_{m'_2 m'_1}(\Omega^{\lambda}_{AB}(\tau))\rangle, \tag{B.58}$$

with:

$$\begin{aligned} \langle D^{l*}_{m_2 m_1}(\Omega^{\lambda}_{AB}(0)) D^{l}_{m'_2 m'_1}(\Omega^{\lambda}_{AB}(\tau))\rangle &= \frac{1}{8\pi^2}\int_0^{2\pi}\int_0^{\pi}\int_0^{2\pi} \sin(\beta)\; d\gamma d\beta d\alpha \qquad \text{(B.59)} \\ &\quad \times D^{l*}_{m_2 m_1}(\Omega^{\lambda}_{AB}(0)) D^{l}_{m'_2 m'_1}(\Omega^{\lambda}_{AB}(\tau)), \\ &= \frac{(-1)^{m_2+m_1}}{2l+1}\delta_{ll'}\delta_{m_2 m'_2}\delta_{m_1 m'_1}, \qquad \text{(B.60)} \end{aligned}$$

where the factor of $1/8\pi^2$ is the uniform probability density of initial orientations specified by the solid angle $\Omega^{\lambda}_{AB}(0)$, and is required for normalization. The autocorrelation function quantifies how rapidly the local magnetic field fluctuates, i.e. how correlated is the field with itself at a later time τ. Fluctuations could be due to the reorientational motions of a small molecule in isotropic solution, or other molecular processes. The autocorrelation function depends on the size of the time-step τ between measurements of the local magnetic field orientation with respect to a reference frame, which is fixed with respect to the molecule. The autocorrelation function $G^{\lambda,\lambda'}_{m,m'}(\tau)$ is written as:

$$G^{\lambda,\lambda'}_{m,m'}(\tau) = \langle A^{\lambda*}_{lm}(t) A^{\lambda'}_{lm'}(t-\tau)\rangle, \tag{B.61}$$

where A^{λ}_{lm} are the spatial tensors of the fluctuating Hamiltonian for the interaction λ, see table 3.2. At a time $\tau = 0$, the autocorrelation function is:

$$G^{\lambda,\lambda'}_{m,m'}(0) = \langle A^{\lambda*}_{lm}(0) A^{\lambda'}_{lm'}(0)\rangle, \tag{B.62}$$

where $G^{\lambda,\lambda'}_{m,m'}(0)$ denotes the root-mean-square amplitude of the fluctuating field, averaged over either the spin ensemble or time, both of which are equivalent. The autocorrelation function is therefore constrained by the boundary conditions: $G^{\lambda,\lambda'}_{m,m'}(0) = 1$ and $G^{\lambda,\lambda'}_{m,m'}(\infty) = 0$, i.e. at short times there is a high degree of correlation, and long times the local magnetic field is completely uncorrelated with itself. For molecular reorientation due to overall tumbling of the spin system in solution, the autocorrelation function is assumed to be continuous, mono-exponentially decaying function:

$$G^{\lambda,\lambda'}_{m,m'}(\tau) = G^{\lambda,\lambda'}_{m,m'}(0)e^{-\tau/\tau_C}, \tag{B.63}$$

which is quantified by a correlation time τ_C related to the stochastic variations of the magnetic field orientation. τ_C can be interpreted as the average time for a molecular axis to reorient by 1 radian.

B.13 Spectral densities

The autocorrelation function $G^{\lambda,\lambda'}_{m,m'}(\tau)$ has the corresponding spectral density:

$$J^{\lambda,\lambda'}_{m,m'}(\omega) = \int_0^\infty d\tau\, G^{\lambda,\lambda'}_{m,m'}(\tau)\, e^{i\omega\tau} = \frac{\tau_C}{1 + (m\omega_0\tau_C)^2}. \tag{B.64}$$

The integral over time translates the autocorrelation function into a spectral density which is sampled at integer values of the nuclear Larmor frequency. The spectral density selects the frequencies of molecular tumbling in solution which are resonant with the nuclear transition frequencies, and therefore provides the probabilities of finding stochastic motions which fluctuate at the chosen resonant frequencies. This is consistent with the notion of noise fluctuating at multiples of the nuclear Larmor frequency and driving nuclear spin relaxation in solution state NMR experiments. The maximum value of $J^{\lambda,\lambda'}_{m,m'}(\omega)$ is found at $\tau_C = 1/\omega_0$, see figure B.2. The case of $\omega_0\tau_C \ll 1$ is described as the regime of isotropic extreme narrowing, where the motional tumbling of the molecule in solution is considerably faster than the nuclear Larmor period. This results in a "flat" spectral density where $G^{\lambda,\lambda'}_{m,m'}(\tau) \to \tau_C$ and all transitions are sampled uniformly. For molecules with moieties that posses uncorrelated motional timescales, more elaborate spectral densities are required, as discussed in chapter 3.

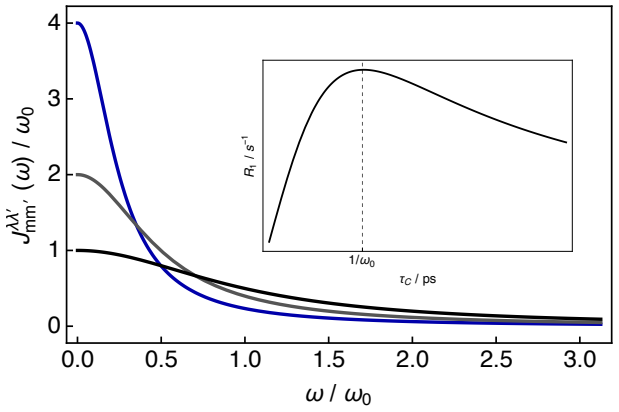

FIGURE B.2: The spectral density function $J^{\lambda,\lambda'}_{m,m'}(\omega)$ in equation B.64 is plotted for different values of the integer $m = 1$, 2 and 4. Inset: longitudinal relaxation rate constant R_1 as a function of τ_C. The maximum value of R_1 is realised at $\tau_C = 1/\omega_0$.

B.14 Liouville bracket

The orthogonality condition for a $N^2 \times N^2$ matrix constructed from N^2 orthogonal basis operators is represented as follows:

$$(\hat{A}_i|\hat{A}_j) = \left\{ \begin{array}{ll} \mathrm{Tr}[\hat{A}_i^\dagger \hat{A}_i] & \text{for } i = j \\ 0 & \text{for } i \neq j \end{array} \right\}. \tag{B.65}$$

where (...|...) is termed the Liouville Bracket, defined as [51]:

$$(\hat{A}|\hat{B}) = \mathrm{Tr}[\hat{A}^\dagger \hat{B}] = \sum_{i,j=1}^{N} \hat{A}^\dagger_{ji} \hat{B}_{ij} = \sum_{ij=1}^{N^2} \hat{A}^*_{ij} \hat{B}_{ij}. \tag{B.66}$$

The sum $\sum_{i,j=1}^{N}$ is valid for the operator matrix representations, whilst the sum $\sum_{ij=1}^{N^2}$ is valid for the supervectors which belong to operators $\hat{A}$ and $\hat{B}$. An operator $\hat{A}$ may be expanded in the operator basis of $\hat{B}$:

$$\hat{A} = \sum_{i=1}^{N^2} \alpha_i \hat{B}_i, \tag{B.67}$$

where the coefficients α_i are given by:

$$\alpha_i = \frac{(\hat{B}_i|\hat{A})}{(\hat{B}_i|\hat{B}_i)} = \frac{\mathrm{Tr}[\hat{B}_i^\dagger \hat{A}]}{\mathrm{Tr}[\hat{B}_i^\dagger \hat{B}_i]}, \tag{B.68}$$

and in a suitable, orthonormal basis $(\hat{B}_i|\hat{B}_i) = 1$, which allows the superoperator matrix representation of the superoperator $\hat{\hat{Q}}$:

$$\hat{\hat{Q}}_{ij} = (\hat{B}_i|\hat{\hat{Q}}|\hat{B}_j) = \mathrm{Tr}[\hat{B}_i^\dagger \hat{Q} \hat{B}_j]. \tag{B.69}$$

B.15 ^{13}C inversion recovery experiments

^{13}C longitudinal relaxation times $T_1(^{13}\mathrm{C})$ were estimated experimentally by using the inversion recovery pulse sequence. The ^{13}C 90° pulse length was determined from a nutation frequency experiment to be 10 μs at 41 W pulse power and 25°C sample temperature. Experiments used a delay of 70 s after each data point was recorded. The incremented delays (in seconds) between π and $\pi/2$ pulses were as follows: 0.1, 0.2, 0.5, 1, 2, 5, 8 ,12, 16, 20, 25, 30, 40, 50, 60, 75. The resulting recoveries were fit to a monoexponential function of the following form:

$$y(t) = A - Be^{-t/T_1}, \tag{B.70}$$

where A and B were left as adjustable free parameters to guarantee the best fit of the experimental data, and T_1 is the longitudinal relaxation time. Uncertainties were estimated from the fit quality of the data by using the *Mathemtica* routine "ParameterTable".

Appendix C

Published and publishable papers

- **Stuart J. Elliott**, Lynda J. Brown, Jean-Nicolas Dumez and Malcolm H. Levitt, Long-lived nuclear spin states in monodeuterated methyl groups, *Phys. Chem. Chem. Phys.*, **18**, 17965-17972 (2016).

- **Stuart J. Elliott**, Lynda J. Brown, Jean-Nicolas Dumez and Malcolm H. Levitt, Long-lived nuclear spin states in rapidly rotating CH_2D groups, *J. Magn. Reson.*, **272**, 87-90 (2016).

- James Eills, Gabriele Stevanato, Christian Bengs, Stefan Glöggler, **Stuart J. Elliott**, Javier Alonso-Valdesueiro, Giuseppe Pileio and Malcolm H. Levitt, Singlet order conversion and parahydrogen-induced hyperpolarization of ^{13}C nuclei in near-equivalent spin systems, *J. Magn. Reson.*, **274**, 163-172 (2017).

- Stefan Glöggler, **Stuart J. Elliott**, Gabriele Stevanato, Richard C. D. Brown and Malcolm H. Levitt, Versatile magnetic resonance singlet tags compatible with biological conditions, *RSC Adv.*, **7**, 34574-34578 (2017).

- O. Maduka Ogba, **Stuart J. Elliott**, David A. Kolin, Lynda J. Brown, Sebastian Cevallos, Stuart Sawyer, Malcolm H. Levitt and Daniel J. O'Leary, Origins of small proton chemical shift differences in monodeuterated methyl groups, *J. Org. Chem.*, **82**, 8943-8949 (2017).

- Javier Alonso-Valdesueiro, **Stuart J. Elliott**, Christian Bengs, Benno Meier and Malcolm H. Levitt, Testing Signal Enhancement Mechanisms in the Dissolution NMR of Acetone, *J. Magn. Reson.* **286**, 158-162 (2018).

- Sally Bloodworth, Shamim Alom, Karel Kouřil, **Stuart J. Elliott**, Christian Bengs, Neil Wells, Anthony J. Horsewill, Salvatore Mamone, Mónica Jiménez-Ruiz, Stéphane Rols, Urmas Nagel, Toomas Rõõm, Malcolm H. Levitt and Richard J. Whitby, Synthesis and properties of open fullerenes encapsulating ammonia and methane, *Accepted in Chem. Phys. Chem.* (2017).

- **Stuart J. Elliott**, Christian Bengs, Karel Kouřil, Benno Meier, Shamim Alom, Richard J. Whitby and Malcolm H. Levitt, NMR lineshapes and scalar relaxation of the water-endofullerene $H_2{}^{17}O@C_{60}$, *Accepted in Chem. Phys. Chem.* (2017).

- **Stuart J. Elliott**, Benno Meier, Basile Vuichoud, Gabriele Stevanato, Lynda J. Brown, Javier Alonso-Valdesueiro, Lyndon Emsley, Sami Jannin and Malcolm H. Levitt, Hyperpolarized long-lived nuclear spin states in monodeuterated methyl groups, *Submitted to Phys. Chem. Chem. Phys.* (2017).

- Benno Meier, Karel Kouřil, Christian Bengs, Hana Kouřilova, Timothy C. Barker, **Stuart J. Elliott**, Shamim Alom, Richard J. Whitby and Malcolm H. Levitt, Spin isomer conversion of water at room temperature and quantum rotor induced polarization in the water-endofullerene $H_2O@C_{60}$, *Submitted to Phys. Rev. Lett.* (2017).

- **Stuart J. Elliott**, Lynda J. Brown, Joseph T. Hill-Cousins, Christian Bengs, Daniel J. O'Leary, Giuseppe Pileio and Malcolm H. Levitt, Singlet-scalar relaxation of the second kind in the slow fluctuation regime, *In Prep.* (2017).

- **Stuart J. Elliott**, Pavel Kadeřávek, Lynda J. Brown, Mohamed Sabba, Stefan Glöggler, Daniel J. O'Leary, Richard C. D. Brown, Fabien Ferrage and Malcolm H. Levitt, Field-cycling long-lived-state NMR of $^{15}N_2$ spin pairs, *In Prep.* (2017).

References

[1] R. Atkinson and V. Saudek, *FEBS Lett.*, 2002, **510**, 1–4.

[2] D. E. Sosnovik, R. Wang, G. Dai, T. G. Reese and V. J. Wedeen, *J. Cardiovasc. Magn. Reson.*, 2009, **11**, 47.

[3] I. I. Rabi, J. R. Zacharias, S. Millman and P. Kusch, *Phys. Rev.*, 1938, **53**, 318–318.

[4] F. Bloch, *Phys. Rev.*, 1946, **70**, 460–474.

[5] E. M. Purcell, H. C. Torrey and R. V. Pound, *Phys. Rev.*, 1946, **69**, 37–38.

[6] F. Bloch, W. W. Hansen and M. Packard, *Phys. Rev.*, 1946, **69**, 127–127.

[7] J. van der Waals, *Encyclopedia of Magnetic Resonance*, 1996, **1**, 667–680.

[8] H. J. Dyson and P. E. Wright, *Chem. Rev.*, 2004, **104**, 3607–3622.

[9] G. Finch, A. Yilmaz and M. Utz, *J. Magn. Reson.*, 2016, **262**, 73–80.

[10] S. Cavadini, J. Dittmer, S. Antonijevic and G. Bodenhausen, *J. Am. Chem. Soc.*, 2005, **127**, 15744–15748.

[11] P. Wenter, G. Bodenhausen, J. Dittmer and S. Pitsch, *J. Am. Chem. Soc.*, 2006, **128**, 7579–7587.

[12] A. G. Palmer, *Chem. Rev.*, 2004, **104**, 3623–3640.

[13] F. Ferrage, M. Zoonens, D. E. Warschawski, J.-L. Popot and G. Bodenhausen, *J. Am. Chem. Soc.*, 2003, **125**, 2541–2545.

[14] M. Carravetta, O. G. Johannessen and M. H. Levitt, *Phys. Rev. Lett.*, 2004, **92**, 153003.

[15] M. Carravetta and M. H. Levitt, *J. Am. Chem. Soc.*, 2004, **126**, 6228–6229.

[16] M. Carravetta and M. H. Levitt, *J. Chem. Phys.*, 2005, **122**, 214505.

[17] G. Pileio and M. H. Levitt, *J. Magn. Reson.*, 2007, **187**, 141–145.

[18] R. Sarkar, P. R. Vasos and G. Bodenhausen, *J. Am. Chem. Soc.*, 2007, **129**, 328–334.

[19] A. K. Grant and E. Vinogradov, *J. Magn. Reson.*, 2007, **193**, 177–190.

[20] G. Pileio, M. Carravetta, E. Hughes and M. H. Levitt, *J. Am. Chem. Soc.*, 2008, **130**, 12582–12583.

[21] W. S. Warren, E. Jenista, R. T. Branca and X. Chen, *Science*, 2009, **323**, 1711–1714.

[22] M. C. D. Tayler, S. Marie, A. Ganesan and M. H. Levitt, *J. Am. Chem. Soc.*, 2010, **132**, 8225–8227.

[23] Y. Feng, R. M. Davis and W. S. Warren, *Nat. Phys.*, 2012, **8**, 831–837.

[24] G. Pileio, J. T. Hill-Cousins, S. Mitchell, I. Kuprov, L. J. Brown, R. C. D. Brown and M. H. Levitt, *J. Am. Chem. Soc.*, 2012, **134**, 17494–17497.

[25] M. C. D. Tayler, I. Marco-Rius, M. I. Kettunen, K. M. Brindle, M. H. Levitt and G. Pileio, *J. Am. Chem. Soc.*, 2012, **134**, 7668–7671.

[26] M. H. Levitt, *Annu. Rev. Phys. Chem.*, 2012, **63**, 89–105.

[27] G. Pileio, S. Bowen, C. Laustsen, M. C. D. Tayler, J. T. Hill-Cousins, L. J. Brown, R. C. D. Brown, J.-H. Ardenkjaer-Larsen and M. H. Levitt, *J. Am. Chem. Soc.*, 2013, **135**, 5084–5088.

[28] M. B. Franzoni, L. Buljubasich, H. W. Spiess and K. Münnemann, *J. Am. Chem. Soc.*, 2012, **134**, 10393–10396.

[29] J.-N. Dumez, J. T. Hill-Cousins, R. C. D. Brown and G. Pileio, *J. Magn. Reson.*, 2014, **246**, 27–30.

[30] K. Claytor, T. Theis, Y. Feng and W. S. Warren, *J. Magn. Reson.*, 2014, **239**, 81–86.

[31] K. Claytor, T. Theis, Y. Feng, J. Yu, D. Gooden and W. S. Warren, *J. Am. Chem. Soc.*, 2014, **136**, 15118–15121.

[32] Y. Zhang, P. C. Soon, A. Jerschow and J. W. Canary, *Angew. Chem. Int. Ed.*, 2014, **53**, 3396–3399.

[33] G. Pileio, J.-N. Dumez, I.-A. Pop, J. T. Hill-Cousins and R. C. D. Brown, *J. Magn. Reson.*, 2015, **252**, 130–134.

[34] Y. Zhang, K. Basu, J. W. Canary and A. Jerschow, *Phys. Chem. Chem. Phys.*, 2015, **17**, 24370–24375.

[35] G. Stevanato, J. T. Hill-Cousins, P. Håkansson, S. S. Roy, L. J. Brown, R. C. D. Brown, G. Pileio and M. H. Levitt, *Angew. Chem. Int. Ed.*, 2015, **54**, 3740–3743.

[36] W. Gerlach and O. Stern, *Z. Phys.*, 1922, **9**, 349–352.

[37] E. D. Commins, *Annu. Rev. Nucl. Part. Sci.*, 2012, **62**, 133–157.

[38] P. A. M. Dirac, *Proc. R. Soc. A*, 1928, **117**, 610–624.

[39] A. Rae, *Quantum Mechanics Fifth Edition*, Taylor and Francis, Oxford, UK, 2008.

[40] P. Dirac, *The Principles of Quantum Mechanics*, University Press, Oxford, UK, 1958.

[41] M. H. Levitt, *Spin Dynamics: Basics of Nuclear Magnetic Resonance, 2nd Ed.*, John Wiley and Sons Ltd., Chichester, 2001.

[42] S. Blundell, *Magnetism in Condensed Matter*, University Press, Oxford, UK, 2001.

[43] A. Einstein and W. de Haas, *Proc. KNAW*, 1915, **18**, 696–711.

[44] S. Gasiorowicz, *Quantum Physics*, Wiley, Chichester, UK, 2003.

[45] J. Keeler, *Understanding NMR Spectroscopy*, Wiley, Chichester, UK, 2010.

[46] R. A. Freedman, L. Ford and H. D. Young, *University Physics*, Pearson, San Francisco, USA, 1949.

[47] B. Cowan, *Nuclear Magnetic Resonance and Relaxation*, University Press, Oxford, UK, 1997.

[48] H. C. Torrey, *Phys. Rev.*, 1956, **104**, 563–565.

[49] J. Kowalewski and L. Mäler, *Nuclear Spin Relaxation in Liquids: Theory, Experiments, and Applications*, CRC Press, Boca Raton, 2006.

[50] M. Duer, *Solid-State NMR Spectroscopy: Principles and Applications*, Blackwell Sciences, Oxford, UK, 2002.

[51] J. Jeener, *Adv. Magn. Opt. Reson.*, 1982, **10**, 1–51.

[52] A. Holevo, *Rep. Math. Phys.*, 1977, **12**, 251–271.

[53] D. Brink and G. Satchler, *Angular Momentum*, Clarendon Press, Oxford, 1993.

[54] M. C. D. Tayler and M. H. Levitt, *J. Am. Chem. Soc.*, 2013, **135**, 2120–2123.

[55] D. Mammoli, B. Vuichoud, A. Bornet, J. Milani, J.-N. Dumez, S. Jannin and G. Bodenhausen, *J. Phys. Chem. B*, 2015, **119**, 4048–4052.

[56] S. J. Elliott, L. J. Brown, J.-N. Dumez and M. H. Levitt, *Phys. Chem. Chem. Phys.*, 2016, **18**, 17965–17972.

[57] J. D. van Beek, M. Carravetta, G. C. Antonioli and M. H. Levitt, *J. Chem. Phys.*, 2005, **122**, 244510.

[58] A. S. Dubin and S. I. Chan, *J. Chem. Phys.*, 1967, **46**, 4533–4535.

[59] T. Burke and S. I. Chan, *J. Magn. Reson. (1969)*, 1970, **2**, 120–140.

[60] T. E. Bull, *J. Chem. Phys.*, 1976, **65**, 4802–4815.

[61] G. B. Matson, *J. Chem. Phys.*, 1977, **67**, 5152–5161.

[62] A. Jhajharia, E. M. M. Weber, J. G. Kempf, D. Abergel, G. Bodenhausen and D. Kurzbach, *J. Chem. Phys.*, 2017, **146**, 041101.

[63] L. Olsen, O. Christiansen, L. Hemmingsen, S. P. A. Sauer and K. V. Mikkelsen, *J. Chem. Phys.*, 2002, **116**, 1424–1434.

[64] K. M. Brindle, S. E. Bohndiek, F. A. Gallagher and M. I. Kettunen, *Magn. Reson. Med.*, 2011, **66**, 505–519.

[65] D. M. Hoang, E. B. Voura, C. Zhang, L. Fakri-Bouchet and Y. Z. Wadghiri, *Magn. Reson. Med.*, 2014, **71**, 1932–1943.

[66] M. Levitt and R. Freeman, *J. Magn. Reson.*, 1979, **33**, 473–476.

[67] H. Kovacs, D. Moskau and M. Spraul, *Prog. Nucl. Magn. Reson. Spectrosc.*, 2005, **46**, 131–155.

[68] D. J. Russell, C. E. Hadden, G. E. Martin, A. A. Gibson, A. P. Zens and J. L. Carolan, *J. Nat. Prod.*, 2000, **63**, 1047–1049.

[69] C. Suarez, *Chem. Educ.*, 1998, **3**, 1–18.

[70] J. H. Lee, Y. Okuno and S. Cavagnero, *J. Magn. Reson.*, 2014, **241**, 18–31.

[71] J.-H. Ardenkjær-Larsen, B. Fridlund, A. Gram, G. Hansson, L. Hansson, M. H. Lerche, R. Servin, M. Thaning and K. Golman, *Proc. Natl. Acad. Sci. U.S.A.*, 2003, **100**, 10158–10163.

[72] C. R. Bowers and D. P. Weitekamp, *J. Am. Chem. Soc.*, 1987, **109**, 5541–5542.

[73] R. A. Green, R. W. Adams, S. B. Duckett, R. E. Mewis, D. C. Williamson and G. G. R. Green, *Prog. Nucl. Magn. Reson. Spectrosc.*, 2012, **67**, 1–48.

[74] M. G. Pravica and D. P. Weitekamp, *Chem. Phys. Lett.*, 1988, **145**, 255–258.

[75] J. Eills, G. Stevanato, C. Bengs, S. Glöggler, S. J. Elliott, J. Alonso-Valdesueiro, G. Pileio and M. H. Levitt, *J. Magn. Reson.*, 2017, **274**, 163–172.

[76] D. Gajan, A. Bornet, B. Vuichoud, J. Milani, R. Melzi, H. A. van Kalkeren, L. Veyre, C. Thieuleux, M. P. Conley, W. R. Grüning, M. Schwarzwälder, A. Lesage, C. Copéret, G. Bodenhausen, L. Emsley and S. Jannin, *Proc. Natl. Acad. Sci.*, 2014, **111**, 14693–14697.

[77] J. H. Ardenkjaer-Larsen, S. Macholl and H. Jóhannesson, *Appl. Magn. Reson.*, 2008, **34**, 509–522.

[78] D. T. Peat, A. J. Horsewill, W. Kockenberger, A. J. P. Linde, D. G. Gadian and J. R. Owers-Bradley, *Phys. Chem. Chem. Phys.*, 2013, **15**, 7586–7591.

[79] J. R. Owers-Bradley, A. J. Horsewill, D. T. Peat, K. S. K. Goh and D. G. Gadian, *Phys. Chem. Chem. Phys.*, 2013, **15**, 10413–10417.

[80] M. L. Hirsch, N. Kalechofsky, A. Belzer, M. Rosay and J. G. Kempf, *J. Am. Chem. Soc.*, 2015, **137**, 8428–8434.

[81] M. L. Hirsch, B. A. Smith, M. Mattingly, A. G. Goloshevsky, M. Rosay and J. G. Kempf, *J. Magn. Reson.*, 2015, **261**, 87–94.

[82] D. T. Peat, M. L. Hirsch, D. G. Gadian, A. J. Horsewill, J. R. Owers-Bradley and J. G. Kempf, *Phys. Chem. Chem. Phys.*, 2016, **18**, 19173–19182.

[83] C. Cudalbu, A. Comment, F. Kurdzesau, R. B. van Heeswijk, K. Uffmann, S. Jannin, V. Denisov, D. Kirik and R. Gruetter, *Phys. Chem. Chem. Phys.*, 2010, **12**, 5818–5823.

[84] D. I. Hoult and R. E. Richards, *J. Magn. Reson.*, 2011, **213**, 329–343.

[85] D. . Hoult and P. C. Lauterbur, *J. Magn. Reson. (1969)*, 1979, **34**, 425–433.

[86] D. I. Hoult, *Sensitivity of the NMR Experiment*, John Wiley & Sons, Ltd, 2007.

[87] S. J. Nelson, J. Kurhanewicz, D. B. Vigneron, P. E. Z. Larson, A. L. Harzstark, M. Ferrone, M. van Criekinge, J. W. Chang, R. Bok, I. Park, G. Reed, L. Carvajal, E. J. Small, P. Munster, V. K. Weinberg, J. H. Ardenkjaer-Larsen, A. P. Chen, R. E. Hurd, L.-I. Odegardstuen, F. J. Robb, J. Tropp and J. A. Murray, *Sci. Transl. Med.*, 2013, **5**, 198.

[88] A. W. Overhauser, *Phys. Rev.*, 1953, **92**, 411–415.

[89] S. G. Zech, A. J. Wand and A. E. McDermott, *J. Am. Chem. Soc.*, 2005, **127**, 8618–8626.

[90] K. R. Thurber and R. Tycko, *J. Chem. Phys.*, 2012, **137**, 084508.

[91] K. R. Thurber and R. Tycko, *J. Chem. Phys.*, 2014, **140**, 184201.

[92] S. R. Chaudhari, P. Berruyer, D. Gajan, C. Reiter, F. Engelke, D. L. Silverio, C. Coperet, M. Lelli, A. Lesage and L. Emsley, *Phys. Chem. Chem. Phys.*, 2016, **18**, 10616–10622.

[93] E. Besson, F. Ziarelli, E. Bloch, G. Gerbaud, S. Queyroy, S. Viel and S. Gastaldi, *Chem. Commun.*, 2016, **52**, 5531–5533.

[94] D. J. Kubicki, G. Casano, M. Schwarzwalder, S. Abel, C. Sauvee, K. Ganesan, M. Yulikov, A. J. Rossini, G. Jeschke, C. Coperet, A. Lesage, P. Tordo, O. Ouari and L. Emsley, *Chem. Sci.*, 2016, **7**, 550–558.

[95] D. Kurzbach, E. M. M. Weber, A. Jhajharia, S. F. Cousin, A. Sadet, S. Marhabaie, E. Canet, N. Birlirakis, J. Milani, S. Jannin, D. Eshchenko, A. Hassan, R. Melzi,

S. Luetolf, M. Sacher, M. Rossire, J. Kempf, J. A. B. Lohman, M. Weller, G. Bodenhausen and D. Abergel, *J. Chem. Phys.*, 2016, **145**, 194203.

[96] L. Becerra, G. Gerfen, B. Bellew, J. Bryant, D. Hall, S. Inati, R. Weber, S. Un, T. Prisner, A. McDermott, K. Fishbein, K. Kreischer, R. Temkin, D. Singel and R. Griffin, *J. Magn. Reson, Ser A*, 1995, **117**, 28–40.

[97] A. B. Barnes, G. De Paëpe, P. C. A. van der Wel, K.-N. Hu, C.-G. Joo, V. S. Bajaj, M. L. Mak-Jurkauskas, J. R. Sirigiri, J. Herzfeld, R. J. Temkin and R. G. Griffin, *Appl. Magn. Reson.*, 2008, **34**, 237–263.

[98] T. V. Can, J. J. Walish, T. M. Swager and R. G. Griffin, *J. Chem. Phys.*, 2015, **143**, 054201.

[99] E. P. Saliba, E. L. Sesti, F. J. Scott, B. J. Albert, E. J. Choi, N. Alaniva, C. Gao and A. B. Barnes, *J. Am. Chem. Soc.*, 2017, **139**, 6310–6313.

[100] E. L. Dane, T. Maly, G. T. Debelouchina, R. G. Griffin and T. M. Swager, *Org. Lett.*, 2009, **11**, 1871–1874.

[101] W. T. Wenkebach, T. J. B. Swanenburg and N. J. Poulis, *Phys. Rep.*, 1974, **14**, 181.

[102] D. Wollan, *Phys. Rev. B*, 1976, **13**, 3671.

[103] T. Maly, G. T. Debelouchina, V. S. Bajaj, K.-N. Hu, C.-G. Joo, M. L. Mak-Jurkauskas, J. R. Sirigiri, P. C. A. van der Wel, J. Herzfeld, R. J. Temkin and R. G. Griffin, *J. Chem. Phys.*, 2008, **128**, 052211.

[104] T. R. Carver and C. P. Slichter, *Phys. Rev.*, 1953, **92**, 212–213.

[105] C. D. Jeffries, *Phys. Rev.*, 1957, **106**, 164–165.

[106] A. Abragam and W. Proctor, *C. R. Acad. Sci.*, 1958, **246**, 2253.

[107] W. Wencheback, *Appl. Magn. Reson.*, 2008, **34**, 227–235.

[108] A. Abragam and M. Goldman, *Rep. Prog. Phys.*, 1978, **41**, 395.

[109] S. Jannin, *Dynamic Nuclear Polarization for NMR Spectroscopy*, 2013.

[110] C. Ramanathan, *Appl. Magn. Reson.*, 2008, **34**, 409.

[111] Y. Hovav, A. Feintuch and S. Vega, *J. Chem. Phys.*, 2011, **134**, 074509.

[112] A. A. Smith, B. Corzilius, A. B. Barnes, T. Maly and R. G. Griffin, *J. Chem. Phys.*, 2012, **136**, 015101.

[113] F. Mentink-Vigier, S. Paul, D. Lee, A. Feintuch, S. Hediger, S. Vega and G. De Paepe, *Phys. Chem. Chem. Phys.*, 2015, **17**, 21824–21836.

[114] F. Kurdzesau, B. van den Brandt, A. Comment, P. Hautle, S. Jannin, J. J. van der Klink and J. A. Konter, *J. Phys. D Appl. Phys.*, 2008, **41**, 155506.

[115] E. V. Kryukov, M. E. Newton, K. J. Pike, D. R. Bolton, R. M. Kowalczyk, A. P. Howes, M. E. Smith and R. Dupree, *Phys. Chem. Chem. Phys.*, 2010, **12**, 5757–5765.

[116] X. Ji, A. Bornet, B. Vuichoud, J. Milani, D. Gajan, A. J. Rossini, L. Emsley, G. Bodenhausen and S. Jannin, *Nat. Commun.*, 2017, **8**, 13975.

[117] A. Kessenikh and A. Manenkov, *Sov. Phys. Solid State*, 1963, **5**, 835.

[118] K.-N. Hu, C. Song, H.-H. Yu, T. M. Swager and R. G. Griffin, *J. Chem. Phys.*, 2008, **128**, 052302.

[119] Y. Hovav, A. Feintuch and S. Vega, *J. Magn. Reson.*, 2012, **214**, 29–41.

[120] K.-N. Hu, V. S. Bajaj, M. Rosay and R. G. Griffin, *J. Chem. Phys.*, 2007, **126**, 044512.

[121] D. Shimon, Y. Hovav, A. Feintuch, D. Goldfarb and S. Vega, *Phys. Chem. Chem. Phys.*, 2012, **14**, 5729–5743.

[122] V. K. Michaelis, A. A. Smith, B. Corzilius, O. Haze, T. M. Swager and R. G. Griffin, *J. Am. Chem. Soc.*, 2013, **135**, 2935–2938.

[123] D. Banerjee, D. Shimon, A. Feintuch, S. Vega and D. Goldfarb, *J. Magn. Reson.*, 2013, **230**, 212–219.

[124] T. Can, Q. Ni and R. Griffin, *J. Magn. Reson.*, 2015, **253**, 23–35.

[125] P. van Bentum, M. Sharma, S. van Meerten and A. Kentgens, *J. Magn. Reson.*, 2016, **263**, 126–135.

[126] A. Redfield, *Phys. Rev.*, 1955, **98**, 1787–1809.

[127] B. N. Provotorov, *Sov. Phys. Jetp-Ussr*, 1961, **14**, 1126–1132.

[128] M. Borghini, *Phys. Lett. A*, 1968, **26**, 242.

[129] M. Borghini, *Phys. Rev. Lett.*, 1668, **20**, 419.

[130] M. Goldman, *Appl. Magn. Reson.*, 2008, **34**, 219–226.

[131] S. Jannin, A. Comment and J. J. van der Klink, *Appl. Magn. Reson.*, 2012, **43**, 59–68.

[132] H. Gutte, A. E. Hansen, H. H. Johannesen, A. E. Clemmensen, J. H. Ardenkjær-Larsen, C. H. Nielsen and A. Kjær, *Am. J. Nucl. Med. Mol. Imaging*, 2015, **5**, 548–560.

[133] F. A. Gallagher, M. I. Kettunen, D.-E. Hu, P. R. Jensen, R. I. Zandt, M. Karlsson, A. Gisselsson, S. K. Nelson, T. H. Witney, S. E. Bohndiek, G. Hansson, T. Peitersen, M. H. Lerche and K. M. Brindle, *Proc. Natl. Acad. Sci. U.S.A.*, 2009, **106**, 19801–19806.

[134] S. E. Day, M. I. Kettunen, F. A. Gallagher, D.-E. Hu, M. Lerche, J. Wolber, K. Golman, J. H. Ardenkjaer-Larsen and K. M. Brindle, *Nat. Med.*, 2007, **13**, 1382–1387.

[135] J. Milani, B. Vuichoud, A. Bornet, P. Miéville, R. Mottier, S. Jannin and G. Bodenhausen, *Rev. Sci. Instrum.*, 2015, **86**, 024101.

[136] P. Miéville, S. Jannin and G. Bodenhausen, *J. Magn. Reson.*, 2011, **210**, 137–140.

[137] K. V. Kovtunov, V. V. Zhivonitko, I. V. Skovpin, D. A. Barskiy, O. G. Salnikov and I. V. Koptyug, *J. Phys. C*, 2013, **117**, 22887–22893.

[138] D. A. Barskiy, O. G. Salnikov, K. V. Kovtunov and I. V. Koptyug, *J. Phys. Chem. A*, 2015, **119**, 996–1006.

[139] R. Ernst, G. Bodenhausen and A. Wokaun, *Principles of nuclear magnetic resonance in one and two dimensions*, Clarendon Press, Oxford, UK, 1987.

[140] P. R. Vasos, A. Comment, R. Sarkar, P. Ahuja, S. Jannin, J.-P. Ansermet, J. A. Konter, P. Hautle, B. van den Brandt and G. Bodenhausen, *Proc. Natl. Acad. Sci. U.S.A.*, 2009, **106**, 18469–18473.

[141] B. Meier, J.-N. Dumez, G. Stevanato, J. T. Hill-Cousins, S. S. Roy, P. Håkansson, S. Mamone, R. C. D. Brown, G. Pileio and M. H. Levitt, *J. Am. Chem. Soc.*, 2013, **135**, 18746–18749.

[142] Y. Feng, T. Theis, X. Liang, Q. Wang, P. Zhou and W. S. Warren, *J. Am. Chem. Soc.*, 2013, **135**, 9632–9635.

[143] A. Bornet, X. Ji, D. Mammoli, B. Vuichoud, J. Milani, G. Bodenhausen and S. Jannin, *Chem. – A Eur. J.*, 2014, **20**, 17113–17118.

[144] G. Stevanato, S. Singha Roy, J. Hill-Cousins, I. Kuprov, L. J. Brown, R. C. D. Brown, G. Pileio and M. H. Levitt, *Phys. Chem. Chem. Phys.*, 2015, **17**, 5913–5922.

[145] Y. Zhang, X. Duan, P. C. Soon, V. Sychrovský, J. W. Canary and A. Jerschow, *ChemPhysChem*, 2016, **17**, 2967–2971.

[146] T. Theis, G. X. Ortiz, A. W. J. Logan, K. E. Claytor, Y. Feng, W. P. Huhn, V. Blum, S. J. Malcolmson, E. Y. Chekmenev, Q. Wang and W. S. Warren, *Sci. Adv.*, 2016, **2**, 1501438.

[147] J.-N. Dumez, B. Vuichoud, D. Mammoli, A. Bornet, A. C. Pinon, G. Stevanato, B. Meier, G. Bodenhausen, S. Jannin and M. H. Levitt, *J. Phys. Chem. Lett.*, 2017, **8**, 3549–3555.

[148] S. Gloggler, S. J. Elliott, G. Stevanato, R. C. D. Brown and M. H. Levitt, *RSC Adv.*, 2017, **7**, 34574–34578.

[149] G. Pileio and M. H. Levitt, *J. Chem. Phys.*, 2009, **130**, 214501.

[150] G. Pileio, M. Carravetta and M. H. Levitt, *Proc. Natl. Acad. Sci. U.S.A.*, 2010, **107**, 17135–17139.

[151] M. H. Levitt, *Encyclopedia of Magnetic Resonance*, 2010, **9**, John Wiley and Sons Ltd.

[152] G. Pileio, *J. Chem. Phys.*, 2011, **135**, 174502.

[153] G. Pileio, *J. Chem. Phys.*, 2011, **134**, 214505.

[154] Y. Feng, T. Theis, T.-L. Wu, K. Claytor and W. S. Warren, *J. Chem. Phys.*, 2014, **141**, 134307.

[155] J.-N. Dumez, P. Håkansson, S. Mamone, B. Meier, G. Stevanato, J. T. Hill-Cousins, S. S. Roy, R. C. D. Brown, G. Pileio and M. H. Levitt, *J. Chem. Phys.*, 2015, **142**, 044506.

[156] M. C. D. Tayler and M. H. Levitt, *Phys. Chem. Chem. Phys.*, 2011, **13**, 5556–5560.

[157] S. J. DeVience, R. L. Walsworth and M. S. Rosen, *Phys. Rev. Lett.*, 2013, **111**, 173002.

[158] T. Theis, Y. Feng, T. Wu and W. S. Warren, *J. Chem. Phys.*, 2014, **140**, 014201.

[159] A. S. Kiryutin, H. Zimmermann, A. V. Yurkovskaya, H.-M. Vieth and K. L. Ivanov, *J. Magn. Reson.*, 2015, **261**, 64–72.

[160] Z. Zhou, K. Claytor, W. S. Warren and T. Theis, *J. Magn. Reson.*, 2016, **263**, 108–115.

[161] B. M. Goodson, *J. Magn. Reson.*, 2002, **155**, 157–216.

[162] G. Buntkowsky, H.-H. Limbach, F. Wehrmann, I. Sack, H.-M. Vieth and R. H. Morris, *J. Phys. Chem. A*, 1997, **101**, 4679–4689.

[163] P. A. M. Dirac, *Proc. R. Soc. A*, 1927, **114**, 243–265.

[164] A. Redfield, *J. Res. Dev.*, 1957, **1**, 19–31.

[165] E. Vinogradov and A. K. Grant, *J. Magn. Reson.*, 2008, **194**, 46–57.

[166] O. W. Sørensen, G. W. Eich, M. H. Levitt, G. Bodenhausen and R. R. Ernst, *Prog. Nucl. Magn. Reson. Spectrosc.*, 1984, **16**, 163–192.

[167] M. Goldman, *Quantum Description of High-Resolution NMR in Liquids*, University Press, Oxford, UK, 1988.

[168] A. N. Pravdivtsev, A. V. Yurkovskaya, H.-M. Vieth, K. L. Ivanov and R. Kaptein, *ChemPhysChem*, 2013, **14**, 3327–3331.

[169] K. L. Ivanov, A. N. Pravdivtsev, A. V. Yurkovskaya, H.-M. Vieth and R. Kaptein, *Prog. Nucl. Magn. Reson. Spectrosc.*, 2014, **81**, 1–36.

[170] A. N. Pravdivtsev, A. V. Yurkovskaya, N. N. Lukzen, H.-M. Vieth and K. L. Ivanov, *Phys. Chem. Chem. Phys.*, 2014, **16**, 18707–18719.

[171] O. W. Sørensen, *J. Magn. Reson. (1969)*, 1990, **86**, 435–440.

[172] M. H. Levitt, *J. Magn. Reson. (1969)*, 1992, **99**, 1–17.

[173] M. H. Levitt, *J. Magn. Reson.*, 2016, **262**, 91–99.

[174] S. S. Roy, J.-N. Dumez, G. Stevanato, B. Meier, J. T. Hill-Cousins, R. C. Brown, G. Pileio and M. H. Levitt, *J. Magn. Reson.*, 2015, **250**, 25–28.

[175] P. R. Bunker and P. Jensen, *Molecular Symmetry and Spectroscopy, 2nd Ed.*, NRC Research Press, Ottawa, 2006.

[176] M. Icker and S. Berger, *J. Magn. Reson.*, 2012, **219**, 1–3.

[177] M. Icker, P. Fricke and S. Berger, *J. Magn. Reson.*, 2012, **223**, 148–150.

[178] M. Icker, P. Fricke, T. Grell, J. Hollenbach, H. Auer and S. Berger, *Magn. Reson. Chem.*, 2013, **51**, 815–820.

[179] F. A. L. Anet and M. Kopelevich, *J. Am. Chem. Soc.*, 1989, **111**, 3429–3431.

[180] A. Restelli and J. S. Siegel, *J. Am. Chem. Soc.*, 1992, **114**, 1091–1092.

[181] B. D. Allen, and D. J. O'Leary, *J. Am. Chem. Soc.*, 2003, **125**, 9018–9019.

[182] B. D. Allen, J.-C. Cintrat, N. Faucher, P. Berthault, B. Rousseau and D. J. O'Leary, *J. Am. Chem. Soc.*, 2005, **127**, 412–420.

[183] S. J. Elliott, L. J. Brown, J.-N. Dumez and M. H. Levitt, *J. Magn. Reson.*, 2016, **272**, 87–90.

[184] O. M. Ogba, S. J. Elliott, D. A. Kolin, L. J. Brown, S. Cevallos, S. Sawyer, M. H. Levitt and D. J. O'Leary, *J. Org. Chem.*, 2017, **82**, 8943–8949.

[185] G. Binsch and G. R. Franzen, *J. Am. Chem. Soc.*, 1969, **91**, 3999–4000.

[186] F. A. L. Anet and M. Kopelevich, *J. Chem. Soc., Chem. Commun.*, 1987, **0**, 595–597.

[187] D. A. Forsyth and J. A. Hanley, *J. Am. Chem. Soc.*, 1987, **109**, 7930–7932.

[188] D. A. Forsyth and V. Prapansiri, *Tetrahedron Lett.*, 1988, **29**, 3551–3554.

[189] P. Morse, *Phys. Rev.*, 1929, **34**, 57–64.

[190] D. Lide, *CRC Handbook of chemistry and physics 87th edition*, Taylor and Francis, Oxford, UK, 2006.

[191] P. Atkins and J. de Paula, *Atkins Physical Chemistry*, University Press, Oxford, UK, 2014.

[192] J. Bigleisen, *J. Chem. Phys.*, 1949, **17**, 675–678.

[193] K. Laidler, *Chemical Kinetics 3rd Edition*, Harper and Row, New York, USA, 1987.

[194] W. Saunders and L. Melander, *Reaction Rates in Isotopic Molecules*, Wiley, New York, USA, 1981.

[195] A. Abragam, *Principles of Nuclear Magnetism*, Clarendon Press, Oxford, 1961.

[196] E. R. Henry and A. Szabo, *J. Chem. Phys.*, 1985, **82**, 4753–4761.

[197] D. E. Woessner, *J. Chem. Phys.*, 1962, **36**, 1–4.

[198] SpinDynamica, *SpinDynamica code for Mathematica, programmed by Malcolm H. Levitt, with contributions by Jyrki Rantaharju, Andreas Brinkmann, and Soumya Singha Roy, available at www.spindynamica.soton.ac.uk.*

[199] A. Jerschow, *Prog. Nucl. Magn. Reson. Spectrosc.*, 2005, **46**, 63–78.

[200] K. Beshah, E. T. Olejniczak and R. G. Griffin, *J. Chem. Phys.*, 1987, **86**, 4730–4736.

[201] A. Mittermaier and L. E. Kay, *J. Am. Chem. Soc.*, 1999, **121**, 10608–10613.

[202] M. Prager and A. Heidemann, *Chem. Rev.*, 1997, **97**, 2933–2966.

[203] A. Horsewill, *Prog. Nucl. Magn. Reson. Spectrosc.*, 1999, **35**, 359–389.

[204] R. B. Calvert and J. R. Shapley, *J. Am. Chem. Soc.*, 1978, **100**, 7726–7727.

[205] A. Bornet, R. Melzi, A. J. Perez Linde, P. Hautle, B. van den Brandt, S. Jannin and G. Bodenhausen, *J. Phys. Chem. Lett.*, 2013, **4**, 111–114.

[206] Q. Chappuis, J. Milani, B. Vuichoud, A. Bornet, A. D. Gossert, G. Bodenhausen and S. Jannin, *J. Phys. Chem. Lett.*, 2015, **6**, 1674–1678.

[207] K. W. Lipsø, S. Bowen, O. Rybalko and J. H. Ardenkjær-Larsen, *J. Magn. Reson.*, 2017, **274**, 65–72.

[208] R. Buratto, D. Mammoli, E. Chiarparin, G. Williams and G. Bodenhausen, *Angew. Chem. Int. Ed.*, 2014, **53**, 11376–11380.

[209] R. Buratto, A. Bornet, J. Milani, D. Mammoli, B. Vuichoud, N. Salvi, M. Singh, A. Laguerre, S. Passemard, S. Gerber-Lemaire, S. Jannin and G. Bodenhausen, *ChemMedChem*, 2014, **9**, 2509–2515.

[210] B. Vuichoud, A. Bornet, F. de Nanteuil, J. Milani, E. Canet, X. Ji, P. Miéville, E. Weber, D. Kurzbach, A. Flamm, R. Konrat, A. D. Gossert, S. Jannin and G. Bodenhausen, *Chem. – A Eur. J.*, 2016, **22**, 14696–14700.

[211] A. Bornet, J. Milani, B. Vuichoud, A. J. P. Linde, G. Bodenhausen and S. Jannin, *Chem. Phys. Lett.*, 2014, **602**, 63–67.

[212] A. Bornet, A. Pinon, A. Jhajharia, M. Baudin, X. Ji, L. Emsley, G. Bodenhausen, J. H. Ardenkjaer-Larsen and S. Jannin, *Phys. Chem. Chem. Phys.*, 2016, **18**, 30530–30535.

[213] G. R. Fulmer, A. J. M. Miller, N. H. Sherden, H. E. Gottlieb, A. Nudelman, B. M. Stoltz, J. E. Bercaw and K. I. Goldberg, *Organometallics*, 2010, **29**, 2176–2179.

[214] M. C. D. Tayler and M. H. Levitt, *Phys. Chem. Chem. Phys.*, 2011, **13**, 9128–9130.

[215] J. Cavanagh, W. J. Fairbrother, A. G. Palmer-III and N. Skelton, *Protein NMR Spectroscopy, 1st Ed.*, Academic Press, Massachusetts, 1995.

[216] A. Gryff-Keller and D. Kubica, *J. Phys. Chem. A*, 2012, **116**, 9632–9638.

[217] E. Chiavazza, E. Kubala, C. V. Gringeri, S. Düwel, M. Durst, R. F. Schulte and M. I. Menzel, *J. Magn. Reson.*, 2013, **227**, 35–38.

[218] D. Kubica, A. Wodyński, A. Kraska-Dziadecka and A. Gryff-Keller, *J. Phys. Chem. A*, 2014, **118**, 2995–3003.

[219] A. Gryff-Keller, S. Molchanov and A. Wodyński, *J. Phys. Chem. A*, 2014, **118**, 128–133.

[220] P. Bernatowicz, D. Kubica, M. Ociepa, A. Wodyński and A. Gryff-Keller, *J. Phys. Chem. A*, 2014, **118**, 4063–4070.

[221] H. Hogben, M. Krzystyniak, G. Charnock, P. Hore and I. Kuprov, *J. Magn. Reson.*, 2011, **208**, 179–194.

[222] A. Shaka, J. Keeler and R. Freeman, *Journal of Magnetic Resonance (1969)*, 1983, **53**, 313–340.

[223] F. Schick, *Eur. Radiol.*, 2005, **15**, 946–959.

[224] J. F. Dechent, L. Buljubasich, L. M. Schreiber, H. W. Spiess and K. Munnemann, *Phys. Chem. Chem. Phys.*, 2012, **14**, 2346–2352.

[225] R. Buratto, D. Mammoli, E. Canet and G. Bodenhausen, *J. Med. Chem.*, 2016, **59**, 1960–1966.

[226] K. Nagashima, D. K. Rao, G. Pagès, S. S. Velan and P. W. Kuchel, *J. Biomol. NMR*, 2014, **59**, 31–41.

[227] R. Sarkar, P. Ahuja, D. Moskau, P. R. Vasos and G. Bodenhausen, *Chem. Phys. Chem.*, 2007, **8**, 2652–2656.

[228] *UK patent application 1710181.7*.

[229] A. Brinkmann and M. H. Levitt, *J. Chem. Phys.*, 2001, **115**, 357–384.